UNIVERSITA' DEGLI STUDI DI PADOVA

Sede Amministrativa: Università degli Studi di Padova
Sede Consorziata: Università degli Studi di Trieste

Dipartimento di Ingegneria Chimica

SCUOLA DI DOTTORATO DI RICERCA IN INGEGNERIA INDUSTRIALE
INDIRIZZO: INGEGNERIA CHIMICA
CICLO XXI

MULTI-SCALE MOLECULAR MODELLING FOR ENVIRONMENTAL SYSTEMS

Direttore della Scuola: Ch.mo Prof. Paolo Bariani
Supervisore: Ch.mo Prof. Maurizio Fermeglia

Dottorando: Paolo Cosoli

TABLE OF CONTENTS

Summary

This thesis aims at exploring the potentialities of multiscale molecular simulation techniques for studying phenomena and processes of environmental interest. Multiscale molecular simulation techniques represent the bond among different computational techniques which operate on different time and length scales. These techniques are able to obtain different series of information in the thermodynamic, chemical or physical field. Continuity is made possible by the possibility of using output data for a system described at a higher (or lower) scale as input data for different simulation, at different scales, to obtain other sets of information. In this way it is always possible, at least theoretically, to describe or predict systems (or processes) behaviours starting from sub-atomic levels (quantum-mechanics) up to finite element simulations or process simulations for macroscopic properties calculations.

Today this use is relatively common and it is in continuous growth for material and life science applications. It offers certain advantages of time and money savings, and reveals also new potentialities, thanks to the possibility of studying phenomena which are difficult to observe with traditional experimental sessions.

The application to chemical – environmental engineering is a wide and original field itself, as it was not treated previously in an explicit way by other studies. Thus, this work has the aim of verifying the applicability and adaptability of the most commonly employed techniques at different scales: quantum-mechanics, molecular mechanics and dynamics, Monte Carlo methods, mesoscale, finite element methods. Due to the enormous potentialities offered by these techniques, we also wanted to demonstrate the advantages of their use in three main areas, defined as the main areas for identifying the environmental engineering applications. The final goal consists in defining and limiting the possibilities of applications in such huge, heterogeneous and multidisciplinary sector, and verifying if and when procedures developed for specific cases could be replied and / or generalised.

After a first description of the state of the art, relative to the molecular simulation techniques applications in the environmental engineering field, the thesis describes the most commonly employed molecular simulation techniques. For quantum-mechanics techniques, *ab initio* Hartree-Fock methods, Density Functional Theory and semiempirical methods are described. Base concepts and characterising equations of classic molecular mechanics and dynamics (MM/MD), and Monte Carlo (Canonical, Grand Canonical, Reactive Monte Carlo) methods at atomistic level are described. At mesoscale level, Dissipative Particle Dynamics (DPD) and Mesodyn methods are described. Then, for the finite element methods (FEM, or micro-FEM), principles and application fields of Mesoprop software (fixed grid system discretisation) and Palmyra (variable grid system discretisation) are presented.

The applications described in this thesis are described in order to try to represent the following representative areas of interest:

- Recycling and requalification of scrap materials
- Pollution removal
- Description and modelling of pollution phenomena

Inside each area a specific application field was chosen. For the first area, the study deals with the requalification of polymeric material in food packaging (bottles) to delay the end of life of the material and increase their duration. In this area the problem of recycling and requalification of scrap material of the automotive industry (rear lamp components) was also afforded. The problem regarded polymer blends and nanocomposites. Pollution removal from gaseous streams by adsorption on various matrices (crystalline and disordered structures) was the task of the second area. We started from simpler, single gas adsorption and we progressively afforded more complex (and realistic) systems with mixtures, non-ideality conditions, and simultaneous adsorption and reaction phenomena. Then, in the last area of interest, we studied the pesticide contamination into soils, by examining adhesion and diffusion phenomena of contaminants.

Therefore, we developed different kinds of case studies with practical interests, with the scope of verifying the applicative potentialities of multiscale simulation, and of testing the versatility and the possibility to implement the procedures. Thus, as a general statement, we proceeded from simple cases up to examining more and more realistic and complex systems.

In the first part we therefore afforded the problem of recycling and requalification of scrap materials of industrial interest. The first case regarded the barrier effect improvement of PET (a highly recyclable polymer commonly used for food packaging) by blending the same with 8 and 20 % of PEN; this aim also implies a polymer life improvement and final disposal procrastination. We studied polymer characteristics at atomistic level (MM/MD) to obtain fundamental parameters to be used for morphologic studies in the mesoscale. Mesoscale simulation confirmed some common experimental evidences: PET and PEN are normally immiscible, although repeated or long extrusions lead to the formation of block copolymers, due to transesterification reactions. PET/PEN copolymers become more random in nature as long as the extrusion process proceeds, and these blocks act as compatibilisers. Simulations have been carried out with an improving degree of randomness (i.e. increasing the presence of block copolymers), up to the ideal situation, in which PEN is present only in the copolymer. It can be noticed how, from a complete phase segregation (no transesterification) the system can evolve to a situation of a quite perfect miscibility (complete transesterification). In the

following phase, with FEM simulations we obtained permeability and diffusivity of mixtures at different conditions, by using density distributions obtained from mesoscale. Permeability and diffusivity data of pure polymers were obtained by experimental literature data. A crystalline, impermeable fraction, which is typical of the two polymers, was also considered. Results demonstrated how barrier effects to gases (oxygen) are evident, but not too pronounced; moreover, when phase segregation occurs the barrier effect is higher, due to the fact that the formation of PEN clusters hinder gas molecule pathways.

In the second case we started from the ABS (acrylonitrile – butadiene – styrene) blend, studying morphology and mechanical properties (Young's modulus). We studied the possibility of recycling ABS, PC, PMMA (commonly used for lamps in the automotive sector) scraps in blends. Compositions, extrusion temperature and mechanical properties of single components were known previously. Morphology and mechanical properties predictions have been obtained by following procedures very close to the ones of the previous case, even if they have been applied for different systems and properties. Simulation results revealed a specific ABS structure (confirmed by literature data): a "rubbery" phase, given by the presence of butadiene, partly segregates in the form of spherical domains and is surrounded by a rigid phase (styrene-acrylonitrile). This kind of structure is maintained even when ABS is blended with PC and/or PMMA. Therefore, we evaluated the mechanical properties of the PC/ABS/PMMA blend, where the percentage of PC was fixed (55%) and the ratio ABS/PMMA) was variable. Even in this case, FEM simulations to determine Young's modulus obtained results very close to the ones given by experimental tests on the same blends.

The following part of this work was dedicated to the requalification of the scrap, by the transformation of the ABS into a nanocomposite. As filler we considered the montmorrillonite clay (MMT), whose layers are commonly exfoliated by the introduction of compatibilisers (quats) in order to facilitate the polymer intercalation for the subsequent complete exfoliation and MMT dispersion. Thus, atomistic simulations have been performed to evaluate the ABS compatibility inside the ABS/MMT/quat complex (by the binding energy calculation for the considered complexes), and to determine the spacing between the MMT channels, given by different quats. In this way the best quat (cloisite 20A) by thermodynamics and spacing evaluations was chosen; ABS behaviour inside the nanocomposite was also studied. In fact, as also shown by microscope images available in literature, it usually happens that MMT exfoliates only partly. Stacks of MMT lamellae with an intercalation of the rigid phase (styrene-acrylonitrile, SAN) are created; these blocks are dispersed in a rigid (SAN)

phase, while the rubbery phase is confined in spherical domains, outsides the stacks. Once the MMT percentage and the exfoliation degree have been fixed, this kind of structure has been recreated for FEM simulations to calculate Young's modulus; once again, results compared with experimental data revealed a good agreement.

The second area of interest regarded the pollution removal of gaseous streams by adsorption. Employed methods have been quantum-mechanics techniques, atomistic Monte Carlo, and MM/MD. In this phase of the research, we considered different case-studies, progressively more complex.

We started with single gas systems (VOCs) to be removed by adsorption on non-polar zeolites. Adsorption isotherms have been obtained with Grand Canonical Monte Carlo (GCMC) simulations for each considered zeolite and for each pollutant; thus it was possible to determine a ranking of the most suitable zeolite for VOCs removal. Data obtained have then successfully been fitted with the well known, robust Langmuir model.

In the following step we considered a typical gas mixture (biogas, mainly constituted by CH_4 and CO_2), from where a component (H_2S), which was present in small quantities, had to be removed by adsorption: a more realistic situation. Polar and non polar zeolites have been considered, and adsorption isotherms have been obtained with GCMC simulations both for H_2S only and for the mixture, considering also the zeolites selectivity. The best zeolite for H_2S removal was the NaY. Moreover, higher H_2S partial pressures lead to a competition for the adsorption sites in the zeolites, which is won by H_2S at the expenses of the less polar CH_4; on the other side, for non polar zeolites (MFI) this phenomenon does not take place, where selectivity for H_2S remains low. This behaviour is also confirmed and reinforced by the energy distribution and isosteric heats of adsorption calculations, but also by parallel experiments of deterministic MM/MD, where gas molecule trajectories and binding energies have been studied.

A further step was made in the following case study, where benzene removal from exhaust gases of combustion was examined with GCMC simulations. Two kinds of matrices have been considered for adsorption (non polar zeolite and a disordered structure, which was representative of an activated carbon). In this way, we were able to determine the best material, but also the optimal condition for adsorption (total pressure and temperature). Then, a simple, macroscopic fitting model for adsorption of mixtures was used (Sips model). The model gave good results from a qualitative point of view.

Finally, the last case study of this area regarded a more complex system, where NO_X reaction phenomena (dimerisation) took simultaneously place with adsorption on activated carbon

structures. Activated carbons have been previously modelled with the Hybrid Reverse Monte Carlo method (HRMC). The considered gas mixture was constituted of nitrogen monoxide (NO), together with its dimer $(NO)_2$. This study was conducted in collaboration with the Academy of Science of Prague, during the period of research in Czech Republic. A new, in-house developed software was used (Reactive Monte Carlo, RxMC), which was adapted to simulate at the same time reaction and adsorption phenomena. Data of the adsorption isotherms obtained for mixtures were then fitted with different macroscopic thermodynamic models commonly used for mixtures. The dimerisation reaction is shifted towards the reagent at normal, non confined condition (bulk phase), but it is much more pronounced in the confined phase (inside the pores) together with dimer adsorption, which is favoured by the presence of two centres of attraction. Then, the most effective thermodynamic models (qualitatively and quantitatively) have been the simplest and robust ones (Sips and Multisite Langmuir), as they describe better also isotherm behaviours for less ideal situations.

The last area of interest, the description of pollution phenomena, was afforded through the study of soil contamination by pesticide, in particular atrazine, in an ideal model of sandy, superficial and saturated soil. In this procedure, which combined Canonical Monte Carlo methods and NVT/NPT MM/MD methods, H_2O and atrazine molecules are inserted into the galleries between silica layers: an ideal atomistic model of inorganic soil only. We studied adhesion (by the binding energy evaluation for the complex silica-water-atrazine) and diffusion phenomena (calculation of self-diffusion coefficients) of atrazine, as a function of variable atrazine concentration (with fixed silica interlayer distance) and, in the second case, as a function of variable interlayer distances (with fixed atrazine concentration), to mimic a different porosity. Simulations revealed in both cases a partial tendency of atrazine to adhere to silica walls and to form aggregations, although the presence in the aqueous phase is thermodynamically more favoured. The result confirms the significant role played by the organic substance for the adsorption of this pesticide. Speaking about the diffusion, there is a moderate concentration dependency in the first case, while in the second case the influence of the interlayer distance is very strong, up to a constant, limit condition, where the diffusion coefficient reaches a plateau (maximum) and the silica layers can be seen at infinite distance, as if the atrazine was considered in water. These studies have been developed for one case of interest only, but they can be used or even implemented for analogous situations at different conditions, or used for system modelling with simulations at higher level (FEM).

As a conclusion, we demonstrated how the adopted procedures for each area of interest in the environmental field can be implemented for more realistic (and complex) systems, or can be

adapted for studies in similar contexts. Therefore, multiscale molecular simulation, if applied for the study in environmental fields, offers the same powerful advantages to the ones given for material or life science applications, and presents remarkable margins of improvement in the next decades.

Riassunto

Le finalità del presente lavoro di tesi riguardano l'esplorazione delle potenzialità della simulazione molecolare multiscala nello studio di fenomeni e processi di interesse nel campo ambientale. La simulazione molecolare multiscala rappresenta il legame tra un insieme di tecniche computazionali operanti su scale di tempi e distanze diverse; tali tecniche sono in grado di ottenere diverse informazioni di tipo termodinamico, chimico o fisico. La continuità è resa possibile dal fatto che i dati in uscita da un sistema a scala inferiore o superiore possono essere usati come dati di ingresso per una scala diversa. E' così sempre possibile, almeno in via teorica, descrivere o predire i comportamenti di un sistema o di un processo a partire da livelli sub-atomici (quantomeccanica) fino alle simulazioni agli elementi finiti, per il calcolo di proprietà macroscopiche, o alla simulazione di processo.

Tale impiego, oggi relativamente diffuso e in continua crescita nel campo dei materiali e delle scienze della vita, offre indubbi vantaggi di tipo economico e temporale e rivela anche nuove potenzialità per lo studio di fenomeni difficilmente osservabili tramite tradizionali sessioni sperimentali.

L'applicazione al campo dell'ingegneria chimica ambientale è di per sé un argomento vasto e originale, non essendo stato trattato precedentemente in modo esplicito in lavori di tipo analogo. Lo studio si è proposto quindi di verificare l'applicabilità e l'adattabilità delle tecniche più comunemente utilizzate su scale diverse: quantomeccanica, dinamica e meccanica molecolare, metodi Monte Carlo, mesoscala, metodi agli elementi finiti e dimostrare, date le notevoli potenzialità espresse, i vantaggi delle stesse in tre macroaree, che potessero essere caratteristiche ed identificative dell'ingegneria ambientale. Ciò allo scopo di circoscrivere i possibili ambiti di intervento all'interno di un settore vasto, eterogeneo e intrinsecamente multidisciplinare, e verificare se e quanto le procedure sviluppate per casi specifici possano essere replicate e generalizzate.

Dopo una prima descrizione dello stato dell'arte relativo alle applicazioni delle tecniche di simulazione molecolare in campo ambientale, si descrivono le tecniche di simulazione più comunemente utilizzate. Per la quantomeccanica vengono descritti i metodi *ab initio* (Hartree – Fock), la Density Functional Theory e i metodi semiempirici. Si enunciano i concetti base e le equazioni caratteristiche dei metodi di meccanica e dinamica molecolare classica (MM/MD) e il metodo Monte Carlo (insiemi Canonico e gran Canonico, Reactive Monte Carlo) per simulazioni su scala atomistica. A livello di mesoscala, vengono descritti i metodi impiegati in DPD (Dissipative Particle Dynamics) e Mesodyn, mentre per ciò che concerne i metodi agli elementi finiti (FEM, o micro-FEM) vengono descritti i principi e i campi di

applicazione dei software Mesoprop (discretizzazione degli elementi con griglia fissa) e Palmyra (a griglia variabile).

La tesi, nella sua parte applicativa, affronta quindi le seguenti tre macroaree, rappresentative di questo campo:

- Il riciclaggio e la riqualificazione dei materiali di scarto
- La rimozione di inquinanti
- La descrizione e la modellazione di fenomeni di inquinamento

All'interno di ogni area è stato scelto un possibile settore di interesse; Per la prima area, lo studio ha riguardato la riqualificazione di materiale polimerico per packaging alimentare (bottiglie) in modo tale da procrastinarne il periodo d'uso e aumentarne la durata. Sempre in quest'area, inoltre, è stato affrontato il problema del recupero e della riqualificazione del materiale di scarto dell'industria automobilistica (corpo fanale), passando dunque dalle miscele polimeriche ai nanocompositi. Nella seconda area, ci si è dedicati allo studio per la rimozione di inquinanti da *stream* gassosi tramite adsorbimento su matrici cristalline e non; ciò, partendo dapprima da un unico componente, fino ad arrivare a miscele più complesse, con fenomeni di non idealità e adsorbimento contemporaneo a reazione. Infine, la terza parte ha riguardato lo studio specifico della contaminazione da pesticidi (fenomeni di adesione e diffusione) in terreni.

Si sono quindi sviluppati dei casi di studio di tipo diverso, ma di interesse pratico, con il duplice scopo di verificare le potenzialità applicative della simulazione multiscala, ma anche di testare la duttilità e l'implementabilità delle procedure. In linea generale, dunque, da un caso più semplice si è passati progressivamente ad esaminare sistemi più complessi e realistici.

La prima parte dello studio ha dunque riguardato il problema del riciclaggio e della riqualificazione di materiali di scarto, in particolare di materiali di interesse industriale. Il primo caso ha rappresentato il tentativo di aumentare l'effetto barriera del PET (polimero tipicamente usato per il packaging, ed altamente riciclabile), tramite la miscelazione del PET stesso con PEN (all'8 e al 20%), aumentandone quindi anche la durata e procrastinandone quindi il suo smaltimento. Si sono studiate le caratteristiche dei due polimeri a livello atomico (MM/MD), in modo da ricavarne parametri essenziali per lo studio della morfologia della miscela a livello di mesoscala. Le simulazioni di mesoscala hanno confermato quanto normalmente emerge da prove sperimentali: PET e PEN sono sostanzialmente immiscibili. Tuttavia, estrusioni ripetute o dalla lunga durata portano alla formazione, mediante reazioni di

transesterificazione, di copolimeri a blocchi (dai blocchi progressivamente più random), che fungono da compatibilizzanti. Si sono quindi svolte simulazioni con grado crescente di randomness (con presenza quindi crescente di copolimero a blocchi), fino ad arrivare ad una situazione ideale, in cui tutto il PEN viene assorbito nel copolimero. Si nota quindi come, da una totale segregazione di fase (PET/PEN senza transesterificazione) si passi, nel caso ideale con completa transesterificazione, ad una miscibilità pressoché perfetta. Nella fase successiva, utilizzando dati sperimentali di letteratura di solubilità e diffusività di PET e PEN (puri) all'ossigeno, si sono svolte simulazioni di tipo FEM partendo dalle distribuzioni di densità ottenute in mesoscala, allo scopo di ottenere permeabilità e diffusività delle miscele. E' stata anche introdotta una frazione di fase cristallina (impermeabile ai gas), caratteristica dei due polimeri. Si nota come l'aumento dell'effetto barriera, pur evidente, non sia molto marcato, e come in realtà nei casi in cui la segregazione di fase è più marcata l'effetto barriera sia maggiore, a causa della presenza di cluster di PEN che rallentano il cammino delle molecole di gas.

Nel secondo caso si è partiti dall'ABS, studiandone morfologia e caratteristiche meccaniche (modulo di Young). Si è, infatti, studiata la possibilità di riutilizzare ABS, PMMA e PC (ampiamente utilizzati come materiali per il corpo fanale) di scarto miscelandoli assieme e valutandone le caratteristiche. Composizioni, temperatura di estrusione e caratteristiche meccaniche dei singoli componenti dei materiali di scarto erano note. In questo caso di studio, inoltre, le procedure adottate sono state del tutto analoghe al caso precedente, pur studiando materiali e proprietà del tutto diverse. I risultati delle simulazioni hanno rivelato una morfologia particolare dell'ABS (confermata anche da dati di letteratura): vi è una fase gommosa, data dalla presenza del butadiene, che forma domini di tipo sferoidale circondati dalla fase rigida, con parziale segregazione di fase. Le strutture di tali domini vengono mantenuti anche nel caso di miscele con PC e/o PMMA. A questo punto, si sono valutate le caratteristiche meccaniche della miscela PC/ABS/PMMA, con frazione di PC costante (55%) e frazione ABS/PMMA variabile. Anche in questo caso, le simulazioni FEM per la determinazione del modulo di Young hanno dimostrato un'ottima rispondenza con i dati sperimentali ottenuti sulle stesse miscele.

Una fase successiva di questo caso di studio ha invece riguardato la riqualificazione dell'ABS di scarto, tramite trasformazione in nanocomposito. Come filler si è considerata la montmorillonite (MMT), che normalmente viene esfoliata tramite l'ausilio di un compatibilizzante (quat), per procedere poi all'intercalazione del polimero, per la successiva,

completa esfoliazione e dispersione della MMT. Si sono svolte dunque delle simulazioni atomistiche per valutare la compatibilità dell'ABS all'interno del sistema ABS/MMT/quat (tramite il calcolo delle energie di binding dei complessi considerati) e per determinare la spaziatura tra le gallerie di MMT, data dai diversi tipi di quat considerati. In tal modo è stato possibile scegliere il miglior quat (nel caso specifico, la cloisite 20A) in termini termodinamici e di spaziatura offerta, e di studiare anche il comportamento dell'ABS all'interno del nanocomposito. Ciò che accade, infatti, confortato anche da immagini al microscopio disponibili in letteratura, è che l'esfoliazione della MMT è solo parziale: si formano infatti delle pile di lamelle di MMT, al cui interno vi è la fase rigida (stirene-acrilonitrile, SAN); tali blocchi di lamelle sono immersi in una matrice di SAN, mentre la fase gommosa rimane confinata in grandi domini sferoidali all'esterno delle pile stesse. Si è dunque ricreata tale struttura, allo scopo di valutarne le caratteristiche meccaniche tramite simulazioni FEM, una volta fissato il grado di esfoliazione e la percentuale di MMT. Le simulazioni hanno dimostrato una buona rispondenza con i dati sperimentali disponibili.

La seconda area di interesse ha riguardato la rimozione di inquinanti da stream gassosi tramite adsorbimento. I metodi adottati sono stati principalmente tecniche di quanto-meccanica, Monte Carlo (a livello atomistico) e MM/MD. Nel corso di questa fase della ricerca, si sono considerati casi diversi, via via più complessi.

Si è inizialmente partiti da sistemi con gas singolo (VOC) da rimuovere tramite adsorbimento su zeoliti non polari. Si sono ottenute dunque le isoterme di adsorbimento, tramite il metodo Monte Carlo Gran Canonico (GCMC) per ogni zeolite ed ogni VOC considerato, e, dunque, un ranking per la scelta delle zeoliti più idonee per la rimozione. I dati ottenuti sono stati infine interpolati con un modello termodinamico di fitting semplice ma robusto (Langmuir), che si è dimostrato efficace nel descrivere le isoterme di adsorbimento.

Nel passo successivo si è considerata una miscela (biogas, costituito prevalentemente da CH_4 e CO_2) da cui rimuovere un componente, presente in piccole quantità (H_2S), tramite adsorbimento su zeoliti polari e non polari: una situazione dunque più realistica. Si sono confrontate le isoterme per il gas singolo (H_2S) tramite metodo GCMC e per la miscela, considerando anche la selettività delle zeoliti stesse. La migliore zeolite per l'adsorbimento di H_2S è risultata essere la NaY. Inoltre, pressioni parziali di H_2S superiori comportano una competizione per i siti di adsorbimento, vinta nelle zeoliti polari dall'H_2S a spese del metano, meno polare; il fenomeno non si verifica invece in zeoliti non polari (MFI), dove per l'H_2S la selettività nei confronti del CH_4 rimane bassa. Il fenomeno, congruamente dimostrato e

spiegato anche da dati quali distribuzioni di energia e calori isosterici di adsorbimento, è stato spiegato e dimostrato anche tramite simulazioni di tipo deterministico (studio delle traiettorie e delle energie di binding in simulazioni di MM/MD) considerando la zeolite NaY.

Il caso di studio successivo ha riguardato la rimozione del benzene da un prototipo di stream gassoso (gas esausti post-combustione) tramite uso del metodo GCMC. Si sono studiate due tipi di matrici (zeolite non polare, MFI, e una struttura disordinata, rappresentativa di un carbone attivo), in modo tale, in questo caso, di effettuare la scelta del materiale più idoneo e delle condizioni di processo ottimali (temperatura e pressione totale). Infine, si è utilizzato un semplice modello macroscopico di fitting per miscele delle isoterme di adsorbimento, che ha dato risultati qualitativamente più che accettabili (modello di Sips).

L'ultima fase è stata dedicata allo studio di un sistema ulteriormente complesso, con fenomeni di contemporanea reazione di NO_X (dimerizzazione) ed adsorbimento su carboni attivi. Le strutture dei carboni attivi sono state precedentemente ottenute tramite il metodo Hybrid Reverse monte Carlo (HRMC). La miscela di gas considerata è stata il monossido di azoto (NO) assieme al suo dimero, $(NO)_2$. Tale studio è stato svolto in collaborazione con l'Accademia delle Scienze, durante il periodo all'estero a Praga. Si è utilizzato un nuovo tipo di software (Reactive Monte Carlo, RxMC), adattato per simulare fenomeni simultanei di reazione e adsorbimento. I dati (isoterme di adsorbimento) così ottenuti per le miscele sono poi stati sottoposti ad un fitting con i modelli termodinamici macroscopici più utilizzati per le miscele. La reazione di dimerizzazione, poco spostata verso la produzione di dimero in condizioni normali (fase *bulk*, non confinata) è estremamente pronunciata in fase confinata (nei pori dei carboni attivi), analogamente all'assorbimento del dimero, favorito dalla presenza di due centri di attrazione. Infine, i modelli termodinamici migliori in termini qualitativi e quantitativi, in grado di descrivere meglio i comportamenti delle situazioni meno ideali, sono risultati i modelli più semplici e robusti (Sips e Multisite Langmuir).

L'ultimo settore di interesse è stato affrontato mediante lo studio della contaminazione di terreni da pesticidi, in particolare di terreni sabbiosi saturi e superficiali, contaminati da atrazina. La procedura, che combina simulazioni NPT/NVT di MM/MD e Monte Carlo (insieme canonico), prevede l'inserimento delle molecole di atrazina e di acqua all'interno delle gallerie presenti tra gli strati di silice, un modello ideale costituito dalla sola matrice inorganica. Si sono studiati in tal modo i fenomeni di adesione (tramite la valutazione delle energie di binding del complesso H_2O-atrazina-silice) e diffusione dell'atrazina, in funzione di una concentrazione variabile (e a distanza tra gli strati di silice fissata) e con concentrazioni

costanti, ma distanza tra gli strati variabili, in modo da simulare una porosità variabile. Le simulazioni hanno evidenziato una parziale tendenza dell'atrazina ad aderire alle pareti di silice e a formare aggregazioni, privilegiando tuttavia, dal punto di vista termodinamico, una presenza in fase acquosa; il risultato conferma quindi il ruolo preponderante della sostanza organica per l'assorbimento di tale pesticida. Per ciò che riguarda la diffusione, invece, è evidente una moderata dipendenza dalla concentrazione, e una più marcata dipendenza dalla distanza tra gli strati di silice, sino ad arrivare ad un plateau, in cui gli strati di silice sono posti a distanza infinita, e quindi l'atrazina si trova nell'acqua. Tali studi, sviluppati per un solo caso di interesse, possono essere utilizzati, se non implementati, per studiare situazioni analoghe, in condizioni diverse, ed i dati possono essere usati per modelli su scala maggiore (FEM).

In conclusione, si è dimostrato come le procedure adottate per ogni area di interesse in campo ambientale siano implementabili per sistemi via via più realistici (complessi) o adattabili a contesti simili. La simulazione molecolare multiscala, applicata allo studio di tematiche di interesse ambientale offre dunque analoghi, potenti vantaggi rispetto a quelli offerti per applicazioni nel campo dei materiali o delle scienze della vita, e presenta notevoli margini di crescita per i prossimi decenni.

Chapter 1

Introduction

Summary

In this chapter, the importance of the present research, its background and motivation are presented.

The aim of this thesis is to explore of the potentialities of the most common molecular simulation methods for the study of environmental applications, or for systems of environmental interest. For this study, we considered commercial and in-house developed software, or platforms in which different length and time scale methods are integrated.

Environmental implications of human activities, in particular of engineering fields, have received more and more attention in last decades, at a level in which they can no more be neglected by each field of scientific research, or in technical applications. At the same time, in recent years, thanks to the improved capabilities of processing speed or memory capacity in computers, a set of *in-silico* techniques had progressively gained much interest, due to the enormous advantages in time, money saving, and property disclosure both at "micro" and "macro" level.

Today these so-called multi-scale molecular simulation techniques are able to describe a great number of physical and chemical phenomena from the molecular level up to the real process, by a length and time scale integration, as described in following chapters. Thus, the possibility of coupling multi-scale molecular modelling techniques to the description of environmentally-related phenomena is something very attractive, although this field has not been fully investigated explicitly up to our days. After a description of the state of the art and the current available applications described in literature, we summarise the description of the most relevant simulation techniques in a scale-by-scale approach. In Figure 1.1 the general idea of the time and length scale involved in multi-scale molecular simulation techniques can be deduced.

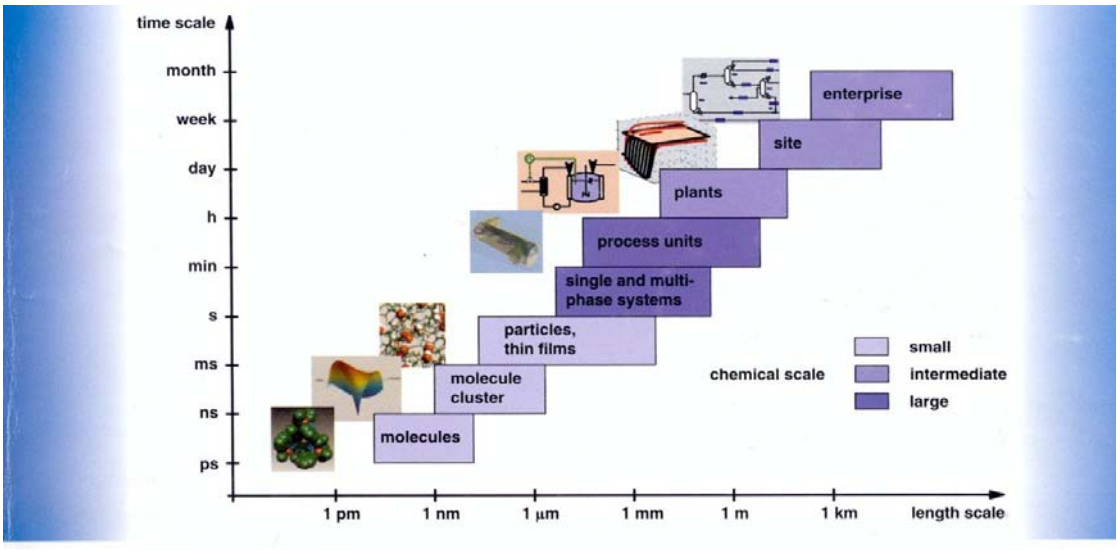

Figure 1.1: Time and length scales of multi-scale modelling.

As potentialities of this huge application field are not fully explored, we tried to take into consideration three different application areas, to give some examples of successful, technically applicable cases, and to show how generalisations to wider fields may be possible. Moreover, we aim at demonstrating the flexibility of the procedures specifically developed; therefore, these procedures can be applied or adapted to a wide range of similar kinds of calculations. In these cases, implementation of applied techniques to more complex cases has been also described, passing from simpler systems to more sophisticated ones, to show how multi-scale approach can be used as a powerful and versatile tool.

Due to the huge application field, the case-study presentations have been restricted, as the work was intended to cover three of the most representative areas of interest in chemical and environmental engineering; these have been:

- Polymer scraps recycling, material properties amelioration for industrial applications in the field of sustainable processes.
- Adsorption of different streams, both single-gas systems and mixtures, with or without reaction, by ordered and disordered structures, in the field of pollution removal
- Pollution pathways and behaviour, for polluted and saturated soils, in the field of transport and modelling of pollutants in the environment.

After each case discussion and generalisation, we present a final, general part of conclusions, where environmental applications of multi-scale molecular simulation techniques are examined, commented and discussed in their complex.

Chapter 2

Molecular simulation tools for environmental applications

Summary

In this chapter, a general overview of multi-scale molecular simulation potentialities for environmental applications is presented, together with some of the most relevant studies.

2.1 Molecular modelling and multi-scale modelling

Molecular simulation methods are computational techniques; they are able to describe molecular behaviour at specific thermodynamic conditions. They rely upon the theoretically exact or empirically determined description of energy contributions of each of the characteristic representative units, as electrons, atoms, group of atoms. Molecular simulation techniques are able to describe characteristic states or behaviours, up to some mechanical, physical or chemical properties of the examined systems.

Computer-aided simulation techniques provide a direct route from the microscopic details of a system to macroscopic properties of experimental and technological interest (Allen and Tildeslay, 1987). This also is why, as computational technology proceeded, scientist community started to develop more complex mathematical models to describe and mimic molecular systems behaviour; the first computer simulation of liquids was carried out more than 50 years ago (Allen and Tildesley, 1987; Frenkel and Smit, 1996). From that point, models describing vapour, solid (amorphous and crystalline) have been developed and used for practical studies.

Throughout the implementation of microscopic models, the continuous improvement of processing speed or memory capacity in computers is still confirming Moore's law (Wikipedia, 2008a); due to the huge improvement in hardware and software tools, today we can simulate (and investigate) systems which are more and more complex in a reasonable amount of time. This results in considerable time and money savings, as experimental trial-and-error efforts can be reduced.

Therefore, experimental results can be integrated with *in-silico* information; molecular modelling potentialities are not confined to property prediction or process optimisation, but can also give more insights to understand process mechanisms at molecular level, where experimental sessions are sometimes difficult to perform, if not impossible.

In the last decade, new progresses have been made thanks to the possibility of coupling and integrate different time and length scale models: the so-called multi (or many) scale modelling. The integration of different scale modelling techniques, due to the realisation of commercial, non-commercial or in house-developed platforms (OCTA, 2008; Accelrys, 2008; CULGI, 2008) has given the researchers the possibility to examine processes and phenomena from the very beginning (i.e. quantum mechanics, the description of a molecule with its

electrons) up to process (or phenomena) simulation software, a process that may be called message-passing multi-scale modelling. On the other side, theoretically, a reverse-mapping strategy can be used in a top-down time and length scale strategy (see Figure 1.1). These powerful approaches make one able to theoretically simulate a complete system, from electrons behaviour to the entire process.

Recent advances provide analytical and computational modelling frameworks to describe the mechanics of materials on scales ranging from the atomistic, through the microstructure or transitional, and up to the continuum. If fact, although higher scale modelling techniques (such as finite element methods) can lose some information in comparison with lower scales, it is quite obvious that large calculations with very complex systems are unfeasible, as they are time consuming and require bigger CPUs. Thus, this is one more reason for which multi-scale modelling approaches are recognized as valid tools to complement continuum and atomistic analyses methods (Ghoniem et.al., 2003).

Multi-scale information-passing philosophy is the core of multi-scale modelling idea: output data obtained from an upper (or lower) scale in terms of time and length scale are used as input data in a different scale, to obtain different properties (Figure 2.1). Thus in a few time there could be the hoped possibility to describe or design a process with a completely *in-silico* procedure.

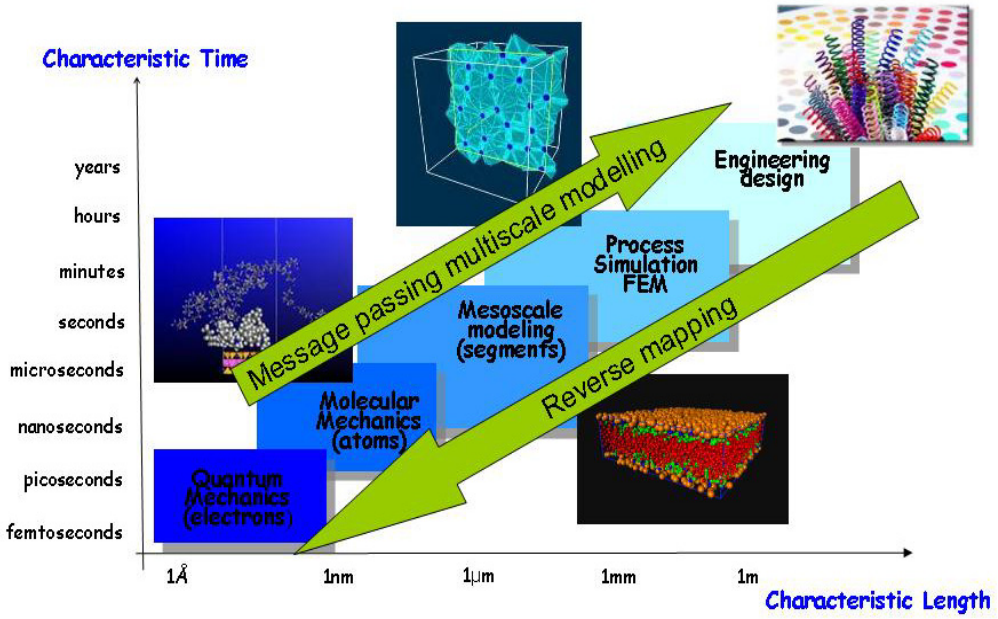

Figure 2.1: Time and length scales of multi-scale modelling.

For sake of correctness, it should be mentioned the fact that both terms "many-scale" and "multi-scale" simulation are used at present, thus they are not clearly unequivocal. In this work I will use the term "many-scale simulation" or "many-scale modelling".

2.2 Potentialities in environmental fields

Increasing knowledge and consciousness about environmental processes and sustainable technologies have determined, since some decades, new perspectives of research in the scientific community. Environmental implications of human activities are taken into account in each field of scientific research; thus, this holistic approach is widely recognized as necessary to mitigate effects and purpose alternatives in terms of impact mitigation. This approach has also determined a straightforward run to improve all the instruments, both practical and theoretical, which might be used to study human activities in relationship with the surrounding environment, in order to quantitatively / qualitatively describe, minimise or mitigate their effect, or to propose valid alternatives.

Thus, physics and chemistry are two of the most relevant sciences to be continuously used by engineers to describe phenomena and customize solutions. Analogously, even in the branch of environmental engineering or chemical environmental engineering nowadays this approach is very common. In recent years, there is also a new kind of research which has revealed great potentialities. This powerful tool is represented by the use of molecular simulation techniques, which involve molecular chemistry and physics and thermodynamics.

Recently (in the last two decades) the interest of the scientific community about molecular simulation techniques for applications in various chemical engineering fields has increased. At the same time, studies and applications about environmental fields gained more and more importance. Nowadays there is a huge interest in the enormous potentialities for discovering chemical properties, morphologies, and thermodynamics of different materials and processes for direct environmental applications (Charpentier, 2002). Moreover, the rapid developments of hardware/software available tools allow scientists to expand the scope and complexity of the investigated systems.

Nowadays, a rough division between areas of interest in molecular simulation defines two main branches as life science and material science, and a large part of commercial software is usually specifically developed for one of them. Nevertheless, molecular modelling potentialities are quite unique, and today several disciplines make large use of these techniques and are also focused on the scale integration. Till now there are no specific

reviews about molecular simulation for environmental applications. But there is a relatively large number of works where molecular simulation tools have been explicitly used for systems of environmental interest. Pollutant interaction with water, soil and atmosphere, pollutant confinement and removal, fate and pathways of contaminants and mitigation techniques for industrial process optimisation, and new, less impacting material studies are often investigated by the support of molecular simulation (sometimes with multi-scale molecular simulation) tools.

A more general, but not less important motivation is the fact that current models of environmental systems lack predictive capability. This is due to the fact that such systems are extraordinarily complex: length scales range spatially from the distance between molecules to roughly the diameter of the Earth; time scales range from fast chemical reactions to the age of the Earth. At these scales, different physical, chemical, and biological processes are not completely understood. Data are often sparse and noisy. Hence, development of environmental models both accurate and ranging over considerable time and space scales remains a major challenge.

Certain advantages gained by multi- scale molecular simulation techniques, such as time and money savings, the possibility of new insights at molecular level, the possibility of processing large number of data and performing in parallel a lot of *in-silico* experimental sessions are surely very attractive also for this kind of applications. Moreover, the possibility of studying thermodynamic, chemical and physical properties of the systems, give the chance of extending the investigation up to real scale properties and to generalise methods and procedures. This possibility offers a real support in terms of:

- process or phenomena prediction;
- choice of sustainable technologies;
- mitigation and pollutant removal techniques studies.

With this idea as the main focus of the work structure, in the next section we will examine some of the most recent and meaningful (not certainly exhaustive) researches in the already defined areas of interest. In Figure 2.2 a general scheme of possible areas of interest, together with the general potentialities of the software mentioned in this thesis are exposed.

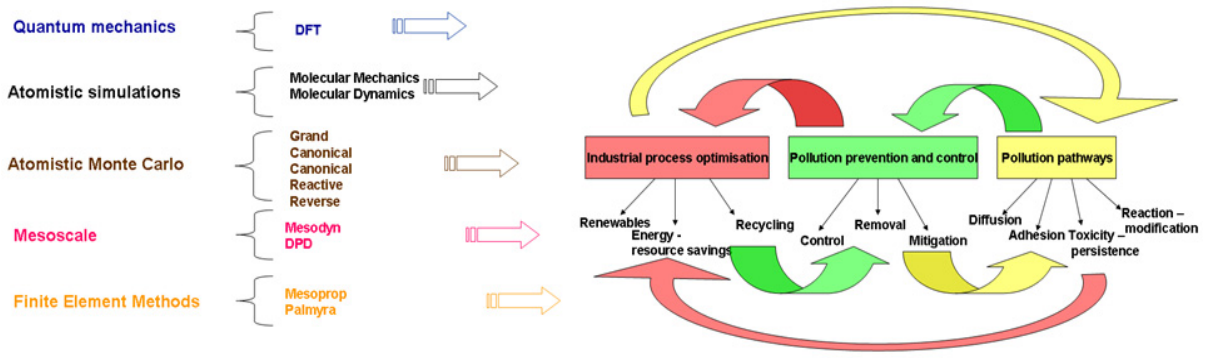

Figure 2.2: possible areas of interest for environmental application, and useful molecular simulation tools.

2.2 Applications

Most of the environmental applications of molecular simulation regard pollutant pathways and destinations. Adhesion, in particular adsorption phenomena (Dabrowski, 2001), diffusion and, generally, interaction in specific systems, such as soil like clays (among many others: Norman et.al., 2000; Shevchenko and Bailey, 1998; van Duin and Larter, 2001; Teppen et.al., 1997; Yu et.al., 2002), sand (Luo and Farrell, 2003), humic substances (Kubicki and Apitz, 1999; Alvarez-Puebla et.al., 2005; R. Sutton and G. Sposito, 2006), and water (Hendy, 2004; Reis et.al., 2005; Minofar et.al., 2005), but also in gaseous mixtures (Kotdavala et.al., 2007;), or in atmospheric pollution (Tong et.al., 2004) have been widely studied. More, there are also specific works about soil behaviour, as clay (bentonite) consolidation (Ichikawa et.al., 2004), clay swelling (M.B.M. Lupe, 1997), or even studies about clay barrier effects for radioactive waste disposal (Nakano et.al., 2006; Greathouse et.al., 2002).

In another category we can include the study of adsorption properties of pollutant confinement and removal, both from aqueous and gaseous phases: amorphous or crystalline membranes, in particular zeolites (among many others: Jobic et.al., 2004; Beauvais et.al., 2005; Yazaydin and Thompson, 2006; Guillemot et.al., 2007), carbon nanotubes (Kowalczyk and Holyst, 2008), polymers (Li et.al., 2008), silica gel (Vuong and Monson, 1998); some procedures have been specifically developed to mimic ion-exchange processes, electro-osmosis and reverse osmosis (Murad and Lin, 2002; Murad et.al., 1998). Again, from this category we can also mention the research about gas separation (carbon dioxide from methane, or multicomponent mixtures, for instance Akten et.al., 2003) or storage (such as carbon dioxide sequestration or hydrogen separation, Tenney and Lastoskie, 2006) for

industrial application and new ways for energy recovery (Yin et.al., 2000; Song and No, 2007; W.A. Goddard III et.al., 2006).

Catalysis studies have also to be mentioned, since they are important in various processes of environmental interests (again, W.A. Goddard III at.al., 2006). There are also several studies about the possibility of modelling disordered structures as activated carbons: it is possible to simplify the systems with the use of traditional codes (for instance, Wang et.al., 1999; Liu and Monson, 2005), but recently new simulation approaches and codes have been developed to mimic heterogeneous, disordered structures as they are (Thomson and Gubbins, 2000) and, very recently, to model systems where reaction and adsorption take place simultaneously (Johnson et.al., 1994; Lisal et.al., 2004). All these studies can concern the determination of physical, thermodynamic, chemical processes; they are able to identify a possible ranking of best process, procedures, materials, conditions from a pre-determined list, or purpose material or process modifications.

A certain number of publications also deal with reactions which have an environmental relevance, as compounds formation (among the most recent: Alexeev et.al., 2004; Bagchi and Ghosh, 2006).

Another crucial sector is the development of new materials, such polymer and polymer blends (Müller-Plathe, 2003), biodegradable polymers (Fermeglia et.al., 2004) and nanocomposites (Valavala and Odegard, 2003) with improved physical, mechanical or chemical properties that also allow extending their application, contribute to increase material life and recycling possibilities.

A different branch, which deals with environmental effects prediction (such as toxicity) of chemical compounds, should be mentioned, even if not treated in this thesis. These works make use of quantum chemistry models (Sandler et.al., 2002), or predictive models such as Quantitative Structure Activity Relationship (QSAR), where chemical structures are quantitatively correlated with a specific property, as chemical activity or reactivity (Leach, 2001). In some cases, QSAR have been used also to predict atmospheric pollutant persistency, mobility and reactivity (Gramatica and Papa, 2007; Papa et.al., 2007).

Now it should be clear how molecular simulation can be applied to multi-disciplinary studies that, implicitly or not, can reveal useful potentialities for property and process prediction, process customization, phenomena description, each of which have environmental relevance.

In fact, although the major part of this studies have been historically carried out in Chemical, Chemical Engineering, Physics departments or institutes, in recent years also Environmental departments, or agencies, are investing much more time and money in computational

techniques research; for instance, this is the case of the Environmental Protection Agency in the USA (National Center for Computational Toxicology (NCCT) of EPA's Office of Research and Development, 2008), or, in Italy, the Consiglio nazionale delle Ricerche (CNR, 2008).

The improvement in these sectors suggested us to develop specific investigation about computer-aided simulation multi-scale techniques in main areas of environmental technologies.

Chapter 3

Molecular simulation techniques

Summary

This chapter illustrates molecular simulation techniques used in this thesis, and a general description of hardware and software.

3.1 Quantum mechanics

Computational quantum chemistry methods are the most accurate molecular simulation techniques to describe molecular behaviours of atoms and molecules, where electrons are explicitly represented in the calculation. Most of the low-energy physics, chemistry, materials science and biology can be explained by the quantum mechanics (QM) of electrons and ions and that, in many cases, the properties and behaviour of materials derive from the quantum-mechanical description of events at the atomic scale. The ability of QM to predict the total energy, the atomic structure of a system of electrons and nuclei and, thus, chemical reaction investigation, is also an important benefit (Ghoniem et.al., 2003).

Due to the enormous number of theories and methods, the heaviness of mathematical concepts, and the relatively limited direct use of QM methods in this work, I will only provide a general overview and a brief description of some techniques, although a more detailed description of Density Functional Theory (DFT), which has been used in this work, is provided. All specific details of the employed procedures will be listed in Chapter 5, where QM has been used to calculate bond length and partial charges to be used in higher scale simulations.

The starting point for any discussion about QM methods is the time-independent form of the Schrödinger equation (Leach, 2001):

$$\left\{-\frac{\hbar^2}{2m}\nabla^2 + V\right\}\Psi(\vec{r}) = E\Psi(\vec{r}) \qquad [1.3]$$

Equation [1.3] refers to a single particle of mass m, moving through the space with position $\vec{r}$ at the time t, under the influence of an external field, V (e.g., the electrostatic potential of molecule nuclei); $\hbar$ is the Planck's constant divided by 2π, E is the energy of the particle and Ψ is the wavefunction, which is the characteristic of the particle motion; ∇^2 has the form:

$$\nabla^2 = \frac{\partial^2}{\partial x^2} + \frac{\partial^2}{\partial y^2} + \frac{\partial^2}{\partial z^2} \qquad [2.3]$$

And the left side of Equation [1.3] is often abbreviated to $H\Psi$, where H is the Hamiltonian operator (Leach, 2001).

It is well known that, with the exclusion of the simplest molecular species, Equation 1 can not be solved exactly. Thus, the Born-Oppenheimer approximation is usually introduced to decouple electronic motion from nuclei motion in the many-body wave function, in the form:

$$\Psi_{tot}(nuclei, electrons) = \Psi(electrons)\Psi(nuclei) \quad [3.3]$$

which means that the electrons respond instantaneously to any changes in the positions of the nuclei, due to their much smaller atomic mass; conversely, nuclei positions are considered as fixed.

Considering *N* electrons moving in a system with fixed nuclei, *H* takes the form (in atomic units):

$$H = \sum_{i=1}^{N} -\frac{1}{2}\nabla_i^2 + \sum_{i=1}^{N} v_{\sigma_i}(\vec{r}_i) + \frac{1}{2}\sum_i \sum_{i \neq j} \frac{1}{|\vec{r}_i - \vec{r}_j|} \quad [4.3]$$

where the first term is the kinetic energy operator, the second one is the one-electron spin-dependent external potential (e.g. the electron–nucleus interaction), and the third term represents the effect of the electron–electron interactions which poses the most difficult problem in any electronic structure calculation.

3.1.1 Hartree-Fock methods

Methods that do not include empirical or semi-empirical parameters in their equations are called *ab initio* methods, although solutions are not exact ones; they are all approximate quantum mechanical calculations. The simplest one is the Hartree-Fock (HF) approximate method, where the ground-state wavefunction and ground-state energy of a quantum many-body system can be determined by solving the Schrödinger's equation. The principle of the method assumes that the energy of a given wavefunction Ψ is higher or equal to the ground-state energy of the system; lower expectation energy values lead to better Schrödinger's solutions.

The solutions to the resulting non-linear equations behave as if each particle is subjected to the mean field created by all other particles. The equations are almost universally solved by means of an iterative, fixed-point type algorithm. In the restricted HF method, the atom or molecule is a closed-shell system where all orbitals (atomic or molecular) are doubly occupied, while in open-shell systems, some of the electrons are not paired.

As a general overview, from the Schrödinger's equation, we can assume, for a two-particle system:

$$\Psi(\vec{x}_1, \vec{x}_2) = \chi_1(\vec{x}_1)\chi_2(\vec{x}_2) \quad [5.3]$$

where the wave function of a many-particle system is approximated to the product of properly chosen wave functions (the one-particle wavefunction χ_i which depends on the position and

spin) of the individual particles, for which the position is given. As this wavefunction is not symmetric, it does not satisfy the Pauli Exclusion Principle (it is impossible for two identical fermions to occupy the same quantum state, i.e. in the same energetic level can coexist only two electrons, which must have opposed spin):

$$\Psi(\vec{x}_1,\vec{x}_2) = -\Psi(\vec{x}_1,\vec{x}_2) \qquad [6.3]$$

Thus, the problem is overcome by taking a linear combination of both Hartree products:

$$\Psi(x_1,x_2) = \frac{1}{\sqrt{2}}\{\chi_1(x_1)\chi_2(x_2) - \chi_1(x_2)\chi_2(x_1)\} = \frac{1}{\sqrt{2}}\begin{vmatrix}\chi_1(x_1) & \chi_2(x_1)\\ \chi_1(x_2) & \chi_2(x_2)\end{vmatrix} \qquad [7.3]$$

For an N electron system, the equation becomes the Slater determinant:

$$\Psi(x_1,x_2,...,x_N) = \frac{1}{\sqrt{N!}}\begin{vmatrix}\chi_1(x_1) & \chi_2(x_1) & ... & \chi_N(x_1)\\ \chi_1(x_2) & \chi_2(x_2) & ... & \chi_N(x_2)\\ ... & ... & ... & ...\\ \chi_1(x_N) & \chi_2(x_N) & ... & \chi_N(x_N)\end{vmatrix} \qquad [8.3]$$

The variational solution is assumed to be a linear combination of a finite number of basis functions, which are usually chosen to form an orthonormal set.

Applying the theorem that the value of a determinant is unchanged by any non-singular linear transformation, we may choose the χ_i to be an orthonormal set. We now introduce a Lagrange multiplier ε_i to impose the condition that the χ_i are normalised, and minimise with respect to the χ_i:

$$\frac{\partial}{\partial\chi}\left[\left\langle\hat{H}\right\rangle - \sum_j \varepsilon_j \int |\chi_j|^2 d\vec{r}\right] = 0 \qquad [9.3]$$

This simplifies the expressions for the orbitals χ_i. They reduce to a set of one-electron equations of the form:

$$-\frac{1}{2}\nabla^2\chi_i(\vec{r}) + V_{ION}(\vec{r})\chi_i(\vec{r}) + U(\vec{r})\chi_i(\vec{r}) = \varepsilon_i\chi_i(\vec{r}) \qquad [10.3]$$

where $U(\vec{r})$ is a non-local potential and the local ionic potential is denoted by V_{ION}. The one-electron equations resemble single-particle Schrödinger equations. The full HF equations are given by:

$$\varepsilon_i\chi_i(\vec{r}) = \left(-\frac{1}{2}\nabla^2 + V_{ION}(\vec{r})\right)\chi_i(\vec{r}) + \sum_j \int d\vec{r}' \frac{|\chi_j(\vec{r}')|^2}{|\vec{r}-\vec{r}'|}\chi_i(\vec{r}) - \sum_j \delta_{\sigma_i,\sigma_j}\int d\vec{r}' \frac{\chi_j^*(\vec{r}')\chi_i(r')}{|\vec{r}-\vec{r}'|}\chi_j(\vec{r}) \qquad [11.3]$$

The right hand side of the equations consists of four terms. The first and second are the kinetic energy contribution and the electron-ion potential. The third term, or Hartree term, is the simply electrostatic potential arising from the charge distribution of N electrons. As written, the term includes an unphysical self-interaction of electrons when $j = i$. This term is cancelled in the fourth, or exchange term. The exchange term results from our inclusion of the Pauli principle and the assumed form of the wavefunction. The effect of exchange is for electrons of like-spin to avoid each other. Each electron of a given spin is consequently surrounded by an "exchange hole", a small volume around the electron which like-spin electron avoid.

The aim of the method is to find the specific state for which energy is at its minimum; the problem is solved numerically and, due to the nonlinearities introduced by the HF approximation, the equations are solved using nonlinear iterative methods. A finite basis set, assumed to be approximately complete, is used to specifically approximate each one-particle wavefunction. Moreover, Post Hartree-Fock methods should be cited; they have been developed to improve on the HF methods or self-consistent field (SCF) method. They add electron correlation which is a more accurate way of including the repulsions between electrons than in the HF method where repulsions are only averaged.

3.1.2 Density Functional Theory

More versatile, usually accurate and computationally faster than *ab initio* methods are based on the density Functional Theory (DFT). The main concept of the theory assumes the energy of a molecule as generated by the electronic density, rather than the wavefunction. The many-body electronic wavefunction is replaced by with the electronic density as the basic quantity. Whereas the many-body wavefunction is dependent on $3N$ variables, three spatial variables for each of the N electrons, the density is only a function of three variables and is a simpler quantity to deal with both conceptually and practically.

DFT (Hohenberg and Kohn 1964) has been proven to be a very powerful quantum-mechanical method in investigating the electronic structure of atoms, molecules and solids. Here, the electron density $\rho(\vec{r})$, or spin density $\rho_\sigma(\vec{r})$, is the fundamental quantity, rather than the total wave function employed for example in HF theory. The DFT makes successful predictions of ground-state properties for moderately correlated electronic systems. DFT can provide accurate ground-state properties for real materials (such as total energies and energy differences, cohesive energies of solids and atomization energies of molecules, surface

energies, energy barriers, atomic structure, and magnetic moments) and provides a scheme for calculating them (Ghoniem et.al., 2003).

In what follows we give some of the essential DFT concepts, assuming that this will be by no means an exhaustive description. The bases of the idea are the correlations between fundamental molecular properties with electronic density. Hohenberg and Kohn (1964) proved that the total energy, including exchange and correlation, of an electron gas (even in the presence of a static external potential) is a unique functional of the electron density. The minimum value of the total-energy functional is the ground-state energy of the system, and the density that yields this minimum value is the exact single-particle ground-state density.

Kohn and Sham (1965) then showed how it is possible, formally, to replace the many-electron problem by an exactly equivalent set of self-consistent one-electron equations:

$$\left(-\frac{1}{2}\nabla^2 + \nu_\sigma(\vec{r}) + \int d^3r' \frac{\rho(\vec{r}')}{|\vec{r}-\vec{r}'|} + \nu_{xc}^{\sigma}(\vec{r})\right)\psi_{k\sigma}(\vec{r}) = \varepsilon_{k\sigma}\psi_{k\sigma}(\vec{r}) \qquad [12.3]$$

where $\Psi_{k\sigma}$ are the Kohn–Sham orbitals, and the spin-dependent exchange-correlation potential is defined as:

$$\nu_{xc}^{\sigma}(\vec{r}) = \frac{\delta E_{xc}[\rho_\uparrow, \rho_\downarrow]}{\delta\rho_\sigma(\vec{r})} \qquad [13.3]$$

Here, $E_{xc}[\rho_\uparrow, \rho_\downarrow]$ is the exchange–correlation energy and the density of electrons of opposite spins σ is found by summing the squares of the occupied orbitals:

$$\rho_\sigma(\vec{r}) = \sum_k |\psi_{k\sigma}(\vec{r})|^2 \theta(\mu - \varepsilon_{k\sigma}) \qquad [14.3]$$

where $\theta(x)$ is the step function and μ is the chemical potential. The exchange–correlation energy is largely responsible for the binding of atoms to form molecules and solids. The total electronic density is:

$$\rho(\vec{r}) = \rho_\uparrow(\vec{r}) + \rho_\downarrow(\vec{r}) \qquad [15.3]$$

Aside from the nucleus-nucleus repulsion energy, the total energy is:

$$E = \sum_{k\sigma}\left\langle \Psi_{k\sigma}\left| -\frac{1}{2}\nabla^2 \right| \Psi_{k\sigma}\right\rangle \theta(\mu - \varepsilon_{k\sigma}) + \sum_\sigma \int d^3r\, \nu_\sigma(\vec{r})\rho_\sigma(\vec{r}) + U[\rho] + E_{xc}[\rho_\uparrow, \rho_\downarrow] \qquad [16.3]$$

where

$$U[\rho] = \frac{1}{2}\int d^3r \int d^3r' \frac{\rho(\vec{r})\rho(\vec{r}')}{|\vec{r}-\vec{r}'|} \qquad [17.3]$$

is the Hartree self-repulsion of the electron density.

The Kohn–Sham equations represent a mapping of the interacting many-electron system on to a (tractable) system of non-interacting electrons moving in an effective non-local potential owing to all the other electrons. These equations must be solved self-consistently, so that the occupied electron states generate a charge density that produces the electronic potential that was used to construct the equations. New iterative diagonalisation approaches can be used to minimize the total-energy functional (as an example, Car and Parrinello, 1985). These are much more efficient than the traditional diagonalisation methods. If the exchange–correlation energy functional were known exactly, then taking the functional derivative with respect to the density would produce an exchange–correlation potential that included the effects of exchange and correlation exactly.

The complexity of the real many-body problem is contained in the unknown exchange–correlation potential $v_{xc}^{\sigma}(\vec{r})$. Nevertheless, making simple approximations, we can hope to circumvent the complexity of the problem. Indeed the simplest possible approximations, that are the local-density (LDA) or local-spin-density (LSDA) approximation, have been proven very successful (Kohn and Sham 1965, von Barth and Hedin 1972), although in last decades many other functional approximations have been employed.

3.1.3 Semi-empirical methods

Semi-empirical quantum chemistry methods are based on the Hartree-Fock formalism, but make many approximations and obtain some parameters from empirical data. They are very important in computational chemistry for treating large molecules where the full HF method without the approximations is too expensive, as they are computationally faster. The use of empirical parameters appears to allow some inclusion of electron correlation effects into the methods.

Within the framework of HF calculations, some pieces of information (such as two-electron integrals) are sometimes approximated or completely omitted. In order to correct for this loss, semi-empirical methods are parameterised, that is their results are fitted by a set of parameters, normally in such a way as to produce results that best agree with experimental data, but sometimes to agree with *ab initio* results. Semi-empirical calculations are much faster than their *ab initio* counterparts. Their results, however, can be very wrong if the molecule being computed is not similar enough to the molecules in the database used to parameterise the method.

3.2 Molecular mechanics and dynamics

As mentioned above, quantum-mechanics methods are more rigorous, but limited by present-day computers to systems containing a few hundred atoms and few picoseconds at most (Ghoniem et.al., 2003); many of the problems one would like to tackle in molecular modelling are too large to be considered by quantum mechanics. Thus, for larger ensembles, Molecular Mechanics and Dynamics methods (MM/MD), or, more generically, force field methods, or atomistic methods, are commonly used. In many cases force field methods can provide answers that are as accurate as the highest-level quantum mechanics calculations, in a fraction of the computer time (Leach, 2001).

The conceptual description of MM/MD simulations have been described almost elsewhere; in what follows we will mainly refer to the works of Leach (2001), Frenkel and Smith (1996) and Allen and Tildesley (1987).

The basic idea is to eliminate all electronic degrees of freedom and to assume that the electrons are glued to the nuclei. The first assumption is the Born-Oppenheimer approximation, without which it would be impossible to write the energy as a function of the nuclear coordinates. Thus, the interaction between two atoms is represented by a potential function that depends on the atomic configuration (i.e. relative displacement) and the local environment (i.e. electrons). Based on the electronic structure database, or alternatively using experimental measurements of specific properties, approximate effective potentials can be constructed. According to classical Newtonian mechanics, the dynamic evolution of all atoms can be fully determined by numerical integration. In principle, once the positions and velocities of atoms in the finite ensemble within the simulation cell are known, all thermodynamic properties can be readily extracted.

MM and MD are closely related, but they are used for different purposes. MM methods deal with energy minimisation methods to study potential energy surfaces of the system (i.e. the most probable structural displacement), or properties such energy barriers, or steepness of a potential energy surface around a local minimum. MD methods are commonly used to model molecular motions, although they can be applied to simulate annealing, or to explore more deeply the existence of local minima of the potential energy, $E(R)$.

In this model, $E(R)$ is not described by the Schrödinger's Equation [1.3], but via an empirical form, the so-called force field. A Force Field, which represents an empirical form of description of $E(R)$, modelled as a function of nuclei coordinates. As quantic effects are

neglected, due to the nuclei heaviness, Equation [1.3] can be substituted, for each atom *i*, by the well known Newton's equation:

$$-\frac{dE\left(\vec{R}_i\right)}{d\vec{R}} = m_i \frac{d\vec{R}_i^{\,2}}{dt^2} \qquad [18.3]$$

Where $\vec{R}_i$ is the position of the atom *i*, and m_i is its mass.

Thus, while MM is mainly involved in finding local or global $E(R)$ minima and their associated molecular geometries, MD aims at exploring the dynamic evolution of the system: this aim deals with the resolution of Equation [18.3].

A force field contains all the elements which are necessary to calculate energy (and forces) that act on a molecular system. It contains the functional forms of the $E(R)$ components, a series of numerical parameters, and a database of atomic types and charges. In the $E(R)$ expression, 3 kinds of contributions can be identified:

1. valence contributions, which involve bonds;
2. non-bond contributions
3. cross terms

Valence contributions are the sum of bond, angle, torsion and out of plane terms.

$$E_{BOND} = \frac{1}{2} K_{ij} \left(r_{ij} - r_{ij}^0\right)^2 \qquad [19.3]$$

where the K_{ij} parameter represents bond stiffness, r_{ij} is the effective bond length and r_{ij}^0 is the ideal bond length between atoms *i* and *j*.

In some cases, E_{BOND} is expressed with the Morse function:

$$E_{BOND} = D_{ij}\left[e^{-\alpha_{ij}\left(r_{ij}-r_{ij}^0\right)} - 1\right]^2 - S \qquad [20.3]$$

with D_{ij} the energy of the bond, S a corrective constant and α the Morse scale factor:

$$\alpha = \sqrt{\frac{K_{ij}}{2D_{ij}}} \qquad [21.3]$$

For angle contributions:

$$E_{ANGLE} = \frac{1}{2} C_{ijk} \left[\cos\theta_{ijk} - \cos\theta_{ijk}^0\right]^2 \qquad [22.3]$$

where C_{ijk} represents the stiffness of the angle and θ_{ijk}, θ_{ijk}^0 the effective and the ideal angles between i, j, k atoms.

Torsion terms are evaluated as follows:

$$E_{TORSION} = \frac{1}{2} E_N \left[1 - \cos\left(n\phi_{ijkl}\right)\right] \quad [23.3]$$

with E_N the torsional energy barrier, n the periodicity and Φ_{ijkl} the angle of torsion.

The out of plane (oop) contribution has the form of:

$$E_{OOP\theta} = \frac{1}{2} K_{OOP}^{\chi} \theta^2 \quad [24.3]$$

where θ is the improper torsion angle and K the spring constant.

Non-bond contributions include Van der Waals, Coulomb and (in few force fields) explicit hydrogen bond terms.

Van der Waals terms, representing the steric hindrance of the atom, are usually written with the Lennard-Jones expression:

$$E_{VdW} = \frac{n\varepsilon}{n-m}\left[\frac{n}{m}\left(\frac{r_{ij}}{r^*}\right)^{-n} - \left(\frac{r_{ij}}{r^+}\right)^{-m}\right] \quad [25.3]$$

with n = 12 and m = 6, and where ε is the energy minimum, r^* the interatomic distance corresponding to the energy minimum (the well depth), and r_{ij} the interatomic current distance between atoms i and j.

Coulomb (electrostatic) contributions are expressed in this form:

$$E_{COUL} = \frac{q_i q_j}{K r_{ij}} \quad [26.3]$$

Where r_{ij} is the interatomic current distance between atoms i and j, q_i, q_j the partial charges of atoms i and j, and K the Coulomb constant.

It should be emphasised that several different methods are used to consider non-bond contributions; they introduce some approximations, contemporarily allowing faster calculations. These methods involve the radius of influence of non bond interactions and differentiate for classes of simulations. In the application part of the following chapters more details will be given for each specific procedure.

Cross contribution is a term that evaluates deviations for the ideal behaviour and takes into account atom, bonds and angles closed to each considered atom:

$$E_{CROSS} = \sum_i \sum_j g_i f_j \quad [27.3]$$

Where g_i and f_i are a couple of function describing angle, torsion and bond contributions; the sums are made over all molecule bonds, angles and torsions.

Different force fields are commonly employed for different kinds of calculations. Generally speaking, they can be grouped in 3 categories: dedicated force fields, mainly applied to

specific molecules and applications, universal (more versatile but less precise) force fields, and second generation force fields, reliable and versatile at the same time for different kinds of calculations.

Given the energy of the system $E(R)$, MM methods deal with the gradient and second derivative calculation to find the minima; thus for *i, j = 1, ..., N* in a N-atoms system:

$$g_i = \frac{\partial E}{\partial R_i},\ h_{ij} = \frac{\partial^2 E}{\partial R_i \partial R_j} \qquad [28.3]$$

Different minimisation algorithms, with different levels of accuracy to assess convergence can be used. They will be listed in following chapters as they have been used.

MD calculations involve atom positions and motions (thus the kinetic energy, *K*). Thus the Hamiltonian of the system may be written as the sum of the kinetic and potential (V) contributions, and as a function of coordinates $\vec{R}$ and momenta $\vec{p}$ of each atom:

$$H(\vec{R}, \vec{p}) = K(\vec{p}) + V(\vec{R}) \qquad [29.3]$$

with

$$\vec{R} = (\vec{R}_1, ..., \vec{R}_N)\ ;\ \vec{p} = (\vec{p}_1, ..., \vec{p}_N) \qquad [30.3]$$

Kinetic contribution is expressed as:

$$K(\vec{p}) = \sum_{i=1}^{N} \sum_{\alpha} \frac{\vec{p}_{i\alpha}}{2m_i} \qquad [31.3]$$

where m_i is the mass of atom *i* and α the coefficient that takes into account the components of the vector $\vec{p}$. Applying the Newton's equation, for *i = 1, ..., N*, the force acting on the *i* atom is:

$$\vec{F}_i = m_i \ddot{\vec{R}}_i \qquad [32.3]$$

and, introducing the potential $V(R)$:

$$\vec{F}_i = -\nabla_{R_i} V(\vec{R}) \qquad [33.3]$$

as the force field is time and velocity independent, the determination of the atom position and velocity is given by the resolution of a system with *6N* first-order differential equations, if we write [32.3] as:

$$\vec{p}_i = -\nabla_{R_i} V(\vec{R}) = \vec{F}_i \qquad [34.3]$$

$$\ddot{\vec{R}}_i = \frac{\vec{p}_i}{m_i} \qquad [35.3]$$

And the resolution is usually given by the use of finite difference methods (FDM); the most employed integration algorithm is the Verlet algorithm (Verlet, 1967).

The double integration of the Newton's equation [32.3] gives a position for the atom *i* with the well known relation:

$$\vec{R}_i = \frac{1}{2} a_i t^2 + \vec{v}_i t + b_2 \qquad [36.3]$$

The Verlet algorithm assigns a set of *i* positions and accelerations values at the time *t* and the velocity $\vec{R}_i$ at the previous step *t*-δt. Using the Taylor expansion at the 3rd order:

$$\vec{R}(t-\delta t) = \vec{R}(t)\delta t + \frac{1}{2}\ddot{\vec{R}}(t)\delta t^2 - \frac{1}{3!}\dddot{\vec{R}}(t)\delta t^3 + O(\delta t^4) \qquad [37.3]$$

$$\vec{R}(t+\delta t) = \vec{R}(t) + \dot{R}(t)\delta t + \frac{1}{2}\ddot{\vec{R}}(t)\delta t^2 + \frac{1}{3!}\dddot{\vec{R}}(t)\delta t^3 + O(\delta t^4) \qquad [38.3]$$

The algebraic sum of [37.3] and [38.3] gives the equation which is the base for the integration process:

$$\vec{R}(t+\delta t) + \vec{R}(t-\delta t) = 2\vec{R}(t) + \ddot{\vec{R}}(t)\delta t^2 + O(\delta t^4) \qquad [39.3]$$

and, considering equation [35.3]:

$$\ddot{\vec{R}}(t) = \frac{\vec{F}}{m} = -\frac{\nabla V(\vec{R}(t))}{m} \qquad [40.3]$$

And analogously, for velocities:

$$\dot{\vec{R}}(t) = \frac{\vec{R}(t+\delta t) - \vec{R}(t-\delta t)}{2\delta t} \qquad [41.3]$$

which is used for the kinetic energy evaluation. It must be pointed out that the algorithm is not self-starting, as velocities are calculated one step behind (for *t=0*, velocities are calculated at *t*=-δt): initial values can be assigned on the basis of starting assumptions. Moreover, this kind of Taylor expansion generates a local error of the order of δt^4. Anyway, this algorithm is energy momenta conservative and its use, sometimes with small modifications to improve its performance, is very common. Obviously, the choice of a correct integration time step is crucial for the success of the virtual experiment.

Another important characteristic of atomistic simulations are the boundaries of the system, and the kind of ensemble where calculations are performed.

In some cases, when complex molecular systems are considered, such as gaseous, liquid or solid systems, many molecules have to be taken into account; in this case, it is common to construct an ideal box where molecules are confined, but also multiplied in the 3 directions to

generate an infinite lattice: the Periodic Boundary Conditions (PBC). This allows maintaining a constant density, as a molecule exiting from one side, will re-enter from the opposite side of the cell; simulations can thus be performed using a relatively small number of molecules. In some cases, periodicity can be conveniently used only over 2 dimensions.

Different statistical ensemble can be used to model the system, depending on the properties we are looking for; the most used thermodynamic ensembles are NVE (microcanonical), NVT (canonical) and NPT (isobaric-isotherm) systems. The number of particles N is always conserved; in NVE the total energy and the volume are maintained constant. NVT and NPT maintain constant, respectively, temperature (where thermostatting algorithms, or Thermostats, allow to exchange heat with an external bath) and volume, and temperature and pressure (where different algorithms for pressure control, or Barostats, with consequent volume and shape modifications, are used).

3.3 Monte Carlo techniques

While atomistic MM/MD simulations are deterministic, there is a different class of simulation techniques, mainly (but not only) focused on the atomistic scale. This class of simulation techniques, called Monte Carlo (MC) techniques, relies upon stochastic methods, in particular on importance sampling methods (Leach, 2001). The basic computational method was developed by first by (Metropolis et.al., 1953) and is now used worldwide, with several adaptations, in very different fields.

In general, MC methods generate a class of trials configurations and, using acceptance criteria, accept or reject the configuration. This class of methods, based on repeated random samplings, are able to generate states of low energy (thus most probable), enabling properties to be calculated correctly. MC methods are extensively used for complex molecules constructions (such polymer chains), in systems where the temporal evolution is not significant for properties calculation, or in all cases where MM/MD could fail due to the complexity of the system, or to due to the heaviness of the calculation.

As a general statement, the mean value of a thermodynamic property $\left\langle A\left(r^N\right)\right\rangle$ can be obtained by the following multi-dimensional integral, considering the $3N$ degrees of freedom of the N particles of the system:

$$\left\langle A\left(r^N\right)\right\rangle = \int A\left(r^N\right)\rho\left(r^N\right)dr^N \qquad [42.3]$$

where $\rho\left(r^N\right)$ is the probability of obtaining the configuration r^N, which depends on the potential energy *E* of the considered configuration, and $\beta = \frac{1}{kT}$:

$$\rho\left(r^N\right) = \frac{\exp\left[-\beta E\left(r^N\right)\right]}{\int \exp\left[-\beta E\left(r^N\right)\right]dr^N} \qquad [43.3]$$

The integrals of equation [40.5] cannot be calculated nor analytically or numerically. The solution can be the use of the MC method; this, as said before, involves the creation of a great number of trials configurations r^N, substituting the integration with the summation of a finite number of random configurations:

$$\left\langle A\left(r^N\right)\right\rangle = \frac{\sum_{i=1}^{N_{trial}} A_i\left(r^N\right)\exp\left[-\beta E_i\left(r^N\right)\right]}{\sum_{i=1}^{N_{trial}} \exp\left[-\beta E_i\left(r^N\right)\right]} \qquad [44.3]$$

This approach is too simple, as a totally-random sampling leads to considerate a great number of configurations: only some of the states generated in such a way can give a significant contribution for properties description. To effectively considerate significant states only, in the Metropolis method (Metropolis et.al., 1953), a Markov chain is generated. This satisfies these 2 conditions (Leach, 2001):

1. the outcome of each trial depends only upon the preceding trial and not upon the previous trials;
2. each trial belongs to a finite set of possible (acceptable) configurations.

Thus this series of configurations are generated with a probability of $\exp\left[-\beta E\left(r^N\right)\right]$ with the same weight, while in the more simple MC method, states of equal probability have a weight equal to $\exp\left[-\beta E\left(r^N\right)\right]$.

This means that a new state can be accepted only if is more favourable than the previous one, according to the selection criteria (in the case of molecular simulation, a state with a lower energy). In particular, the first condition clearly demonstrated the main difference with deterministic, MD methods, where all the states are time-connected. In MC simulations, the potential energy depends upon atomic positions, and not upon their momenta.

Usually, MC simulations are performed with algorithms and by the use of loops; in each loop the molecules of the system are shifted, and the new configuration is accepted or rejected according to the specific acceptance criteria.

Like MD methods and depending on the kind of in silico experimentation, MC simulations can be carried on in different ensembles, which can be classified in 2 main categories: closed ensembles where the number of particles is conserved, and open ensembles where the number of particles can vary. Microcanonical, canonical, isobaric-isotherms ensembles belong to the first class. Grand-canonical (where chemical potentials μ_i, volume V and temperature T are constant) ensemble belongs to the second class: here the system is in open contact with an ideal, external reservoir, and can exchange molecules. Trial moves or molecule constructions in the system follow different rules, according to the considered ensemble.

Based on MC methods assumptions, many other kind of stochastic simulations have been developed in recent decades, such as methods for taking into account dynamic evolutions (Kinetic Monte Carlo, for instance, Chatterjee and Vlachos, 2007), Quantum Monte Carlo, to simulate quantum systems (Foulkes et.al., 2001), Reactive Monte Carlo to simulate chemical reactions (Johnson et.al., 1994), or methods aiming at improving Metropolis MC for long, flexible molecules, such as Configurational Bias (Siepmann and Frenkel, 1992) or the RIS (Rotational isomeric State) method for polymer systems modelling (Teodorou and Suter, 1985). Specific descriptions of the methods used in this thesis will be given in following chapters.

3.4 Mesoscale modelling: DPD and Mesodyn

In some cases, there could be the necessity to model systems where characteristic dimensions and the time involved are too large for classical MM/MD simulations. In analogy with the QM vs. MM/MD scale-hopping, there is the need to improve time and length scale to describe the system correctly.

Since approximately 15 years, mesoscale theories and software give us the possibility to introduce new approximations, and, consequently, group of homogeneous atoms together in what are commonly called *beads*, and allow simulating larger systems. The starting point for the mesoscale simulations is a coarse grained model for the diffusive and hydrodynamic phenomena in phase-separation dynamics (Altevogt et.al., 1999). The philosophy of mesoscale simulations is a coarse grained model for the diffusive and hydrodynamic phenomena in phase separation dynamics. The familiar atomistic description of a molecule is lumped into beads of material (representing the collective degree of freedom of many atoms). These beads interact through pair-potentials which capture the underlying interactions of the constituent atoms.

Generally speaking, mesoscale techniques are important because represent the bridge between atomic-level simulations and the finite element or process simulation techniques at the real scale, a link that was absent since few years ago. Between different theories and software recently developed, we will focus on two of the most common ones, which also represent two kinds of approaches for mesoscale structure description: Dissipative Particle Dynamics (DPD), (Hoogerbrugge and Koelman, 1992) and Mesodyn (Altevogt et.al., 1999). They mainly treat phase transitions of liquid (or polymer) mixtures, their morphology and the microphase separation upon certain thermodynamic conditions. The first one is particle-based; the second one uses a dynamic variation of the mean-field density functional theory, coupling distribution functions, densities and an external potential.

3.4.1 DPD

In the DPD simulation method, particles move according to Newton's equation of motion, and interact with a dissipation force. If the mass of all particles is set to equal to unity, the time evolution of the positions ($\mathbf{r}_i(t)$) and momenta ($\mathbf{p}_i(t)$) is given by the well-known relationships (Groot and Warren, 1997):

$$\frac{d\mathbf{r}_i}{dt} = \mathbf{v}_i(t) \quad \frac{d\mathbf{v}_i}{dt} = \mathbf{f}_i(t) \qquad [45.3]$$

where $\mathbf{r}_i$, $\mathbf{v}_i$, and $\mathbf{f}_i$ are the position vector, velocity, and total force, respectively, acting on particle i.

The force acting on the particles, which is pairwise additive, can be decomposed into three elements: a conservative ($\mathbf{F}_{ij}^C$), a dissipative ($\mathbf{F}_{ij}^D$), and a random ($\mathbf{F}_{ij}^R$) force. Accordingly, the effective force $\mathbf{f}_i$ acting on a particle i is given by:

$$\mathbf{f}_i = \sum_{i \neq j} \left(\mathbf{F}_{ij}^C + \mathbf{F}_{ij}^D + \mathbf{F}_{ij}^R \right) \qquad [46.3]$$

where the sum extends over all particles within a given distance r_c from the ith particle. This distance constitutes the only length scale in the entire system. Therefore, it is convenient to set the cutoff radius r_c as a unit of length (i.e., $r_c = 1$), so that all lengths are measured relative to the particles radius. The conservative force is a soft repulsion, given by:

$$\mathbf{F}_{ij}^C = \begin{cases} a_{ij}\left(1 - r_{ij}\right)\hat{\mathbf{r}}_{ij} & \left(r_{ij} < 1\right) \\ 0 & \left(r_{ij} \geq 1\right) \end{cases} \qquad [47.3]$$

where a_{ij} is the maximum repulsion between particles i and j, r_{ij} is the magnitude of the particle-particle vector $\mathbf{r}_{ij} = \mathbf{r}_i - \mathbf{r}_j$ (i.e., $r_{ij} = |\mathbf{r}_{ij}|$), and $\hat{\mathbf{r}}_{ij} = \mathbf{r}_{ij} / r_{ij}$ is the unit vector joining particles i and j. The other two forces, $\mathbf{F}_{ij}^D$ and $\mathbf{F}_{ij}^R$, are both responsible for the conservation of the total momentum in the system, and incorporate the Brownian motion into the larger length scale. They are given by the following expressions:

$$\mathbf{F}_{ij}^D = -\gamma\, \omega^D r_{ij} \left(\hat{\mathbf{r}}_{ij} \cdot \mathbf{v}_{ij}\right) \hat{\mathbf{r}}_{ij}$$

$$\mathbf{F}_{ij}^R = \sigma\, \omega^R r_{ij}\, \theta_{ij}\, \hat{\mathbf{r}}_{ij} \qquad [48.3]$$

where $\mathbf{v}_{ij} = \mathbf{v}_i - \mathbf{v}_j$, ω^D and ω^R are r-dependent weight functions tending to zero for $r = r_c$, and θ_{ij} is a randomly fluctuating variable with zero mean and unit variance. One of the two weight functions in Eq. [48.3] can be chosen arbitrarily, thereby fixing the other weight function. However, the weight function and constants should obey:

$$\left[\omega^R(r)\right]^2 = \omega^D(r) \quad \sigma^2 = 2\gamma k_B T \qquad [49.3]$$

where k_B is the Boltzmann constant. As mentioned before, in DPD atoms or molecules are coarse-grained into beads. These beads represent local "fluid packages" able to move independently. Incorporation of chain molecules simply requires the addition of a harmonic spring force between the beads:

$$\mathbf{F}_{ij}^{spring} = K\, \mathbf{r}_{ij} \qquad [50.3]$$

By means of this spring, the beads can interconnect to highly complex topologies. In this work, however, the calculations are performed with linear chains only.

Finally, the integration DPD method uses a modified version of Verlet algorithm to determine the set of positions and velocities.

The method needs some input data that can be obtained experimentally, from literature or atomistic simulations, such as repulsive interactions (usually computed via the use of the Flory-Huggins theory, Flory, 1953) or beads length.

3.4.2 Mesodyn

The other mesoscale method described here is Mesodyn. As told before, here the mean-field density functional theory is dynamically modified in a dynamic density functional model (Altevogt et.al., 1999). It is assumed that with an external potential it is possible to reproduce the distributions of the real system at the same density.

The starting point is a coarse grained model for the diffusive and hydrodynamic phenomena in phase-separation dynamics. The thermodynamic forces are obtained via a mean-field density functional theory, assuming a Gaussian chain as a molecular model. The melt dynamics are described by a set of stochastic partial differential equations (functional Langevin equations) for polymer diffusion. Noise sources, with correlations dictated by the fluctuation-dissipation theorem, introduce the thermal fluctuations. The numerical calculations involve the time-integration of functional Langevin equations, given an implicit Gaussian density functional expression for the intrinsic chemical potentials.

Like DPD model, the mesoscale molecular model used by MesoDyn consists of beads of various types *I,J*.... The intramolecular interactions among the beads are described by harmonic oscillator potentials in a Gaussian chain (ideal interactions), $F^{id}[\rho]$. Intermolecular interactions between the chains (nonideal interactions) are introduced by a mean-field potential F^{nid} of the form:

$$F^{nid}[\rho] = \frac{1}{2}\sum_{I,J}\int\int \in_{IJ} (|\mathbf{r}-\mathbf{r}'|)\rho_I(\mathbf{r})\rho_J(\mathbf{r}')\,d\mathbf{r}\,d\mathbf{r}' \qquad [51.3]$$

in which $\rho_I(\mathbf{r})$ is the density of bead type *I* at $\mathbf{r}$ (local bead concentration), and $\in_{IJ}(\mathbf{r}-\mathbf{r}')$ is a cohesive interaction between beads *I* at $\mathbf{r}$ and *J* at $\mathbf{r}'$, chosen to have a Gaussian form:

$$\in_{IJ}(|\mathbf{r}-\mathbf{r}'|) = \in_{IJ}^{0}\left(\frac{3}{2\pi a^2}\right)^{3/2} e^{-(3/2a^2)(\mathbf{r}-\mathbf{r}')^2} \qquad [52.3]$$

In Equation (4), *a* is the Gaussian bond length, and $\in_{IJ}^{0}$ is the constant cohesive interaction between beads *I* and *J* which can be taken equal to the Flory-Huggins parameter χ.

The total free energy of the system is then defined as:

$$F[\rho] = F^{id}[\rho] + F^{nid}[\rho] \qquad [53.3]$$

If additional external potentials $U_I(\mathbf{r})$ are coupled to the Hamiltonian of the system in order to constrain the density fields $\rho_I(\mathbf{r})$ to the observed densities $\rho_I^0(\mathbf{r})$, then the corresponding free energy functional can be defined as:

$$F[\psi] = \mathrm{Tr}(\psi H^{id} + \beta^{-1}\psi\ln\psi) + \sum_I \int_V U_I(\mathbf{r})[\rho_I[\psi](\mathbf{r}) - \rho_I^0(\mathbf{r})]d\mathbf{r} + F^{nid}[\rho^0] + \lambda[\mathrm{Tr}\,\psi - 1] \qquad [54.3]$$

in which ψ is the configurational distribution, that is, the distribution of the bead positions, H^{id} is the Hamiltonian of the Gaussian chain, and $\beta^{-1}\psi ln\psi$ is the entropy of the distribution. Tr is defined as:

$$T_r = \frac{1}{n!\Lambda^{3nN}} \int \mathrm{d}r_{11} \ldots \mathrm{d}r_{nN} \qquad [55.3]$$

where Λ is the de Broglie thermal wavelength, n the number of chains, and N the number of beads per chain. The last term in Equation [54.3] normalizes the distribution ψ, λ being a Lagrange multiplier. Accordingly, the minimization of $F[\psi]$ with respect to ψ leads to a distribution that is determined by the external potential $U_I(\mathbf{r})$. At every simulation time step, the distribution ψ is the one that minimizes the free energy, and constrains the density fields $\rho_I(\mathbf{r})$. These, in turn, are determined by ψ. This results in the bijectivity concept (that is a one-to-one relation between the external potentials and the density fields) which is fundamental for the method.

The dynamics of the model are described by the following set of diffusion equations (generalized time-dependent Ginzburg-Landau model):

$$\frac{\partial \rho_I(\mathbf{r},t)}{\partial t} = \sum_{J=1}^{N} \int D_{IJ}(\mathbf{r},\mathbf{r}',t) \frac{\delta F}{\delta \rho_J}(r',t)\, \mathrm{d}\mathbf{r}' + \eta_I(\mathbf{r},t) \qquad [56.3]$$

with the diffusion operator D_{IJ}, and noise η_I, with correlations given by:

$$\langle \eta_I(\mathbf{r},t) \rangle = 0 \qquad [57.3]$$

$$\langle \eta_I(\mathbf{r},t)\eta_J(\mathbf{r}',t') \rangle = -2\beta^{-1} D_{IJ}(\mathbf{r},\mathrm{r}',t)\delta(t-t') \qquad [58.3]$$

The set of diffusion equations is closed by the expression for the free energy:

$$\frac{\delta F}{\delta \rho_I} = -U_I(\mathbf{r}) + \frac{\delta F^{nid}}{\delta \rho_I} \qquad [59.3]$$

If a local coupling approximation is used, the diffusion operator is given by:

$$D_{IJ}(\mathbf{r},\mathbf{r}') = \beta D \delta_{IJ} \delta(\mathbf{r}-\mathbf{r}') \nabla_{\mathbf{r}} \cdot \rho_J(\mathbf{r}) \nabla_{\mathbf{r}'} \qquad [60.3]$$

where D is the self-diffusion constant.

Both Mesodyn and DPD outputs are density distribution profiles, which can define the presence of phase segregation and the morphology of the system, but can also be useful as input data for simulations at the upper level (Finite Element Methods) to calculate macroscopic properties.

3.5 Finite elements methods

Finite Element methods (FEM, or micro-FEM, due to the scale length involved), is a kind of technique developed to find approximate solutions of partial differential equations, or integral equations, approximating the value of the considered function in specific points. As a general statement, FEM provide a mesh discretisation (in tetrahedrons for 3-dimensional systems, for instance) of the domain into a set of discrete sub-domains. It is applied to many fields, at different time and length scale. In multi-scale modelling it is generally seen as the step before process simulation at the real scale (see Figure 2.1 in Chapter 2). In fact, it is possible to transfer the simulated mesoscopic structure to finite elements modelling tools for calculating macroscopic properties for the systems of interest (Gusev, 2001).

Due to the very large fields of applications of FEM methods, in this chapter we will focus on two specific techniques, commonly used to predict both physical and mechanical macroscopic properties of materials. The first (Mesoprop, distributed by Accelrys® and developed by Matsim®, Switzerland) uses a fixed grid for system discretisation; the second one (Palmyra, Matsim®, Switzerland) has a variable grid, generated by a Monte Carlo method, which can be refined next to edges, and can also import objects with specific shape and density (such as fillers in nanocomposites). Both can import density fields obtained by previous calculations (such as Mesodyn or DPD). In this type of simulations, typical dimensions involved in modelling are about some μm.

Fixed-grid Mesoprop simulations uses a numerical method to determine the overall properties of composites with arbitrary morphologies from the properties of the components based on small homogeneous grid elements (Gusev, 1997). Morphologies are defined by a number of phases in a periodically continued base cell of cubic or orthorhombic shape, where the resolution depends on the fixed number of grid elements used. To avoid boundary effects three dimension periodic boundary conditions are applied. By applying a displacement-based finite element method to the volume mesh, the responses to external deformations are calculated (Gusev, 2001). The solver works on the basis of a space-filling tetrahedral mesh, i.e. without voids. The mapping of cubic grid elements to a tetrahedral mesh results in six isochoric tetrahedrons for each cubic grid element. The number of mesh elements is six times the number of grid nodes, which is equal to the number of grid elements.

Variable-grid Palmyra FEM software also uses a numerical method to determine the overall properties of composites with different morphologies from the properties of the components (Hine et.al., 2002; Lusti et.al., 2003). The morphology here can be defined by a number of

inclusion objects in a periodically continued base cell of cubic or orthorhombic shape where cell and inclusions may consist of any material. The inclusions can be arranged manually or by means of a Monte Carlo simulation in order to get representative samples of different morphologies; Monte Carlo packing allows to change the volume fraction of the inclusions in the periodic cell. Starting from random points on the surfaces of the inclusions, three-dimensional mesh of hundred thousands of non-overlapping tetrahedron elements are built; they fully cover the volume of the periodic cell. The sizes of the mesh tetrahedrons vary with the local morphology in order to get a higher resolution at the interfaces and where inclusion objects are very close. By applying a displacement-based finite element method to the volume mesh, the responses to external deformations are calculated.

Both in fixed grid and in variable grid simulations, mechanical properties (like elastic constants and stiffness) can be calculated using an elastic tensor of 21 independent parameters. In order to calculate mechanical properties and thermal expansion coefficients a thermo-elastic solver is used. It applies six different infinitesimally small deformations to the composite and minimizes the total strain energy for each of these deformations in order to calculate the elastic composite properties. Since composite materials are usually anisotropic, the symmetry class of the tensor is triclinic; if materials have some symmetry, tensor specifications may be simplified. For thermo-elastic properties, the total elastic energy F, which is a quadratic function of the displacements of the nodes, is defined as the sum over the element contributions:

$$F = \sum_{t=1}^{n_{Tetr}} f_t = \frac{1}{2} \sum_{t=1}^{n_{Tetr}} V_t C_{ik} e_i e_k \qquad [61.3]$$

where f_t is the elastic energy of tetrahedron t , V its volume, C_{ik} the elastic constants, and e_i the local strains. In general, the e_i are made up of mechanical and thermal parts, L is the length unit of the simulation cell.

The local stresses are calculated from the nodal displacements at the end of each minimization run, assuming linear elastic behaviour. They correspond to an applied mechanical strain of 1% or a temperature change of 1 K.

The local hydrostatic pressures P are calculated for each tetrahedron as the sum of the principal components of the stress tensor of that volume element:

$$P = \frac{1}{3}\left(\sigma_{XX} + \sigma_{YY} + \sigma_{ZZ}\right) \qquad [62.3]$$

The deviatoric von Mises stress for a mesh element is defined as:

$$\tau = \sqrt{\left[\left(\sigma_{xx} - \sigma_{yy}\right)^2 + \left(\sigma_{yy} - \sigma_{zz}\right)^2 + \left(\sigma_{xx} - \sigma_{yy}\right)^2\right]/2 + 6\left(\sigma_{xx}^2 + \sigma_{yy}^2 + \sigma_{zz}^2\right)^2} \qquad [63.3]$$

This value is listed in the output file for every applied deformation; τ typically controls the appearance of first inelastic events in metals and organic polymers. For example, in many organic polymers, the first inelastic events such as plasticity start occurring when the von Mises stress reaches a level of 50-100 MPa.

For transport properties (such as diffusion, or thermal conductivity), dielectric constants calculations, optical properties, a Laplace solver is used; this applies a field of forces and find a unique minimum, minimising the total energy (Gusev, 2001); the Laplace equation, which is able to describe these phenomena, has the form:

$$div\varepsilon(\vec{r})grad\varphi = 0 \qquad [64.3]$$

where ε is the phase property (for instance, for permeability calculations is the permeability P) and φ the local variable (in case of permeability calculations, the chemical potential μ). The solver applies an external field of forces and minimizes the energy with the gradient conjugate (Gusev, 2001).

3.6 Hardware and Software

Simulations have been performed in the Molecular Simulation Engineering (MOSE) laboratory at the University of Trieste and, for the study concerning the use of Reactive Monte Carlo techniques, at the Institute of Chemical Process Fundamentals (ICPF) of the Academy of Sciences in Prague. As local server for terminal server access we used a Microsoft® Window 2000 Server® Intel (RAID). Calculations have been carried out with the aid of different workstations, as Intel bi-processors XEON-32 bit, Intel quad-core bi-processor Xeon x5355 and Silicon Graphics Origin 200.

For this thesis, we used the commercial platform Materials Studio (Accelrys®, San Diego, CA, USA), Cerius^2 (a molecular modeling and simulation package, Accelrys®, San Diego, CA, USA), the FEM Palmyra software (MatSim, Zürich, CH), and in-house developed software.

Chapter 4

Industrial scraps recycling and life product improvement

Summary

In this chapter the results of molecular simulation studies for polymer scrap recycling and life product improvement are described. This work has ben described in the following publications:
Fermeglia M., Cosoli P., Ferrone M., Piccarolo S., Mensitieri G., Pricl S., PET/PEN Blends of Industrial Interest as Barrier Materials. Part I. Many-Scale Molecular Modeling of PET/PEN Blends, Polymer, 47, p.5979, (2006).
P.Cosoli, M. Fermeglia, M. Ferrone, P. Posocco, S. Pricl, G. Scocchi, "New materials from multiscale modelling procedures: properties prediction and customisation of polymeric nanocomposites", I-Cheap-8, The eight International conference on Chemical & Processing engineering, Ischia, (2007).
P. Cosoli, M. Fermeglia, M. Ferrone, S. Pricl, L. Toma, "Molecular simulation techniques for sustainable technology and environmental applications - general overview and case studies", CISAP-3, 3° International conference on safety and environment in the process industry, Roma, 2008. P. Cosoli, G. Scocchi, S. Pricl, M. Fermeglia, "Many-scale molecular simulation for ABS-MMT nanocomposites: upgrading of industrial scraps", Microporous and Mesoporous Materials, 107, p.169, (2008).

4.1 Industrial scraps: legislation and upcoming issues

In recent years local and European legislations gave more importance to the necessity of waste recycling improvement. This need generically implies the necessity to reduce the quantity of waste, but has also an implication in the way of producing and using goods, thus it would have a considerable impact in the industrial field. The huge importance of the problem can be revealed, for instance, examining how in developed countries the amount of waste is increased, in which way the composition is changed and how the amount of recycling is improved. This is testified, for instance, by examining Figure 4.1 a and b. It can be noticed how the waste production in the US is increased in the last 40 years, together with the quantity recovered.

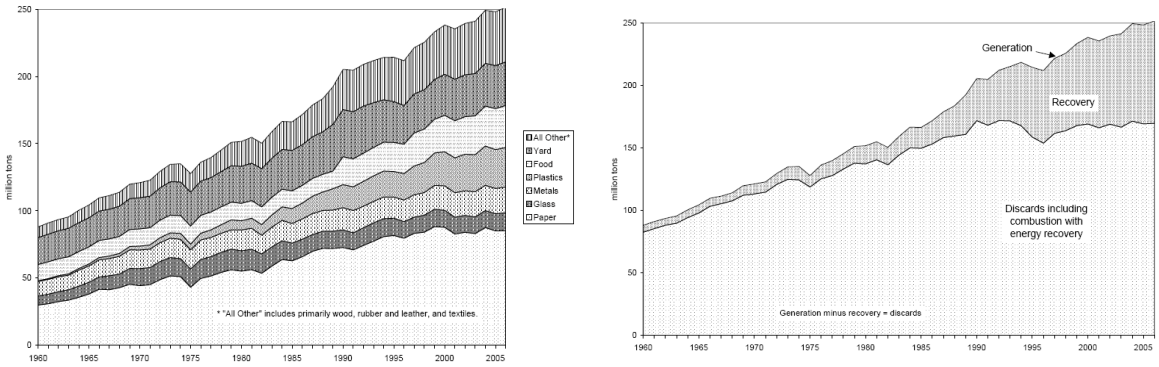

Figure 4.1; a: generation of materials in municipal solid waste; b: recovery and discards of materials in municipal solid waste. Data collected from 1960 to 2006 in US. Source: EPA, 2006.

In many cases, such in Europe (and also in Italy) the legislation decidedly tends to address the problem also to industry, limiting the amount of waste generated by industrial processes, and fostering industrial scraps recycling.

In this sense, the 2006 European 2006/12/CE directive (EU 2006) about waste reduction and recycling can be mentioned, together with the new Italian law, Dlgs 152/2006 (Borsa dei Rifiuti, 2008). They also tend to shift the attention on the waste "producer", anyone whose activities produce waste and has the burden of waste disposal.

Thus, for worldwide industrial production there is the need to improve productive processes, minimize waste production, recycle scraps as much as possible, and improve the product life cycle before waste disposal.

In this chapter we present two case studies dealing with waste reduction and recycling:

- The improvement of barrier effect for polymers in food packaging, with the aim of retarding the product end-of-life;
- The recycling of automotive polymeric industrial scraps.

4.2 Polymer for barrier effect in food packaging

In the first case, we examined the necessity of improving the barrier effect of polymers in food packaging, in particular for bottles. In recent years the quantity of polymer-made bottles containing liquids has improved. For various reasons, drinks has often to be stored in plastic bottles, but there is the need to limit the CO_2 loss, or the O_2 penetration, due to the relatively high permeability of the plastic films, with the aim at contributing to improve the durability.
The case-study involve the polyethylene terephthalate (PET), commonly used for food packaging and for drinks storage, and the mixing with polyethylene naphthalate (PEN), a less permeable, but more expensive polymer.
Properties of PET and PEN blends have been widely investigated in this decade, due to the enhanced mechanical, thermal and barrier properties (making them attractive especially in food packaging and preservation) conferred to these mixtures by the presence of a small amount of PEN polymer (Wu and Cuculo, 1999; Patcheak and Jabarin, 2001). PET and PEN homopolymers, however, are known to be essentially immiscible at any temperature and composition (Guo and Zachmann, 1993; Ihm et.al., 1996). Nonetheless, miscibility near and above melting temperature is increased as a transesterification reaction takes place, resulting in the formation of PET and PEN copolymers that act as compatibiliser between the PET and PEN phases (Ihm et.al., 1996).
Transesterification reactions are influenced by different factors, including temperature, annealing time, catalytic system, blend starting composition, viscosity ratio of the two homopolymers, and PET/PEN terminal hydroxyl group capping (Shi and Jabarin, 2001). Yet, as the extent of the transesterification reaction increases, basically two phenomena take place: in the early stages, more and longer block copolymers are formed, further improving blend miscibility, whilst, at later times, the PET and PEN sequence lengths of the existing PET/PEN block copolymer begin to decrease, yielding copolymers of a more random nature. Finally, past some critical level of the so-called degree of randomness (*DR*) of the forming copolymers, the blend properties become constant, being only a function of the initial blend composition. Eventually, when *DR* =1 (i.e., at 100% reaction level), the blend becomes equivalent to a statistical random copolymer as synthesized by melt polymerization. Recently,

it has been demonstrated that an extent of the transesterification reaction of at lest 10% is required for a miscible PET/PEN blend; this condition should be granted by a longer annealing time, or by multiple extrusion cycles (Medina et.al., 2004; Baltà-Calleja et.al., 1997).

In this part of the thesis we present the results obtained for the application of a multi-scale molecular simulation strategy for the characterization of PET/PEN blends at two different compositions (80/20 and 92/8 wt%, respectively), and at several different extents of transesterification reaction, ranging from zero (that is, immiscible systems) to the maximum degree of transesterification theoretically achievable (i.e., PEN has been completely included in the block copolymer); the simulation involves the use of MM/MD, mesoscale and FEM techniques. The aim is to evaluate PET/PEN miscibility, and to quantify the permeability and diffusivity for the oxygen at different conditions.

The main characteristics of the systems considered in this work are summarized in Table 4.1. The selected simulation temperature was chosen according to the typical extrusion process thermal conditions reported, for instance, by (Tharmapuram and Jabarin, 2003), while 18000 g/mol is a typical value for the molecular weight of industrial employed PET and PEN polymers. Although in some cases low shear rates can be applied during extrusion, at first approximation PET/PEN systems can be modelled in the absence of shear [25]. In the event of a complete transesterification reaction, the calculation of the corresponding degree of randomness, and the estimation of the PET/PEN sequence length in the copolymer have been taken from previous works (Yoon et.al., 1997; Patcheak and Jabarin, 2001). Further, in these simulations the content of the hetero sequence in the whole blend is about 40%, as all PEN monomers ideally migrate from the PEN homopolymer into the copolymer.

Simulation	T	PET/PEN copolymer	PET M_w	PEN M_w	Blend composition
	(K)	(%wt)	(g/mol)	(g/mol)	(PET/PEN, %wt)
Set 1	583	0, 8, 15, 30, 40	18000	18000	80 / 20
Set 2	583	0, 8, 15	18000	18000	92 / 08

Table 4.1: characteristics of the simulated PET/PEN blend systems.

As mentioned in Chapter 2, the input parameters for higher scale simulations (e.g., mesoscale) are obtained by performing calculations at lower scales (e.g., MD and MC). The Compass forcefield (FF) (Sun, 1998) was used in all MD calculations. The first, key parameter of the MS calculations - the Flory-Huggins interaction parameter χ - was obtained for each system

via the solubility parameter δ of the polymers, following the procedure described in details by (Fermeglia and Pricl, 2003), and based on the derivation of the cohesive energy density e_{coh} through MD simulations. Accordingly, each polymer constitutive repeating unit (CRU) with explicit hydrogens was polymerized to the corresponding M_w, and six different amorphous structures for each species were generated by coupling the method originally proposed by Theodorou and Suter (Teodorou and Suter, 1985), based on the Rotational Isomeric State (RIS) algorithm (Mattice and Suter, 1994) and corrected for incorporation of long-range interactions, with the "scanning method" of (Meirovitch, 1983). Thus, an amorphous phase of a glassy polymer is created in two stages. The conformations of the chains are assumed to resemble those of the unperturbed chains. Initially, a proposed structure can be generated by using the RIS theory that described the conformations of the unperturbed chains. Subsequently, the initial structures are minimized by turning on, progressively, the potential energy interactions in a manner such that the more severe overlaps are relaxed first (atomic radii of half the actual size and no-rotational barriers) and, gradually, the minimum is reached by switching on the full potential (radii of actual size, rotational barriers, and attractive interactions). In the scanning method, all possible continuations of the growing chain are taken into account in the calculation of the conditional probabilities. This hybrid scheme method has proved to yield good initial guesses that do not depart much from the random coil hypothesis, have a rather uniform spatial chain segment distribution, and possess a relatively low energy. For each polymeric system, 10 chains were packed in a cubic simulation box with 3D periodicity. Where available, the initial density of each cell was set equal to the corresponding literature value, in order to minimize discrepancies in the final density values obtained from MD simulations. To avoid the system trapping in metastable local high-energy minima, the relaxed structures were subjected to a combined molecular mechanics/molecular dynamics simulated annealing (MDSA) protocol: accordingly, the simulation cells underwent five repeated temperature cycles (from 583 K to 1000 K, and from 298 K to 1000 K, and back) using MD conditions in the NVT ensemble. At the end of each annealing cycle, the structures were again minimized via FF, and only those structures corresponding to the minimum energy were used for further modelling. From the fully relaxed models, MD experiments in NPT ensemble were run at 583 K for all systems, and at 298 K for the PET and PEN pure homopolymers. The Newton equation of motions of the 100 ps MD equilibration phase, and of the following 500 ps MD production phase were integrated by the Verlet leapfrog algorithm, using an integration step of 1 fs. The calculations at 298 K were performed with the purpose of testing the selected intermolecular potential/simulation

protocol by comparing the theoretically predicted and literature available solubility parameter values.

Now, in general e_{coh} is defined as the ratio of the cohesive energy E_{coh} and the molar volume V at a given temperature; E_{coh} is in turn defined as the increase in internal energy per mole of substance if all intermolecular forces are eliminated. In our simulated systems, other chains that are simply displaced images of the chains themselves surround the polymer chains. E_{coh} is the interaction energy between these images. The values of E_{coh} at different temperatures can be obtained from simulation by calculating the difference between the non-bonded energy of the periodic structure, $E_{nb}^{periodic}$, and the corresponding value for an isolated parent chain in vacuum $E_{nb}^{isolated}$:

$$E_{coh} = E_{nb}^{isolated} - E_{nb}^{periodic} \quad [1.4]$$

To this purpose, 10 parent chains for each polymer (copolymer) were generated, and their energy minimized according to the procedure described above. The MDSA protocol was again applied to provide thermal energies to cross energy barriers between conformation local minima. *NVT* MD simulations were then performed on the single chains (again the 10 best relaxed chains for each system) in vacuum at the same temperature conditions applied to the simulation of the relevant periodic systems. The appropriate δ values were thus obtained as:

$$\delta = \sqrt{e_{coh}} = \sqrt{E_{coh}/V} \quad [2.4]$$

The corresponding Flory-Huggins parameters were estimated as:

$$\chi_{1,2} = \frac{(\delta_1 - \delta_2)^2}{RT} V_{1,2} \quad [3.4]$$

where $V_{1,2}$ was considered as the average molecular volume of the different CRUs present in the system, weighted over the corresponding volume fractions.

The theory underlying the methodology for the calculations of the next set of MS input parameters - the number N_{meso} and the bond length a of the MS beads - is similar to the classical dynamic random phase approximation (RPA) (de Gennes, 1979). The polymer chains are modelled as Gaussian chains consisting of beads, each bead representing a number of monomers of the real polymer. The mapping of the real polymer chains onto Gaussian chains can be obtained via the characteristic ratio C_∞, by imposing the mean-square end-to-end distance, and the length of the freely-jointed chain to be equal for the real and the Gaussian chain. Thus, we have:

$$C_\infty = \lim_{n \to \infty} \frac{\langle r^2 \rangle_0}{\sum_i n_i l_i^2} \quad [4.4]$$

in which $\langle r^2 \rangle_0$ denotes the mean-square end-to-end distance of an unperturbed chain molecule in solution, n is the number of bonds along the shortest path across the backbone, and n_i is the number of times the jth bond which has a length of l_i, occurs along this shortest path. If we consider the real chain to be constituted by N monomers of length l, then it can be approximated by a freely-jointed equivalent chain characterized by a smaller number of segments, N_{meso}, each with a higher bond length a. The choice of n and a must therefore comply with the following two conditions: the first is given by Equation (4), so that:

$$\left\langle r^2 \right\rangle_0 = C_\infty N l^2 = N_{meso} \bar{a}^2 \quad [5.4]$$

whilst the second condition sets that:

$$N_{meso} a = l_{max} \quad [6.4]$$

where a is the modulus of the bond vector $\bar{a}$, and l_{max} is the length of the fully extended chain, given in turn by:

$$l_{max} = Nl \sin\frac{\theta}{2} \quad [7.4]$$

Substituting Equations [7.4] in Equation [6.4], and dividing Equation [5.4] by Equation [6.4], we finally get the relevant expressions for the mesoscale input parameters N_{meso} and a:

$$a = \frac{C_\infty l}{\sin\frac{\theta}{2}} \quad [8.4]$$

$$N_{meso} = \frac{N}{C_\infty} \sin^2\frac{\theta}{2} \quad [9.4]$$

Generally speaking, the best-known method for calculating the conformational properties of polymer chains is the RIS theory described above, which was used to predict C_∞. From an operative standpoint, starting from the minimized polymer chains generated to be employed in the MD simulations, $2 \cdot 10^5$ MC steps were used in the equilibration stage, and $1 \cdot 10^6$ steps constituted the production portion of the MC simulation. Again, two calculation sets were performed: at T = 583 K and T = 298 K, for comparison with available literature data. The maximum number of rotable backbone bonds separating two atoms, at which the non-bonded interactions are still included in the energy calculation during the MC simulation was set to 8.

The core of the work is represented by the use of Mesodyn software. The principles of the method have already been described in Chapter 3, thus we will only provide the setting parameters.

Input parameters, obtained via the atomistic simulation approach outlined above, have been employed with the following operative settings for the integration of the dynamic equations: cell dimension = 73.8 nm, grid dimensions = 32 ×3 2 × 32, grid spacing = 2.305 nm, noise factor = 75, time step = 50 ns, number of steps = 15000, maximum number of iterations per step = 100.

Finally, the density distributions obtained from mesoscale simulations have been used as input data for finite-elements calculations with the MesoProp software. In our case, grid morphologies were obtained for all systems studied by importing the corresponding density distributions from the relevant MS simulations. Density, diffusivity and permeability values for oxygen in pure, amorphous homopolymers have been taken from the literature (Hiltner et.al., 2005) To a first approximation, the degree of crystallinity of the polymers was taken into consideration by assuming the van Krevelen relationships [61] for gas diffusivity D and solubility S:

$$D_{SC} = D_G(1 - X) \qquad [10.4]$$

$$S_{SC} = S_G(1 - X) \qquad [11.4]$$

where D_{SC} and S_{SC} are the diffusivity and solubility of semi-crystalline homopolymers characterized by a degree of crystallinity equal to X, respectively, and D_G and S_G are the diffusivity and solubility values for the corresponding pure amorphous chains. The well-known relation between S and D, $P = S \times D$, coupled to Equations [10.4] and [11.4], finally yields the corresponding expression the permeability of semi-crystalline systems as:

$$P_{SC} = S_G D_G (1 - X)^2 \qquad [12.4]$$

As a first step, the correctness of the atomistic simulation strategy employed to calculate the input parameters for MS simulations of the systems under consideration was examined. To this purpose, the values of the solubility parameter δ and the density ρ, obtained from MD simulations, and the characteristic ratios C_∞, calculated from MC simulations, are shown in Table 4.2, along with literature data for comparison (Hiltner et.al., 2005; Mc Gonigle et.al., 2001; Van Krevelen, 1990; Mark, 1997). As can be seen from this Table, the agreement between simulated and literature values is excellent; accordingly, these evidences can be taken as a validation of the computational procedure adopted to calculate these molecular parameters.

	δ_{sim} ($MPa^{1/2}$)	δ_{lit} ($MPa^{1/2}$)	$C_{\infty,sim}$ (–)	$C_{\infty,lit}$ (–)	ρ_{sim} (g/cm^3)	ρ_{lit} (g/cm^3)
PET	21.9	19.9-21.9	4.02	4.11	1.329 ± 0.003	1.336
PEN	18.1	-	5.27	5.33	1.334 ± 0.004	1.327

Table 4.2: solubility parameters δ, densities ρ, and characteristic ratios C_∞ for PET and PEN homopolymers obtained from atomistic MD and MC simulations at 298 K. The 2nd, 4th and 6th columns list the corresponding literature data, for comparison.

The entire set of MS input parameter obtained from lower scale molecular simulations is listed in Table 4.3. It should be noticed that bead self-diffusion coefficient D was appropriately set to 2×10^{-7} cm^2/s to avoid the simulation dimensionless time step τ (i.e., the product of the time step and the bead diffusion coefficient, divided by the square of the grid spacing) to exceed the recommended limit (Fraajie, 1997). It has been seen, however, that the self-diffusion parameter does not have an appreciable effect on the final structure of the MesoDyn simulation (data not shown). The compressibility parameter K was left at its default values of 10.

	C_∞ (–)	δ ($MPa^{1/2}$)	D (cm^2/s)	K (m^2kgs^{-2})	χ (–)	N_{meso} (–)	a (nm)
PET	4.02	21.9	2×10^{-7}	10	0.523	23	2.661
PEN	5.27	18.1	2×10^{-7}	10	0.523	14	2.661

Table 4.3: MS input parameter set for PET/PEN systems.

As the first case, PET/PEN homopolymer blends miscibility in the absence of transesterification reaction has been examined. In agreement with the corresponding experimental evidences these systems show complete phase segregation at the processing temperature considered (583 K), as shown by the three-dimensional bead volumetric density distribution reported in Figure 4.2 (a). From this Figure we can infer that a little amount of immiscible PEN homopolymers will slowly find a way for aggregation in separated clusters. Moreover, it can be seen that the smaller the quantity of species, the longer the pathway they have travel to ensemble into aggregates.

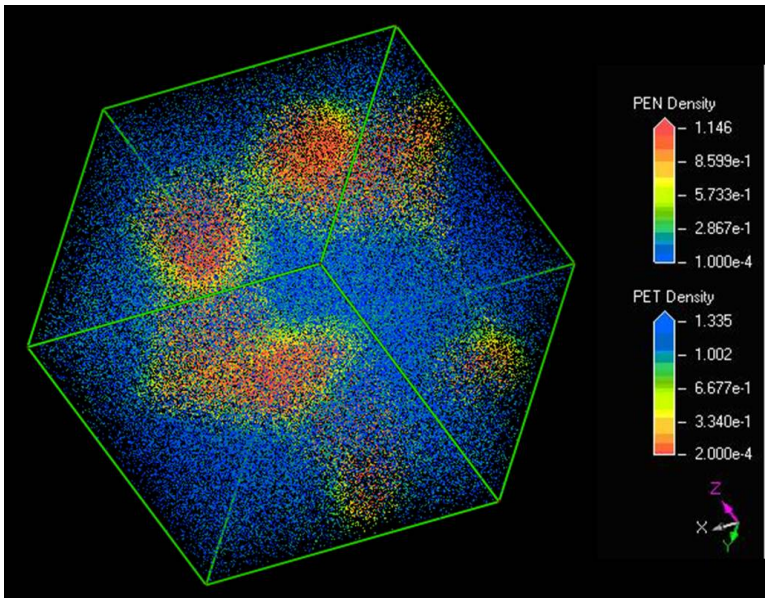

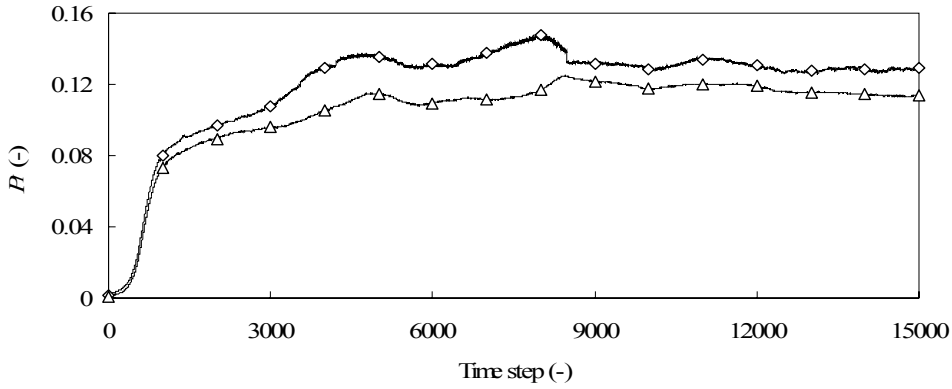

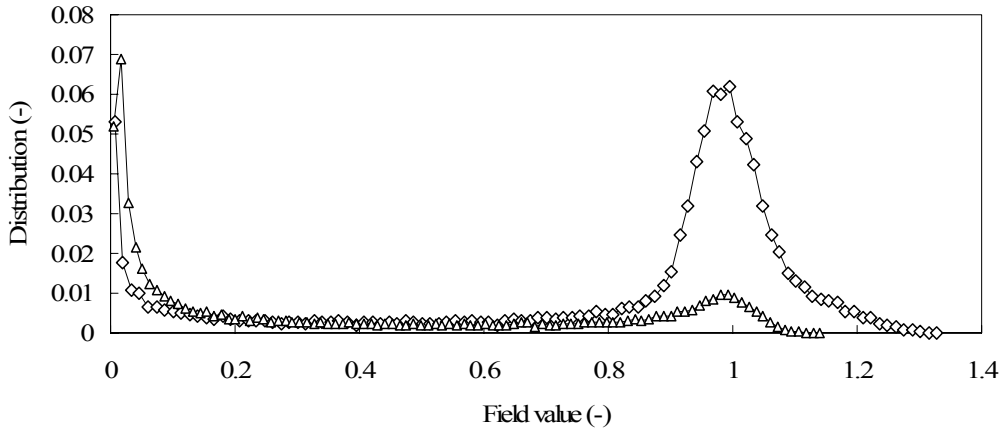

Figure 4.2: Three-dimensional bead volumetric density distribution (a, top), order parameter P_1 (b, centre) and density field distribution (c, bottom) of the phase segregation for the 80% PET - 20% PEN blend system at 583 K and in the absence of transesterification reaction. Symbols: (◇), PET; (△), PEN.

Due to the low PEN concentration in the 80% PET - 20% PEN blend, the system shows a slow convergence towards a free energy stable condition. This can be evaluated by controlling the so-called order parameter P_I, defined for each species I as the deviation from the mean bead density at homogeneity:

$$P_I = \frac{1}{V}\int_V \left[\theta_I^2(\mathbf{r}) - \theta_{I,0}^2\right]\mathrm{d}\mathbf{r} \qquad [13.4]$$

where θ is a dimensionless density (volume fraction) for bead species I, and the index 0 denotes average values at homogeneity. According to Equation [13.4], order parameters with large values indicate strong phase segregation. Conversely, very small values of P_I correspond to homogeneous systems. The behaviour of P_I for this PET/PEN system is illustrated in Figure 1b, from which both the long times involved in system free energy equilibration and high final values of the P_I parameter are quite evident. Lastly, Figure 1c reports the density field distribution of the PET and PEN species. It should be noticed that probability densities of PET and PEN have two small peaks at different bead densities, which is a clear indication that segregation occurs: PET and PEN are both present at densities close to 0 and close to 1.Utterly analogous results were obtained for the blend characterized by a lower amount of PEN, i.e., 92% PET / 8% PEN.

When the transterification reaction takes place, pure homopolymers are progressively substituted by block copolymers that became more random in nature as long as the reaction proceeds. Patcheak and Jabarin (2001), proposed the following equations for the estimation of the average sequence lengths of ethylene terephthalate and naphthalate units - L_T and L_N, respectively- in the copolymers:

$$L_T = \frac{1}{(1-X_T)DR} \qquad [14.4]$$

$$L_N = \frac{1}{(1-X_N)DR} \qquad [15.4]$$

where X_T and X_N are the molar fraction of PET and PEN, respectively, and DR is the degree of randomness. DR can be defined as the sum of the probabilities of finding a naphthalate unit next to a terephthalate one (P_{tn}), and a terephthalate unit next to a naphthalate one (P_{nt}). Ihm et al. (1996), examined the extent of transesterification in a 50/50 PET/PEN blend as a function of the annealing time: they found that the longer the annealing time, the higher the DR and the shorter the block sequence length into the copolymer. In order to simplify the situation for the MS simulations, we assumed as the first case of study that an ideal, complete transesterification reaction takes place (40% wt of copolymer in the blend, see Table 4.1);

accordingly, the corresponding block copolymer model structure contains short blocks of each repeating units. The number of beads for each repeating unit in the copolymer was then calculated as:

$$B_{N_i} = \frac{r}{C_\infty} \qquad [16.4]$$

where r is the number of repetitions of each CRU in the blocks, and B_{N_i} is the bead number for each block. For further sake of simplicity, we decided to alternate PET and PEN beads; the copolymer weight was arbitrarily fixed at 36000 g/mol, which corresponds to ideal condensation of one chain of PET and one of PEN. As previously remarked, all PEN homopolymer has been incorporated into the copolymer. Accordingly, with reference to the MS input parameters reported in Table 4.3, the number of beads of the molecule types become 23 for PET, 0 for PEN and 14 + 23 (suitably alternated) for PEN and PET in the copolymer, all other values being equal to those listed in Table 4.3. We also performed further simulations at intermediate transesterification degrees, both for the 80% PET – 20% PEN, and the 92% PET - 8% PEN blend systems (see Table 4.1). Finally, in order to visualize and emphasize the displacement of PET beads in the simulation grid, PET beads in the copolymer were given a different nomenclature (i.e., PETCO), although they are obviously characterized by the same χ parameter of the PET beads in the PET homopolymer.

The results obtained from the MS simulation at complete transesterification clearly differ from the previous case, as can be observed looking at the corresponding 3D – bead volumetric density distribution (Figure 2a), the order parameter P_I, and the density field distribution (Figure 2b and 2c), respectively. The homogeneity of the system is qualitatively well evidenced by the uniform yellow-green colour throughout the cell, corresponding to average bead densities close to their initial values (see Figure 3a). The equilibrium values of P_I are at least 2 orders of magnitude lower than the corresponding case without transesterification (see Figure 3b), and the probability density profiles show a single well-defined peak for each species, further featuring a narrow distribution around the mean initial value (see Figure 3c).

The sensible, rather obvious explanation for the improved miscibility envisaged in this system can be the compatibilisation effect induced by the copolymer, which is able to compensate the repulsion between PET and PEN beads. Short blocks in the copolymer exert a sort of "bridging" effect between the homopolymers, reducing the mean displacement of the beads, and avoiding phase segregation into bigger clusters.

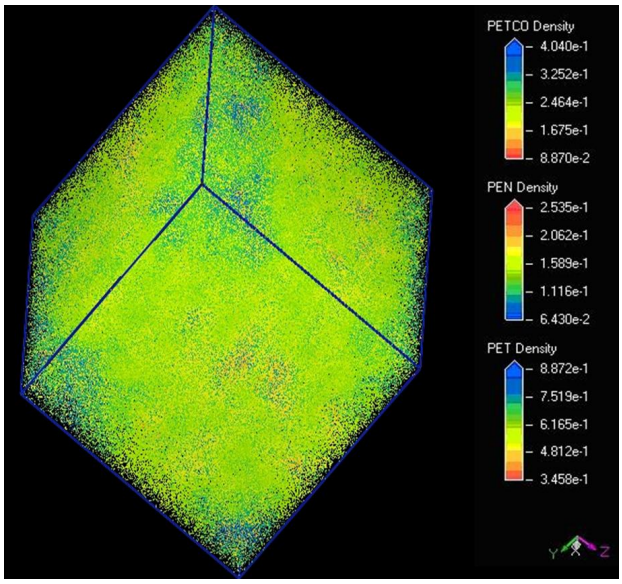

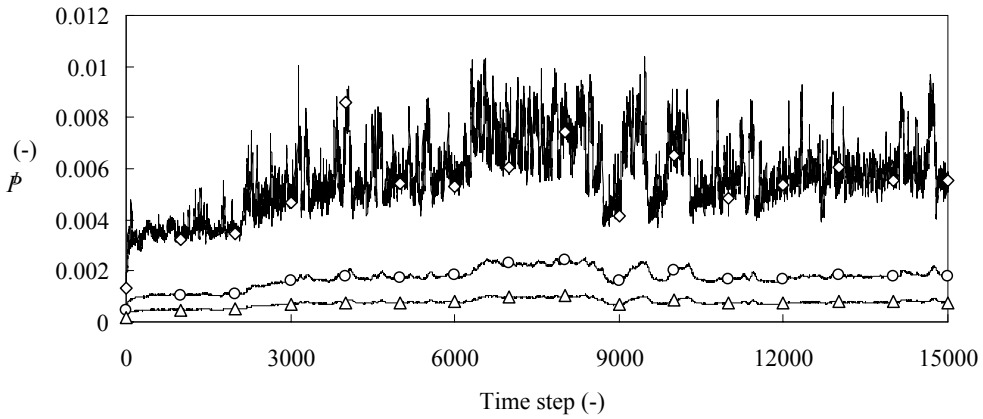

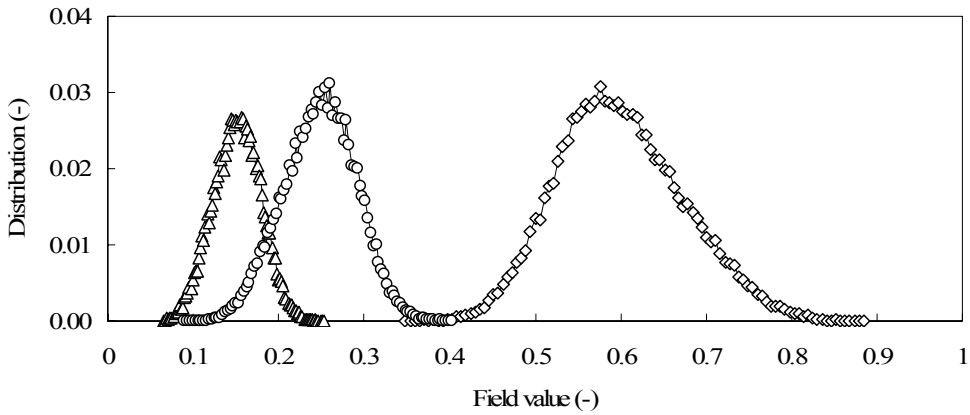

Figure 4.3: Three-dimensional bead volumetric density distribution (a, top), order parameter P_1 (b, center) and density field distribution (c, bottom) of the phase segregation for the 80% PET - 20% PEN blend system at 583 K and in the presence of complete transesterification reaction. Symbols: (◇), PET; (△), PEN; (○), PETCO.

As intermediate situations are more common in nature, further simulations have been performed in order to evaluate the influence of different extent of transesterification. Also, according to the foregoing discussion, the evaluation of miscibility for different degrees of transesterification may reveal some interesting information from an industrial point of view, as the amount of copolymer formed depends upon time, temperature and type of extrusion. According to the literature evidences, that report PET and PEN sequence length reduction with transesterification, we evaluated the phase segregation effect upon transesterification assuming that the block copolymers, as previously mentioned, become more random in nature as the transesterification proceeds. This practically corresponds to a shorter bead sequences in the copolymer mesoscale architecture. As the charts in Figure 4.4 clearly show, the order parameters decay almost linearly with increasing the extent of the transesterification reaction, that is, as the compatibiliser copolymer becomes progressively more and more random in its primary sequence.

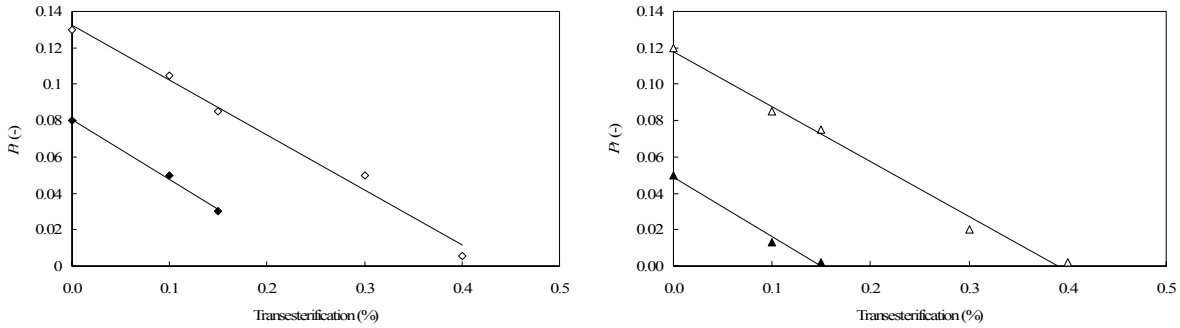

Figure 4.4: Order parameter P_I for PET (a, left) and PEN (b, right) as function of the extent of the transesterification reaction. Open symbols: blend composition 80% PET / 20% PEN; filled symbols: blend composition 92% PET / 8% PEN.

Interpreting density field distributions in a many-phase system to decide whether segregation takes place is not always easy (Ihm et.al., 1996). In some cases segregation occurs when the systems shows different glass transition temperatures, T_g; here, the segmental size responsible for a single T_g is about 100 Å, a dimension almost comparable to the one involved in our simulations (about 74 nm). Such a dimension is however smaller than, for example, the limit of the optical range, where the crucial factor is the haziness. In this case, optical clarity can be reached with a lower degree of transesterification, as bigger segregation domains may not exclude homogeneity. Definitely, the response depends upon the size of heterogeneities which define phase separation.

In order to evaluate barrier effects such as permeability and diffusivity of oxygen in the PET/PEN blends, we performed simulations on both 80% PET / 20% PEN and 92% PET / 8% PEN systems at a finite-element level and in the two limit conditions: i) without transesterification, and ii) in the presence of a complete transesterification. Importantly, the density distributions obtained from the relevant MS were used as input data for these calculations. As PET and PEN polymers are both endowed with a certain degree of crystallinity, for these simulations we used the literature available values of the degree of crystallinity, *P* and *D*, and Equations [10.4-12.4] to obtain the corresponding values of the semi-crystalline homopolymers, as shown in Table 4.4.

	P_G (barrer)	D_G (cm^2/s)	S_G ($cc(STP)cm^{-3}atm^{-1}$)	X (-)	P_{SC} (barrer)	D_{SC} (cm^2/s)	S_{SC} ($cc(STP)cm^{-3}atm^{-1}$)
PET	$7.05 \cdot 10^{-2}$	$5.2 \cdot 10^{-9}$	0.103	0.31	$3.35 \cdot 10^{-2}$	$3.6 \cdot 10^{-9}$	0.0711
PEN	$2.54 \cdot 10^{-2}$	$1.6 \cdot 10^{-9}$	0.121	0.43	$8.20 \cdot 10^{-3}$	$9.1 \cdot 10^{-10}$	0.0690

Table 4.4: Literature values for oxygen permeability P_G, diffusion D_G, solubility S_G [60], and degree of crystallinity X for amorphous PET and PEN homopolymers [61], and values of P_{SC} D_{SC} and S_{SC} for the corresponding semi-crystalline species as calculated via Equations [10.4]-[12.4]. 1 barrer = 7.5005 x 10^{-18} $m^2 \cdot s^{-1} \cdot Pa^{-1}$.

Figures 4.5a and 4.6a below illustrate the O_2 permeability *P* of the blends along the *z* axis for the 80% PET / 20% PEN system, in the case of no transesterification and with complete transesterification reaction, respectively. Figures 4.5b and 4.6b visualise the corresponding distributions of *P* in the xy plane. Analogous results have been obtained in the *x* and *y* directions, and for the diffusivity *D* (data not shown). The average values for *P* and *D* as obtained from the simulations are listed in Table 4.5.

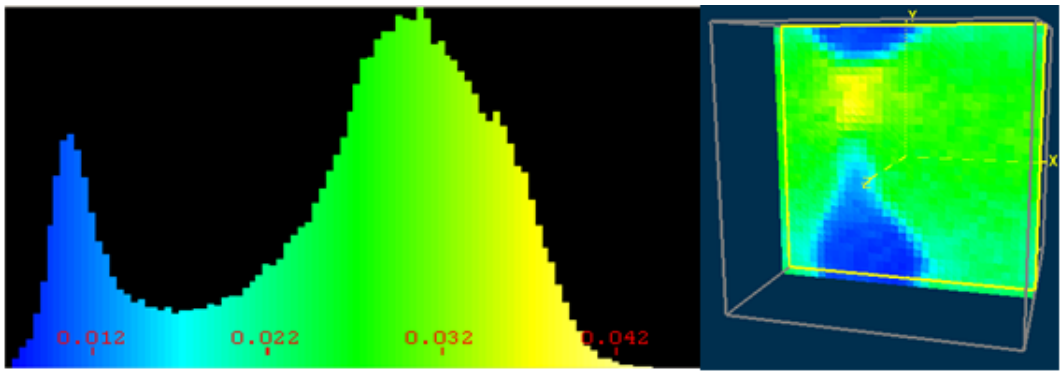

Figure 4.5: Oxygen permeability *P* along the *z* axis (a, left) and permeability distribution in the *xy* plane (b, right) for the 80% PET – 20% PEN system without transesterification.

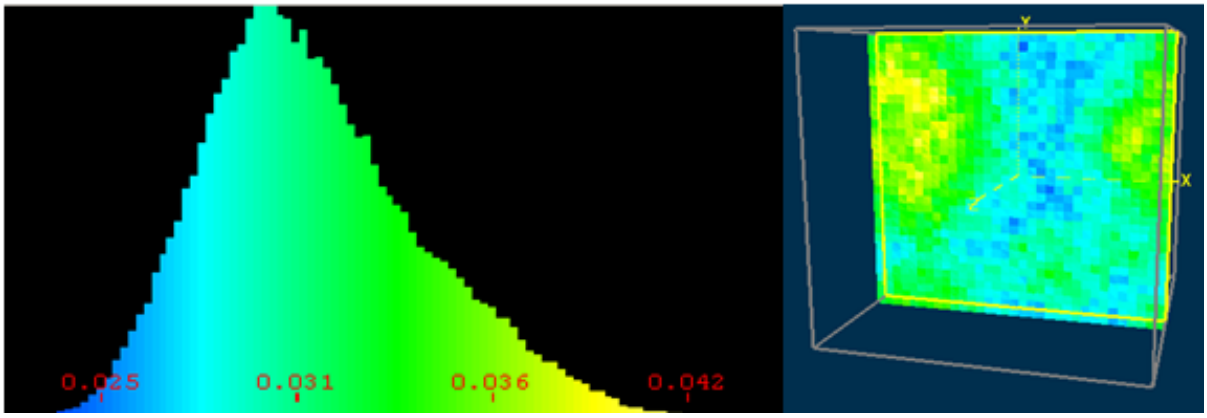

Figure 4.6: Oxygen permeability *P* along the *z* axis (a, left) and permeability distribution in the *xy* plane (b, right) for the 80% PET – 20% PEN system with transesterification.

	P (barrer)	*D* (cm^2/s)
PET	$3.35 \cdot 10^{-2}$	$3.59 \cdot 10^{-9}$
PEN	$8.20 \cdot 10^{-3}$	$9.10 \cdot 10^{-10}$
80% PET / 20% PEN no transesterification	$2.71 \cdot 10^{-2} \pm 1.45 \cdot 10^{-4}$	$2.92 \cdot 10^{-9} \pm 1.17 \cdot 10^{-11}$
80% PET / 20% PEN complete transesterification	$2.96 \cdot 10^{-2} \pm 2.80 \cdot 10^{-6}$	$3.18 \cdot 10^{-9} \pm 1.21 \cdot 10^{-12}$
92% PET / 8% PEN no transesterification	$3.07 \cdot 10^{-2} \pm 1.23 \cdot 10^{-4}$	$3.29 \cdot 10^{-9} \pm 1.33 \cdot 10^{-11}$
92% PET / 8% PEN complete transesterification	$3.18 \cdot 10^{-2} \pm 5.57 \cdot 10^{-5}$	$3.41 \cdot 10^{-9} \pm 2.80 \cdot 10^{-12}$

Table 4.5: Average values for oxygen permeability *P* and diffusion *D* in 80% PET / 20% PEN systems without transesterification and with complete transesterification. 1 barrer = 7.5005 x 10^{-18} $m^2 \cdot s^{-1} \cdot Pa^{-1}$.

Blends without transesterification clearly show two peaks (see Figure 4.5(a)), due to the presence in the cell of two separated phases with quite different barrier properties. This also

justifies the higher standard deviations for *P* and *D* in such systems (see Table 4.5), as these parameters strongly vary in the cell. On the other hand, in miscible blends *P* and *D* show one peak only, with lower standard deviations, in harmony with the more homogeneous structural topology. A glance to Table 4.5 further reveals that barrier properties are only moderately improved by blending PET with PEN, at least up to 20% PEN. The analysis of both permeability and diffusivity suggests that when segregation occurs, the barrier effect increases slightly. This is probably caused by the hindering effect of the larger domains of PEN, that partly obstacle the oxygen displacement in the system. This further seems to indicate that in PET/PEN blends barrier effects are enhanced by larger amount of PEN, possibly with a higher degree of crystallization, and preferably with the creation of large domains which are improved when segregation phase occurs.

Figure 4.7 summarizes the estimated barrier effect improvement due to the presence of PEN in the case of both 92% PET - 8% PEN and 80% PET - 20% PEN. As clearly demonstrated, permeability and diffusivity changes are confined, especially if compared, for instance, with industrial food packaging permeability requirements (1 or even more order of magnitude less). In any case, the trend for blends with higher PEN percentage seems to exclude the fact that notable barrier properties could be achieved in the PEN concentration range considered. Considering the high market cost of the PEN material, all these evidences may suggest that, when the ultimate goal consists in the achievement of high improvements in barrier properties, alternative routes should be pursued such as, for instance, the design of suitable PET-organoclay nanocomposites.

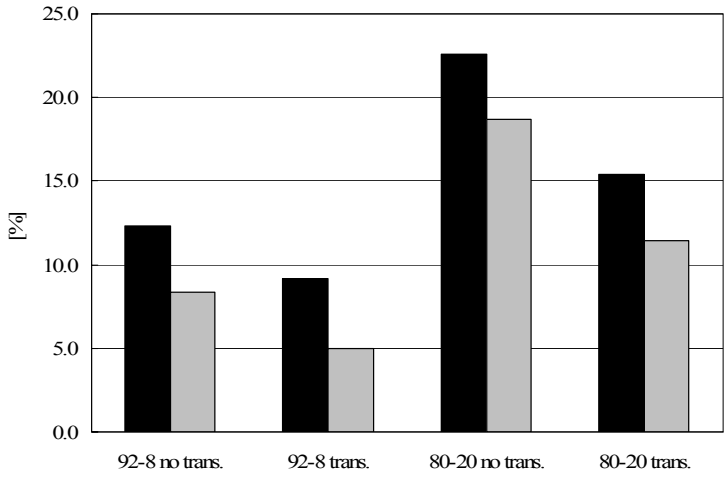

Figure 4.7: Comparison of barrier effect improvement for oxygen permeability (black bars) and diffusivity (grey bars) in semi–crystalline PET/PEN blends as estimated according to the many–scale molecular simulation approach.

In this part of the work, we have investigated the phase behaviour of PET/PEN blends both in the absence and presence of a transesterification reaction, and calculated some transport properties of oxygen in these blends in the light of possible applications as barrier materials.

According to the multi-scale molecular modelling procedure proposed here, the input parameters necessary to perform calculations at a higher length scale level (e.g., mesoscale) have been obtained by performing simulations at a lower length scale (e.g., atomistic molecular dynamics and/or Monte Carlo). The procedures have been validated against experimental evidences, showing excellent agreement.

Summarising the results obtained, mesoscale molecular modelling of PET/PEN homopolymer blends has demonstrate complete immiscibility for these systems, in net agreement with literature results provided by previous experimental tests. As a transesterification reaction usually occurs during the extrusion process of these materials, the many-scale simulation approach adopted in this work demonstrates that miscibility is improved by a longer annealing process or, in other words, by longer transesterification times. In particular, by assuming an ideal situation according to which a complete transesterification is achieved, the system is completely mixed. Differences between the segregated and mixed systems are quite evident, as the relevant order parameters differ by two orders of magnitude, and, in the case of transesterification, probability densities are narrowly distributed around a single value.

Imposing a higher degree of randomness in the copolymer favours miscibility, as at the end of the simulation bead density distribution varies weakly in each grid. The trend that testifies a higher induced miscibility with a deep transesterification has been fully confirmed by mesoscale molecular modelling. Simulations can be helpful to predict the behaviour of the blend at different levels of transesterification, temperature and, at the occurrence, shear rate.

Finally, further investigation with finite-difference simulations have been performed to obtain physical properties of the blends. Barrier effects such as permeability and diffusivity were calculated for miscible and immiscible blends. In the first case, the effects can be summarized by a quasi-Gaussian distribution with one neat peak, while in the second case the creation of large domains due to segregations reflects the presence of two peaks. Globally, however, only a modest increment of the barrier properties in the immiscible blends can be detected, as the creation of larger domains partially hinders the displacement of the gaseous molecules. Therefore, alternative routes such as PET/organoclay nanocomposites could constitute a better and more efficient way to confer higher barrier effect to this polymeric material.

4.3 The case of automotive polymer scraps

4.3.1 Aims of the study

The world annual consumption of plastic materials has increased from around 5 million tons in the 50s to nearly 100 million tons today (Waste on Line, 2008). At the end of the service-time of plastic wares, as well as along the pathway of their production processes, large amounts of scrap arise. Therefore, the question of the disposal of used plastics has gained increasing importance in the public discussion because of the environmental problems resulting from the rapid growth of plastic waste amounts during last years.

A further, topical solution to cost saving is internal recycling. The major problem in the recycling of used plastics is connected to a great inhomogeneity of the polymers present in the waste. The eventual incompatibility of these components is the most important reason of the difficult processing and inferior mechanical properties of the resulting products from mixed, chemically different polymers. The detailed knowledge of the microstructure of the systems, coupled with the operative process parameters and the eventual effects of a compatibiliser can reduce or prevent this die build-up, and can allow recycling of laminated film scrap.

Nowadays, alternative destinations for industrial scraps are studied to reduce the percentage of plastic materials to be landfilled or incinerated; European legislation foresees that, in case of automotive components, within 2015 the percentage of recycling should rise up to 95 % (Directive 2000/53/EC, 2000). Even if companies are not so far from the target, a major effort is needed to meet this requirement, as represented in Figure 4.8.

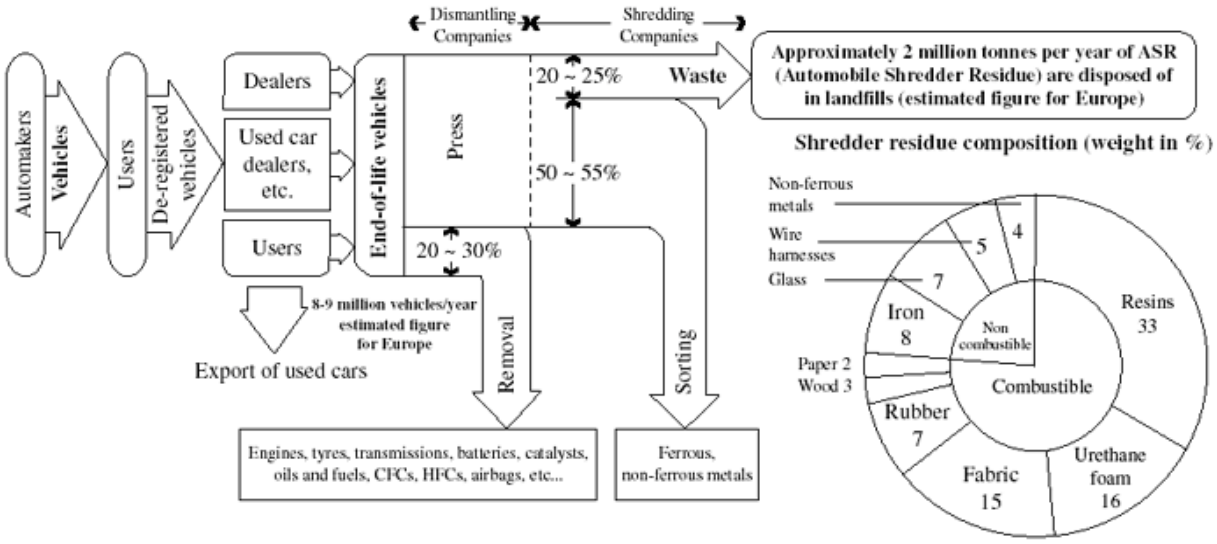

Figure 4.8: major steps for end-of-life vehicles recycling according to EU directive, taken from Kanari et.al., 2003).

Nowadays polymers constitute also an important part of car composition, such as lights, internal components, parts of the engine. Although plastic components constitute a relatively small amount in weight of motor cars wastes, it has increased from about 5% to 12% by weight in 30-35 years (Wuppertal Institute, 2001).

Thus it is not surprising how companies are involved in supporting and financing research in this field. For instance, Toyota was one of the first companies to commit a study about polymer – clay nanocomposites in the late 70es (Okada and Usuki, 2006) to improve durability and performances of materials. And few years later, in the 80es, Toyota was the first company to directly use nanocomposites in car components. Today, it should not be surprising how one of the most challenging tasks for car companies deals with recycling of polymer scraps, due to new European Directives.

In what follows, we present a multiple-step research for rear-light polymeric scrap recycling, a study that coupled multi-scale molecular simulations and experimental techniques in laboratory for comparison, starting from polymer blends, up to the creation of nanocomposites. All recycling alternatives considered in the research include materials of a relatively high quality, as they represent post-processing scraps.

These works have been carried on with the collaboration of CRP (Centro Ricerche Plast Optica) of Centro Ricerche FIAT (CRF).

4.3.2 Polymer blends: morphologies and mechanical properties

In this part of the study, we investigated the properties of two polymers (or polymer blends); the aim was to mix together these different scraps, to obtain a blend which is acceptable in terms of homogeneity and mechanical properties to be employed for the same purpose. The considered polymers were ABS (acrylonytrile – butadiene – styrene blend) and the PC (polycarbonate) and PMMA (polymethylmethacrylate).

The ABS material today is used also in automotive industry. ABS is a two phase polymer blend. The continuous phase of styrene acrylonitrile copolymer (SAN) confers to this material its well known rigidity, hardness, and heat resistance. The toughness of ABS is instead the result of submicroscopically fine polybutadiene rubber particles uniformly distributed in the SAN matrix. The structure is eventually reinforced by the formation of crosslinks. Given the complexity of this material, we decided to adopt an approximated molecular model for it, constituted of three molecular species: i) a butadiene homopolymer (polyB); ii) an acrylonitrile-styrene block copolymer (SAN), and iii) a ramified macromolecule having a butadiene main backbone and styrene-acrylonitrile copolymer branches (B-SAN).

It should be mentioned that PC is considered the best material (but also the most expensive one), followed by ABS and PMMA. Thus what follows is an investigation about mixing properties of PC/PMMA/ABS, and the relevant mechanical properties of interest.

The procedure followed in this work is similar to the one described in Paragraph 4.3.1, as from MM/MD or MC simulations we investigated blend morphologies at the mesoscale (with Mesodyn software), to calculate mechanical properties with FEM simulations. Thus in this case only the most relevant details are given, being the input parameters for mesoscale simulation obtained with the same procedures.

Temperature was chosen according to the extrusion temperature employed in the process (550 K), as the process usually imposes a rapid quench (1000 K/min) that “freezes” the structure. Some characteristics of polymers were given by CRP, together with the percentages of each component. Thus, the main work here regards the exploration of possible morphologies, the relationship morphology – mechanical properties (locally and globally). We examined the ABS blend, and then we mixed it with PC and PMMA.

The ABS material is a two phase polymer blend. The continuous phase of styrene-acrylonitrile copolymer (SAN) confers to this material its well known rigidity, hardness, and heat resistance. The toughness of ABS is instead the result of submicroscopically fine poly(butadiene-styrene-acrylonytrile), B-SAN rubber particles uniformly distributed in the

SAN matrix. The structure is eventually reinforced by the formation of crosslinks. Given the complexity of this material, we decided to adopt an approximated molecular model for it, constituted of two molecular species: i) an acrylonitrile-styrene block copolymer (SAN), and ii) a ramified macromolecule having a butadiene main backbone and styrene-acrylonitrile copolymer branches (B-SAN). The ABS considered in this study has a very low percentage of free butadiene, which has been neglected. The ABS considered has a ratio SAN:B-SAN=2:1 and a molecular weight of 25000 amu. A schematization of the bead subdivision adopted is exposed in Figure 4.9.

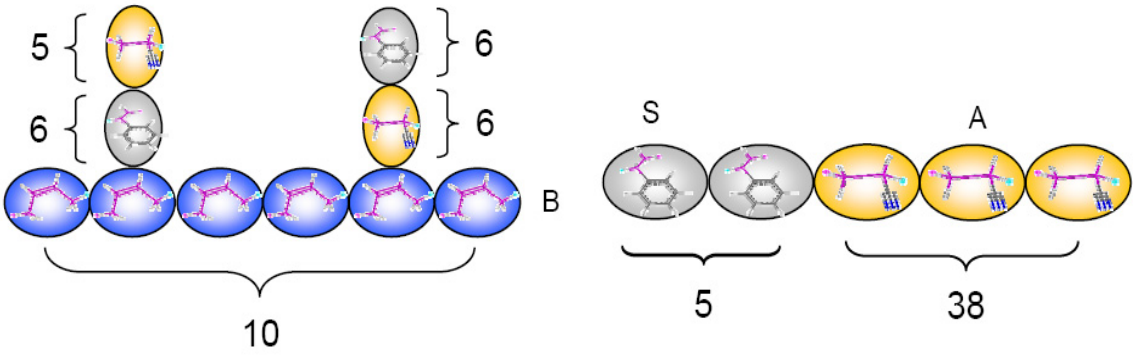

Figure 4.9: bead structure schematisation of B-SAN (left) and SAN (right).

In the case of PC, to comply with the mesoscale simulation requirement of similar bead dimensions, the entire constitutive repeating unit (CRU) was divided into two separate structural units, PC01 and PC02, while PMMA monomers constituted a single structural unit. Flory-Huggins parameter χ for all components and C_∞ have been calculated with the procedure exposed in the previous paragraph. Morphologies have been evaluated with the Mesodyn software; then mechanical properties have been obtained with FEM calculations (Mesoprop software). In Table 4.6, the characteristics of each constitutive unit of the blends, as considered in Mesoprop software, are exposed. PC and PMMA values are given by CRP, B and SAN values by linear regression with the Synthia modulus of Materials Studio. This modulus uses group additive methods to predict the molecular properties, and is based upon a database of group contributions and connectivity indices, the contents of which are obtained by fitting to experimentally observed properties of interest (Bicerano, 2002).

	PMMA	PC	B	SAN
Density [kg/m^3]	1170	1200	916	1126
Young's modulus [GPa]	3,078	2,35	$2{,}435 \cdot 10^{-3}$	3,2
Poisson's modulus [-]	0,399	0,405	0,422	0,382

Table 4.6: input data for FEM calculations.

The ABS blend morphology was firstly examined; in Figure 4.10 the Order Parameter OP (a) and the density distributions (b) are shown, together with the ABS morphology (c, d).

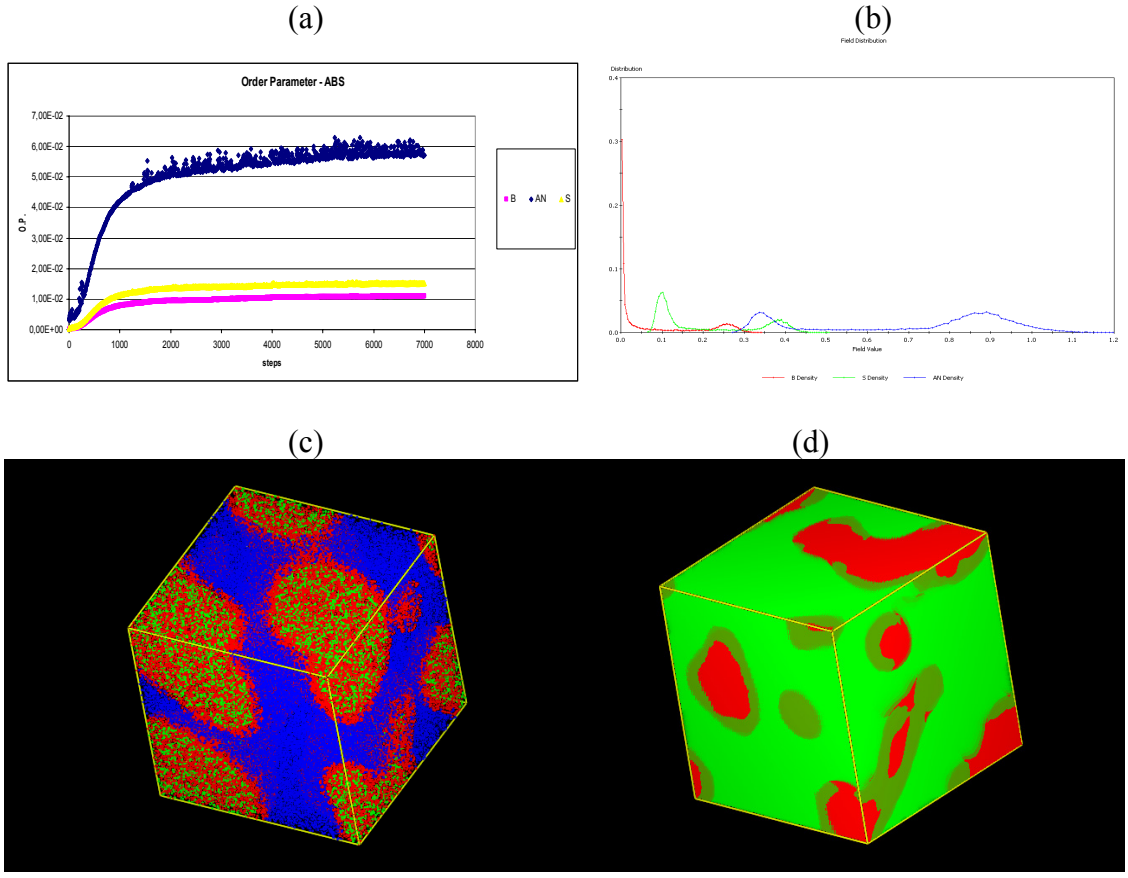

Figure 4.10: a, OP for AN, B, S; b, density distributions for AN, S, B; c: 3D visualization of ABS (AN: blue, B: green, S: red); d: 3D visualisation of ABS, where only B-SAN (rubbery phase, red) and SAN (green) are evidenced.

It should be noticed how a partial phase segregation occurs, mainly due to the repulsions between the most polar AN, and the other components, as demonstrated by the OP and the density distributions, where different peaks are present. As mentioned in several works (see

the paper of Stretz et.al., 2005), the rubbery phase, here constituted by the B-SAN structure, remains in separate domains of spheroidal shape: this is evidenced in Figure 4.10 d.

Substantially, mesoscale simulations confirm and reinforce the well known hypothesis about ABS morphologies.

Young's modulus of ABS was calculated by importing density distributions of mesoscale simulations. Due to the particular morphology, we used two values for Young and Poisson's modulus (rubbery B and rigid SAN, as listed in Table 4.6). The overall Poisson's modulus obtained was 2.42 GPa with an experimental value of 2.2 GPa given by CRP.

A PC / ABS blend was then considered; the first aim was to examine blend morphologies as a function of PC percentage. As a general statement, the partial phase segregation implies the separation of the most polar AN (yellow-orange in Figure 4.11 a) in islands surrounded by S (yellow-green). The less polar B acts like a compatibiliser, lowering the less favourable interactions between PC and AN, thus bridging between these two kind of beads. This is also testified by the density distributions and the OP trend (Figure 4.11 b and c, respectively) for a PC/ABS = 45/55.

It should be noticed, however, that phase segregation implies the formation of separate domains at "mesoscale" level: separate domains have no more than 10-20 nm. In all the other cases similar behaviours can be observed, even though where PC percentages are higher (and AN percentage is lower) phase segregation is less evident.

Then, mechanical properties and local non-homogeneity phenomena have been evaluated. Table 4.7 reports Young's modulus and Poisson's modulus as a function of PC %; local deviations from homogeneity of mechanical properties are also acceptable, if not negligible.

(a) (b)

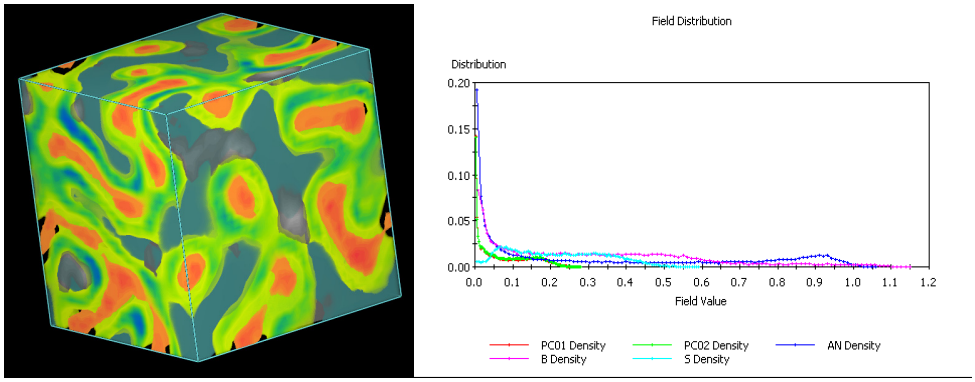

(c)

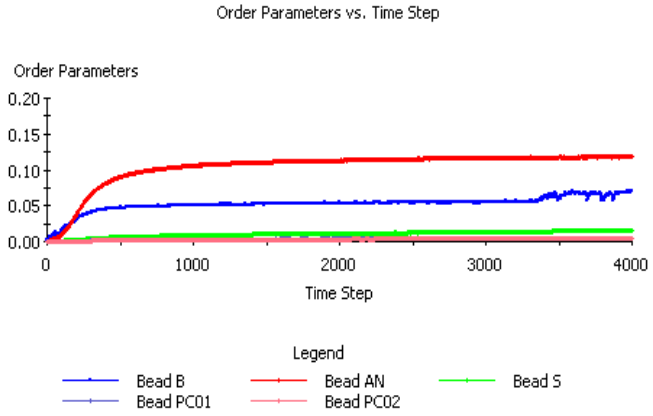

Figure 4.11: a, 3D visualisation of PC /ABS = 55 / 45 blend; b: density distributions; c: OP.

PC (%)	0	10	15	30	35	50	55	70	85	90	100
G [GPa]	2,2	2,23	2,25	2,29	2,3	2,35	2,35	2,4	2,34	2,45	2,35
v [-]	0,381	0,389	0,39	0,39	0,401	0,400	0,401	0,404	0,405	0,404	0,405

Table 4.7: FEM simulations for PC / ABS blends at different compositions. G: Young's modulus; v: Poisson's modulus.

The final step was the PC / ABS / PMMA modelling; following the instructions of CRP, the PC percentage was kept constant in weight (55 %), in order to guarantee a sufficient glass - transition temperature (higher than 430 K) to the blend. Thus, in the ternary blend, only the percentages of ABS and PMMA varied. Then we decided to model the system in such a way that the ABS could be progressively substituted by the less expensive PMMA:

1) PC 55 %, ABS 40,5 % ,PMMA 4.5 %;
2) PC 55 %, ABS 31,5 %, PMMA 13,5 %,
3) PC 55 %, ABS 13,5 %, PMMA 31,5 %.

With the same models and procedures of the previous simulations, we obtained rather similar morphologies; it can be noticed (Figure 4.12) how PMMA (yellow) is mainly placed in opposite positions with respect with PC and AN (violet), due to the unfavourable interactions. Even if the presence of PMMA heavily contributes to improve phase segregation, the usual ABS rubbery structure is generally maintained.

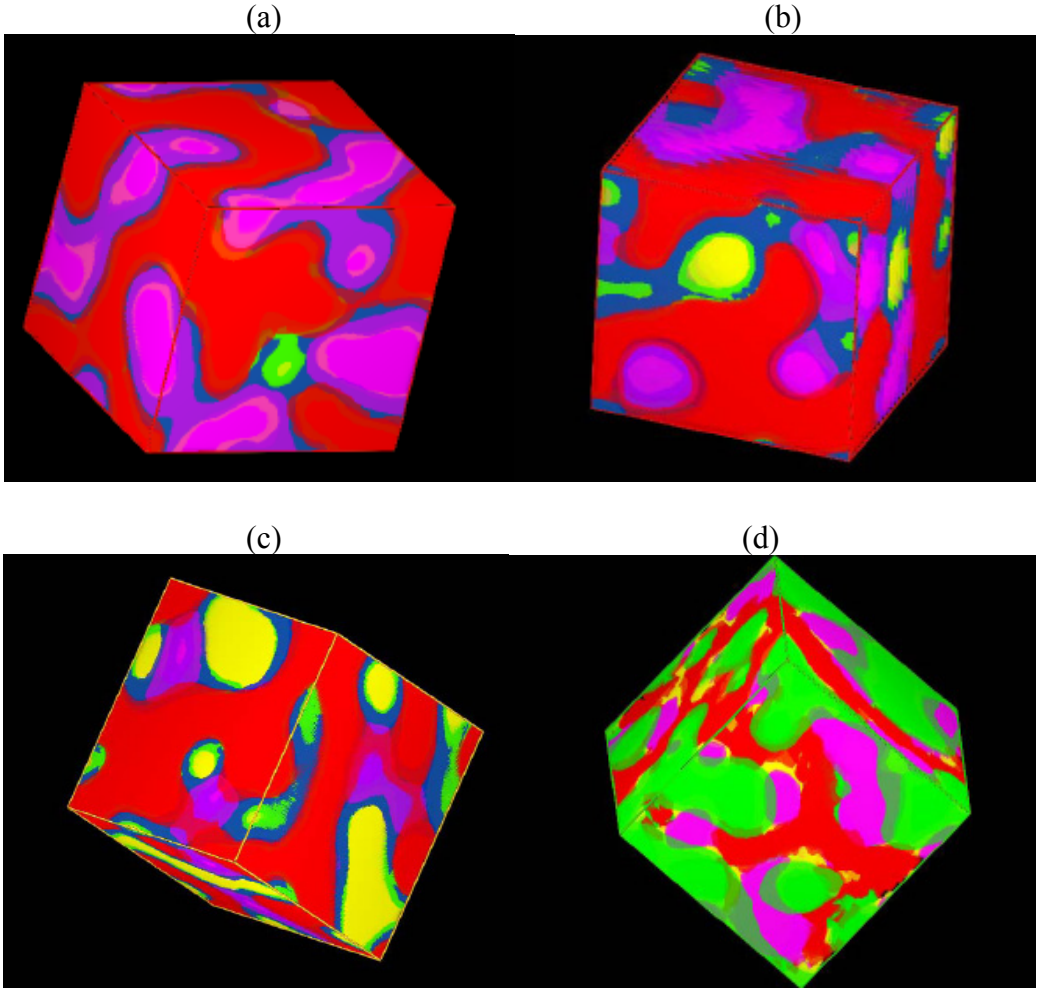

Figure 4.12: ABS / PC /PMMA morphologies as a function of PMMA %; a: PC 55 %, ABS 40,5 % ,PMMA 4.5 %; b: PC 55 %, ABS 31,5 %, PMMA 13,5 %; c: PC 55 %, ABS 13,5 %, PMMA 31,5 %; d: PC 55 %, ABS 40,5 % ,PMMA 4.5 %, "rubbery phase (polyB-SAN) is evidenced (pink). Yellow: PMMA, red: PC.

Mechanical properties are shown in Figure 4.13, together with the experimental comparison provided by CRP. The improvement is almost constant; even if the overall values are higher than the experimental ones, one should bear in mind that the starting Young's modulus of

ABS obtained from molecular modelling is slightly overestimated. Thus the procedure adopted is able to give an affordable prediction.

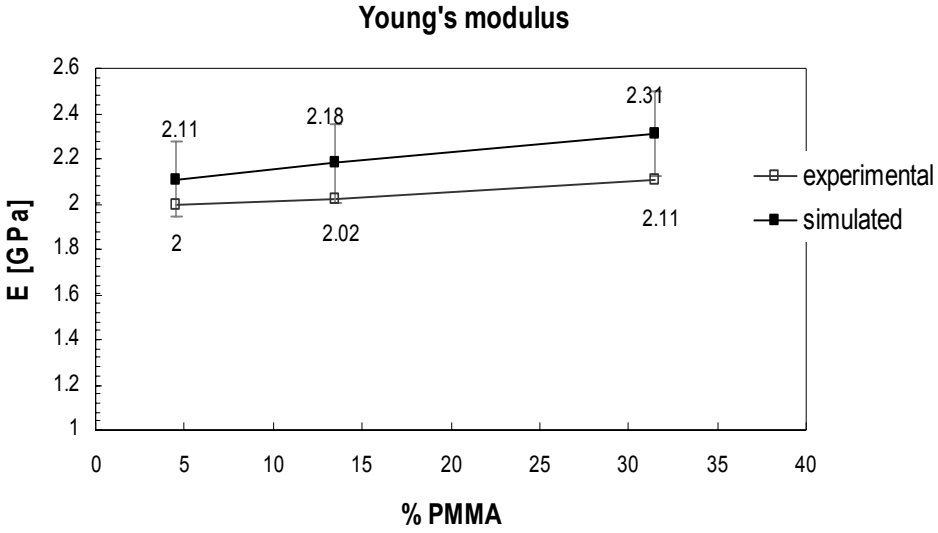

Figure 4.13: experimental and calculated Young's modulus for the PC/PMMA/ABS blend as a function of PMMA fraction.

As a conclusion, multi-scale molecular modelling for such complex systems is able both to predict morphologies and to give affordable values of mechanical properties, even though ideal values can slightly differ from the experimental ones, based on real samples. In general, morphologies are dominated by the rubbery-like structure of ABS, mechanical properties of ABS can be improved (not dramatically) by adding PMMA or PC, and local inhomogeneities in density distributions do not affect appreciably local mechanical properties.
To considerably improve mechanical properties of ABS scraps, as a second step we modelled ABS nanocomposites (clay-based) structures.

4.3.3 Nanocomposites: morphologies and mechanical properties

In the last decade, nanotechnologies have opened new avenues in the field of materials science, which are not yet fully explored. Accordingly, in this part of the work we focus our attention on the procedure of embedding small quantities of nanoparticles (2-5 % in weight), such as montmorillonite layers (MMT) modified by quaternary ammonium organic salts (quats) in the recycled polymer matrix, a technique which yields a considerable improvement of physical and mechanical properties of the scrap, ultimately increasing life cycles and versatility of such materials (Utracki, 2004). In details, we have applied a multi-scale simulation approach to study the nanostructure morphology of recycled ABS (acrylonitrile –

butadiene – styrene polymer blend), with MMT layers intercalated into the blend. To date, there are only a few publications dealing with the synthesis and characterization of ABS nanocomposites (Stretz et.al., 2005; Wang et.al., 2003), upon which we based some of our theoretical assumptions and which we used for validation of the calculated morphologies and mechanical properties.

According to our computational procedure, starting from quantum-mechanical and atomistic-based molecular mechanics/molecular dynamics (MM/MD) simulations, we developed and applied a procedure to choose the more appropriate clay compatibilisers (i.e., quats) for MMT layers exfoliation, in terms of interaction/binding energy and basal spacing values. We then performed mesoscale level (10-100 nm) simulations to determine ABS blend morphology, and evaluate blend density distributions of domains. Lastly, this information has been imported into finite element methods calculations (FEM), so as to obtain the mechanical properties of the final nanocomposite (ABS-MMT).

The proposed procedure relies solely on input data obtained by molecular simulations, exception made for the experimental value of the Young modulus of the filler. This computational recipe constitutes a sort of innovative, *ab initio*, step-by-step procedure, in which each level calculations yield information necessary to perform simulation at the next, higher level length/time scale. Once again, the computational part related to the calculation of input parameters for mesoscale simulations is similar to the one described in the previous paragraphs (see Paragraph 4.2), thus here we will only give details of novel procedures.

Atomistic simulations of quat intercalation between MMT layers, and MMT exfoliation by polymer insertion have been performed following a well-established procedure already described in details in our previous papers [8-11]. We built a simplified MMT structure, in which the chemical structure is derived from the mineral pyrophyllite by random substituting Al ions by Mg ions. The principal building element MMT are 2-D arrays of aluminum-oxygen-hydroxyl octahedra sandwiched between two 2-D arrays of silicon -oxygen tetrahedra, overall forming a three-layered platelet.

Typical ammonium quaternary salts have been considered to modify MMT layers, with the final goal of rendering them less hydrophilic, and ultimately facilitating polymer intercalation (i.e., compatibilisers). Given the experimental values of the ion exchange capacity of commercial MMTs, in the relevant, 3D model building we assumed a complete ion exchange process in which all Na ions present over MMT surface were quantitatively exchanged with quats.

Polymer chains constructions have been performed by the use of the already mentioned RIS

method, while quats 3D model building and charge calculations have been obtained by classical quantum-mechanics methods (Tanaka and Goettler, 2002).

After each component was modelled, (MMT platelet, quat and polymer), the overall, ternary system was built. The bond between the quaternary nitrogen and the methylene group of each quat was oriented perpendicularly to the *xy* plane of the mineral, and the same N atoms was positioned just above the corresponding magnesium ion; this procedure ensures that the dispersive term of the van der Waals forces are favoured over the repulsive one.

The lattice constant *c* of the MMT cell with five quat molecules on one side was extended to 125–150 Å, depending on the length of quats and polymer molecules, to simulate an exfoliated structure. Further, this guarantees that the polymer chain is attracted to the quat-MMT surface by favourable non-bonded interactions, but is still far away enough, so that its initial conformation hardly affects the equilibrium states of the system.

The first set of MD simulations has been performed on ternary systems MMT-quat-polymer in the canonical (i.e., NVT) ensemble, to evaluate the interfacial strength between the supposed already-dispersed clay platelet, the quat and the polymer chain (see Figure 4.14).

Figure 4.14: 3D periodic cell of MMT (light grey and white stick-and-ball representation, lower part of the Figure), quat (cloisite 10A®, dark grey and white stick-and-ball representation, middle part of the Figure) and SAN polymer (grey stick representation, upper part of the Figure) employed for binding energies calculation.

This information can be obtained by calculating the binding energies between the system components which, in turn, are the negative of the MD interaction energies for the corresponding binary and ternary systems, as given below (Fermeglia et.al., 2004).

$$E_{pol-MMT-quat} = E_{pol} + E_{MMT} + E_{quat} + E_{MMT-quat} + E_{MMT-pol} + E_{pol-quat} \quad [17.4]$$

where the first three terms represent the energy of polymer, MMT and quat (consisting of both valence and non-bonded energy), and the last three terms are the interaction energies between each of two component pairs, made up of non-bonded terms only. In a straightforward fashion, the binding energies of binary systems (MMT-polymer, MMT-quat, and polymer-quat) can be defined as follows:

$$\begin{aligned} E_{MMT-pol} &= E_{(MMT+pol)} - \left(E_{MMT} + E_{pol}\right) \\ E_{MMT-quat} &= E_{(MMT+quat)} - \left(E_{MMT} + E_{quat}\right) \\ E_{pol-quat} &= E_{(pol+quat)} - \left(E_{pol} + E_{quat}\right) \end{aligned} \quad [18.4]$$

Moreover, the results of these MD simulations allowed us to explore the ABS interlayer structure in the corresponding nanocomposite, and to evaluate the most favoured polymer chain for gallery intercalation. Indeed, ABS blends are extremely complex systems; they are mainly constituted by acrylonitrile-styrene block copolymers chains (SAN) - the most rigid phase - and butadiene branched with SAN lateral chains (polyB-SAN) constituting the "rubbery" phase. To perform this set of simulations, after simulated-annealing MD (Fermeglia et.al., 2004) to relax the structures, NVT MD experiments were run at 550 K. A high temperature was chosen in order to equilibrate faster the system. During these simulations, the positions of the MMT and K^+ atoms/ions were fixed, but the polymer molecule and the quats were allowed to move accordingly. System equilibration was monitored by recording the instantaneous values of total, potential and non-bonded energy. After reaching equilibrium, the MD data collection phase was extended up to 300 ps. To calculate each binding energy values of Eq. [18.4], the following procedure was adopted, here illustrated only for the first line of Eq. [18.4] for the sake of brevity. We first created an ABS–MMT system deleting the quat molecules from a specific energy minimized conformation of the ternary ABS-MMT-quat system, and calculated the corresponding potential energy $E_{pol\text{-}MMT}$ without further minimization. Next, again from the ternary system we deleted the MMT platelet and the quats, leaving the ABS system components alone; this yields the E_{pol} term. Similarly, we deleted the ABS components and the quats from the ternary system, and calculated the E_{MMT} term. The same procedure is then repeated straightforward to obtain the values of the terms of the other two lines in the same equation.

Basal spacings of intercalated quats into MMT layers have been evaluated using isobaric-isothermal (NPT) MD simulations of the MMT-quat under 3D periodic binary conditions. In this case, whilst the *x* and *y* cell dimensions are kept fixed, constraints on *z* axis (normal to MMT layers) are removed, in order to reach the equilibrium distance between the layers. During each MD, both montmorillonite layers were treated as rigid bodies, while all atoms in the interlayer space including K^+ cations were allow to move (Toth et.al., 2004). The ultimate information afforded by these calculations is then the available space for polymer insertion after MMT modification by a given quat (see Figure 4.15).

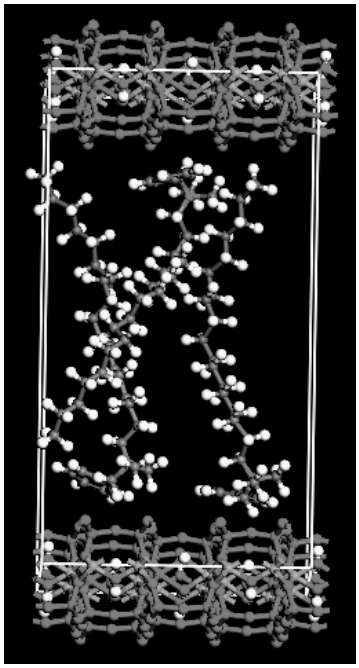

Figure 4.15: 3D periodic cell of MMT (grey stick-and-ball representation, upper and lower parts of the Figure) and quat (cloisite 10A®, white and grey stick-and-ball representation, central portion of the Figure) employed for basal spacing calculations.

The exfoliation process for this kind of composite blend is difficult to be evaluated by MM/MD techniques if treated with a single, conventional scaled polymer in a ternary periodic system. To overcome problems related to complex copolymer chains introduction and orientation, we performed a plethora of different simulations of the exfoliated structure, in order to analyze binding energies and chain orientations; each polymer structure was properly re-scaled to few monomers, however still maintaining the proportionality between main and side chains. Overall, the systems considered for this task were the following:

- MMT, quat and butadiene (B), styrene (S), acrylonitrile (AN) single homopolymers;
- MMT, quat and SAN, the last component oriented both with AN and S towards the MMT

surface;

- MMT, quat and polyB-SAN, the last component oriented either parallel or normal to the MMT surface along his B chain.

All results in terms of basal spacing and block copolymer insertion and interaction with the inorganic framework have been averaged and analyzed, with the dual purpose of formulating a criterion for the choice of the best compatibiliser, and to gather preliminary information on the system morphology.

A more, in-depth investigation of blend morphology, segregation at the mesoscale and density distributions was attained by performing simulations of the ABS structure at the mesoscopic level using mean-field density functional theory (Mesodyn software).

Two sets of simulations have been performed at the mesoscopic level. One maintained the visualization of AN, B, S beads in the 3D density distribution cell, while in the second simulation set beads belonging to SAN and polyB-SAN are visualized in the same way, since we were also interested in evaluating the morphology of the rigid phase (SAN) and the rubbery phase (polyB-SAN), respectively. FEM simulations for ABS have been performed with the MesoProp software with the aim of calculating the mean mechanical properties of the sole ABS bulk.

The simulation theory about Mesodyn and Mesoprop software is fully reported in Chapter 3, whilst the details of the procedure used for obtaining input parameters is similar to the one described in previous paragraphs of Chapter 4.

As anticipate a few lines above, grid morphologies were obtained for all systems studied by importing the corresponding density distributions from the relevant Mesodyn simulations. Young modulus and densities for S, AN and B chains have been calculated with the Synthia modulus of Materials Studio. The aim of calculating mechanical properties of the sole blend was to evaluate anisotropies/inhomogeneities in the bulk, and to compare the mean ABS value with the nanocomposite one.

Finally, we examined and simulated the entire ABS-nanocomposite structure at the FEM level. Considerations based upon morphological behaviour of ABS blends (Mesodyn simulations), thermodynamic properties (MM/MD simulations), and experimental evidence [7], indicate how to describe our molecular model in FEM simulations with variable grid, performed with Palmyra software, already described in Chapter 3. In this type of simulations, typical dimensions involved in modelling are about some μm, these dimensions stemming from MMT platelet diameters (2-400 nm) and polymer phase domains.

As mentioned before, mechanical properties and densities of single phases and MMT layers

have to be determined a priori. To this aim, we used densities and mechanical properties of polymer chains calculated with Synthia, while MMT Young modulus and Poisson modulus were taken from (Chen et.al., 2007). Only the 2 phases, polyB-SAN and SAN, have been considered. Synthia calculates properties for homopolymers or random copolymers only; accordingly, its use is suitable for B main chain properties calculations. For SAN blocks in polyB-SAN and SAN copolymer, we averaged the mean values obtained with Synthia for S and AN, respectively. All obtained parameters, which have also been employed in MesoProp calculation, are shown in Table 4.

Although it might be possible to obtain reliable results about elastic constants and, then, mechanical properties from quantum-mechanical calculations (Milman and Warren, 2004), those are time-consuming (due to the presence of a relatively large MMT cell), and this kind of calculations, even if theoretically achievable, were out of the scope of our research.

The procedure for the calculation has been split in 2 parts, according to the morphology of the system: (i) partially exfoliated MMT layers are treated in a first simulation as a stack; and (ii) Young modulus and Poisson modulus obtained from (i) have then been used in a further simulation, in which the whole system is considered. All parameters employed for modelling are shown in Tables 4.8, 4.9, 4.10, 4.11.

	AN - S	AN - B	S - B
X [-]	2.002	2.877	0.286

Table 4.8: mesoscale beads interaction parameters.

	Architecture	Volume fraction
polyB-SAN	S 5 AN 38	33 %
SAN	B 1 B [S 6 AN 5] B 3 B [AN 6 S 6] B 2	67 %

Table 4.9: ABS composition and architecture. Branching chains are enclosed in squared brackets.

a [nm]	1.909
D [cm^2/s]	$3.0 \cdot 10^{-7}$
T [K]	550
Number of steps	5000
Step length [ns]	50
Cell dimension [nm]	52.9 x 52.9 x 52.9

Table 4.10: mesoscale simulations input parameters and features.

	B	SAN
Density [$kg \cdot m^{-3}$]	1.100	1.045
Young modulus *G* [GPa]	$2.435 \cdot 10^{-3}$	3.205
Poisson's ratio ν [-]	0.422	0.382

Table 4.11: input parameters for ABS MesoProp calculation

In the first part of this work, we focused on the choice of the MMT compatibilisers; in particular, two commercial quats, largely used in actual polymer-clay nanocomposite production, have been considered: cloisite10A® and cloisite20A® (Nanoclay, 2006). These two quaternary ammonium salts usually represent a good compromise between basal spacing between MMT layers and favourable binding energy interactions.
The calculated binding binary energies for both quats obtained from NVT MD simulations are shown in Tables 4.12 and 4.13. These Tables also list the corresponding basal spacing values, as obtained from NPT MD simulations.

Polymer	$E_{MMT\text{-}pol}$	$E_{MMT\text{-}quat}$	$E_{pol\text{-}quat}$	Basal spacing
PS	24	1216	32	3.108
PB	7	1266	16	
PAN	41	1248	100	
SAN	9	1165	36	
ANS	15	1102	146	
polyB-SAN	5	1386	116	
polyB-SANa	19	1230	71	

Table 4.12: binary binding energy (kcal/mol) and basal spacing (Å) with cloisite 20A® and MMT for homopolymers AN, S, B and block copolymer SAN and polyB-SAN. SAN = acrylonitrile-styrene copolymer oriented with S next to MMT surface; ANS = acrylonitrile-styrene copolymer oriented with AN next to MMT surface; polyB-SAN = B chain oriented parallel to MMT surface; polyB-SAN = B chain oriented normal to MMT surface.

Polymer	$E_{MMT\text{-}pol}$	$E_{MMT\text{-}quat}$	$E_{pol\text{-}quat}$	Basal spacing
PS	60	1565	22	2.343
PB	101	1537	67	
PAN	7	1560	83	
SAN	64	1566	126	
ANS	30	1562	27	
polyB-SAN	96	1560	88	
polyB-SANa	71	1561	62	

Table 4.13: binary binding energy (kcal/mol)and basal spacing (Å) with cloisite 10A® and MMT for homopolymers AN, S, B and block copolymer SAN and polyB-SAN. SAN = acrylonitrile-styrene copolymer oriented with S next to MMT surface; ANS = acrylonitrile-styrene copolymer oriented with AN next to MMT surface; polyB-SAN = main chain of B oriented parallel to MMT surface; polyB-SAN = main chain of B oriented normal to MMT surface.

All binding energies are positive: this confirms the favourable interactions between all three system components (MMT, quat and polymer). If we carefully examine the binding energy values listed in these Tables, we can clearly see that the energy values depend on the component relative orientation. Moreover, examining the values of the $E_{pol\text{-}quat}$ component (4th column in both Tables), we find that the most polar AN homopolymer is more affine to both quats than all other ABS chain components. In an analogous way, B homopolymer binding energies are smaller. Finally, if we take into account the mean binding energy of SAN and ANS (i.e., 91.0 kcal/mol for 20A and 76.5 kcal/mol for 10A, respectively) and the binding energy for AN, the corresponding values are, respectively, very similar. The same can be noticed if we compare the mean values of the binding energy for polyB-SAN (93.5 kcal/mol for 20A and 83.5 kcal/mol for 10A, respectively), and SAN or AN. This can be sensibly explained with a minor contribution afforded to the total binding energy by the S and B blocks. This last consideration ultimately led us to consider the smaller, rigid and less ramified SAN block copolymer into MMT layers, as the most probable mode of insertion.

If we now compare the mean $E_{MMT\text{-}quat}$ values for the case SAN/ANS and cloisite10A®, we see that they are slightly smaller then the one obtained for cloisite 20A®; more importantly, the corresponding basal spacing is much higher for 20A®, mainly ascribable to the presence two hydrocarbonic tails on this quat. All the considerations developed above led us to conclude that, among the two, cloisite20A® was the most effective compatibiliser for the ABS-MMT nanocomposite system.

The experimental paper by (Stretz et.al., 2005) confirmed both our calculations and conclusion. In their work, in fact, these authors prepared and analyzed ABS/MMT nanocomposite systems. Their TEM images clearly show that exfoliation takes place only in part: only the SAN copolymers enter between MMT layers, creating stacks. The rubber phases, isolated in the shape of round islands, remain next to the stacks, as schematized in Figure 4.16a, while SAN copolymer essentially constitute the matrix phase, as shown in Figure 4.16b [7].

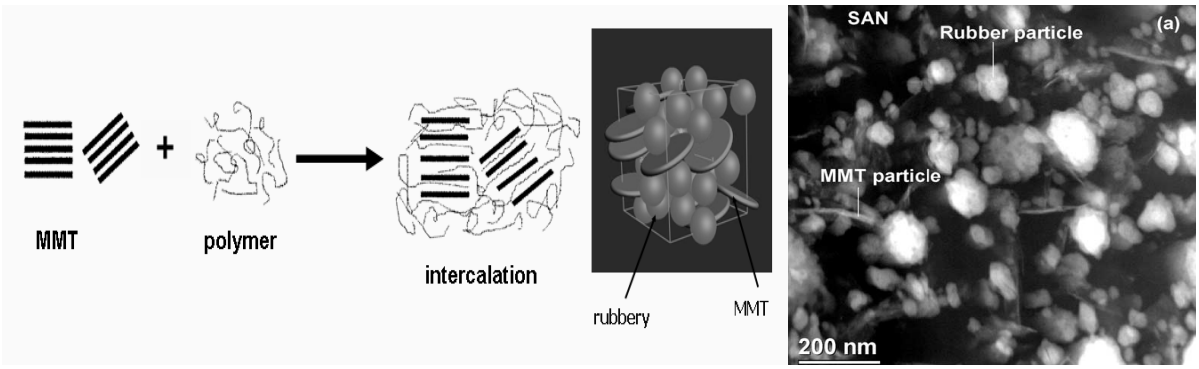

Figure 4.16: (a, left): intercalation and partial exfoliation process model for MMT-ABS; (b, right): TEM visualisation of the ABS-MMT nanocomposite (reproduced from Stretz et.al., 2005, with permission).

In order to estimate ABS morphology, and to import density distributions in MesoProp calculations to evaluate ABS Young modulus, we then performed and analyzed mesoscale simulations with Mesodyn. The relevant results, shown in Figure 4.17a and b, clearly prove that a neat phase segregation take place at the nanoscale level.

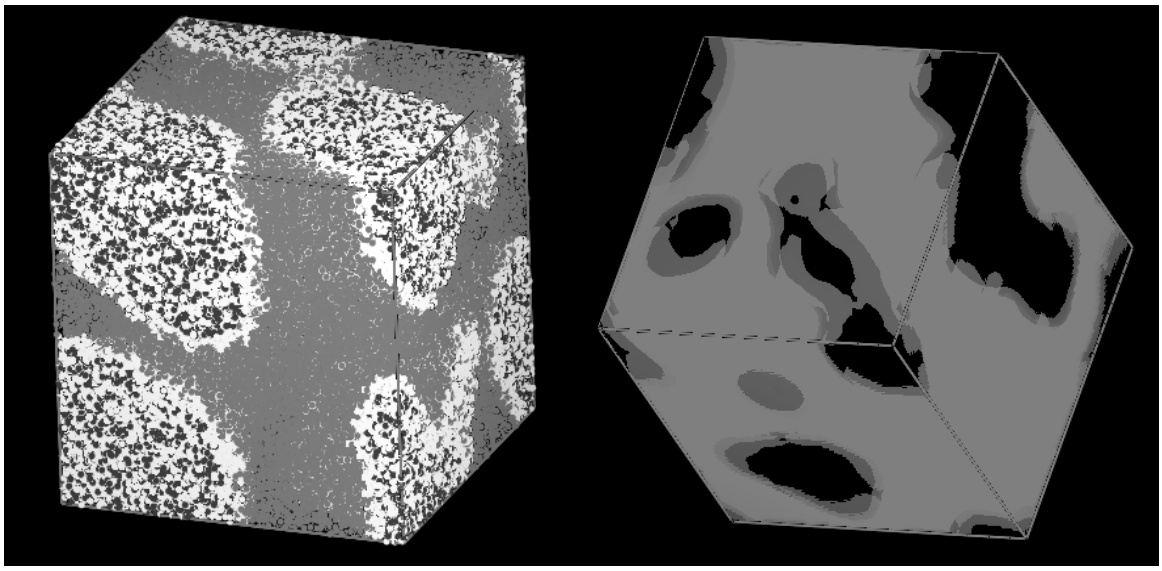

Figure 4.17: 3D visualization of ABS mesoscale simulations. (a, left) AN (grey matrix), B (white) and S (black); (b, right) polyB-SAN (dark) and SAN (clear).

The extent of segregation can be quantitatively estimated considering the values of the order parameter P_I (see Figure 4.18) and the relevant density distributions (see Figure 4.19).

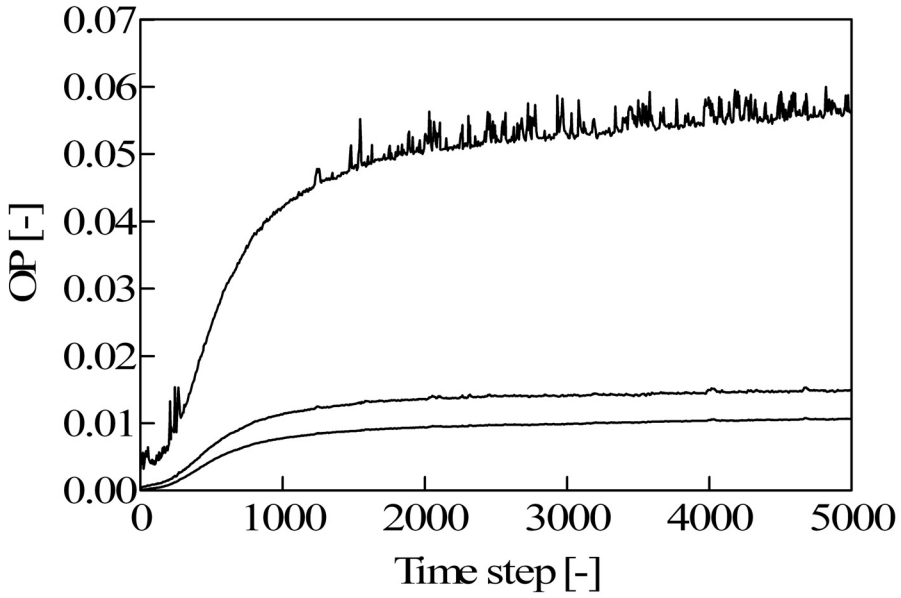

Figure 4.18: P_1 for AN (upper curve), S (middle curve) and B (lower curve) beads.

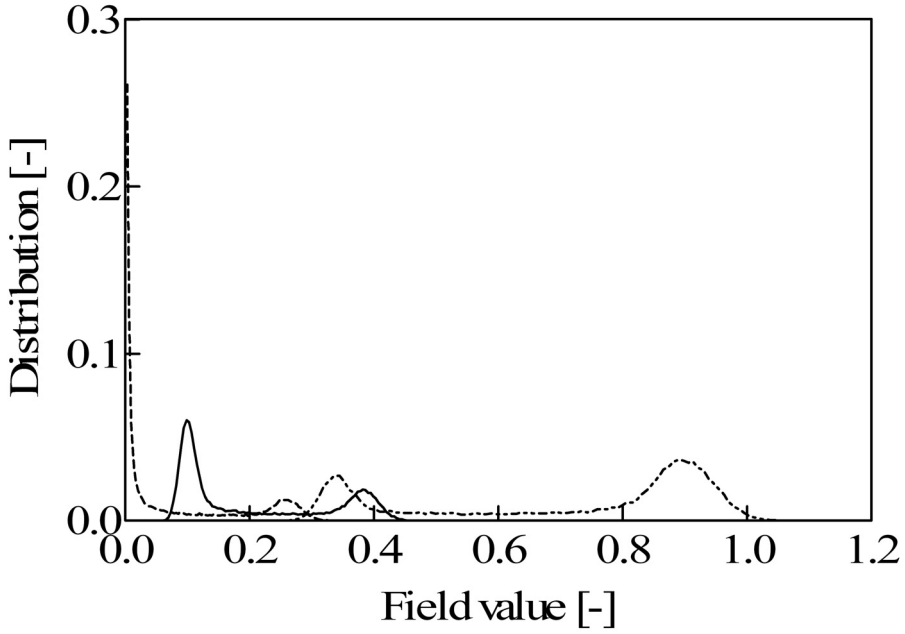

Figure 4.19: density distribution for B (- - -), S (—) and AN (·· - ·· -) beads.

Specifically, in Figure 4.19, probability densities have more than one peak at different bead densities, which are a clear indication that segregation occurs. As we can see, the polar AN beads are shifted from the S and B beads. In particular, if we look again at Figure 4.17b, where only polyB-SAN and SAN structure are visualized, we can also observe that even in

the sole ABS matrix there is a clear distinction between rigid and rubbery phases (islands).
From MesoProp simulations carried out using these morphological evidences, we obtained the mechanical properties of pure ABS in terms of the Young and Poisson moduli. The overall results are shown in Table 4.11, from which we can see that they perfectly match the range of a typical ABS (Matsim, 2003).
We also noticed that there is a distribution of Young modulus values, exemplified in Figure 4.20 (plane cut normal to the *x* axis, (a), and von Mises stress along the same axis, (b)), but, as expected, values along all three axes are very similar, as no shear conditions were applied; accordingly, the segregated phases appear as unoriented spheroids.

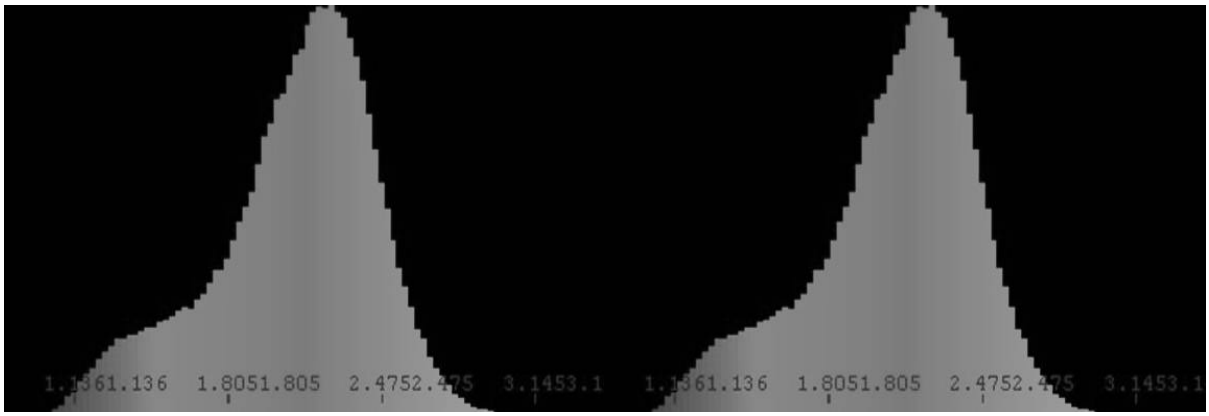

Figure 4.20: (a, left) Plane cut normal to the *x* axis (zy plane) of MesoProp simulation showing Young modulus distribution of values, and (b, right) and von Mises stress along the *x* axes for ABS.

FEM simulations with the Palmyra software, as mentioned before, have been carried out in 2 steps. To perform the calculations, we first fixed the total MMT content to 2% w/w. The results from all our other simulations, validated by comparison with the experimental of (Stretz et.al., 2005) led to the prediction of the morphology of the ABS nanocomposite, basically constituted by the presence of stacks of MMT layers (SAN intercalation) dispersed in a SAN bulk phase, in which rubbery islands (polyB-SAN) remain outside (but close to) the stacks. Then, we arranged the first set of simulations as follows: we considered a stack of 10 MMT parallel platelets (with 3nm spacing), intercalated with SAN copolymers – this, as a matter of fact, implies that the degree of exfoliation has been virtually imposed *a priori*. Mechanical properties of single phases were taken from our previous simulations or from literature (Hine et.al., 2002). Platelet aspect ratio *p*, defined as:

$$p = d/h \qquad [19.4]$$

where d is the platelet diameter and h its thickness (1 nm), has been set to 100, a value which was compatible with the calculation (mesh construction) and reliable for MMT nanocomposites (Utracki, 2004). We also verified that simulations with increasing values of p do not show appreciable differences of the Young modulus G for p values above 70 (data not shown), a value after which G reaches a plateau.

In the second simulation set, we used the mechanical property values obtained from the first simulation set for larger platelets (MMT and SAN), which have been randomly dispersed in the matrix maintaining a proportionality between phase dimensions. The bulk itself has been modelled as a SAN matrix, in which polyB-SAN rubbery phases are represented as bubbles (d = 227 nm) occupying 32% of the total ABS volume (see Table 4.9).

Figure 4.21a and 4.21b show the 3D visualization of the results obtained in the first and second simulation set, respectively, confirming the similarity of our model to the real morphology, shown in Figure 4.16.

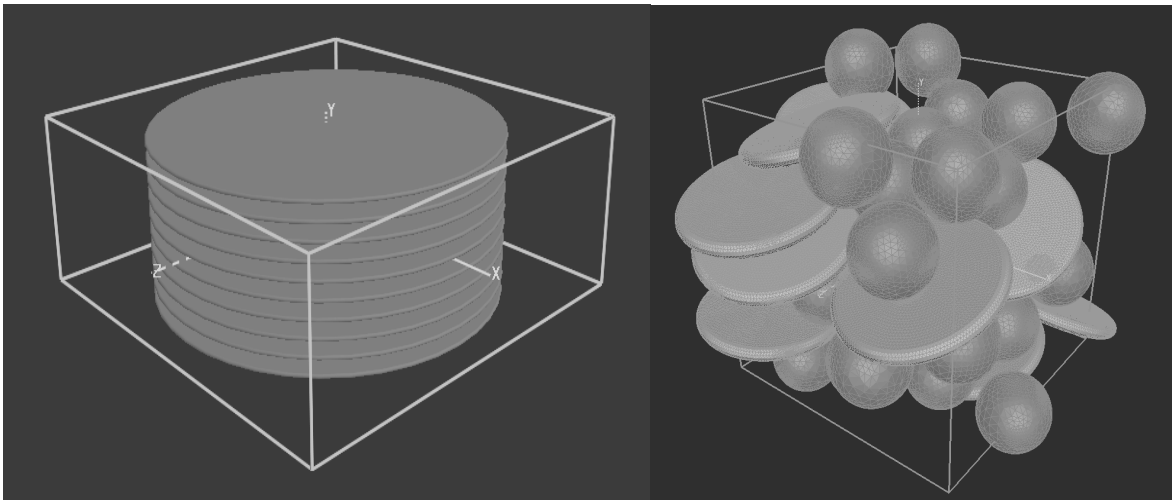

Figure 4.21: 3D visualisation of the results obtained (a, left) in the first simulation set with Palmyra (MMT stack with SAN), and (b, right) in the second simulation set with the complete system (MMT-SAN stacks, SAN matrix and rubbery phase as spheres.

Again, the numerical results obtained, as listed in Table 4.14, have been compared with literature data (Stretz et.al., 2005), finding a good agreement. As expected, effects of nanocomposite reinforcement allow a considerable improvement in Young modulus (more than 30% over mean value).

Young's moduli G	G_{xx}		G_{yy}		G_{zz}		G_{ABS} (mean)
G_{ii} [GPa]	3.108		3.188		3.155		2.416
Poisson ratio ν	ν_{yx}	ν_{zx}	ν_{xy}	ν_{zy}	ν_{xz}	ν_{yz}	ν_{ABS} (mean)
ν_{ij} [-]	0.372	0.387	0.382	0.379	0.393	0.375	0.381 (mean)

Table 4.14: Young's modulus and Poisson tensor components for ABS and ABS-MMT.

Thus, for the first time, a complete many-scale molecular simulation procedure has been developed and validated to afford polymer blend reinforcement design, from an industrial and environmental point of view. All higher-scale molecular simulations have been carried out on the basis of input data obtained from lower-scale calculations. Each step of molecular simulations procedure has been confirmed and validated by comparison with experimental data.

At a molecular level, we obtained useful indications about the most favourable MMT modifiers in the design of ABS-MMT nanocomposites, and ABS blend behaviour after polymer insertion into the MMT galleries. Mesoscale simulation confirmed morphologies and phase segregation at the nanoscale level, yielding important information about the mechanical properties and structures of the blend. Finally, with finite element simulations at the highest scale level (microns) we evaluated mechanical properties improvements for the nanocomposite.

In this way, we have developed a proof-of-concept for the possibility of (i) understanding structure, phase morphologies and mechanical properties of a rather complex polymer-clay nanocomposite system, (ii) formulating criteria leading to the correct choice of the best MMT modifier, and (iii) predict macroscopic properties improvements upon new nanocomposites.

4.4 Case study generalisation

In this chapter we examined some specific applications of multi-scale molecular simulation techniques to the study of industrial scraps recycling. Information gained by modelling are useful to predict blend or nanocomposite properties at certain conditions, to customise specific processes to optimise physical, mechanical, or, in some cases, to determine thermal and optical properties.

The use of simulation techniques to complement information obtained from experimental sessions offers new and attractive perspectives. The challenge of waste recycling has to deal with recycled products properties for analogous (or new) utilisations. In particular, it is well known how recycled polymers or polymer blends may loose part of their mechanical properties, being sometimes inappropriate for the same usage and, consequently, reducing their commercial value. Any improvement of the required properties for waste recycling is of crucial importance today. Thus, it is well evident how money savings related to molecular modelling, and the possibility to apply procedures routinely for different blends at different conditions, would give an important contribution to this cause.

In particular, the cases illustrated here are exemplificative of some of the possible applications for plastic recycling (ABS and other blends) or properties amelioration (PET/PEN) to procrastinate the end-of-life of the material. These studies offer also an example of how to develop routine procedures. In fact, all procedures can be generally applied in different contexts, as they have been previously validated against existing experimental data, which sometimes are even obtained for different structures.

Moreover, the last case study is an example of a step-by-step procedure implementation, from a simple blend to more complicated structures, up to nanocomposites studies. Due to the great interest gained by nanotechnologies potentialities, this kind of study reveals also relevant interest and potentialities, as it is relatively easy to be transferred to similar blends or fillers for different applications.

Chapter 5

Pollution removal from gaseous streams

Summary

In this chapter, adsorption techniques and applications via molecular simulation tools for the removal of different gaseous pollutants are presented. This work has ben described in the following publications:
P. Cosoli, M. Ferrone, S. Pricl, M. Fermeglia, "Grand Canonical Monte Carlo simulations for VOCs adsorption in non-polar zeolites", International Journal of Environmental Technology and management, 7, p. 228, (2007).
P. Cosoli, M. Ferrone, S. Pricl, M. Fermeglia, "Hydrogen sulphide removal from biogas by zeolite adsorption-part I: GCMC simulations", The Chemical Engineering Journal, 145, p.86, (2008). P. Cosoli, M. Ferrone, S. Pricl, M. Fermeglia, "Hydrogen sulphide removal from biogas by zeolite adsorption-part II: MD simulations", The Chemical Engineering Journal, 145, p. 93, (2008).
P. Cosoli P., M. Fermeglia, M. Ferrone, "GCMC Simulations in Zeolite MFI and Activated Carbon for Benzene Removal from Exhaust Gaseous Streams", Molecular Simulation, 34, p. 1231, (2008).
M. Lisal, P. Cosoli, W. R. Smith, S. K. Jain, and K. E. Gubbins, Molecular-level simulations of chemical reaction equilibrium for nitric oxide dimerization reaction in disordered nanoporous carbons, Fluid Phase Equilibria, 235, p. 18, 2008.

5.1 Adsorption: techniques and materials

Adsorption phenomena at various interfaces have been studies since many decades, as innumerable physical, chemical and biological processes take place at the boundary between two phases, while others are initiated at that interface. Many of these processes are, directly or not, related with environmental processes. In particular, adsorption techniques for pollutant separation and removal are extremely important processes: the technological and environmental importance of adsorption, for instance, implies its utilization for practical applications in industry and environmental protection (Dabrowski, 2001).

Generally speaking, the phenomenon in which the change in concentration of a given substance at the interface as compared with the neighbouring phases is referred to as adsorption. The resulting separation process is thus generally referred to the involvement of two different, non-homogeneous phases (adsorbent and adsorbate, or sorbate) at the equilibrium, while in absorption processes a substance diffuses into a liquid or solid creating a solution. It should also be noticed that –even in this thesis– the term 'sorption' together with the terms 'sorbent' and 'sorbate' can also be used to denote both adsorption and absorption, when both occur simultaneously, or cannot be distinguished (Dabrowski, 2001). In this Chapter, due to the relevant industrial phenomena of gas mixture separation, mainly carried on with solid, disordered or crystalline adsorbents, we will deal with solid-gas adsorption.

Adsorption of gases into solid adsorbents is a superficial phenomenon; molecules accumulate onto interfacial layers of the two phases. The fundamental concept in adsorption science is that named as the adsorption isotherm. It is the equilibrium relation between the quantity of the adsorbed material and the pressure or concentration in the bulk fluid phase at constant temperature. Due to complex phenomena, such as multilayer adsorption and capillary condensation, adsorption isotherms can take different forms; the most common are those indicated in Figure 5.1.

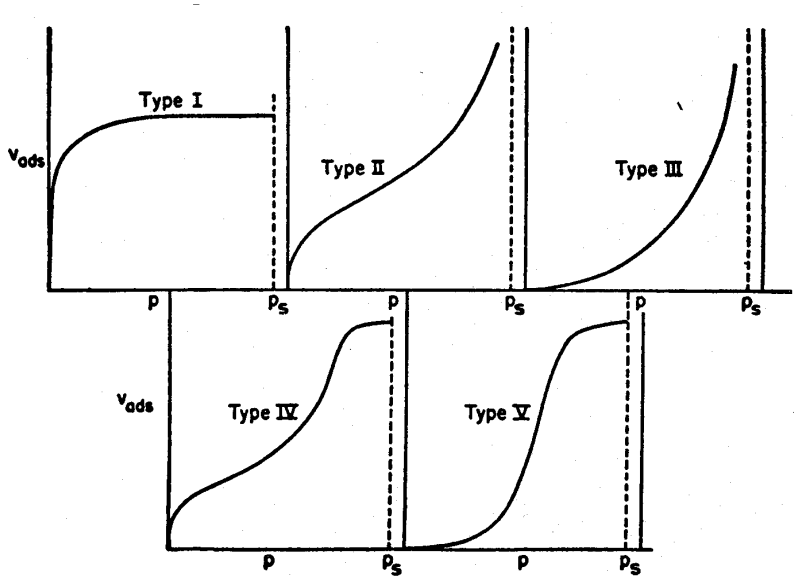

Figure 5.1: main types of adsorption isotherms.

Adsorption can result either from the universal van der Waals interactions (physical adsorption, physisorption) or it can have the character of a chemical process (chemical adsorption or chemisorption). Contrary to physisorption, chemisorption occurs only as a monolayer (Adamson, 1990).

Most of the solid adsorbents of great industrial applications possess a complex porous structure that consists of pores of different sizes and shapes. In terms of the experience of adsorption science, total porosity is usually classified into three groups. According to the IUPAC recommendation (Everett, 1976), the micropores are defined as pores of a width not exceeding 2 nm, mesopores are pores of a width between 2 and 50 nm, but macropores represent pores of a width greater than 50 nm.

Many authors, in the last century, tried to macroscopically explain, and thus model, adsorption processes with a thermodynamic treatment, which could be able to fit experimental results obtained for adsorption isotherms, and predict behaviours over a wider range of pressure or concentration. In what follows we will briefly list some of the most important and used theories about adsorption of single gases and mixtures over solid matrices, together with their hypothesis. As the purpose of this part of the work is not a comprehensive analysis, testing and screening of thermodynamic models, the list is not exhaustive.

One of the most used models for single gas mixtures, and the first to be developed, was studied by (Langmuir, 1916). The first hypothesis of the model is a continuous interchange of adsorbed and desorbed particles at the equilibrium, thus adsorption and desorption velocities are constant; a certain number of particles approaching the adsorbent surface is attracted for a

certain time, and then released. Only monolayer adsorption occurs, as adsorbate molecules can be attracted by free adsorbent surfaces, which have a limited radius of influence; the others bounce elastically when encountering already adsorbed particles. Interaction forces between adsorbed molecules are negligible, and the surface of adsorption is considered as homogeneous.

Applying the gas kinetic theory, considering adsorption and desorption velocities as equal, we obtain Langmuir's equation:

$$\frac{q}{q_m} = \frac{bp}{1+bp} \qquad [1.5]$$

where q is the adsorbed quantity at a given pressure, q_m the maximum loading (corresponding to a given pressure p_m), p is the gas pressure, and b is a constant; b is defined as:

$$b = \frac{\alpha_0 e^{q/kT}}{k_0 (2\pi mkT)^{1/2}} = \frac{\alpha_0 e^{q/kT}}{k_0 (2\pi MRT)^{1/2}} \qquad [2.5]$$

where α_0 is the ratio between adsorbed molecules number and the total number of collisions; q is the heat involved in the adsorption process, k_0 a pre-exponential factor, m the mass of the adsorbed molecules, M the moles, R the gas constant. Thus, as b is considered as a constant, this also means that $k_0 e^{-q/kT}$ is constant. Despite these restrictive hypotheses, Eq. 1.5 is widely used, as in many cases Langmuir's model is valid.

A more general theory was developed some decades later by Brunauer, Emmett e Teller, who developed the so-called BET theory (Brunauer et.al., 1938), which is able to describe more complex phenomena, such Isotherms I and III. This represents an extension of the Langmuir model to a multi-layer adsorption; kinetic hypothesis of Langmuir are maintained and applied separately to each layer of adsorbed molecules. There are two main cases of BET equation; in the first one, adsorption occurs over a free surface of a solid, and the related two-parameter equation is:

$$\frac{q}{q_m} = \frac{cx}{(1-x)(1-x+cx)} \qquad [3.5]$$

where $x = p/p_0$ being p_0 the saturation pressure, and c a constant parameter.

The second BET equation was developed for adsorption in confined pores or layers, where the space, thus the number of layers of adsorbed molecules is limited. In this case the adsorption into the pores takes place with a maximum number of layers, n, and the three-parameter BET equation is:

$$\frac{q}{q_m} = \frac{Kx\left[1-(n+1)x^n + nx^{n+1}\right]}{(1-x)\left[1+(K-1)x - Kx^{n-1}\right]} \qquad [4.5]$$

where K is a fitting parameter; if $n = 0$, Eq. 4.5 becomes the Langmuir equation; if $n = \infty$, 4.5 becomes the two-parameter BET equation.

Many other different empirical, semi-empirical or thermodynamically consistent models are commonly used, such as Freundlich, or Langmuir-Freundlich models; these models have also an extension for gaseous mixtures.

Theories for gaseous mixture adsorption modelling started to be elaborated in recent decades. One way to predict adsorption isotherms for multi-component systems is the extension of some of the previous models, although in this case they do not have a strong theoretical background, being thermodynamically inconsistent. Among the most used ones, we can mention the Extended Langmuir model (Young and Crowell, 1962) for n components; the adsorbed quantity for a generic i component of the mixture is:

$$\frac{q_i}{q_{m,i}} = \frac{b_i p_i}{1+\sum_{i=1}^{n} b_i p_i} \qquad [5.5]$$

Another commonly used equation for mixtures is the extension of the Langmuir-Freundlich model to mixtures, proposed by (Sips, 1948):

$$\frac{q_i}{q_{m,i}} = \frac{b_i p_i^{\alpha_i}}{1+\sum_{i=1}^{n} b_i p_i^{\alpha_i}} \qquad [6.5]$$

A different, thermodynamically consistent (Rao and Sircar, 1999) modification of the Langmuir equation is the Multisite Langmuir model for mixtures (Nitta et.al., 1984), takes into consideration the possibility of different adsorption sites, for different components:

$$p_i = \frac{\theta_i}{b_i\left(1-\sum_{i=1}^{n}\theta_i\right)^{a_i}} \qquad [7.5]$$

where a_i and b_i are the coefficients for species i and $\theta_i = q_i / q_{m,i}$. The model requires that $a_i q_{m,i} = const$ for all components, to satisfy the space balance within the adsorbent.

Ideal Adsorption Solution (IAS) Model and Vacancy Solution Theory (VST) are considered as the most rigorous adsorption models for multi-component systems.

IAS model (Myers and Prausnitz, 1965) is based on solution thermodynamics and the basic thermodynamic equations for the IAS model are the same as those for vapour–liquid

equilibria. The equilibrium between the ideal vapour phase and the ideal adsorbed phase can be expressed for each species *i* as:

$$P_i = x_i P_i^*(\pi) \qquad [8.5]$$

where $P_i^*(\pi)$ is the vapour pressure corresponding to the solution temperature and the solution spreading pressure π. Spreading pressure is not a measurable quantity, but at low pressures it can be derived from the isothermal Gibbs adsorption isotherm for a pure adsorbate *i* as:

$$\frac{\pi_i A}{RT} = \int_0^{P_i^0} \frac{n_i^0(P_i)}{P} dP \qquad [9.5]$$

where $n_i^0(P_i)$ is the pure fluid adsorption isotherm, *A* is the surface area of adsorbent and *R* is the universal gas constant. Therefore, calculation of π requires the knowledge of the pure fluid adsorption isotherms. Prediction of mixture adsorption is then obtained by carrying out the mixing process at constant spreading pressure ($\pi_1 = \pi_2 = ... = \pi_s$), with *n* and n_i obtained from:

$$\frac{1}{n} = \sum_{i=1}^{s} \frac{x_i}{n_i^0\left[P_i^*(\pi)\right]} \qquad [10.5]$$

with $n_i = x_i n$.

VST (Suwanayuen and Danner, 1980a and b) treats the adsorption equilibrium of a gas (or a mixture) as a system where both gases and adsorbed phase were solutions of adsorbates in an ideal, hypothetical solvent called "vacancy"; the vacancy is a vacuum occupying available adsorption sites which can be occupied by adsorbate molecules. The whole system is in thermal equilibrium, and the gases and the adsorbed solutions are in osmotic equilibrium each other: the equilibrium is maintained by a spreading (or osmotic) pressure. The properties of the adsorbed phase are defined as excess properties in relation to a dividing surface. This is located such that the partial molar areas of both adsorbates and vacancies are equal to a constant, which is the reciprocal of the limiting excess adsorption concentration.

The non-ideality of the system is taken into account by considering activity coefficient. As for single-gas adsorption isotherms, they can be evaluated using different models.

The final equation depends on the choice of adsorption isotherms models for pure gases, and takes the general form of:

$$p = \left[\frac{n_1^{s,\infty}}{b_i}\frac{\theta}{1-\theta}\right] \cdot \exp\left(-\int \frac{d\ln\gamma_V^S}{\theta}\right) \cdot \left[\lim_{\theta\to 0} \exp\left(\int \frac{d\ln\gamma_V^S}{\theta}\right)\right] \qquad [11.5]$$

where the first part is actually the Langmuir isotherm; $n_1^{s,\infty}$ is the maximum number of moles of mixture in the surface phase, b_i the Henry's constant for *i*, γ_V^s the activity coefficient of the "vacancy" in the adsorbed phase Taking into account the vacancy, the model assumes a "new" component as it behaves like any other real mixture components, with its own activity coefficient. Thus, for a 2–component mixture, for instance, where x_i^S is a molar fraction in the bulk, we have:

$$x_1^s + x_2^S + x_v^S = 1 \qquad [12.5]$$

And in the mixture, where v represents the vacancy:

$$x_v^S = 1 - \frac{n_m}{n_m^\infty} = 1 - \theta \qquad [13.5]$$

where n_m and n_m^∞ are the total amount adsorbed and its saturation value, respectively.

Thus, the model originated from VST requires the use of activity coefficients, which can be obtained in different ways. Two of the most common methods, for instance, are the use of the Wilson equation (Suwanayuen and Danner, 1980), or the Flory-Huggins form (Cochran et.al., 1985). We used the last form in one of our case study, so we briefly describe the equations.

The Flory-Huggins Vacancy Solution Model (F-H VSM) for a pure adsorbate can be written as:

$$P = \frac{n^{0,\infty}}{b} \cdot \frac{\theta}{1-\theta} \exp\left(\frac{\alpha_V^2 \theta}{1+\alpha_V \theta}\right) \qquad [14.5]$$

where α_V and b are the FH-VSM coefficients. The parameter α_V accounts for the adsorbate-vacancy interactions caused by non-ideality in the adsorbed phase. Similarly as in the previous cases, values of $n^{0,\infty}$, b and α_V were obtained by fitting the pure adsorption isotherms and for $\alpha_V = 0$, the FH-VSM reduces to the Langmuir model. In the case of mixture adsorption, the equation for the distribution of adsorbate i between the ideal vapour reservoir and adsorbent according to the FH-VSM model is given, for $i = 1, \ldots s$, by:

$$P_i = x_i \gamma_i \frac{n}{n^\infty} \cdot \frac{n_i^{0,\infty}}{b_i} \cdot \frac{\exp(\alpha_{Vi})}{1+\alpha_{Vi}} \exp\left\{\left(\frac{n_i^{0,\infty} - n^\infty}{n} - 1\right) \cdot \ln\left[\left(1 - \frac{n}{n^\infty}\right)\gamma_V\right]\right\} \qquad [15.5]$$

where x_i is the mole fraction of species *i* in the adsorbent, γ_i and γ_v are the Flory–Huggins activity coefficients of species i and vacancy, respectively, n is the loading of the mixture, n^∞ is its maximum loading, and α_{Vi} and b_i are FH-VSM coefficients for pure species *i*. Expressions for activity coefficients and other details regarding the FH-VSM can be found elsewhere(Cochran et.al., 1985; Nieszporek, 2006).

Analogously to macroscopic thermodynamic models, many studies involving molecular simulation techniques have been carried on about adsorption over solid adsorbents in the last two decades, as mentioned in Chapter 2. These mainly include QM, molecular dynamics and Monte Carlo techniques, which have been described in Chapter 3, and found considerable interest for practical applications. The main use of these techniques deals with gas separation for industrial applications (e.g., for hydrocarbons storage, or methane/carbon dioxide separation); in this part of the work the coupling of some of these techniques will be used for the removal of harmful components, which are generally present as mixtures and as a small fraction of the total mixture. Adsorbents materials used for these studies were:

- crystalline zeolites (polar and non-polar), known as "molecular sieves" thanks to their selectivity, due to their exact pore spacing and configuration;
- disordered structures which mimic activated carbon adsorbents.

Examining different case studies, with different gaseous streams and different adsorbents, we will also show how, starting from simpler, single-gas models, to more complex mixtures, even to simultaneous reaction and adsorption phenomena, it is possible to implement and refine procedures which are able to reproduce real processes at atomistic level with more accuracy.

5.2 VOCs removal with zeolites

In this case study we aimed at testing some zeolite structure for various volatile organic compounds (VOCs) by adsorption, with Grand-Canonical Monte Carlo (GCMC) techniques. VOCs are among the most common and harmful pollutants emitted by chemical industries dealing with manufacture and processing of a variety of chemicals (e.g., solvents, thinners, degreasers, cleaners, lubricants and liquid fuels), or originated by different sources such as combustion in thermal treatment of municipal solid waste (MSW), or traffic emissions.

Many VOCs have been identified as toxic, carcinogenic or mutagenic at concentrations levels found in urban environment (Edgerton et al., 1989); further, some VOCs participate in atmospheric photochemical reactions, and are also precursor to the formation of ozone, an irritant gas at low concentration levels, and a primary component of smog. The formation of ozone in the troposphere as a consequence of the photochemical reactions of VOCs with atmospheric nitrogen oxides (NOx) is nowadays also well understood (Gupta and Verma, 2002).

Development of efficient and economically feasible technologies for VOCs removal is thus needed. Volatile organic compounds (VOC) removal is a necessary operation to respect imposed standard limits in exhaust gaseous streams; VOC can originate from different sources, such as petrochemical processes, vehicle emissions, combustions and, in general, from all kinds of industrial processes.

Zeolites are arising as a possible relatively new technology to treat air contaminated with these products. Zeolites, or molecular sieves, are a group of microporous, crystalline aluminosilicate minerals, containing cavities and channels of molecular dimensions (Bohn et al., 1985). Molecules that are small enough can pass through the zeolite channel systems, whilst those whose size and shape are not compatible with the apertures of the zeolite remain trapped. As a result of such an unusual crystal structure, zeolites are widely employed in the chemical, biochemical, and petroleum industries for adsorptive separation processes and for heterogeneous catalysis. Accordingly, more than 300 types of zeolites with specific structures, names and properties are known to date (IZA, 2005). As mentioned above, zeolites can be good candidates to replace activated carbon in VOCs adsorption, as the heterogeneously porous structure of activated carbon may lead to competitive adsorption between water vapour and organic compounds, which would eventually reduce its removal effectiveness. Moreover, heat generated from the adsorption process would cause further polymerization of the carbon structure, ultimately leading to a degradation of the activated carbon and, hence, in a decrease of the VOCs adsorption performance (Lawb et al., 2003).

The main characteristics of zeolites for adsorption applications are undoubtedly their pore dimensions and aluminium content. Al atoms can substitute Si in some position in the structure tetrahedrons, and different oxidation states (+3 for Al, +4 for Si) create a neat difference charge, which is neutralized by the presence of “nonframework” ions (e.g. Na+) over zeolite surface (EPA, 1998). The kind of cations used to balance negative charges in the framework may also be essential for the removal efficiency towards specific, strongly polar pollutants.

Most of the zeolites are quite hydrophilic, as the highly polar water molecules interacts with cations; this will prevent VOC adsorption in most of the zeolites; otherwise, zeolites with high silica content are actually hydrophobic, because water is adsorbed less strongly than most organics. Accordingly, hydrophilic zeolites may not separate VOCs well in humid atmospheres, where complete drying may not occur between adsorption events, while hydrophobic zeolites actually can perform better (Blocki, 1999).

As already mentioned in Chapter 2, different studies about adsorption properties of zeolite materials have already been performed by means of molecular simulation. However, to our knowledge, specific molecular simulation studies of VOCs adsorption on zeolites are scarce (Hansenne et al. 2001; Pires et al., 2001; Zhao et al., 1998; Chandak et al., 1997; George et al., 1996). Accordingly, in this work we aimed at evaluating the adsorption properties of several VOC pollutants in zeolite structures with molecular modelling methods such as the Monte Carlo simulations in the Grand Canonical ensemble. We considered the following zeolites: AFR, BOG, and LTL (IZA, 2005), which are constituted only of Si and O and, thus, are hydrophobic. The VOCs considered in this study are 1,1,1 trichloroethane, chlorobenzene, trans-dichloroethylene, and trichloroethylene.

As pointed out in Chapter3, the GCMC ensemble creates, destroys, translates, and rotates molecules in order to obtain thermodynamic equilibrium in an open system. Accordingly, in a GCMC calculation the system chemical potential μ, volume V, and temperature T are kept constant. Chemical potential μ is transformed into the partial pressure (or fugacity) of each component.

The pressure (or the fugacity) of all components and the temperature are fixed as if the framework is in open contact with an infinite sorbate reservoir at a given temperature. The reservoir is completely described by temperature and fugacity of all components, and does not have to be simulated explicitly. Equilibrium is reached when temperature and chemical potential of the external reservoir (i.e., free gas outside the framework) and the framework are equal. The Metropolis sampling method generates chain of configurations with the ensemble probability. Transforming a configuration involves a random displacement of each atom in the system from its actual position. A trial move is accepted if it lowers the configuration energy of the system. If the configuration energy is increased, trials are accepted with a probability proportional to a Boltzmann factor: $P = e^{-\Delta U/kT}$, where ΔU is the configuration energy difference. Equilibrium is achieved when the temperature and the chemical potential of the gas inside the framework are equal to the temperature and chemical potential of the free gas outside the framework. The adsorption isotherms were computed by calculating the mean loading of the sorbate in the zeolite at a specific vapour pressure.

The structural characteristics of the three zeolite crystals studied in this work, AFR, BOG, LTL) are reported in Table 5.1. The corresponding unit cells were taken from the *Cerius*^{2} model structures database, are illustrated in Figure 5.1; for this work, all molecular simulations were computed with the *Sorption* modulus of *Cerius*^{2} (v. 4.2, Accelrys, San Diego, CA, USA). The VOC molecular models were constructed using the *3D Sketcher*

module of *Materials Studio* (v. 3.1, Accelrys, San Diego, CA, USA).

Zeolite	Cell parameters *a*, *b*, *c* [Å]	Cell parameters α, β, γ [°]	Lattice type and centring	Framework density	Channel system
AFR	22.305; 13.567; 6.972	90; 90; 90	Orthorhombic; primitive	15.2 T/1000Å^3	2D
BOG	20.014; 23.580; 12.669	90; 90; 90	Orthorhombic; body centred	16.1 T/1000Å^3	2D
LTL	18.126; 18.126; 7.567	90; 90; 120	Hexagonal; primitive	16.7 T/1000Å^3	1D

Table 5.1: Structural characteristic of zeolites AFR, BOG, LTL (IZA, 2005).

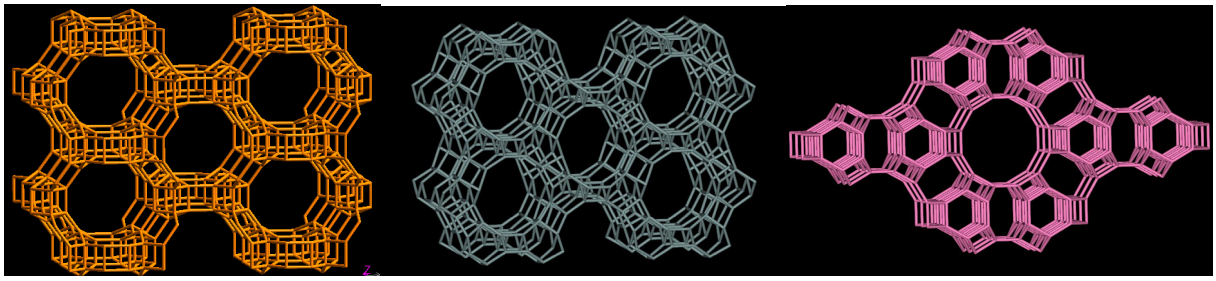

Figure 5.1: From left to right, 3D model representation of AFR, BOG and LTL zeolites.

In this study, we used the Compass force-field (FF), (Sun, 1998). The Compass FF is the first *ab initio* FF that has been parameterised and validated using condensed-phase properties in addition to various *ab initio* and empirical data for molecules in isolation. The bond terms of the Compass FF potential energy function include a quartic polynomial both for bond stretching and bending, a three-term Fourier expansion for torsion, and a Wilson out-of-plane coordinate term. Six cross-terms up through 3rd order are present to account for coupling between the intramolecular coordinates. The final two non-bonded terms represent the intermolecular electrostatic energy and the van der Waals interactions, respectively; the latter employs an inverse 9th power term for the repulsive part rather than a customary 12th power term.

To place each sorbate species into each zeolite structure, we used an approach based on a combination of MC and molecular dynamics (MD) (Haile, 1992) techniques. In the first stage, an MD simulation is performed at a high temperature, in this case 1500 K, generating a library of possible conformations accessible to the adsorbing molecules. In the next stage, an MC algorithm is used to insert a randomly chosen conformation into a random position within the zeolite framework. Initially, high-energy configurations were rejected to save

computational time during the GCMC simulations. These configurations are those in which the sorbate molecules and the framework are too close, i.e., the distance between the atoms of the sorbate and the zeolite atoms is less than their van der Waals radii. Van der Waals energies between the VOC and the zeolite were calculated by summing all pair interactions within a specific volume, in which the radius is determined by a cutoff distance. The van der Waals energy term within the zeolite framework is restricted to the minimum image convention, in which an atom is considered to interact with its closest neighbour atoms in a periodic box around it. In the case of VOC-VOC energy, the interactions are not limited to the atoms within the minimum image border, but to the molecules whose centres of mass are within it. The Coulomb and electrostatic energies between the sorbate and the framework were evaluated using the Ewald summation (Frenkel and Smith, 1996). All aromatic rings and the entire zeolite framework were treated as rigid units during all GCMC calculations.

The various Monte Carlo step sizes for the simulations were adjusted to obtain a 50% acceptance probability. The interaction cutoff was fixed at 8 Å, which is larger than the cavities in the zeolites, so it accounts for all of the necessary interactions. The length of the simulation depends on the sorbate. Initially, we performed several test runs at different length for each VOC until the loading and energy values converged (data not shown). We found out that, for all VOC considered, 10 million steps ensured equilibrium conditions (i.e., small fluctuations of the configuration energy and the number of VOC molecule as a function of MC steps around average values) for all organics. Finally, snapshots of the VOC inside each zeolite framework were analyzed, and the amount of sorbate in the different adsorption channels was monitored.

The thermodynamic of adsorption can also be investigated analyzing the values of the isosteric heat of adsorption, Q_{RF}, which is a measure of adsorption capabilities of a sorbate in an adsorbent framework. Q_{RF} is defined as the difference between the partial molar enthalpy of the sorbate component in the external reservoir (i.e., free gas) and in the framework; accordingly, it is a measure of the enthalpy change involved in the transfer of a solute from the reference state to the adsorbed state at a constant solid phase concentration (Huang and Weber, 1997):

$$Q_{RF} = h_R - h_F \qquad [16.5]$$

Evaluation of Q_{RF} requires the application of Clausius-Clapeyron equation (Huang and Weber, 1997):

$$Q_{RF} = \left(v_S - v_F\right)\left[\frac{dp}{d\left(\ln T\right)}\right] \cong RT\left[\frac{d\left(\ln p\right)}{d\left(\ln T\right)}\right] \quad [17.5]$$

where v_R and v_F are the sorbate partial molar volumes in the reservoir and in the framework, respectively, p the partial pressure, and T the temperature. In the right-hand side term of equation (2), the partial molar volume of the gas molecules in the framework is neglected with respect to that in the reservoir, and the gas behaviour in the reservoir is assumed to be ideal. This leads to the expression of Q_{RF} in the Grand Canonical ensemble, where the free energy G can be calculated:

$$Q_{RF} = RT - G \quad [18.5]$$

A further criterion for investigating adsorption is given by the analysis of the total energy components of the system and the energy distributions. In the first case, the total energy of a specific configuration of the simulation, M, is given by the Coulomb (i.e., electrostatic) and van der Waals (i.e., dispersion) contributions:

$$E_M = E_M^{SS} + E_M^{SF} + U_M^S \quad [19.5]$$

where E_M^{SS} is the intermolecular energy between the sorbate molecules, E_M^{SF} is the interaction energy between the sorbate molecules and the framework, and U_M^S is the total intramolecular energy of the sorbate molecules, as a sum of intramolecular energies of all sorbates. The intramolecular energy of the framework is not included as the framework is fixed throughout the simulation. The energy distribution curves for each sorbate express sorbate-framework interactions over the entire cell volume; in this case, the interaction energy expressions take the form of equation (4) with the obvious exclusion of the last term U_M^S.

Moreover, to rationalise result and to fit *in-silico* predictions with a thermodynamic model, Langmuir adsorption isotherms have been used.

Due to the limited number of literature references about the zeolite/VOC systems here examined, we proceeded to validate the proposed simulation approach by analogy with similar systems. Accordingly, GCMC simulations for sorption of light hydrocarbons (i.e., methane, ethane, propane, and butane) in MFI zeolite (IZA, 2005) at different pressures and temperatures were carried out. These results are shown in Figure 5.2. These simulations, obtained by applying the same procedure described in the previous section for VOCs, are in good agreement with the corresponding available experimental data (Habdul-Reheman et al., 1990; Zhu et al., 1998). The slightly disagreement in the case of data from Zhu et al. (1998) can be sensibly attributed to the fact that their zeolites contained small quantities of Al, while we used an ideal model of MFI zeolite with no Al.

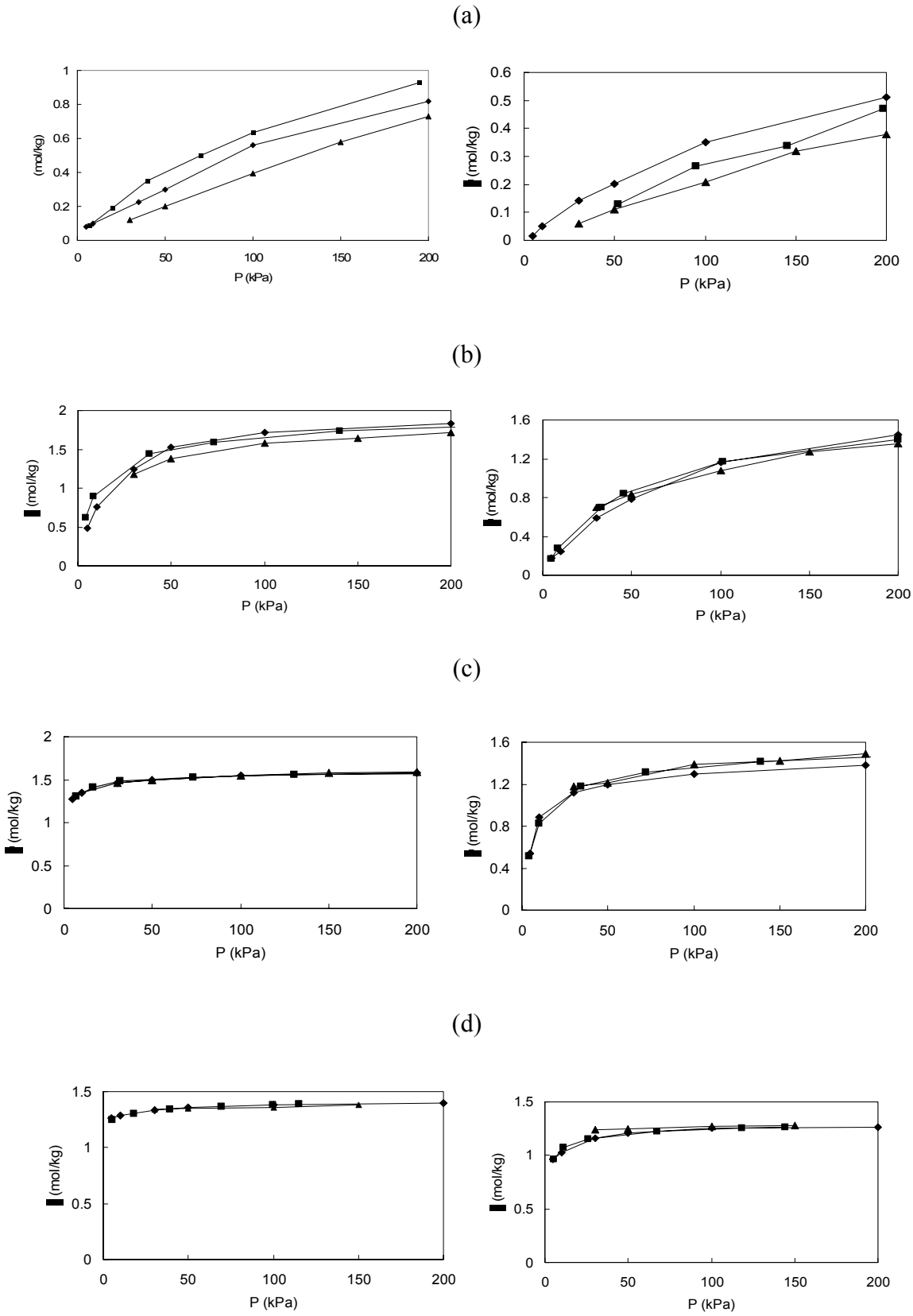

Figure 5.2: Comparison of simulated adsorption curves (◆) of methane (a), ethane (b), propane (c), and butane (d) at 300 K (left) and 350 K (right) on MFI zeolite with experimental data (Habdul-Reheman et al., 1990, ■; Zhu et al.,1998, ▲).

Admittedly, the use of non-polar molecules, such as hydrocarbons, to test the proposed computational procedure for VOCs might raise some doubts. However, VOCs are only slightly polar molecules, with dipole moments confined to small values (see below), and the zeolites considered are hydrophobic, being mainly constituted of Si and O atoms. Accordingly, in all our cases the electrostatic interactions (i.e., Coulombic forces) are expected to play only a minor role in the adsorption process, as has been aptly verified by our calculations.

A further check can be performed on the accuracy of the force field used in the MC and MD simulations, as this strongly influences the calculation results. The simplest way is to estimate the isosteric heat of adsorption ($-\Delta H_{ads}$), and compare it with experimental data. Table 5.2 shows this comparison for all hydrocarbons at 300K as an example. Once again, the agreement between simulation and experiment (Hufton and Danner, 1993; Habdul-Reheman et al., 1990; Guo et al., 1989) is excellent. Accordingly, both comparisons lead us to assume our approach as a valid and reliable procedure for VOCs adsorption simulations.

Sorbate	$-\Delta H_{ads,sim}$ [kcal/mol]	$-\Delta H^{a}_{ads,exp}$ [kcal/mol]	$-\Delta H^{b}_{ads,exp}$ [kcal/mol]	$-\Delta H^{c}_{ads,exp}$ [kcal/mol]
Methane	4.84	4.87	4.89	5.5
Ethane	7.86	7.83	7.13	-
Propane	9.51	9.52	9.69	9.0
Butane	11.56	11.53	12.0	12.0

[a]Habdul-Reheman et al. (1990). [b]Hufton and Danner (1993). [c]Guo et al. (1989).

Table 5.2: Comparison of GCMC simulated isosteric heat of adsorption of light hydrocarbons in MFI at 300K with the experimental data.

As anticipated, GCMC simulations were carried out to estimate the adsorption isotherms at 450K of 1,1,1 trichloroethane, chlorobenzene, trans-dichloroethylene and trichloroethylene on 3 types of zeolites (AFR, BOG, and LTL). The selected temperature ensured that all considered VOCs were in the gas state. Figure 5.3 presents the simulated loading curves obtained in the total pressure range 0.01 – 1 atm. As can be seen from this Figure, VOC adsorptions curves have the usual type I shape, namely an exponential increment in the adsorption as the partial pressure increases, followed by a saturated behaviour.

(a)

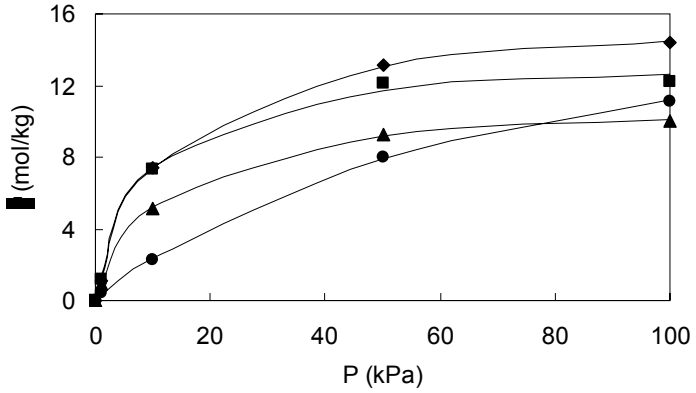

(b)

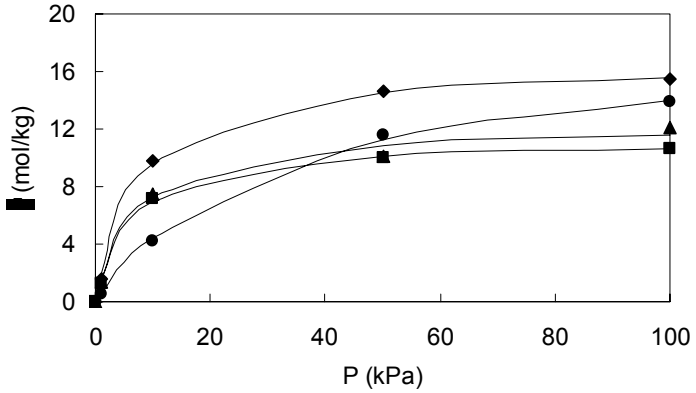

(c)

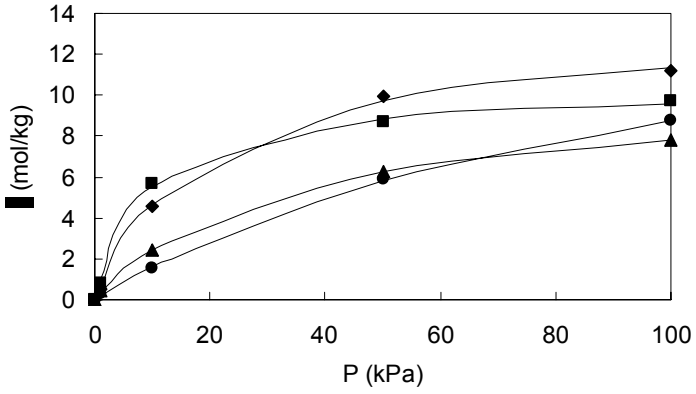

Figure 5.3: GCMC sorption isotherms (symbols) and fitting results using Langmuir model for all VOCs in AFR zeolite (a), BOG zeolite (b), and LTL zeolite (c) at 450 K. Symbols: ▲ : 1,1,1-trichloroethane; ■: chlorobenzene; ●: trans-1,2-dichloroethylene; ◆: trichloroethylene.

These results can also be analyzed by taking into consideration the different geometrical characteristics of both the zeolites and the VOC sorbates. In particular, resorting to a well-validated procedure (Fermeglia and Pricl, 1999 and 2001) we calculated the molecular volumes of the VOCs and the corresponding volume of each zeolite framework available for adsorption. Figure 5.4 illustrates these concepts for 1,1,1-trichloroethane and BOG, as an example, whilst Table 5.3 lists the calculated molecular volume of each VOC, the total volume of the zeolite crystal cells, and the total volume of the zeolite cell accessible to each VOC.

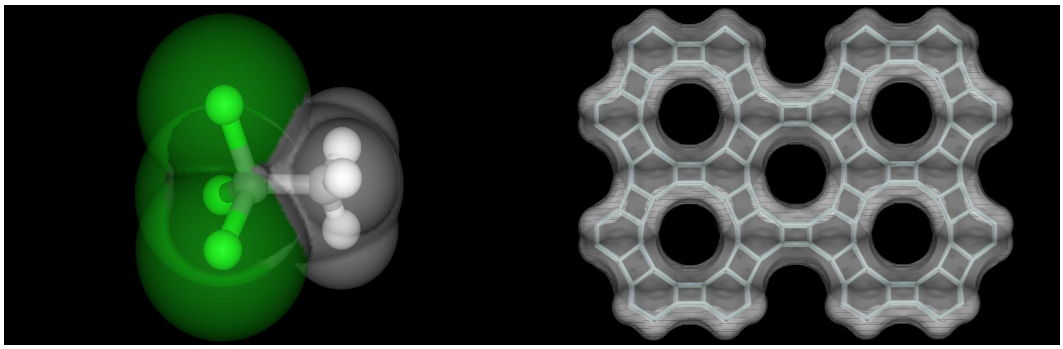

Figure 5.4: Cartoon of the molecular volume of 1,1,1-trichloroethane (left) and volume accessible to this VOC in BOG zeolite (right).

Zeolite	Sorbate	Sorbate volume [Å^3]	Total volume of the cell [Å^3/u.c.]	Total accessible volume [Å^3/u.c.]
AFR	1,1,1-Trichloroethane	87.3	2140	180
	Chlorobenzene	97.7	2140	167
	Trans-dichloroethylene	67.7	2140	215
	Trichloroethylene	81.4	2140	189
BOG	1,1,1-Trichloroethane	87.3	6163	466
	Chlorobenzene	97.7	6163	420
	Trans-dichloroethylene	67.7	6163	580
	Trichloroethylene	81.4	6163	495
LTL	1,1,1-Trichloroethane	87.3	2208	197
	Chlorobenzene	97.7	2208	183
	Trans-dichloroethylene	67.7	2208	229
	Trichloroethylene	81.4	2208	206

Table 5.3: Calculate molecular volumes of VOCs, total volumes of each zeolite cell, and total volume of each zeolite accessible to each of the VOCs.

The BOG zeolite is characterized by the largest volume accessible to all VOCs; accordingly, the VOC loadings in this zeolite are higher than for the other two porous materials. At the same time, the most adsorbed VOC is invariably trichloroethylene. It is interesting to compare this VOC with its saturated counterpart, 1,1,1-trichloroethane, which presents quite lower loading values. These two molecules possess the same amount of chlorine, and are characterized by approximately the same molecular volume (see Table 5.3), however, their dipole moment μ are quite different, as μ(1,1,1-trichloroethane) = 1.8 D and μ(trichloroethylene) = 0.8 D (CRC, 1999). Thus, in this last case the repulsive interactions between the negative partial charges on the chlorine atoms and those on the oxygen atoms of the zeolite framework are smaller than in the case of the more polar saturated compound. Although trans-dichloroethylene is the smallest of all VOCs, it is always the less adsorbed compound in all cases and in the range of pressure analyzed. This is explained by the fact that ClHC=CHCl is a totally apolar molecule (μ(trans-dichloroethylene) = 0 D); accordingly, attractive and repulsive interactions between the VOC atoms and the zeolite framework are perfectly counterbalanced, resulting is a lower adsorption strength.

For the analytical description of the pure isotherms; we used the Langmuir model (Eq. 1.5), where *b* is the Langmuir adsorption coefficient, given by:

$$b = b_0 \exp\left(-\Delta H_{ads} / RT\right) \qquad [20.5]$$

The results obtained from the GCMC data fitting with Equation 1.5 are shown as curves in Figure 5.3, while the corresponding values of the Langmuir parameters are reported in Table 5.4.

Zeolite	Sorbate	θ_m [mol/kg]	b [kPa^{-1}]
AFR	1,1,1-Trichloroethane	11.3	0.0000848
	Chlorobenzene	13.7	0.000117
	Trans-dichloroethylene	19.0	0.0000142
	Trichloroethylene	16.2	0.0000846
BOG	1,1,1-Trichloroethane	12.3	0.000143
	Chlorobenzene	11.3	0.000161
	Trans-dichloroethylene	18.4	0.0000317
	Trichloroethylene	16.7	0.000135
LTL	1,1,1-Trichloroethane	10.3	0.0000309
	Chlorobenzene	10.4	0.000113
	Trans-dichloroethylene	17.5	0.0000101
	Trichloroethylene	13.5	0.0000518

Table 5.4: Langmuir parameters estimated from the GCMC simulated VOC adsorption isotherms shown in Figure 3.

In the limit of high pressures, we can see how, as the size of the molecule increases, the saturation amount adsorbed, θ_m, decreases. This is due to two leading factors: firstly, the possibility for smaller molecules to occupy not only the zeolite main channels but also the smaller ones. In fact, in the low pressure regime, the VOC molecules are exclusively located at the channels intersections. At higher loadings, further molecules can be accommodated only by pushing the VOC into the straight and zig-zag channels. Due to the planar and smaller structure, trans-dichloroethylene can locate within the channel interiors and, hence, attain higher maximum loading values. More importantly, however, at higher pressures the sorbate-sorbate interactions start playing a significant role in the sorption process. Therefore, for molecules such as chlorobenzene, the possibility to form molecular clusters by virtue of the planar structure, and hence increase the sorbate-sorbate interactions at the expenses of the sorbate-framework interactions, becomes more pronounced.

The analysis of the energy distribution in single component systems can be useful to predict the existence of one or more molecular configurations with different energy. This would lead to preferential sites in the framework, which have higher probabilities to adsorb molecules. The energy distributions for all considered molecules, at all pressures, and for all zeolites are negative (i.e., favourable), and show unimodal behaviour. Accordingly, the adsorbed molecules distribute uniformly into the accessible volumes of each zeolite, with no preferred sites. This is also visually confirmed by the 3D inspection of the adsorbed molecules in the zeolite framework. Figure 5.5 shows the energy distribution and the corresponding 3D visualization of the adsorption of 1,1,1-trichloroethane in AFR as an example.

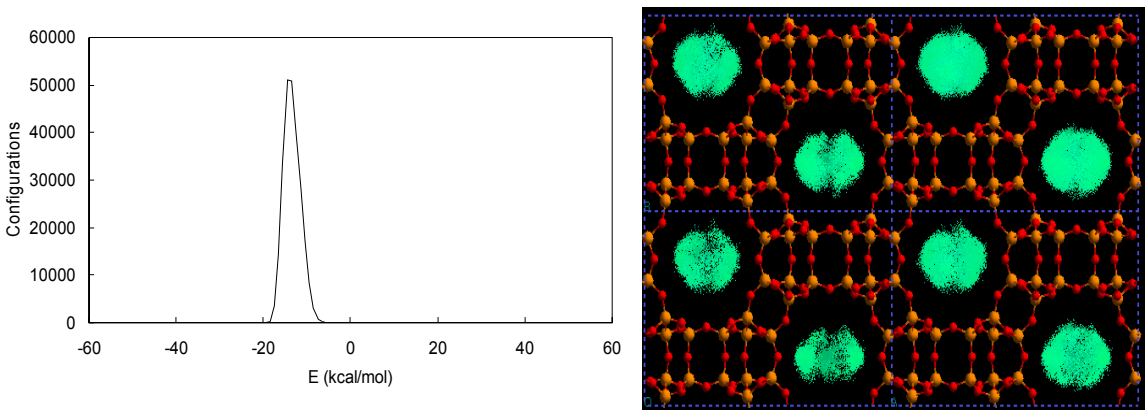

Figure 5.5: Unimodal potential energy distribution (left) and 3D visualization (right) of adsorbed molecules distribution for 1,1,1-trichloroethylene in AFR zeolite.

Different behaviours were obtained from the tests carried out when loading the three zeolites with an equimolar VOC mixture, as shown in Fugure 5.6. Ideally, we assumed that each sorbate had a partial pressure of $p/4$, meaning that each molecule had to compete with the others for the adsorbing sites of the zeolites.

(a)

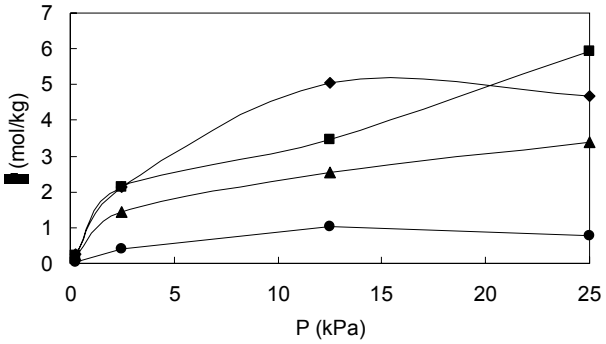

(b)

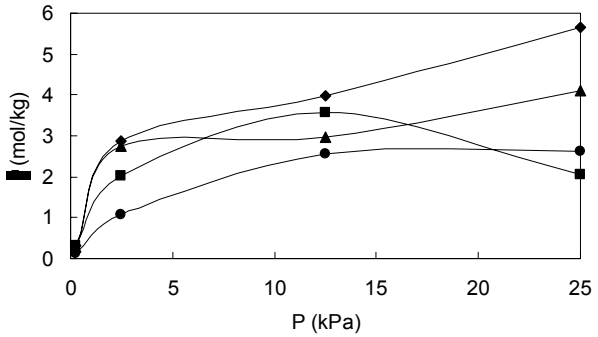

(c)

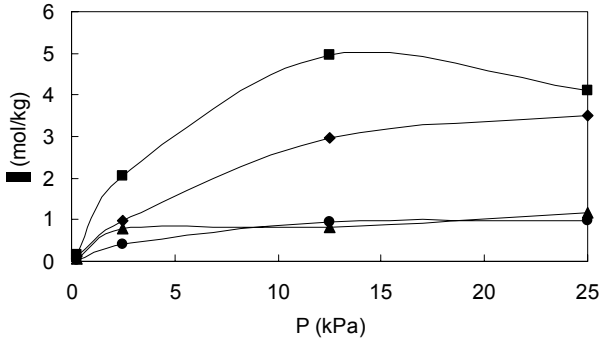

Figure 5.6: GCMC simulation sorption isotherms for all VOCs (equimolar mixtures) in AFR (a), BOG (b), and LTL (c) zeolites at 450 K. Symbols: ▲: 1,1,1-trichloroethane; ■: chlorobenzene; ●: trans-1,2-dichloroethylene; ◆: trichloroethylene. Lines used only as a guide for the eye.

It can be readily noticed that the amount of trichloroethylene and chlorobenzene adsorbed is always larger than for the other two VOCs, with the exception of few points at low pressures in figure 5.6b. Further, only a few of these curves present a final plateau, while others are characterized by the presence of a maximum or by horizontal inflection points. In this latter case, the curve shape corresponds to a type IV isotherm, for which an initial saturation value is observed, followed by another increment of the adsorbed material. This behaviour is well evidence by the sorption curve of 1,1,1-trichloroethane in BOG zeolite (see Figure 5.6(b)). This phenomenon can be expected at high temperatures, such as those considered in this study, where the zeolite has not reached saturation at low pressures. 1,1,1-trichloroethane has more conformational flexibility than all other VOCs considered; accordingly reorganization and reorientation of the molecules is more efficient, and bigger amount of material can be absorbed. Nevertheless, it can also be clearly observed from this Figure that LTL zeolite separates well chlorobenzene and trichloroethylene from 1,1,1-trichloroethane and trans-dichloroethylene. The estimation of saturation values and Langmuir constants, if applied to mixtures (Extended Langmuir equation), is rather problematic. Definitely, this complex behaviour cannot be described by Langmuir equation, but should be modelled by more complex functionalities, which are outside the scope of this first, present work.

To conclude and summarise the results of this first part of work about adsorption and pollution removal, we can notice how simulations in the low pressure regimes (up to 1 atm) showed considerable adsorption properties of VOCs by these zeolites. BOG zeolite, in particular, showed very high adsorption capacities for all the examined VOCs, generally more than AFR and LTL zeolites, by virtue of its larger channels. In all these cases, the isotherms of adsorption could be satisfactorily fitted by Langmuir equations. Energy distributions showed unimodal behaviours for all systems, suggesting that VOC molecules adsorb on zeolites with a uniform distribution in the accessible pores, avoiding preferential dispositions.

For equimolar mixtures, adsorption properties are quantitatively similar, although more complex qualitative behaviours are observed, which cannot be described in terms of simple models such as Langmuir equation. According to our findings, VOCs sorption on zeolite materials confirms to be a competitive alternative over different, although less expensive solutions such as activated carbons.

5.3 Hydrogen sulphide removal with zeolites

5.3.1 Stochastic methods for adsorption isotherms determination

In this part of the work we considered more practical applications, thus more complex systems, aiming at removing pollutant components from gaseous streams. In this case, we studied the hydrogen sulphide (H_2S) removal from biogas, a typical application where in a gaseous mixture there is the need to separate (or considerably reduce) a component, which is present in very small concentrations.

Moreover, pollutant removal from biogas is of crucial importance to guarantee better performances in biogas exploitation processes, and to reduce environmental impact of gaseous emissions. Biogas production and utilization is constantly increasing, as it represents a "green", renewable energy, obtainable in a relatively economical way from anaerobic digestion (Speece, 1996; Marchaim, 1992). Nevertheless, one of the most harmful pollutants, (H_2S), is present in a concentration range spanning from 10-30 to 1000-2000 ppm. Considering that exposure to a concentration of only 300 ppm for 30 minutes is enough to render a worker unconscious, it is clear that this fraction has to be dramatically reduced (Marchaim, 1992) to the lower toxic limit (i.e, at least 10 ppm (Milby and Baselt, 1999)). In some cases, aerobic biological processes, catalytic or oxidative processes can be used (Nishimura and Yoda, 1997; Eow, 2002); the use of adsorption processes, exploiting various types of adsorbents, is also widespread (Bagreev et. al., 2000). Zeolite materials are particularly suitable for adsorption removal processes (Garcia and Lercher, 1992; Cruz et.al., 2005), by virtue of their high selectivity and compatibility towards polar compounds, such as H_2S. Hydrophilic zeolites, with a high content of Al in their tetrahedrical framework, are generally more appropriate for polar molecules adsorption, while hydrophobic zeolites are effective in the entrapment of apolar molecules (EPA, 1999).

In the first part of this work we investigated the potentialities of a series of zeolites for H_2S removal, using molecular simulation techniques such as Grand Canonical Monte Carlo (GCMC), and *ab initio* quantum mechanics (QM).

In what follows we employed molecular simulations for ranking a list of selected zeolites in terms of selectivity and adsorption isotherms, giving also insights on adsorption mechanisms at an atomistic level from a thermodynamic point of view. As relevant experimental data are scarce, and usually given in terms of pure pollutant adsorbed quantity, in order to validate the computational procedure adopted we decided to compare our calculation with experimental adsorption isotherms of pure H_2S on zeolite NaY (Cruz et.al., 2005), and to examine the

differences encountered when adsorption in a realistic situation, a biogas mixture of CO_2, CH_4, and H_2S at low pressures, is also considered. Finally, isosteric heats of adsorption, total energy contributions and energy densities were the selected quantities to investigate adsorption competition at different pressure and zeolite selectivity (Millini, 1998).

In the second part of this work, after the choice of the most suitable zeolite, we investigated in deeper details the results stemming from the previous GCMC simulations. Our idea was to use molecular mechanics and dynamics simulations (MM/MD) to give more insights to the adsorption mechanism and to the pore competition phenomenon for different molecules with a deterministic method.

Simulations were carried out on an Intel bi-processor XEON 32bit workstation. We used *Sorption* and *DMol*^{3} software modules of *Materials Studio* (v. 4.0, Accelrys, San Diego, CA, USA).

Metropolis Monte Carlo (MMC) methods have been used in this work. We also evaluated the possibility of using Configurational Bias methods (CBMC); these methods are widely used to simulate adsorption of rather large and flexible molecules. In a CBMC sorption simulation, a bias is introduced towards high energy values, to avoid attempt of sampling configurations with low probabilities, which are likely to be rejected by the acceptance test (Siepmann and Frenkel, 1992). In this work, adsorbed molecules are rather small if compared to all zeolite pore size; nevertheless, we decided to test both methods. Since the results for biogas adsorption isotherms in zeolites obtained with MMC and CBMC revealed negligible differences, we decided to adopt the MMC technique (already described in previous parts), being computationally faster than CBMC.

Sorbate H_2S molecular models have been built and optimized at the QM density functional theory (DFT) (Levy, 1979) level with the *DMol*^{3} module, due to its flexibility and dipole moment, while the structures of the symmetrical CH_4 and symmetrical and linear CO_2 molecules have been minimized, and partial charges assigned by the selected Force Field (see below). Four zeolites were considered: LTA, FAU NaX, FAU NaY, and MFI. The first three frameworks are hydrophilic, and already employed for H_2S adsorption (Cruz et.al., 2005; Young et.al., 1996; Maugé et. Al., 1995). The last one, MFI, is hydrophobic in nature, and has been taken into account to investigate adsorption differences between these categories. 3D molecular models of LTA (Si/Al = 1), NaX (Si/Al = 1), NaY (Si/Al = 2.5) and dealuminated MFI were available in the structural database of *Materials Studio*. Aluminum substitutions have been performed by following Loewenstein's rule (Loewenstein, 1954), while Na^+ ions position has been assigned by in-house developed software for identifying potential energy

minima and, thus, most probable extra-framework cation positions. The *cvff_aug* (consistence valence augmented force-field) was the potential energy expression of choice in all calculations (Hill et. al., 2000). Electrostatic energy terms have been computed by the Ewald summation method. Van der Waals interactions have been calculated with classical Lennard-Jones function (June et. al., 1990). Cut off for Van der Waals, atom based calculations with cubic spline truncation has been set to 8.5 Å; this distance should be less than a half of the minor cell side, so when necessary (zeolite MFI) we duplicated cells. The cubic spline truncation was set to 1 Å with a buffer of 0.5 Å; in this way, the van der Waals non-bond energy term is splined from its full value to zero within a radio of 1 Å. For electrostatic contributions, the accuracy of Ewald and Group calculation was 0.001 kcal/mol with the same cut off and buffer. At least 1×10^7 productive Monte Carlo steps, preceded by 1×10^6 equilibration steps, have been performed under 3D periodic boundary conditions. Overall, we performed and compared MMC for pure H_2S adsorption (from 10 up to 1000 Pa), and competitive, simultaneous adsorption of H_2S, CH_4 and CO_2, with partial pressure in the range of a typical biogas (CO_2 and CH_4 with low concentrations of H_2S) and a total pressure P_{TOTAL}= 1 atm. The simulation temperature was fixed at 298 K, which is a realistic temperature for a biogas exiting from a mesophilic process (Speece, 1996). Isosteric heats of adsorption, energy components and distributions have been already described in Paragraph 5.2, thus, as dealing with gas mixtures, we only introduce the selectivity factor S_{ij}:

$$S_{ij} = \left(\frac{x_i}{x_j}\right)\left(\frac{y_j}{y_i}\right) \qquad [21.5]$$

where x_i, x_j are the molar fractions of species *i* and *j* in the gas phase, while y_i and y_j are the molar fraction of species *i* and *j* adsorbed in the framework.

Initially, we compared our simulated H_2S adsorption isotherms on zeolite NaY at 298 K with the corresponding, available experimental data (Cruz et. al., 2005). As shown in Figure 5.7, a good agreement is obtained. Small differences may be related, for instance, to the presence of impurities in original zeolite, and to the possibly different Si/Al ratio.

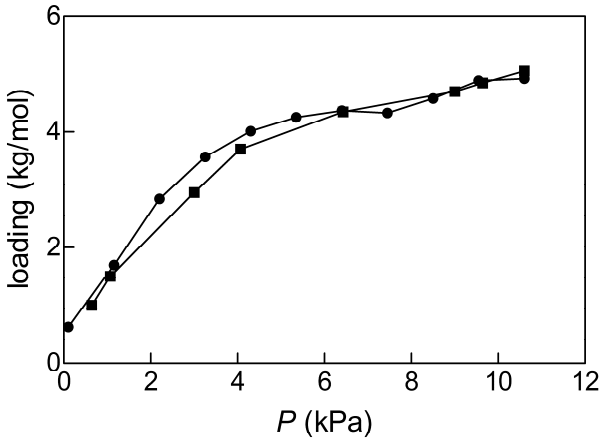

Figure 5.7: comparison between experimental adsorption isotherms (Cruz et. al., 1995) of H_2S on NaY (Si/Al = 2.5) (■), and GCMC calculated adsorption isotherms (●). Lines serve as eye guides.

Simulation results for biogas purification are shown in Figure 5.8. Considerably different behaviours for adsorption isotherms of pure H_2S and for the biogas mixture are obtained. These differences are qualitative, quantitative and suggest a possible ranking of the zeolite performances. Due to the complexity of the systems and, sometimes, to the very low number of H_2S molecules adsorbed, some difficulties in Monte Carlo samplings may arise; a consequence, isotherms are not always smooth, and the error bars for each point, resulting from running multiple simulations in the same conditions, are shown to quantify the variability of the predicted value. Nevertheless, as expected, the adsorption of H_2S on the hydrophobic MFI network is always lower than for all other zeolites; moreover, the considerable differences in loadings (1 to 4 orders of magnitude) allow a ranking among zeolites to be clearly established.

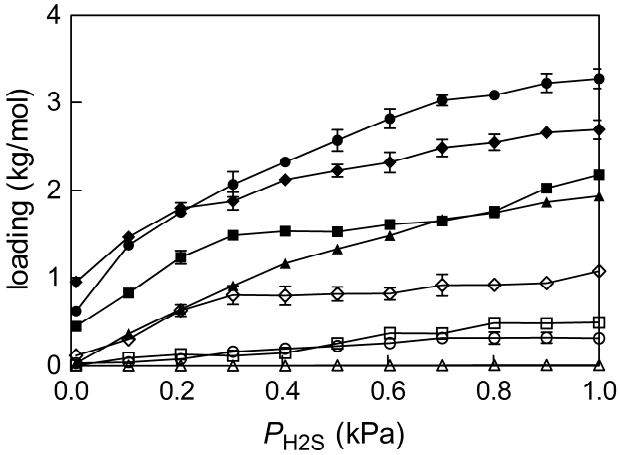

Figure 5.8: sorption isotherms for pure H_2S (a) and H_2S in a biogas mixture (b). Pure H_2S simulations: (♦), NaY; (■), NaX; (●), LTA; (▲), MFI. Biogas mixture simulations: (◊), NaY; (□), NaX; (○), LTA; (Δ), MFI. Lines serve as eye guides.

To complement the information on framework selectivity, it also instructive to examine the adsorption curves for CH_4 and CO_2 reported in Figure 5.9. The isotherms of H_2S are also shown for comparison.

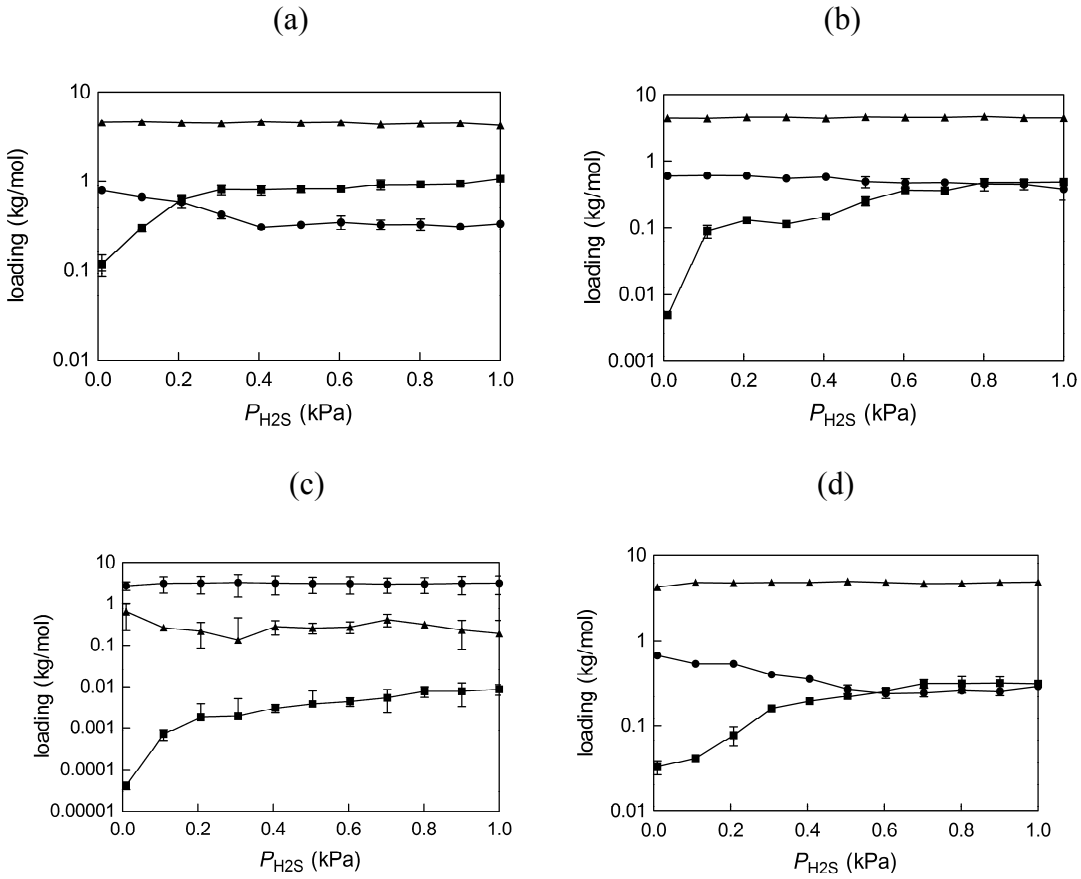

Figure 5.9: H_2S, CO_2 and CH_4 adsorption isotherms as a function of H_2S partial pressure in NaY (a), NaX (b), MFI (c), and LTA (d). Symbols legend: (■), H_2S; (▲), CO_2; (●), CH_4. Lines serve as eye guides.

As expected, in hydrophilic zeolites the amount of H_2S adsorbed increases with increasing H_2S partial pressure; the isotherms of CH_4 slightly decrease, whilst CO_2 adsorption curves remain stable. On the other hand, when considering the apolar MFI framework, the amount of adsorbed H_2S is very low, even when considering pure component adsorption isotherms. During biogas adsorption simulations, however, the CH_4 loading remains stable, while H_2S adsorption increases at the expenses of CO_2. The global results yielded by the MMC simulations are quite sensible. In fact, electrostatic interactions between the polar molecule H_2S and the framework are more favourable in hydrophilic, ion-rich zeolites; at the same time, the increase of H_2S partial pressure is detrimental to the adsorption of the less polar molecule, CH_4. The reverse is true when considering the hydrophobic MFI framework, onto which less polar compounds are more favourably attracted, as expected. Overall, the FAU NaY zeolite seems to be characterized by the highest selectivity towards H_2S, and MFI by the lowest one. The fact that NaY could be the framework of choice, and not the NaX

counterpart, in spite of the higher Si/Al ratio, could be possibly rationalized by invoking greater sterical hindrance imposed by the larger amount of sodium cations and, thus, lower pore dimensions available to H_2S binding. Examining the simulation results from a thermodynamic standpoint allowed us to confirm and further explain these tendencies.

Table 5.5 list the calculated isosteric heats Q_{RF} for each species, averaged over different H_2S input pressures. Table 5.5 also reports the mean total non-bond energy components for the MMC sorption isotherm of the biogas mixture when P_{H_2S} = 1000 Pa as an example. Utterly analogous results are obtained at different H_2S partial pressures. Interestingly, the highly favourable values of the electrostatic components reveal that the different steric hindrance characterizing the three dimensional structure of the zeolite frameworks is not the only responsible for zeolite selectivity. In fact, given that the three gases do not differ very much in their molecular volumes (V_{CO_2} = 34.0 Å³, V_{H_2S} = 30.3 Å³, and V_{CH_4} = 28.20 Å³, respectively), all zeolite pore sizes are all rather large if compared to the mean radius of these molecules. Accordingly, the considered zeolites do not seem to behave predominantly as molecular sieves, but rather their selectivity appears be driven mainly by the electrostatic interactions in terms of total energy contributions.

Zeolite	Q_{RF} [kcal/mol]			Total energy contributions (P_{H_2S} = 1000 Pa) [kcal/mol]	
	H_2S	CO_2	CH_4	van der Waals	Coulomb
FAU NaY	17.9 (0.4)	11.4 (0.1)	7.2 (0.4)	-300.3 (9.4)	-502.9 (13.0)
FAU NaX	15.6 (0.6)	12.3 (0.1)	9.7 (0.1)	-302.3 (8.6)	-541.1 (14.7)
MFI	10.2 (0.4)	9.3 (0.3)	9.1 (0.2)	-179.9 (8.2)	-0.69 (0.7)
LTA	14.5 (0.2)	14.6 (0.1)	9.3 (0.1)	-389.7 (9.5)	-613.6 (13.8)

Table 5.5: Average values of Q_{RF} for a biogas mixture adsorption process, and non-bond energy components relative to adsorption at P_{H_2S} = 1000 Pa. Standard deviations are reported in parenthesis.

As well evident from Table1, Q_{RF} for H_2S is always higher than the corresponding values for CO_2 and CH_4 when the adsorption takes place on polar frameworks; interestingly, however these differences flatten for the adsorption process onto the apolar zeolite. This can be taken as a further piece of evidence that H_2S adsorption on FAU (NaY and NaX), and LTA is favoured, and increases with increasing P_{H_2S}. The density distribution profiles for the total energy confirm the same trend, as the H_2S curves show the most mean negative values in all zeolites except MFI, where this tendency is inverted. Figure 5.10 illustrates this behaviour in the cases of NaY and MFI at P_{H_2S}= 10 and 1000 Pa, respectively, as selected examples.

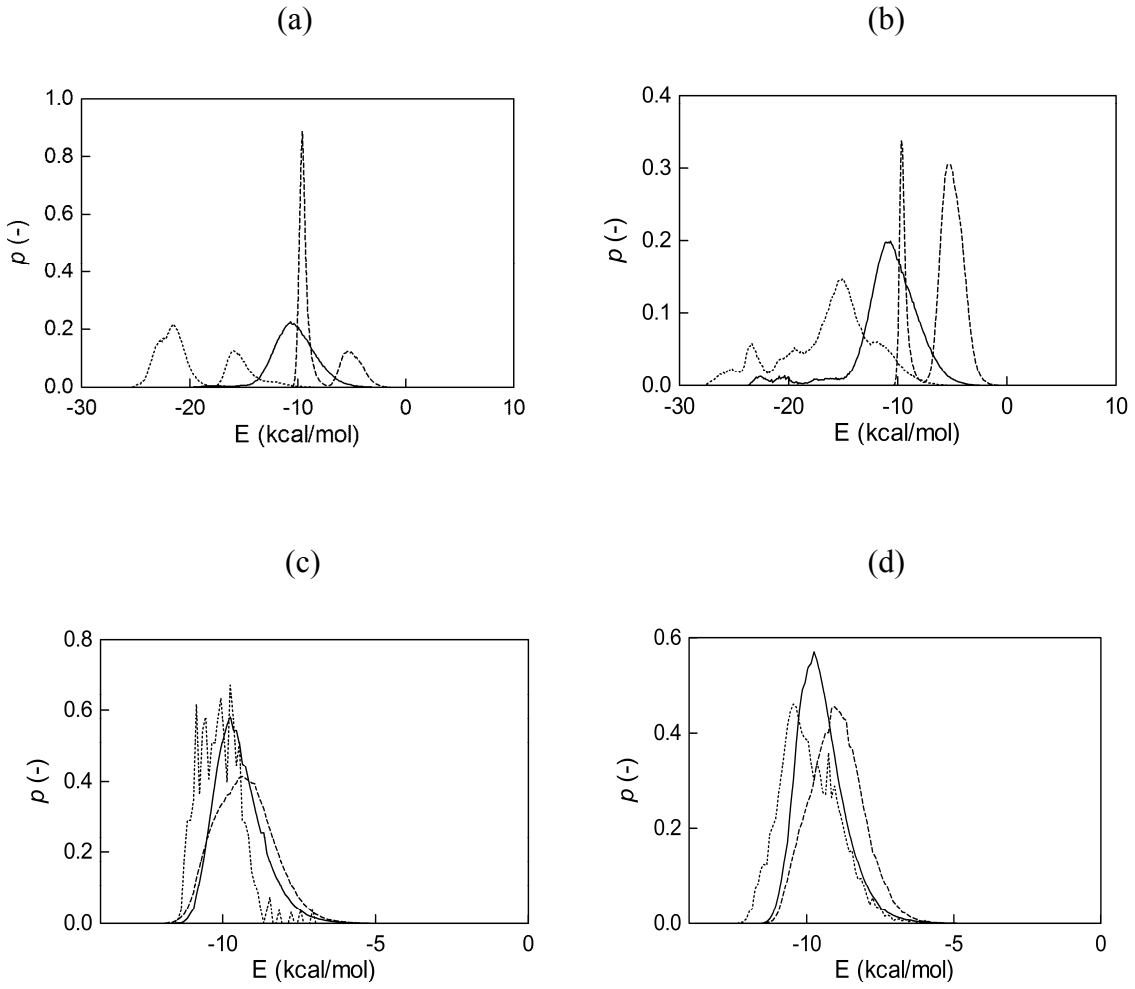

Figure 5.10: Energy density distributions for biogas mixture adsorption on NaY at P_{H_2S} = 10 Pa (a), NaY at P_{H_2S} = 1000 Pa, MFI at P_{H_2S} = 10 Pa (c), and MFI at P_{H_2S} = 1000 Pa (d). Symbols legend: (·····) = H_2S; (–·–·–) = CH_4; (——) = CO_2.

Figure 5.10 shows different peaks for both NaY-H_2S and NaY-CH_4 energy distributions, a trend confirmed for the other hydrophilic zeolites in the entire H_2S partial pressure range. CO_2 curves, on the contrary, exhibit an invariant behaviour characterized by a Gaussian distribution. As a rationale, we can say than CH_4 and H_2S are able to occupy more that one site, or position, in the framework with different probability, so that adsorption sites can be interchanged as P_{H_2S} increases. MFI curves have only one peak for each gas, and each peak is close to each other showing no appreciable differences in *E* values. Accordingly, sorption site interchange is more difficult in this apolar framework. To consider adsorption selectivity in more details, we mapped H_2S selectivity with respect to CH_4 and CO_2 in Figure 5.11. Selectivity factors are generally very high in hydrophilic zeolites; again, according to our simulation results, the best results are achieved with NaY. To find a rationale for these selectivity curves is less straightforward. As a general observation, they tend to decrease quickly for NaY and LTA; accordingly, selectivity is generally higher at low H_2S partial pressures, which indicates that sorption selectivity mechanism seems to work better in the typical low range of biogas H_2S content. Lower selectivity for NaY and LTA may be explained by the fact that, when P_{H_2S} increases, H_2S gains new adsorption sites, for which H_2S is favoured over CH_4 and CO_2 but not as well as for old adsorption sites, at lower P_{H_2S}. Selectivity for NaX shows less variation, probably because selectivity values at low H_2S pressures are already quite low. This, in turn, could be due to the higher steric hindrance exerted by the higher number of cations characterizing this framework. Once again, MFI does not show selectivity for H_2S.

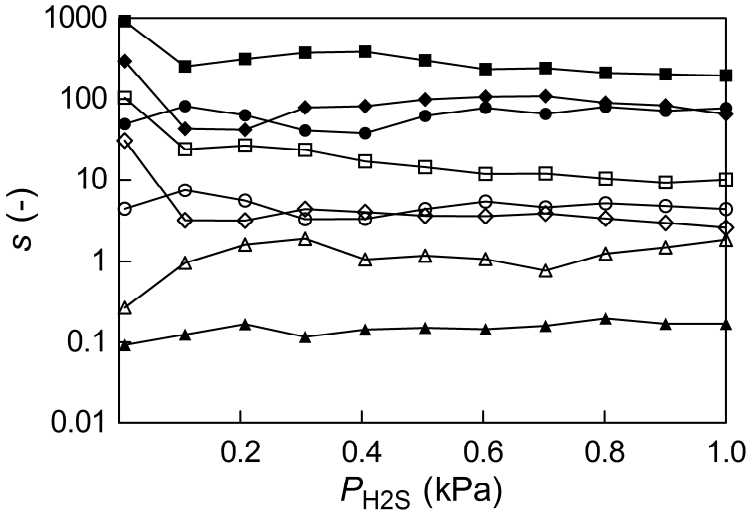

Figure 5.11: Selectivity factor for H_2S with respect to CH_4 (S_{H_2S,CH_4}) (filled symbols) and to CO_2 (S_{H_2S,CO_2}) (open symbols). Symbols legend: (■, □), NaY; (●,○), NaX; (◆,◇), LTA; (▲,△), MFI. Lines serve as eye guides.

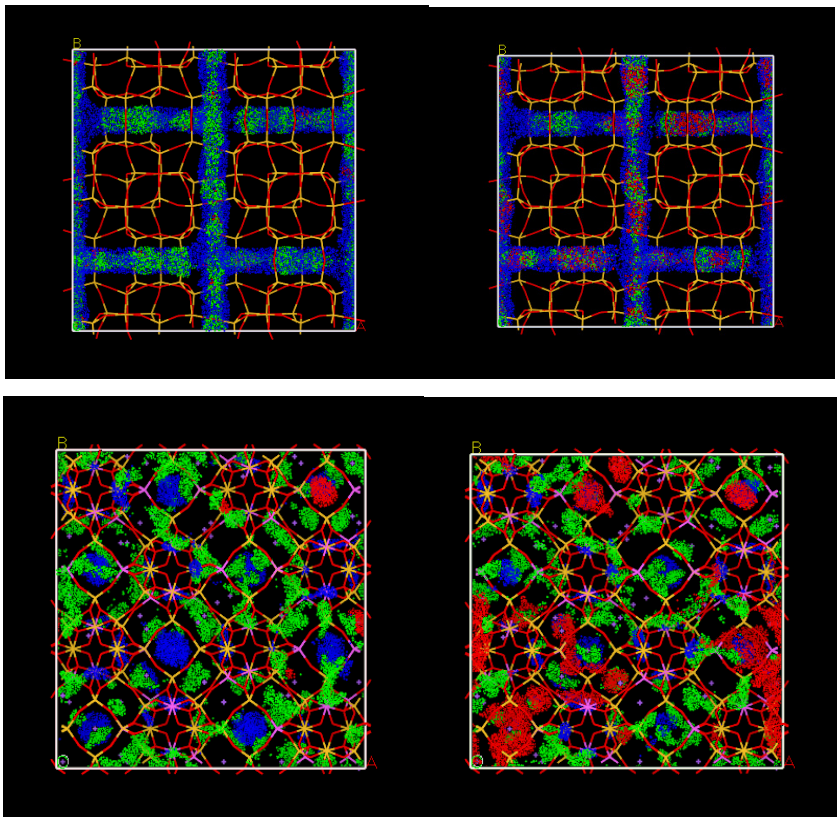

Figure 5.12: density distribution of adsorbed species in MFI (top) and NaY (bottom), P_{H_2S} = 10 Pa (left), and P_{H_2S} = 1000 Pa (right). Molecular colour code: red, H_2S; blue, CH_4; green, CO_2. Density ranges between 0 and 0.3.

We also investigated the density fields in the pores of the zeolite 3D periodic structures (Figure 5.12).

Although for low P_{H_2S} in some cases, distributions are not symmetrical, it is qualitatively evident how H_2S prevalently substitutes CH_4 in sorption sites (especially in larger pores). Zeolites NaX and LTA show similar behaviours, while MFI adsorption site substitutions are much less evident, if at all.

The main results of these sets of simulations confirm that hydrophilic zeolites are more indicated for H_2S adsorption. Differences arise, as evidences by both pure H_2S and biogas mixture adsorption simulations, from adsorption site competition. Adsorption isotherms, isosteric heats of adsorption and energy distributions confirm specific trends and explain adsorption behaviours. Results are of remarkable practical use if considered in terms of selectivity, according to which a ranking for the considered zeolites towards H_2S can be formulated: the FAU NaY framework appears the best choice, being favoured over NaX, which has essentially the same structure but a different Si/Al ratio, ultimately resulting in more sterical hindered pores. In this way, a reasonable ranking for the best zeolite choice has been determined. It should be noticed that for some kinds of zeolites, as LTA or MFI, H_2S is scarcely adsorbed and this affects the shape of adsorption isotherms and, probably, the accuracy of Monte Carlo sampling. In these cases, further analysis may be performed to obtain much quantitative results; this can be obviously done by speeding up calculations or applying new, more efficient sampling methods

5.3.2 Deterministic methods: competition for adsorption sites

In this part we investigate in deeper details the results stemming from our previous GCMC simulations. Starting from the selected zeolite, NaY, we give more insights to the swapping phenomenon, investigating the behaviour of already adsorbed molecules when the ensemble (NaY and adsorbed molecules) is perturbed by a new H_2S molecule which approaches the zeolite external surface. We simulated this dynamic, swapping-like behaviour both for different biogas compositions inside zeolite framework, and for different zeolite loadings. We aimed at explaining and confirm the general trend arising from GCMC simulations from a thermodynamic and deterministic point of view.

Also for this part we used the Materials Studio platform, employing *Sorption, Forcite* and *DMol*^{3} software modules.

Many studies have been performed about self or corrected diffusion (Sanborn and Snurr,

2001; Nagumo et.al., 2001), and about preferential pathways of small molecules in zeolite pores (Sastre and Corma, 2003; Sastre et.al., 2002). The application of these methods seems quite difficult for our complex systems, both in terms of equilibrium dynamics and computing times (Auerbach et. al., 1995), as Kinetic Monte Carlo techniques have been often indicated as the techniques of election. Basing our simulation procedures on previous MD techniques for similar systems (Sastre and Corma, 2003; Sastre et. al., 2002; Sanborn and Snurr, 2001; Auerbach et. al., 1995; Nagumo et. al., 2001), we looked for a correlation between the evident, more favourable tendency of H_2S to enter in NaY pores versus the less favourable adsorption behaviour exhibited by other molecules, especially the less polar CH_4.

To this purpose, we considered the behaviour of an H_2S molecule which is approaching the zeolite surface when the NaY cell is already filled with adsorbed molecules (H_2S, CO_2, CH_4) at different loadings and at different $P_{(H2S)}$. From the previous MC adsorption isotherms calculations we have obtained the number of adsorbed molecules per cell at different $P_{(H2S)}$. In particular, we performed calculations for 1/3, 2/3 and full NaY cell coverage, at $P_{(H2S)}$ of 10, 500 and 1000 Pa, with the number of molecules inserted approximated at the upper integer number. Since the biogas pressure is 1 atm, and $P_{(H2S)}$, as normally expected, is low (i.e., from 10 to 1000 Pa), we can sensibly take the vacuum as the external environment of the zeolite in our length scale of simulations. This means that the interactions between gas molecules are negligible in our model, and, thus, only one H_2S molecule is sufficient to describe the approaching and adsorption mechanisms of the molecule of interest.

The first step of our computational procedure is to run MC simulations in the Canonical Ensemble (NVT), with a fixed loading given by the relevant adsorption isotherms results. 10^6 trial steps, with 10^5 equilibration steps at 298 K have been performed, with the cvff_aug Force Field. The cut-off was fixed at 12.5 Å for both non-bonded energy terms (van der Waals and Coulomb interactions). For van der Waals terms we use a traditional atom based method. For electrostatic terms, the Ewald and group method has been used; in this method, interactions between charge groups are calculated using a group-based sum, while all other interactions are calculated using a Ewald sum. In Table 5.6 details of our MC simulations are exposed.

Non-bond terms	Type	Accuracy [kcal/mol]	Cut-off [Å]	Truncation	Spline width [Å]
Electrostatic	Ewald and group	0.001	12.5	[-]	[-]
Van der Waals	Atom based	[-]	12.5	Cubic spline	1

Table 5.6: non-bond terms in (NVT) MC simulations.

Zeolite partial charges were assigned via the force field, while partial charges of molecules to be adsorbed have been taken from previous quantum-mechanics simulations (H_2S), or assigned by the force field (CH_4, CO_2) [13]. From these simulations, we considered the lowest final energy frames for each system for further considerations.

The 3D periodic cubic cells (25.1 Å for each side) have then been transformed into 2D periodic cells with a (0 0 1) cut plane (normal to *z* axis), and then a new H_2S molecule has been inserted, as shown in Figure 5.13. The molecule has been placed at the centre of the cell length, at a distance of 2 Å from the NaY external surface. Although this is an arbitrary choice, the cell has a cubic symmetry, so the H_2S positioning is not affected by the choice of the cut plane. In this way, adsorbed molecules are free to change adsorption sites or to move outside the zeolite if the non-bonded interactions are less favourable, due to the disequilibrium imposed by the new H_2S molecule approach. The same H_2S molecule is free to move and position inside the cell, or to escape from the zeolite. The zeolite framework for all MD was kept fixed, while Na^+ ions and H_2S, CO_2 and CH_4 molecules had no constraints.

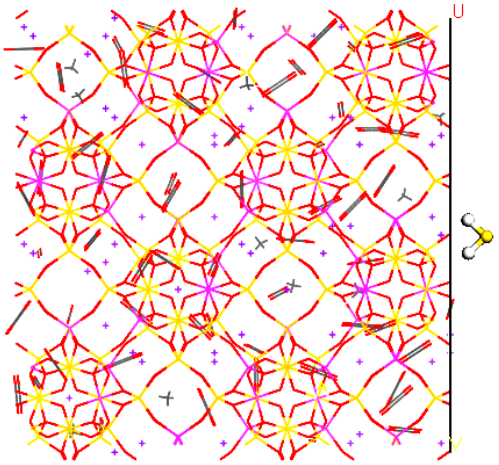

Figure 5.13: 2D periodic cell of NaY structure with H2S molecule approaching the framework.

Equilibration was performed with 20 ps of MD in the NVT ensemble, which allowed reaching sufficient energy stability in all simulations. NVT ensemble has been chosen for equilibration to preserve the cell morphology (Charati and Stern, 1998; Skoulidas and Sholl, 2001). The last frames of NVT simulations have been used to start 500 ps of constant volume-constant energy (NVE) simulations, an ensemble which is usually more indicated to preserve the thermodynamics of the system (Nagumo et. al., 2001; Demontis and Suffritti, 1997), because if an external (artificial) thermostat is used, this will lead to an inevitable error of dynamics (Shinoda et. al., 2004).

The details of NVT and NVE simulations are reported in Table 5.7; it should be noticed that the Ewald calculation method (Karasawa and Goddard, 1992) was used for the calculation of the Coulomb energy component in the 2D periodic systems. The analysis of the MD simulations has been carried out considering:

- the number of molecules of each species escaping from the cell
- the temporal evolution of molecules removal for each species
- the binding energy evaluation for each species over time.

-

	NVT	NVE
van der Waals	Atom based (cut-off = 18.5 Å)	Atom based (cut-off = 18.5 Å)
Coulomb	Ewald (accuracy = 10^{-5})	Ewald (accuracy = 10^{-5})
Thermostat algorithm	Velocity scale	-
Time step	1 fs	1 fs
Simulation time	20000 ps	500000 ps
Temperature	298 K	-
Frame sampling	Each 1000 ps	Each 1000 ps

Table 5.7: details of the 2D dynamic simulations.

Binding energy analysis has been used in molecular simulation to evaluate thermodynamic behaviour and stability of several complexes (Tanaka and Goettler, 2002). In a general case, given a complex of two generic molecules 1 and 2, the expression of the relevant energy of binding can be written as:

$$E_{BIND(1,2)} = E_{1,2} - (E_1 + E_2) \qquad [22.5]$$

where E_1, E_2 and $E_{1,2}$ are, the total energies of the isolated molecules 1 and 2 and the complex, respectively. The calculation of E_1, E_2 is obtained by cancelling the other molecule(s) in a selected frame of MD. Given the method, the bond energy contributions cancel out in the difference, and only the non-bonded energy difference account for the binding energy term in physical complexes, as expected. If the value of E_{BIND} is negative, the complex is supposed to be thermodynamically favoured while, on the contrary, the separation will be favoured (Fermeglia et. al., 2004).

We considered 5 different ensembles in our simulation cell: the whole system itself, the zeolite framework (including Na^+ ions), and the adsorbed molecules (H_2S, CO_2, CH_4). In this way, the binding energies for H_2S, CO_2 and CH_4 have been calculated according to Equation 22.5:

$$E_{BIND(ads,i)} = E_{TOTAL} - (E_{ads,i} + E_{ZEOL}) \qquad [23.5]$$

where $E_{BIND(ads,i)}$ is the binding energy of the specific complex, E_{TOTAL} is the total energy of the whole system, $E_{ads,i}$ is the total energy of the specific adsorbed group of molecules, and E_{ZEOL} is the total energy of the zeolite alone. Binding energies have been analyzed for each

different adsorbate, at different time steps, and taking into account molecular escape events. Binding energies have been then normalized by dividing $E_{BIND(ads,i)}$ for the number of molecules of the considered species inserted in the framework at the beginning.

It was clear, even from the beginning of the NVT MD equilibrations, that the CH_4 molecules have a major tendency to escape from the framework, a phenomenon clearly related to their less polar characteristics. This confirms also the fact that hydrophilic zeolites, such as NaY, exhibit higher affinity for polar molecules (or molecules with a quadrupole moment, like CO_2). For this reason, the perturbation of the equilibrium, reached in the lowest energy frame of NVT-MC simulation, by a new H_2S molecule insertion tends decidedly to mobilize CH_4 molecules. Regarding CO_2 behaviour, although its selectivity and isosteric heat of adsorption given by GCMC simulations is lower than that calculated for H_2S (as it appears in the previous paragraph), it is not severely influenced by the perturbation: CO_2 molecules generally oscillate next to their adsorption sites, and their escaping tendency is very low. This can be ascribed to the fact that the quadrupole moment contributes to CO_2 binding stability, and to the planar, linear CO_2 shape, which allows the molecules to align inside the straight pores of NaY.

Quantitative results can be given both on terms of escaped molecules and in terms of binding energies. In Table 5.8 the list of total escaped molecules for each species is shown. Figure 5.14a, 5.14b and 5.14c shows escape events for each molecule in the NVE simulations. In this Figure, each point represents escaping events at the given time step.

It is important to note that we defined molecules as escaped when their centre of mass is at a distance from the external zeolite surfaces greater than 12.5 Å. It may be observed that CH_4 molecules tend to exit rapidly from the cell along the *z* direction, as exemplified for example by the 3D visualizations of the 2D periodic simulation cell visualized in Figure 5.15.

The equilibrium condition is reached, in each case, well before 500 ps; only few H_2S and CO_2 molecules tend to escape. Generally, however, in correspondence of higher $P_{(H2S)}$, and thus for higher H_2S fractions in the cell and for lower loadings (i.e., Figure 2b and 2c), the equilibrium is reached more slowly. Although this behaviour is difficult to explain, a tentative explanation might be related to the lower occupancy of free adsorption sites, especially for the few CH_4 molecules, which in these cases are allowed to cover longer pathways in relatively empty channels before finding the way to exit the framework.

$P_{(H2S)}$ = 10 Pa	**Loading = 1/3**			**Loading = 2/3**			**Full loading**		
Molecules	**CH_4**	**CO_2**	**H_2S**	**CH_4**	**CO_2**	**H_2S**	**CH_4**	**CO_2**	**H_2S**
Initial number of molecules	3	19	0 (+1)	6	39	0 (+1)	10	59	1 (+1)
Escaped from NVT equilibration	0	0	0	1	0	0	2	2	0
Escaped from NVE simulation	3	0	0	4	0	0	6	0	0
$P_{(H2S)}$ = 50 Pa	**Loading = 1/3**			**Loading = 2/3**			**Full loading**		
Initial number of molecules	2	19	3 (+1)	3	39	7 (+1)	4	58	10 (+1)
Escaped from NVT equilibration	0	0	0	0	0	0	2	1	0
Escaped from NVE simulation	2	0	1	3	1	3	3	0	0
$P_{(H2S)}$ = 1000 Pa	**Loading = 1/3**			**Loading = 2/3**			**Full loading**		
Initial number of molecules	1	18	4 (+1)	3	36	9 (+1)	4	54	13 (+1)
Escaped from NVT equilibration	0	0	0	0	0	2	0	0	2
Escaped from NVE simulation	1	1	1	3	0	1	4	0	1

Table 5.8: escaped molecules from NVT and NVE MD for different loading and different $P_{(H2S)}$.

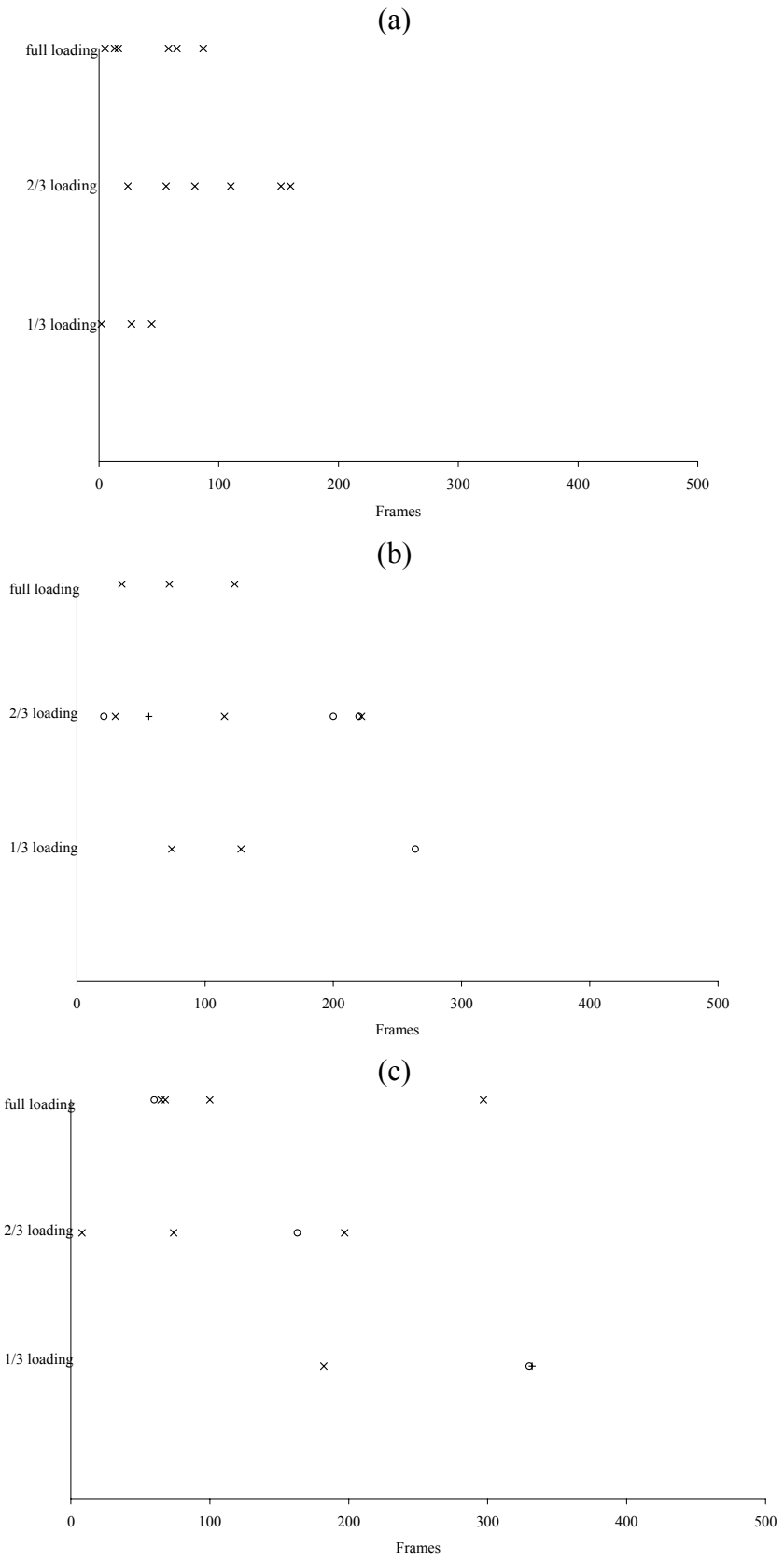

Figure 5.14: escaping molecules events for $P_{(H2S)}$ of 10 Pa (a), 50 Pa (b), 1000 Pa (c); ×: CH_4,: +: CO_2, ○: H_2S. Each frame corresponds to 0.5 ps in NVE MD simulations.

Figure 5.15: 3D visualization of a 2D periodic cell at initial conditions (left) and after 6 ps of MD simulation (NVE ensemble, right); $P_{(H2S)}$ = 10 Pa, full loading. The methane molecules escaping from the cell are represented in gray-and-white CPK representation.

It can also be noticed that, after molecule exits, the temperature of the system tends to increase; this is reasonable, due to the acceleration of the escaping molecule. Both molecule pathways and temperature of the system always show stability within 350 ps, and none of the probe H_2S molecule inserted escapes from the cell.

Considering binding energies, we examined the binding energy behaviour as a function of time (see Figures 5.16, 5.17, 5.18). Each frame in these Figures represents 0.5 ps of NVE MD simulation, and each binding energy value is averaged over the total number *N* of specific molecules inserted.

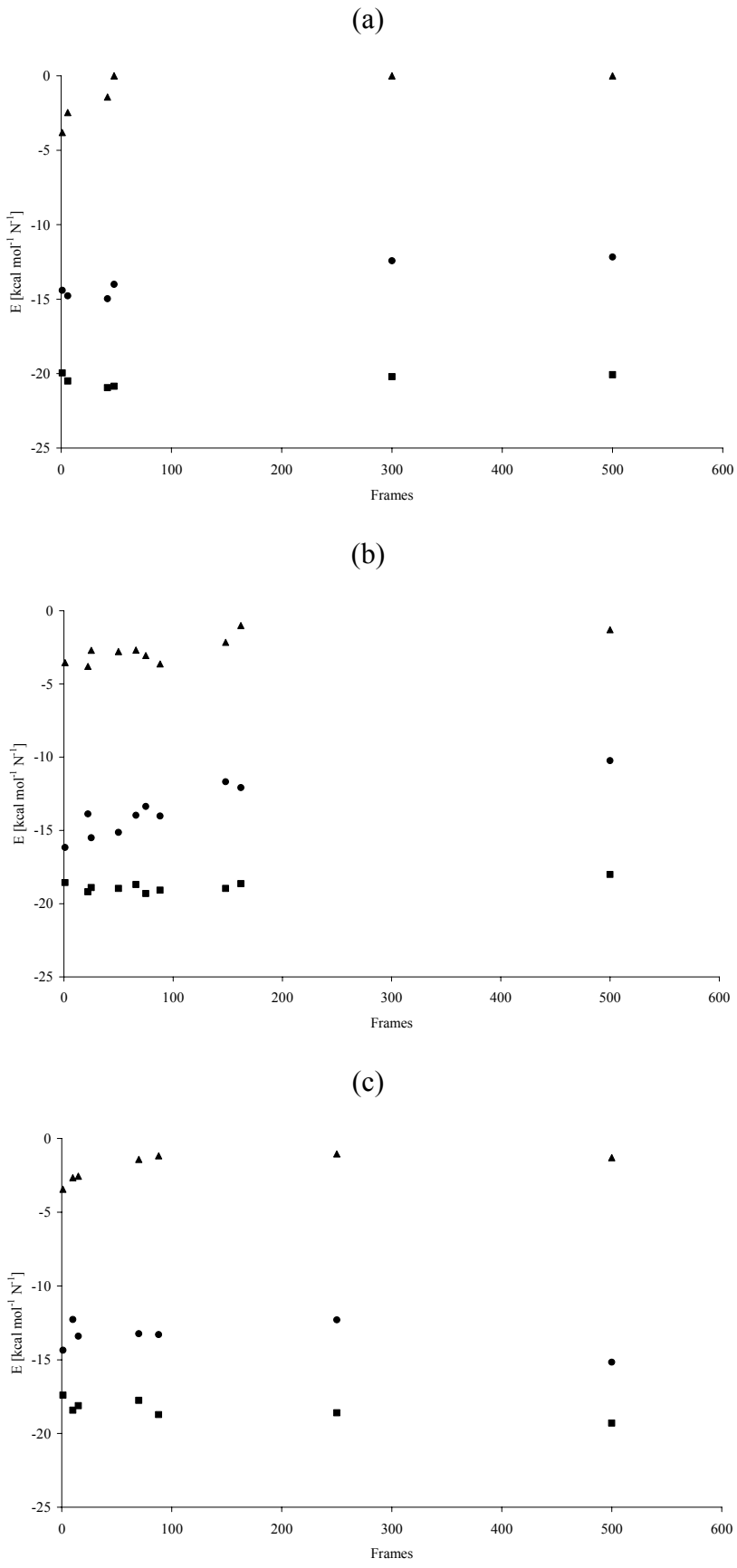

Figure 5.16: binding energies as a function of time frames for NVE MD simulations at $P_{(H2S)}$=10 Pa; (a): 1/3 loading, (b): 2/3 loading, (c): full loading; ●: H_2S, ■: CO_2, ▲: CH_4.

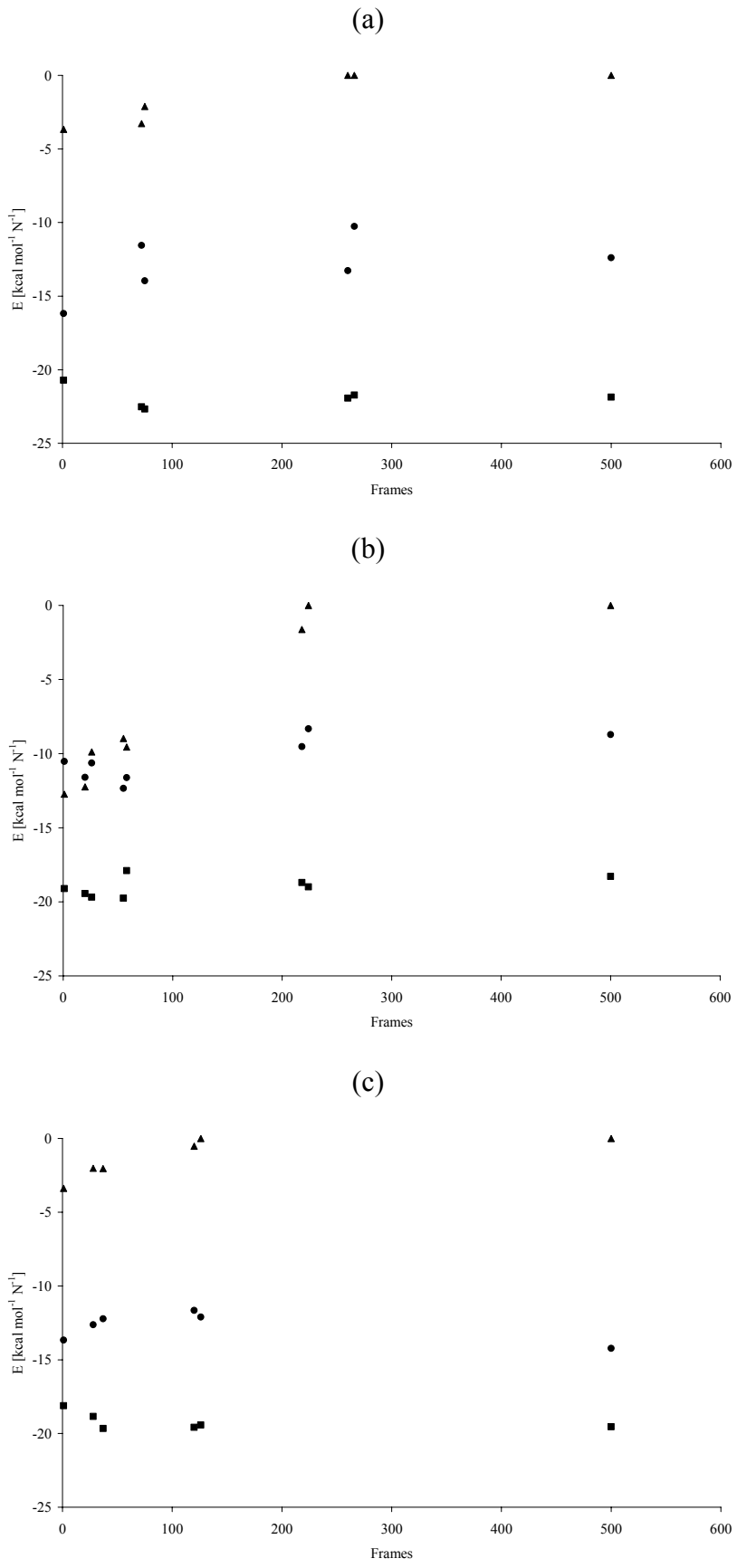

Figure 5.17: binding energies as a function of time frames for NVE MD simulations at $P_{(H2S)}$=50 Pa; (a): 1/3 loading, (b): 2/3 loading, (c): full loading; ●: H_2S, ■: CO_2, ▲: CH_4.

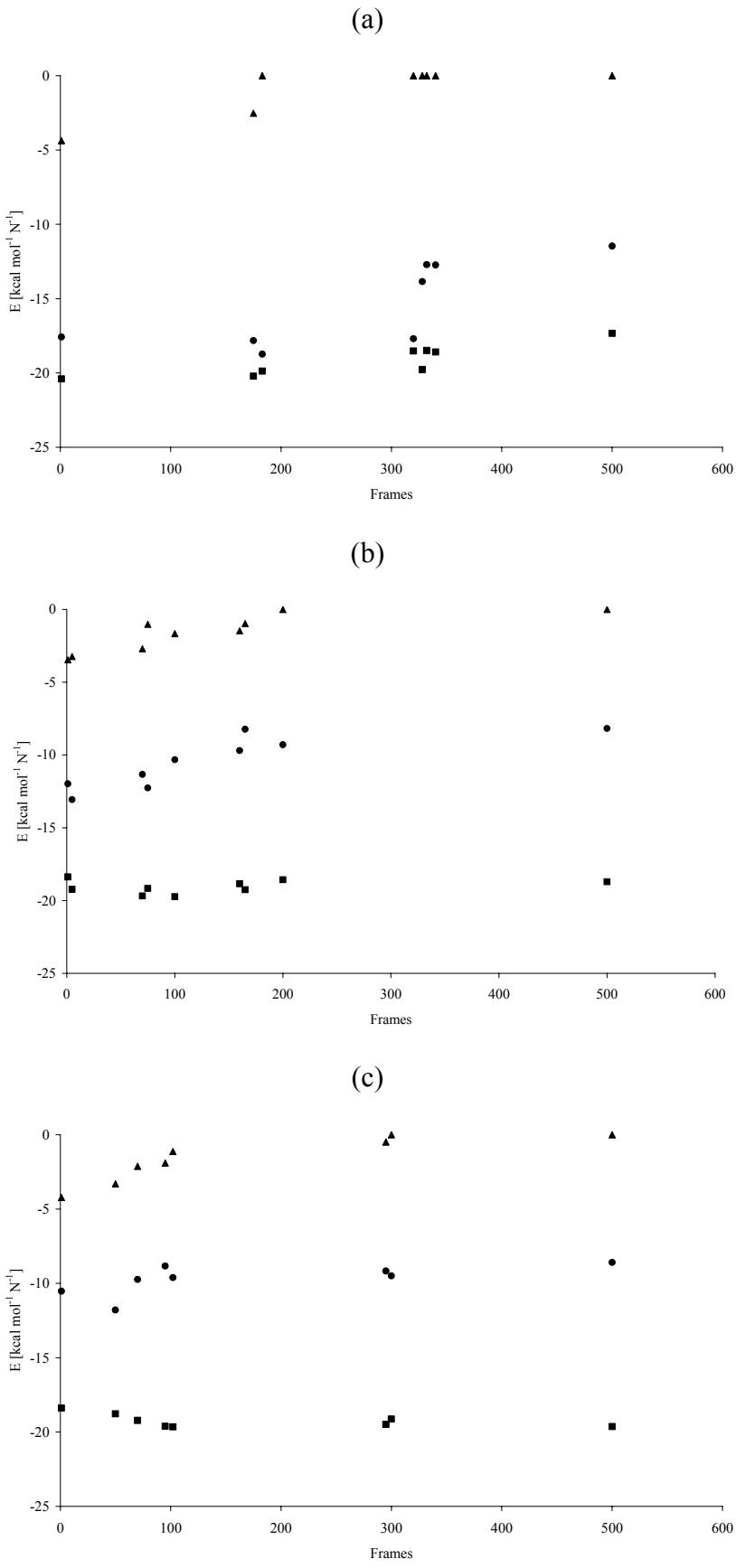

Figure 5.18: binding energies as a function of time frames for NVE MD simulations at $P_{(H2S)}$=100 Pa; (a): 1/3 loading, (b): 2/3 loading, (c): full loading; ●: H_2S, ■: CO_2, ▲: CH_4.

Although an attempt of fitting these curves is rather difficult or even impossible, these charts are helpful to explain adsorbed molecules behaviour obtained by MD simulations. Binding energy evolutions are obviously influenced by molecule exit events; for instance, by considering the MD trajectory of the case shown in Figure 4 b, one CH_4 molecule escapes at frame 66, comes back at frame 80, and then leaves the zeolite again at frame 148. As can be seen from Figure 4 b, the corresponding binding energy trend clearly reflects this behaviour. In general, all trends dramatically confirm the high speed with which methane tend to move out from the zeolite. Only when $P_{(H2S)}$=10 Pa, and thus the number of H_2S molecules is low, some CH_4 molecules remain in the zeolite framework, but generally they all escape before 300 ps. Indeed, values of E_{BIND} = 0 kcal·mol^{-1}·N^{-1} mean that all CH_4 molecules are dispersed outside the cell at a distance higher than imposed cut-offs. Generally, it appears that H_2S binding energies per molecule are considerably higher than those of CH_4; CO_2, on the other hand, shows the most stable behaviour and, generally, is characterized by the most favourable binding energy.

This analysis contributes to explain also the adsorption behaviour at different H_2S pressures (see previous paragraph); when $P_{(H2S)}$ is increased, an adsorption competition process takes place, resulting in a swap of adsorption sites between H_2S and CH_4 molecules; accordingly, the H_2S adsorption increases. Nevertheless, selectivity S_{H_2S,CH_4} is much more enhanced at low H_2S pressures (i.e., lower loadings) due to the fact that more energetically suitable and free pores are available for H_2S. Thus, examining local binding energy evolution, e.g. immediately before and after CH_4 molecules leave the framework, an interesting behaviour can be noticed (see Table 5.9). We considered only events of CH_4 exiting, in the absence of other event which might influence this process (e.g. simultaneous exiting of more than 1 molecule or different molecules). Thus we could calculate the binding energy differences (*BED*) for all considered exiting events, as:

$$BED = E_{BIND,after} - E_{BIND,before} \qquad [24.5]$$

where $E_{BIND,after}$ and $E_{BIND,before}$ are the binding energies for CH_4 or H_2S, calculated immediately after (when CH_4 molecules are far from zeolite boundaries more than 12.5 Å) and before (when CH_4 molecules are still crossing zeolite boundaries) the CH_4 exit.

Molecule	BED [Kcal/mol]	Standard deviation [Kcal/mol]
CH_4	2.816	0.889
H_2S	-2.051	1.950

Table 5.9: mean values of *BED* for H_2S and CH_4 for exiting events and standard deviations.

Although variations are quite high, due to the complexity of the system and the different composition and loading for each set of simulation, there is a clear trend in binding energy modifications after CH_4 exits. After each escape event, as expected, CH_4 binding energy decreases as absolute value, but this phenomenon involves also a decrease in H_2S binding energy, even though the phenomenon is limited in time. This is probably due to the re-equilibration of the NVE system after a few ps. The behaviour testifies that CH_4 molecules tend to exit because of the lower intermolecular attractive forces with the rest of the system; moreover, CH_4 exits seem also to favour the re-allocation of H_2S molecules in adsorption sites, contributing to improve their stability in the framework immediately after each CH_4 exit event.

As a conclusion, we determined a ranking from a list of zeolites for H_2S adsorption for removal. The best one resulted to be FAU – NaY; thus we investigated more deeply the adsorption phenomena and the adsorption sites competition among biogas components. Results of MM/MD confirmed the trend of GCMC simulations, showing from a deterministic point of view how H_2S is more favourably attracted into pores than the other components. This phenomenon is considerably enhanced by the fact that H2S is able to shift other molecules, especially the less polar CH_4, to take their place into the framework. The procedure is easy to replicate and can be adapted to other kinds of adsorbents, or matrices.

5.4 Benzene removal from exhaust gases

In this work we made a further step towards more complex systems. We compared the adsorption isotherms of a gaseous mixture prototype stream, deriving from typical industrial processes (such as combustions) with the aim of pollutant removal. Benzene was chosen as the VOC to be removed from gaseous stream. Adsorption isotherms are obtained for a crystalline adsorbent (zeolite) and disordered structures that mimic activated carbons. GCMC simulations have been carried on at different temperatures and different total pressures.

Results have been compared to obtain a possible ranking at different conditions; we also used a simple thermodynamic model that fitted reasonably the results obtained.

Two kinds of zeolites, hydrophobic MFI and hydrophilic FAU NaY (Si/Al= 2.5), already described in previous paragraphs, have been tested in our work, and then zeolite MFI was used. We also tested and used one disordered structure, called cs1000a, which reproduces an activated carbon fibre, obtained from the pyrolysis of pure saccharose at 1000 °C for 20 hours in a CO_2 atmosphere. This was one of the disordered structures obtained by the Keith Gubbins group using the Hybrid Reverse Monte Carlo method (HRMC), and is now freely available in literature (Jain et. al., 2005; Jain et. al., 2006). Both activated carbon and zeolites have been commonly investigated, and frequently employed, in processes of purification technologies, in particular for VOC and benzene separation (Zhao et. al., 1998; Heuchel et. al., 1997; Sircair et. al., 1996; Song et. al., 2005; Siriwardane and Shen, 2001).

The aim of the work is mainly to establish a flexible and simple procedure to estimate the efficacy of different adsorbents in different conditions, to give more insights to the adsorption process at molecular level, and to understand how the presence of a gaseous mixture, which is usually encountered in these kinds of processes, will affect the predicted adsorption isotherms. In fact adsorption experiments have been performed in different conditions and for a huge kind of matrices and adsorbates, as there is a considerable interest in adsorption processes and technologies, as testified by a huge literature (Sircar, 2000). Nevertheless, in the case complex multicomponent mixtures, especially when the component to be separated is very dilute, data are absent or still very scarce (Wu et. al., 2005), due to the difficulties of experimental procedures. Although, it is demonstrated (as for instance in the previous case study), how competition for pore sites may substantially affect the adsorption mechanism (Gun'ko, 2007).

In our example, we decided to mimic in a simplified way a composition which can be an example of a stream from waste incinerator processes, or from combustions due to industrial processes, or from residual streams of chemical plants. In this way the choice of benzene as pollutant and the specific gaseous composition, are merely exemplificative, and should be intended as a specific case study to explore the effectiveness of the procedure, which may be also adapted to different conditions or changed in the case of a different pollutant removal.

We briefly describe computational details, we provide a validation of our procedure against available data; then we compare results of pure benzene adsorption isotherms at 500 K with the ones in the multicomponent gaseous mixture, and, finally, we analyze and discuss the

results for multicomponent mixtures at different total pressures and temperatures, comparing the obtained results with a simple thermodynamic model for gaseous mixtures.

The Sorption module of Materials Studio platform has been employed again in this work. A mixture of O_2, N_2, H_2O, CO_2 and benzene has been used to approximate and mimic an exhaust gaseous stream from a combustion process. Due to the relatively low pressures considered for all simulations, and accordingly to the aim of our work, we decided to approximate fugacity with partial pressure.

The frameworks of the chosen zeolites, MFI and FAU (NaY), are available in the database of the platform; the Na^+ ions added to balance the total charge have been placed into the NaY cell with a cation locator option, provided in the Sorption module. This allows performing a Metropolis Monte Carlo location of the ions in the cell, according to the lowest energy configuration; acceptance criteria are similar to the ones used for Canonical Monte Carlo simulations, but in this case a specified number of annealing cycles (called simulated annealing) is used to slowly freeze the system, in order to repetitively explore the configurational space determined by the adsorbate (zeolite) and sorbent (Na^+) system, and to avoid local minima (Kirkpatrick et. al., 1983).

The atom positions of the disordered structure cs1000a, have been obtained with the HRMC method (Jain et. al., 2005; Jain et. al., 2006). This method uses an algorithm which attempts to simultaneously minimize the error in the radial distribution function and also the total energy of the system, thus matching the experimental data obtained for the real structure, such as structure factor, porosity and density. Further, a simulated annealing minimization method is also employed to avoid the system to be trapped in local minima.

Once again, the core of this work is the GCMC application with the stochastic Metropolis method for multicomponent gas adsorption. We obtained results for multicomponent adsorption isotherms and the isosteric heats of adsorption.

The characteristics of the 3D periodic cells are described in Table 5.10.

Structure	Dimensions x, y, z [Å]	Composition [% in weight]	Density [kg/m^3]
Zeolite MFI	40.044, 39.798, 26.766	Si 46.7%, O 53.3%	1796
Zeolite FAU (NaY)	25.104, 25.104, 25.104	Si 30.1%, O 48.3%, Al 11.7%, Na^+ 9.9%	1337
Cs1000a	25.000 x 25.000 x 25.000	C 99.2%, H 0.8%	728

Table 5.10: 3D periodic cells characteristics.

In these simulations we used a slightly modified Augmented Consisted-Valence Force Field (cvff_aug), which, as in the previous case studies, is particularly suitable for small molecules adsorption calculations in solid or crystal frameworks. Modifications have been made to take into account the quadrupole moments of some molecules in a more accurate way. Thus, we used the Watanabe-Austin models (Watanabe et. al., 1995) for N_2, O_2, CO_2, which introduce the presence of dummy atoms to simulate charge displacements. We used the standard TIP3P model for water (Jorgensen et. al., 1983); the benzene molecule was constructed and then minimized with the cvff_aug Force Field. Finally, in the activated carbon structure, hydrogen parameters have been set to the ones describing hydrogen bonded to sp^3 carbons.

The representative mixture (N_2 70%, CO_2 10%, H_2O 10% and O_2 11%) contained also a variable amount of benzene (0.05 – 1%). We performed simulations at 500, 750 and 1000 K, and at a total pressure of 101.3, 202.6 and 506.5 kPa (1, 2 and 5 atm, respectively), with the same mixture composition. In this way we aim to establish the most convenient conditions for benzene removal in terms of adsorption isotherms for the considered structures.

For all simulations, we preformed 5000000 of Monte Carlo steps, preceded by 1000000 of equilibration steps. Electrostatic interactions have been taken into account with the Ewald and group summation method with a Ewald accuracy of 0.001 kcal/mol and a cut off distance of 12.5 Å, which is half of the smaller considered cell width. Van der Waals interactions have been described with an atom based summation method, with a cubic spline truncation, splined for 1 Å; the cut off is 12.5 Å.

Finally, we used the Extended Langmuir-Freundlich model developed by (Sips, 1948) to reproduce simulated data for mixtures; the coefficients of the Langmuir-Freundlich model have been obtained from the fitting of simulated adsorption isotherms of pure species.

We performed a set of simulations to validate our procedure, comparing adsorption isotherms with data available in literature. Then we examined the differences between adsorption isotherms of pure benzene and adsorption isotherms of benzene in the multicomponent mixture, i.e. the gaseous emission (N_2 70%, CO_2 10%, H_2O 10% and O_2 11% as partial pressures) to find a reasonable ranking of the most suitable adsorbent and the most convenient thermodynamic conditions.

For validation, we tried to compare adsorption isotherms with data available in literature. In Figure 5.19 the 3D structures used in this work are shown: zeolites MFI and NaY, and disordered, activated carbon cs1000a.

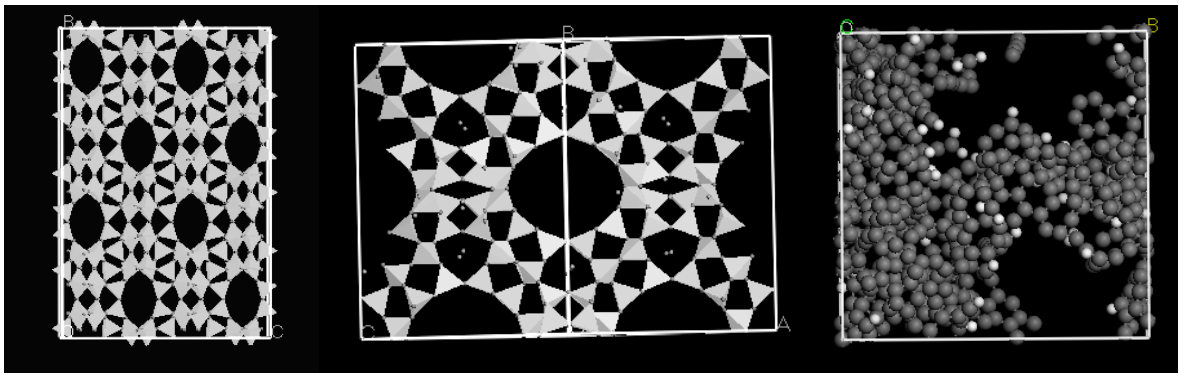

Figure 5.19: From left to right: 3D structures of (a) zeolite MFI, (b) zeolite FAU (NaY), and (c) activated carbon cs1000a.

Figure 5.20 shows the comparison between our data for pure adsorption over MFI zeolite (a) and NaY zeolite (b) and, respectively, the adsorption isotherms of [19] and [38].

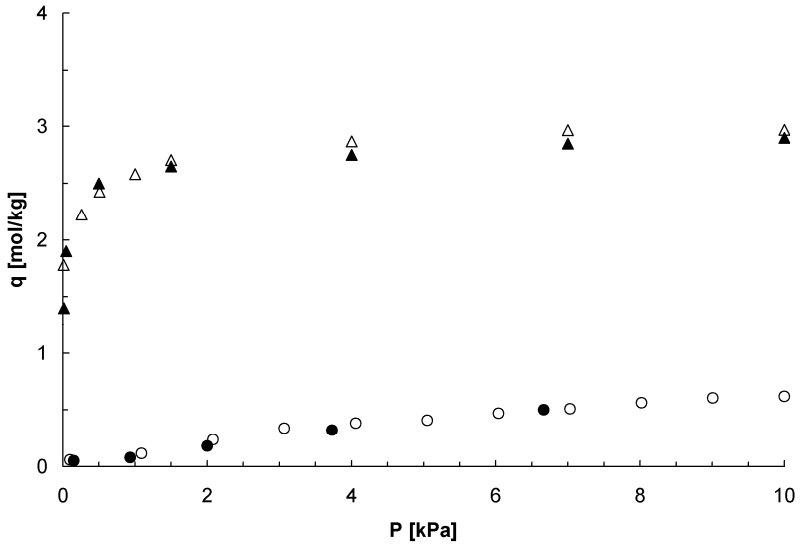

Figure 5.20: Comparison of simulated data (open symbols) with literature data (filled symbols) for benzene adsorption in NaY and MFI zeolites; ▲: NaY, 393 K; ●: MFI, 435 K; q is the loading, P the pressure.

As expected, the agreement is fair for all the considered pressure range, bearing in mind the possible presence of impurities in the real zeolite MFI, and the slightly different Si/Al ratio (2.43 in the case of this publication). Analogous data for activated carbons, although present in several works, are difficult to compare to our specific structure, due to the huge differences which appear in disordered structures with different framework and porosity.

Figure 5.21 shows a comparison between pure benzene adsorption isotherms and benzene adsorption isotherms in the gaseous mixture (N_2 70%, CO_2 10%, H_2O 10% and O_2 11%) at

500 K and at a total pressure of 101.3 kPa (1 atm). Benzene loading is expressed as a function of the benzene pressure.

Results show several differences, which are due to the adsorption site competition inside the pores. These differences are very pronounced at low benzene pressures and for the hydrophilic zeolite NaY, where the most polar groups and the Na^+ ions favour the adsorption of water and oxygen. Accordingly, benzene adsorption in NaY is very low. As expected, MFI and cs1000a are indicated for the non-polar VOC (in particular, benzene) removal, while NaY zeolite is not.

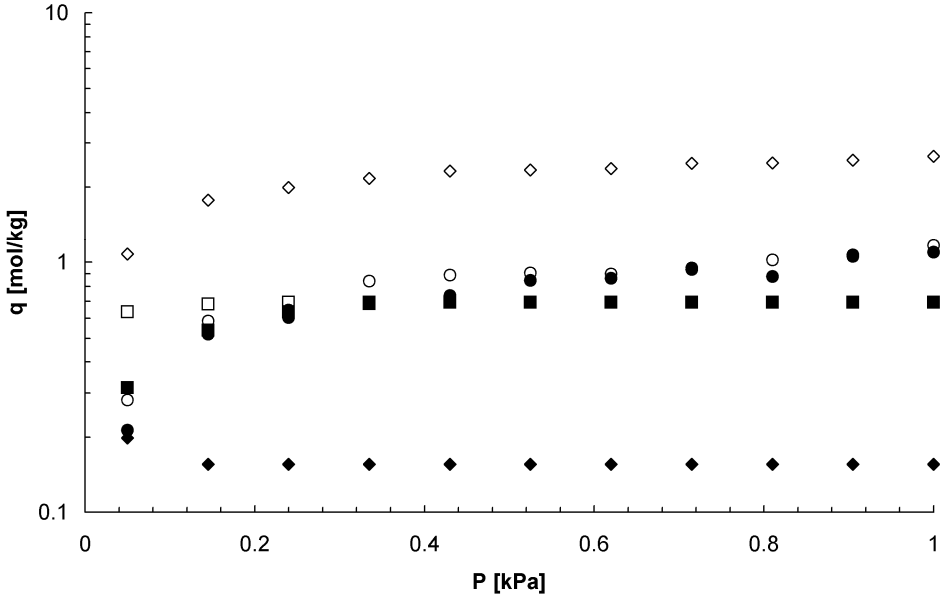

Figure 5.21: Adsorption isotherms for pure benzene (open symbols) and for benzene in the mixture (filled symbols) at 500 K. ◊: NaY; □: MFI; ○: cs1000a; q is the loading, P is the pressure.

Thus, we proceeded by examining the isotherms for mixtures (N_2 70%, CO_2 10%, H_2O 10% and O_2 11%) in cs1000a and MFI. Figure 5.22 show the adsorption isotherms at 500, 750 and 1000 K for MFI and cs1000a, at a total pressure of the system of 101.3, 202.6 and 506.5 kPa (1, 2 and 5 atm, respectively), together with the fitting curves with the Sips model; benzene loading is expressed as a function of the benzene partial pressure.

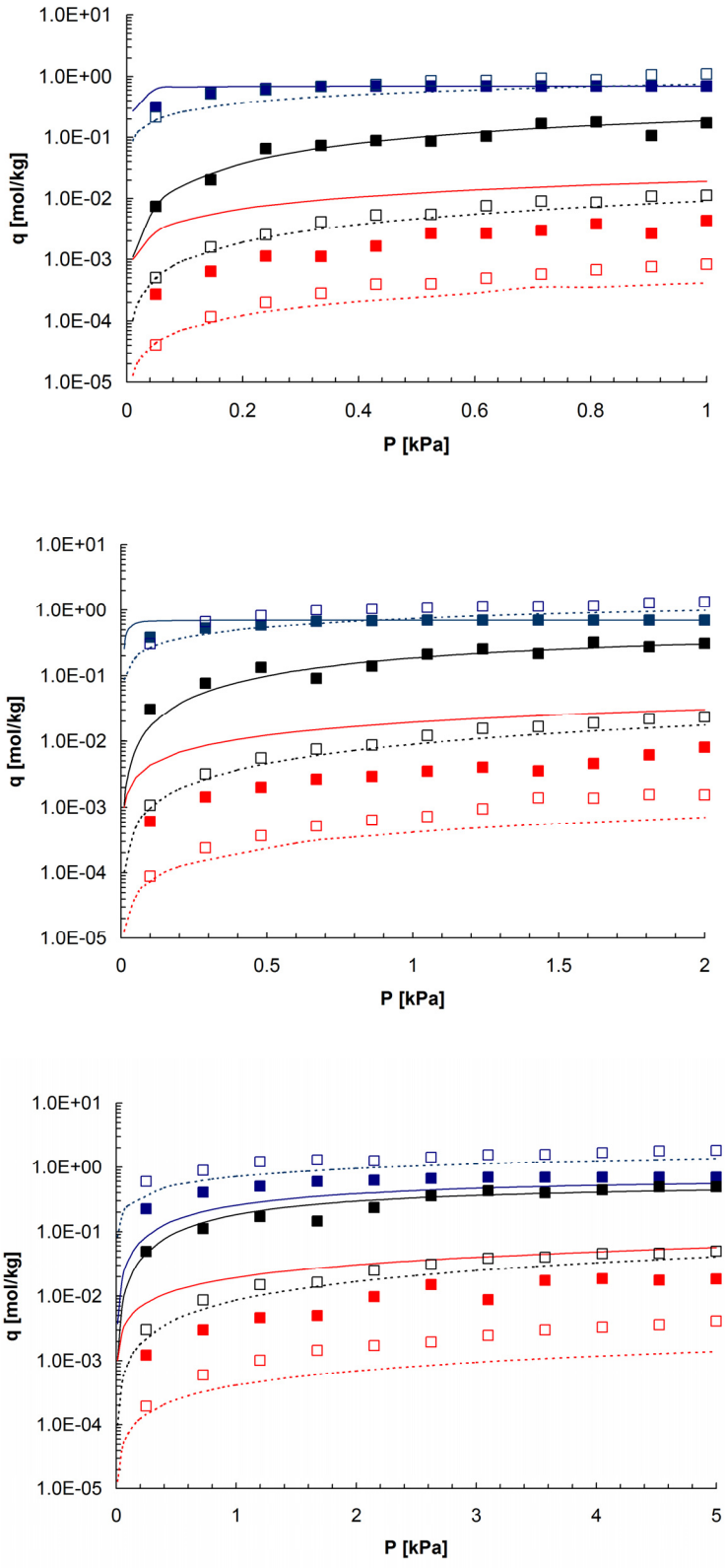

Figure 5.22: Adsorption isotherms for benzene in the multicomponent mixture at a total pressure of 101.3 kPa (a), 102.6 kPa (b) and 506.5 kPa (c). Filled symbols: zeolite MFI; open symbols: activated carbon cs1000a. Blue: 500 K; black: 750K; red: 1000 K. Continue lines: Sips model for MFI; dotted lines: Sips model for cs1000a; q is the loading, P is the pressure.

		Benzene [kcal/mol]	H_2O [kcal/mol]	CO_2 [kcal/mol]	N_2 [kcal/mol]	O_2 [kcal/mol]
MFI (101.3 kPa)	500 K	24.46 (0.12)	10.46 (0.63)	10.99 (0.34)	[-]	[-]
	750 K	24.30 (0.17)	7.98 (0.16)	9.64 (0.15)	[-]	[-]
	1000 K	24.27 (0.17)	7.68 (0.17)	9.68 (0.10)	[-]	[-]
MFI (202.6 kPa)	500 K	24.59 (0.13)	10.32 (0.52)	10.91 (0.40)	[-]	[-]
	750 K	24.35 (0.06)	8.22 (0.26)	9.67 (0.18)	[-]	[-]
	1000 K	24.29 (0.19)	7.75 (0.11)	9.71 (0.06)	[-]	[-]
MFI (506.5 kPa)	500 K	24.39 (0.12)	7.65 (0.12)	9.30 (0.07)	[-]	[-]
	750 K	24.30 (0.15)	8.49 (0.36)	9.96 (0.32)	[-]	[-]
	1000 K	24.03 (0.14)	7.64 (0.07)	9.27 (0.07)	6.45 (0.01)	5.65 (0.04)
Cs1000a (101.3 kPa)	500 K	19.75 (0.20)	3.47 (0.05)	5.32 (0.14)	3.14 (0.05)	2.71 (0.05)
	750 K	16.80 (0.23)	3.38 (0.04)	4.64 (0.03)	3.26 (0.02)	2.97 (0.03)
	1000 K	14.26 (0.49)	3.59 (0.04)	4.62 (0.06)	3.51 (0.01)	3.31 (0.03)
Cs1000a (202.6 kPa)	500 K	19.50 (0.33)	3.53 (0.04)	5.18 (0.14)	3.12 (0.06)	2.68 (0.05)
	750 K	16.98 (0.18)	3.37 (0.04)	4.66 (0.04)	3.27 (0.02)	2.97 (0.02)
	1000 K	14.11 (0.48)	3.60 (0.03)	4.62 (0.04)	3.51 (0.01)	3.30 (0.02)
Cs1000a (506.5 kPa)	500 K	19.21 (0.43)	3.53 (0.07)	5.17 (0.06)	3.08 (0.05)	2.64 (0.03)
	750 K	16.95 (0.16)	3.40 (0.02)	4.67 (0.04)	3.26 (0.01)	2.96 (0.01)
	1000 K	14.26 (0.29)	3.60 (0.02)	4.61 (0.05)	3.52 (0.01)	3.30 (0.02)

Table 5.11: Isosteric heats for multicomponent adsorption in zeolite MFI and activated carbon.

In Table 5.11 we also show the isosteric heats of adsorption for all effectively adsorbed molecules. Values are averaged over all simulated point, standard deviations are in brackets. Empty cells mean no adsorption for the whole pressure range.

Examining isotherms and isosteric heats, it is clear how benzene is favoured over all other components, confirming these structures as suitable for benzene removal. The high benzene loading, even at low partial pressures, corresponds to the other hand to a very low coverage of the other gases. Nevertheless, higher temperatures influence negatively the adsorption for both structures in a quite dramatic way, as differences are up to 3 orders of magnitude. Isosteric heats are quite constant for all isotherms points; they are slightly temperature dependent, especially for benzene adsorbed in the cs1000a structure.

In MFI saturation values at low temperatures are reached before the maximum benzene partial pressure. When total pressure increases, benzene adsorption is slightly decreasing, due to the effect of the higher partial pressure of other components; then, at a total pressure of 506.5 kPa and 1000 K, we can observe how in practice the benzene adsorption is very limited, and decreasing for a higher total pressure. A similar behaviour can be noticed for cs1000a; in this case saturation values, which are also higher, increase with the total pressure of the system. Generally speaking, both for MFI and cs1000a, adsorption is slightly influenced by total pressure. Although the choice of MFI will be favoured for higher temperatures, and lower total pressures, the most indicate and common situation, (moderate pressure and temperature, 101.3 kPa at 500 K) at the outlet of the stream, seems to suggest the use of the considered activated carbon model, with the exception of a very low benzene fraction. Finally, the considered Sips model show a rather acceptable behaviour, as it is able to reproduce qualitatively (and, with the exception of 1000 K, also quantitatively) the trends for both structures. The use of more sophisticated thermodynamic models to take into account non-ideality or framework heterogeneity for such a complex mixture was out of the scope of our work.

5.5 Adsorption and reaction of NOx in disordered structures

In this last case study we analysed the situation in which a gaseous mixture is subjected to simultaneous adsorption and reaction in a porous disordered media, a quite common situation in complex adsorptive phenomena. This work, conducted mainly with in-house, specifically dedicated software, was realised during a period at the Academy of Science (Institute of Chemical Process Fundamentals) in Prague.

As a general statement, the behaviour of chemical reactions in confinement spans a wide range of scientific and engineering interest, including catalyst development and the study of nanoporous materials. For example, in the design of heterogeneous carbon supports (which are often highly nanoporous materials), confinement strongly affects the adsorbed phase, which in turn influences reaction equilibria and kinetics. A chemical reaction confined to a nanoscale environment can have different outcomes compared to the same reaction in the bulk For example, the nanopore phase generally has a higher density than the corresponding bulk phase; Le Chatelier's principle predicts that this results in an increase in yield for reactions in which there is a decrease in the total number of moles. Conversely, a drop in yield occurs in reactions for which the total number of moles increases. Furthermore, some components of the reactive mixture are selectively adsorbed on the solid surfaces, also affecting the reaction equilibrium. In addition, molecular orientations can be strongly influenced by proximity to a solid surface, which can also affect the equilibrium relative to that in the bulk phase. Finally, phase transitions such as capillary condensation have a strong influence on the reaction equilibrium conversion in the nanopores (Santiso and Gubbins, 1998).

In this work we will deal with NO_X adsorption and reaction, studying the NO dimerization reaction into activated carbons. In particular, we continue the studies of (Turner et al., 2001) and of (Lísal et al., 2006) on the NO dimerization reaction, $2NO \leftrightarrow (NO)_2$, in model carbon slit nanopores by focusing on the effects of confinement in disordered nanoporous carbons obtained from sucrose. The NO dimerization reaction is interesting for a number of reasons. The reaction is an exothermic, thermodynamically driven reaction in which there is a decrease in the total number of moles. The reaction is important in atmospheric chemistry as well as in the human body where it regulates blood pressure. Moreover, predicting the effects of confinement on NO dimerization is critical to pollution abatement, since activated carbons are commonly used for the removal of nitrogen oxides from auto exhaust and industrial effluent gas streams. In summary, the investigation of NO dimerization conversion as a function of

temperature, pressure and adsorbent structure is important for the understanding of the underlying phenomena involved in these processes and for determining optimal process parameters.

(Kaneko et al., 1989) were the first to experimentally study confined reaction equilibria. They used magnetic susceptibility measurements and observed a large increase in conversion for the NO dimerization reaction in activated carbons with pores of slit widths from 0.8 to 0.9nm with respect to the vapour phase. In the vapour phase at lower pressures, the system is almost completely monomeric (Guggenheim, 1966). The magnetic susceptibility results suggest that more than 98 mol% of the adsorbed NO molecules at 298K form the dimmers [5]. More recent measurements of the NO dimerization reaction in single-wall carbon nanotubes of a diameter of 1.36 nm by transmission infrared spectroscopy confirmed Kaneko's findings. The transmission infrared spectroscopy results indicate that the maximum amount of adsorbed NO monomer is less than 5mol% in the range of 103–136K.

Laboratory challenges have necessitated the development of thermodynamic and molecular simulation predictive capabilities to complement the experiments. Thermodynamic approaches predict reaction equilibria by minimizing the Gibbs free energy and by requiring that the total number of atoms of each element constituting the chemically reacting species is conserved (Smith and Missen, 1991). Such thermodynamic approaches require accurate equations of state for the reactive mixture.

Carbons such as sucrose coke are disordered nanoporous materials with heterogeneous pore structures. Activated carbons have found a huge variety of applications for gas and liquid stream separation. Due to their disordered nature, the detailed microstructure cannot be deduced from experimental techniques such as X-ray diffraction or high-resolution transmission electron microscopy. Therefore, reconstruction methods such as reverse MC, in which a 3D atomistic model is constructed that is consistent with a set of experimental data, have became widely used (Jain et.al., 2005; Jain et.al., 2006[a]). The three models of the sucrose-based carbons investigated were constructed using a Hybrid Reverse MC (HRMC) procedure, in which the algorithm attempts to simultaneously minimize the error in the carbon–carbon pair correlation function and the configurational energy of the system. The carbon models differ by the temperatures and the atmosphere used in preparation of the corresponding real material (Jain et.al., 2006[b]).

Previous studies on the confined reactive NO system (Lisal et.al., 2006, for instance) were limited to the ordered nanoporous carbon models. Thus, the main goal of this work is to study the effects of the disorder on the NO dimerization reaction equilibrium and compare the

results in the disordered carbons with those in the ordered carbons. In addition, we aim to test conventional thermodynamic models for prediction of confined reaction equilibria.

In this work, we used the RxMC (Reactive Monte Carlo) method to simulate the reaction equilibrium of the dimerization reaction in a model of disordered nanoporous carbon in equilibrium with a vapour reservoir. We also utilized the RxMC method to determine the vapour pressure of the bulk $2NO \leftrightarrow (NO)_2$ system. In addition, we determined the adsorption isotherms for pure NO and $(NO)_2$ using either the Gibbs Ensemble MC (GEMC) (McGrother and Gubbins, 1999) or Grand Canonical MC (GCMC) (Frenkel and Smith, 2002) simulations. The RxMC simulation of a vapour-confined phase system at fixed system temperature T and fixed bulk pressure P establishes the following phase and reaction equilibria conditions:

$$\begin{aligned} \mu_{NO}^{V} &= \mu_{NO}^{S} \\ \mu_{NO2}^{V} &= \mu_{(NO)2}^{S} \\ \mu_{(NO)2} - 2\mu_{NO} &= 0 \end{aligned} \qquad [25.5]$$

where μ_i is the chemical potential of component i, and the superscripts V and S denote the vapour and confined phases, respectively. Note that the last term of [25.5] can be written in either phase. In the RxMC simulation, the bulk and confined phases were represented by cubic simulation boxes in which the minimum image convention, periodic boundary conditions and a cut-off equal to half the box size were applied. The RxMC method consisted of a combination of four types of MC steps: (i) particle displacements/ reorientations in the bulk and confined phases, (ii) volume changes for the bulk phase, (iii) inter-phase NO particle transfers, and (iv) forward and reverse reactions moves in the bulk and confined phases. It should be mentioned that only one species (NO or $(NO)_2$) needs to be transferred between the phases since the reaction moves were carried out in the both phases. We chose NO since its transfer is easier than $(NO)_2$ transfer due to the particle size. The particular MC steps were accepted with appropriate transition probabilities, which have been described in details in previous papers, such as (Turner et.al., 2008), where a large critical review of the method is available.

At low P, where the vapour reservoir can be treated as an ideal-gas mixture, the simulation of the bulk phase can be avoided. It results in substantial reduction of computer time. The volume changes and the inter-phase transfers were then replaced by the GCMC insertion/deletion of NO particles governed by the ideal-gas chemical potentials of the vapour reservoir. The vapour pressure of the bulk $2NO \leftrightarrow (NO)_2$ system was also determined using the RxMC method by performing RxMC simulations for the vapour–liquid system at fixed T. The

simulation strategy was analogous to the RxMC strategy for the vapour-confined phase system, but the pressure cannot be specified in advance. Rather, the equality of pressure in the vapour and liquid phases was achieved by correlated volume changes as in the GEMC simulation of pure substances (Turner et.al., 2008).

Finally, pure fluid adsorption isotherms were predicted by the GEMC simulation for the vapour-confined phase system at fixed (T, P) (McGrother et.al., 1999). The GEMC simulation performed a combination of three types of MC steps: (i) particle displacements/reorientations in the vapour and confined phases, (ii) volume changes for the bulk phase, and (iii) inter-phase particle transfers. Again, at low P to reduce computer time the simulation of the vapour phase was replaced by the GCMC insertion/deletion of particles governed by the ideal-gas chemical potential of the vapour reservoir (Frenkel and Smit, 2002). Pure fluid adsorption isotherms were also used, as a further step, for the macroscopic, thermodynamic modelling of mixture adsorption. For that purpose, some of the most common, reliable and robust models describing multicomponent adsorption have been used.

The RxMC simulations of the vapour-confined phase system were initiated by randomly placing NO molecules into the simulation boxes. The initial number of NO molecules was chosen such that a statistically reasonable number of molecules (~500) were present in the vapour phase once the system had equilibrated. The long-range corrections for the configurational energy and pressure were included in the case of the vapour phase, assuming that the radial distribution function is unity beyond the cut-off radius (Allen and Tindesley, 1987). The long-range correction for the configurational energy was ignored in the case of the confined phase because of the anisotropic structure of the solid.

The RxMC simulations were organized in cycles as follows. Each cycle consisted of four steps: n_D particle displacements/reorientations moves, n_V volume moves, n_ξ reaction moves and n_T inter-phase NO transfers. The four types of moves were selected at random with fixed probabilities, chosen such that the ratio $n_D : n_V : n_\xi : n_T$ in each cycle was $\overline{N} : 1 : \overline{N} : \overline{N}$ where $\overline{N}$ was about 10–20% greater than the equilibrium number of molecules during a simulation run. The acceptance ratios for displacement/reorientation moves, and for volume changes, were adjusted to be approximately 30%. After an equilibration period of ~5×10^4 cycles, we generated $(1-2)\cdot10^5$ cycles to accumulate averages of the desired quantities. The GEMC and GCMC simulations were performed in an analogous way as the RxMC simulations. The precision of the simulated data was calculated using block averages, with 5000 cycles per block. In addition to ensemble averages of the quantities of direct interest, we also carefully

monitored the convergence profiles of the thermodynamic quantities as the system traversed phase space (Nezbeda and Kolafa, 1995).

To be able to compare the results in the disordered carbons with the previous results in the ordered carbons (Turner et.al., 2001; Lisal et.al., 2006) we keep to employ the model proposed by (Kohler et al., 1987) to describe fluid–fluid interactions in the mixture of NO and $(NO)_2$. The model treats NO as a single Lennard–Jones (LJ) sphere and $(NO)_2$ as a two-site LJ molecule, with bond length l equal to the experimental value of 0.2237 nm. For the monomer, the model uses the LJ energy parameter ε/k_B = 125.0K and the LJ size parameter σ = 0.31715 nm. The individual LJ parameters for each site in the dimer are the same as those for the monomer. Due to the weak dipole and quadrupole moments of the molecules, the model neglects electrostatic forces. Although Kohler's models treat NO and $(NO)_2$ in a simple way and more realistic models can be considered, Kohler's models reproduce quite well thermodynamic properties of the NO/$(NO)_2$ mixture in the gas phase (see below) as well as in the liquid phase.

The models for disordered carbons used in this work were previously developed (Jain et.al., 2006), thus we only provide a brief description of the models. We studied three types of sucrose-based carbons denoted by cs400, cs1000 and cs1000a. The cs400 sample (density ~1 g/cm3) was prepared by pyrolyzing pure sucrose ($C_{12}H_{22}O_{11}$) up to 400◦C. The cs400 sample was then heated at 1000 ◦C under nitrogen flow with a heating rate of 4 C°/min to obtain the cs1000 sample (density ~1.5 g/cm3). The cs1000a sample (density ~0.7 g/cm3) was obtained by heating the cs1000 sample in an atmosphere of CO_2 for 20 h (Pikunic et.al., 2003).

The atomistic models for these samples were built using the HRMC method in a box size of 2.5 nm. In the first route, the atomistic models were constructed by considering only carbon atoms. For all carbon structures, the number of carbon atoms corresponded to the experimental density, as measured by mercury porosimetry. In the second route, the atomistic models were constructed by considering the carbon and hydrogen atoms. The number of carbon and hydrogen atoms present was obtained from the density and composition data. The H/C ratio was 0.53 for cs400, 0.15 for cs1000 and 0.091 for cs1000a. The presence of all other hetero atoms, such as oxygen, was neglected since the composition data obtained from experiments revealed that the actual materials have very small amount of the hetero atoms. For example the oxygen content in cs1000a sample is 0.0087 O/C molar ratio. Both routes fit the experimental carbon–carbon pair correlation function, the only experimental available structural information, quite well but the local chemistry is different for the models obtained from the first route and the second route as observed from the neighbour distribution, bond

angle distributions, and ring statistics. The first route leads to simplified representations of the sucrose-based carbons (model S) while the second route results in more realistic representations of the sucrose-based carbons (model R).

The HRMC method simultaneously minimized the error in the carbon–carbon pair correlation function (which is an average quantity) and the configurational energy of the system. The configurational energy of the system was calculated using the reactive empirical bond-order potential (Brenner, 1990) developed for hydrocarbons. The HRMC method further used the simulated annealing minimization algorithm to avoid some local minima, although this technique cannot guarantee location of the global minimum.

The pore size distributions of the models S and models R are shown in Fig. 1. The models R for cs400 and cs1000 have smaller pores as compared to the models S, since the amount of hydrogen present in those samples is significant. However, cs1000a sample contains very small amount of hydrogen; thus, the pores and the pore size distribution are almost the same in the case of the model S and model R. Also, the overall porosity of the models S is larger as compared to the models R for the cs400 and cs1000 samples. In the case of cs1000a sample, the model S has only slightly higher porosity as compared to the model R.

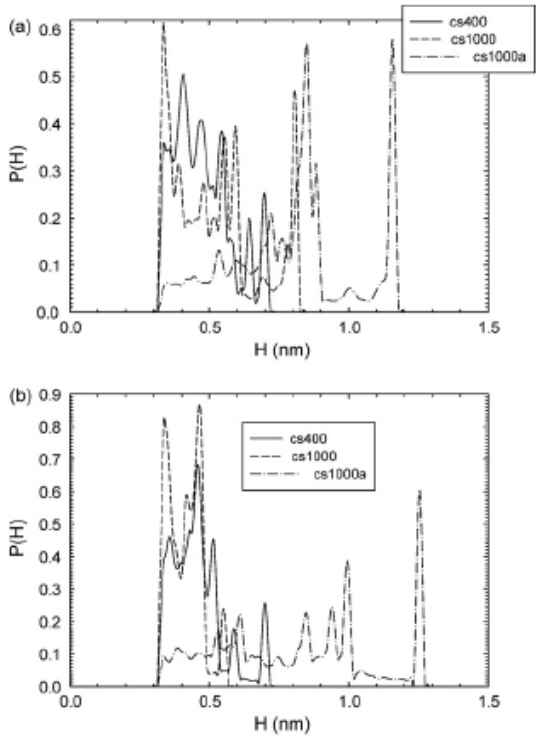

Figure 5.23: Pore size distribution of the three disordered carbon structures: (a) model S and (b) model R.

We represented carbon and hydrogen as LJ spheres with carbon potential parameters ε_{CC}/k_B =28K and σ_{CC} = 0.336 nm, and hydrogen potential parameters ε_{HH}/k_B = 15.08 K and σ_{HH} = 0.242 nm [19].

We then modelled the solid–fluid interactions by a LJ potential with the potential parameters for unlike interactions obtained from the Lorentz–Berthelot mixing rules (Allen, Tildesley, 1987). To examine the carbon structures in more detail in relation to the adsorbates, a common way is to evaluate the free volume of the pores V_i^{free} with respect to the adsorbates. We computed values of V_{NO}^{free} and $V_{(NO2)}^{free}$ for particular carbon structures by means of the Connolly surface algorithm (Connolly, 1983). The radii of probes used in the Connolly algorithm corresponded to spheres of volumes equal to the volumes of NO and $(NO)_2$, as evaluated using the LJ σ and l parameters. The resulting values of are listed in Table 5.12. Differences between V_{NO}^{free} and $V_{(NO2)}^{free}$ are quite small due to the limited difference in the occupancy volume of NO and $(NO)_2$. Examining the free volume differences between the models S and R it can be noticed how the presence of H atoms and consequent re-arrangement in pore shapes affect the free volume availability.

	cs400		cs1000		cs1000a	
	Model S	Model R	Model S	Model R	Model S	Model R
V_{NO}^{free} [nm^3]	5.2	2.9	3.6	2.3	9.4	9.2
$V_{(NO2)}^{free}$ [nm^3]	4.8	2.5	3.3	2.0	9.2	9.0

Table 5.12: Free volumes of the pores, V_{NO}^{free} and $V_{(NO2)}^{free}$, for particular disordered carbon structures as evaluated by means of the Connolly surface algorithm.

Finally, in the next few lines we also give a brief, non-exhaustive description of the thermodynamic models used for data interpolation.

- The Langmuir–Freundlich (LF) model (Freundlich, 1922) is a modification of the most widely used and cited Langmuir model; for a pure adsorbate it is written as:

$$\Theta = \frac{n^0}{n^{0,\infty}} = \frac{bp^a}{1+bp^a} \qquad [26.5]$$

where Θ is the fractional coverage, n^0 is the loading (the number of moles of adsorbate per mass of adsorbent), $n^{0,\infty}$ is the maximum loading, and a and b are LF coefficients. Values of $n^{0,\infty}$, a and b were obtained by fitting the pure fluid adsorption isotherms.

Note that for a = 1, the LF model reduces to the Langmuir model. Extension of LF model to mixture adsorption was proposed by (Sips, 1948), and is given by:

$$\Theta = \frac{n_i^0}{n_i^{0,\infty}} = \frac{b_i P_i^{a_i}}{1 + \sum_{i=1}^{s} b_i P_i^{a_i}} \qquad [27.5]$$

where n_i is the loading of species i, $n_i^{0,\infty}$ is the maximum loading for pure species i, $P_i = y_i P$ is the partial pressure of species i, y_i is its mole fraction in the vapor reservoir, a_i and b_i are LF coefficients for pure species i, and s is the total number of species.

- The Multisite Langmuir (MSL) model (Nitta, 1984) is an extension of the Langmuir model; for a pure adsorbate it is written as:

$$P = \frac{\Theta}{b(1-\Theta)^a} \qquad [28.5]$$

where a and b are MSL coefficients. Similarly as in the case of the LF model, values of $n^{0,\infty}$, a and b were determined by fitting the pure fluid adsorption isotherms; for a = 1, the MSL model reduces to the Langmuir model. It should be mentioned that Eq. (6) is only valid if the adsorbate–adsorbate interactions are neglected. The MSL adsorption model for mixture adsorption is then given by:

$$P = \frac{\Theta_i}{b\left(1 - \sum_{i=1}^{s} \Theta_i\right)^{a_i}} \qquad [29.5]$$

A key requirement for this model is that the quantity $a_i n_i^{0,\infty}$ must be equal for all adsorbates to satisfy the space balance (surface area or pore volume) within the adsorbent. The condition $a_i n_i^{0,\infty} = const$ also makes the MSL model, in contrast to the LF model, thermodynamically consistent.

- We further employed the vacancy solution model combined with the Flory–Huggins activity coefficient equations (FH-VSM) (Cochran et.al., 1985). The FH-VSM for a pure adsorbate can be written as:

$$P = \frac{n^{0,\infty}}{b} \frac{\Theta}{1-\Theta} \exp\left(\frac{\alpha_V^2 \Theta}{1 + \alpha_V \Theta}\right) \qquad [30.5]$$

where α_V and b are the FH-VSM coefficients. The parameter α_V accounts for the adsorbate-vacancy interactions caused by non ideality in the adsorbed phase. Similarly as in the previous cases, values of, $n^{0,\infty}$, b and α_V were obtained by fitting the pure adsorption isotherms and for α_V = 0, the FH-VSM reduces to the Langmuir model.

In the case of mixture adsorption, the equation for the distribution of adsorbate *i* between the ideal vapour reservoir and adsorbent according to the FH-VSM model is given by:

$$P_i = x_i \gamma_i \frac{n}{n^{\infty}} \frac{n_i^{0,\infty}}{b_i} \frac{\exp(\alpha_{vi})}{1+\alpha_{vi}} \exp\left\{ \left(\frac{n_i^{0,\infty} - n^{\infty}}{n} - 1 \right) \ln\left[\left(1 - \frac{n}{n^{\infty}} \right) \gamma_v \right] \right\} \text{(i = 1,..., s)} \qquad [31.5]$$

where x_i is the mole fraction of species *i* in the adsorbent, γ_i and γ_v are the Flory Huggins activity coefficients of species *i* and vacancy, respectively, n is the loading of the mixture, n^{∞} is its maximum loading, and α_{vi} and b_i are FH-VSM coefficients for pure species *i*. Expressions for γ_i and γ_v and other details regarding the FH-VSM can be found elsewhere (Cochran et.al., 1985).

- For completeness, we also tested the performance of the ideal adsorbed solution (IAS) model (Myers and Prausnitz, 1965) for prediction of mixture adsorption. The model is based on solution thermodynamics and the basic thermodynamic equations for the IAS model are the same as those for vapour–liquid equilibria. The equilibrium between the ideal vapour phase and the ideal adsorbed phase can be expressed for each species *i* as:

$$P_i = x_i P_i^*(\pi) \quad (i=1,...,s) \qquad [32.5]$$

where $P_i^*(\pi)$ is the vapour pressure corresponding to the solution temperature and the solution spreading pressure π. Spreading pressure is not a measurable quantity, but at low pressures it can be derived from the isothermal Gibbs adsorption isotherm for a pure adsorbate *i* as:

$$\frac{\pi_i A}{RT} = \int \frac{n_i^0(P)}{P} dP \qquad [33.5]$$

where $n_i^0(P)$ is the pure fluid adsorption isotherm, A is the surface area of adsorbent and R is the universal gas constant. Therefore, calculation of π again requires knowledge of the pure fluid adsorption isotherms. In this work, we employed the LF model for $n_i^0(P)$ in Eq. [33.5]. Prediction of mixture adsorption is then obtained by carrying out the mixing process at constant spreading pressure

$$\pi_1 = \pi_2 = ... = \pi_s \qquad [34.5]$$

While, for *n* and n_i:

$$\frac{1}{n} = \sum_{i=1}^{s} \frac{x_i}{n_i^0\left[P_i^*(\pi)\right]} \qquad [35.5]$$

$$n_i = x_i n \qquad (i = 1, 2, ..., s)$$

It should be emphasized that the purpose of this work is not comprehensive testing and screening of various adsorption models. Rather, we tried to use the most commonly employed models to explain and justify the simulation results. The LF and MSL models are simple surface-layering models while the IAS model and VSM are quite general and, in principle, applicable to both ordered and disordered adsorbants.

The models for mixture adsorption establish the phase equilibria conditions (Eq. 25.5) The reaction equilibrium condition can be solved in either phase. In our case, it is convenient to solve the equation in the vapour phase since the vapour reservoir can be treated as an ideal gas mixture in the T and P ranges investigated. The composition y_{NO} and $y_{(NO)2}$ can then be obtained by simultaneously solving the reaction equilibrium and conservation of mass conditions:

$$N_{NO} = N_{NO}^0 - 2\xi \qquad N_{(NO)2}^0 + \xi$$

$$y_{NO} = \frac{N_{NO}}{N_{NO} + N_{(NO)2}} \quad y_{(NO)2} = 1 - y_{NO} \qquad [36.6]$$

In these equations N_i is the number of molecules of species i, the superscript 0 denotes the initial state and ξ is the extent of reaction. In the case of the ideal-gas, μ_i is given by:

$$\mu_i(T,P) = \mu_i^0(T,P^0) + RT\ln\left(y_i \frac{P}{P_0}\right) \qquad [37.7]$$

where R is the universal gas constant, P^0 is the standard-state pressure and $\mu_i^0(T, P^0)$ is the molar standard chemical potential of species i at T and P^0. Values of $\mu_i^0(T, P^0)$ are typically obtained from thermochemical tables such as the TRC or JANAF tables (Pedley, 1994; Chase, 1998). As a result, we obtain a non-linear equation for ξ, which can be used for the calculation of y_{NO} and $y_{(NO)2}$.

In the vapour reservoir, we performed calculations at three temperatures, (110, 125, 140 K), and pressures P up to the vapour pressure P^*. Values of P_i^* for pure NO and $(NO)_2$ were evaluated using equations of state for LJ and two-site LJ fluids, respectively. The equations of state represent available simulation data within the statistical uncertainties (Lisal et.al., 2004b). Values of P^* for the $2NO \leftrightarrow (NO)_2$ system were determined. by the RxMC simulations. All values of P^*, together with values of the equilibrium constant $K = \exp\left[-\Delta G^0 / RT\right]$ are summarized in Table 5.13. Note that the values of P^* for $(NO)_2$ are about three orders of magnitude smaller than those for NO.

T [K]	P* [bar]			ΔG^0 [kJ/mol]	K
	NO	$(NO)_2$	$2NO \leftrightarrow (NO)_2$		
110	5.39	0.00756	0.676	3.965	$0.13099 \cdot 10^{-1}$
125	13.5	0.0474	3.60	6.032	$0.30164 \cdot 10^{-2}$
140	27.7	0.20	12.6	8.123	$0.93191 \cdot 10^{-3}$

Table 5.13: Vapour pressures *P** of pure NO and (NO)2 and of the dimerization reaction, ideal-gas standard free energy change ΔG^0 and equilibrium constant K as function of temperature T.

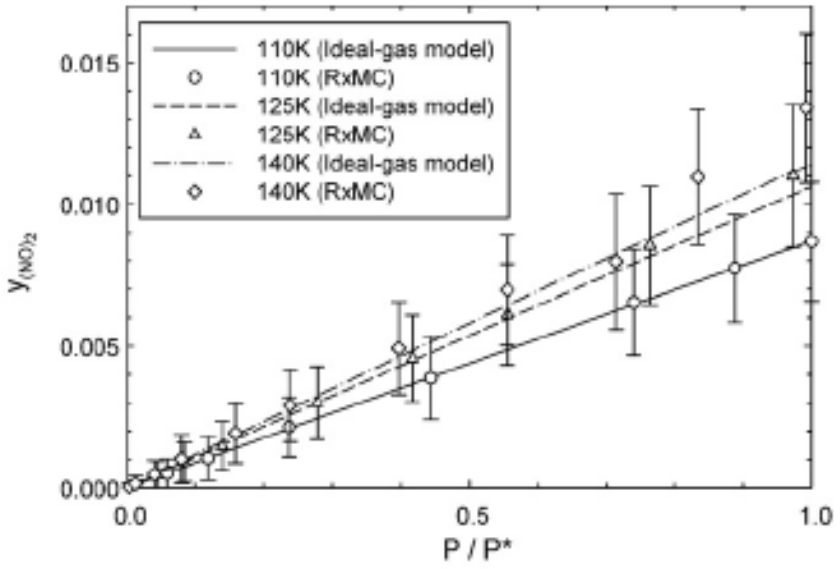

Figure 5.24: Mole fraction of $(NO)_2$, $y_{(NO)2}$, as a function of temperature *T* and pressure *P* obtained from the ideal-gas model (lines) and the RxMC simulations (points); *P** is the vapour pressure of the $2NO \leftrightarrow (NO)_2$ system.

At the T's and P's considered, conversion of NO to $(NO)_2$ in the vapour reservoir is very small and in addition, the vapour reservoir can be treated as an ideal-gas mixture. This is demonstrated in Fig. 5.24 where we show $y_{(NO)2}$ as a function of T and P obtained from the ideal-gas model and the RxMC simulations. We see that the simulation results match the ideal-gas predictions, except for the higher P points (P > 10 bar) at T = 140 K, where the simulation results are 5–10% higher than these for the ideal-gas values. However, even in such cases we can safely neglect non-ideality in the vapour reservoir and assume the fugacity coefficients to be unity within prediction of mixture adsorption by the macroscopic models. Fig. 5.24 further shows that $y_{(NO)2}$ increases with P at fixed T due to Le Chatelier's principle.

The $y_{(NO)2}$ values also increase with T at fixed P/P^* although K decreases with increasing T as a result of P^* increases more than K decreases with increasing T.

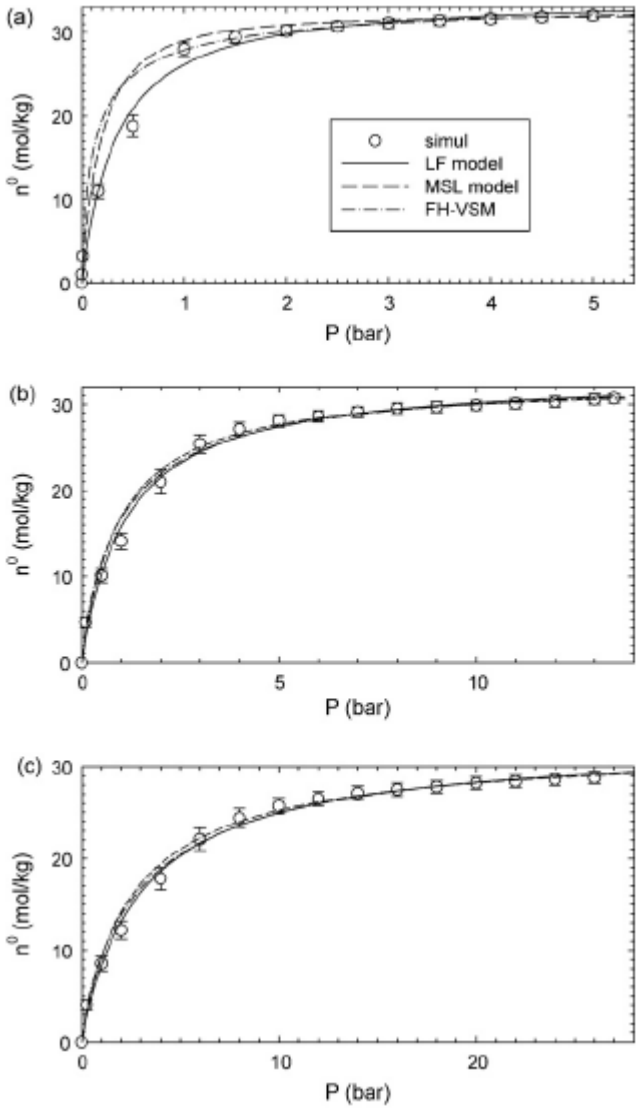

Figure 5.25: Simulated adsorption isotherms of pure NO together with correlations by the Langmuir–Freundlich (LF) and multisite Langmuir (MSL) models, and by the vacancy solution model (FH-VSM) at temperatures (a) 110K, (b) 125K, and (c) 140K in the case of the cs1000a structure (model R); n0 is the loading and P is the bulk pressure.

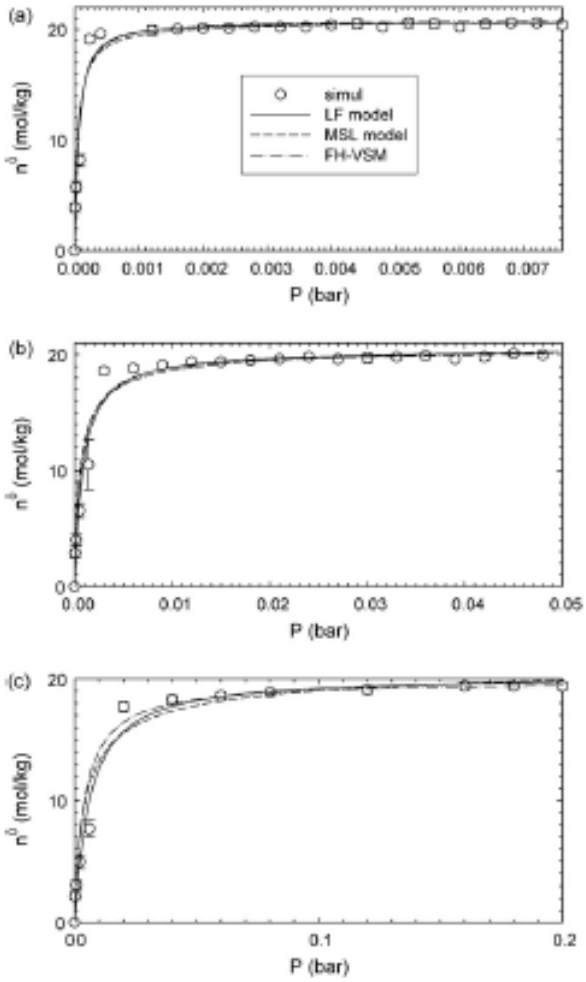

Figure 5.26: Simulated adsorption isotherms of pure $(NO)_2$ together with correlations by the Langmuir–Freundlich (LF) and multisite Langmuir (MSL) models, and by the vacancy solution model (FH-VSM) at temperatures (a) 110K, (b) 125K, and (c) 140K in the case of the cs1000a structure (model R); n_0 is the loading and P is the bulk pressure.

Figures 5.25 and 5.26 show the simulated adsorption isotherms of pure NO and $(NO)_2$ for T={110, 125, 140} K, and P up to P_i*, in the case of the cs1000a structure (model R) as a typical example, together with the correlations by the LF and MSL models, and by the FH-VSM. The pure fluid adsorption isotherms for the other structures exhibited similar behaviour and they are not shown here.

Results of the simulations and correlations for pure adsorption isotherms revealed that: (i) all adsorption isotherms are of type I, (ii) the values of loading n0i decrease with increasing T at fixed P/P_i*, (iii) the ratio of $n_{(NO)2}^{0,\infty}$ to is about 0.6 for all structures, and (iv) the n0i values are lower for the models R in comparison with these for the models S. In addition, the (NO)2

adsorption isotherms show very high values of loading even at low P's as a result of the high affinity between the $(NO)_2$ dimer and the carbon structures. This is caused by the presence of two interaction centres that are able to enhance the binding effect between the (NO)2 dimer and the framework of the structures.

The ratios $n_{(NO)2}^{0,\infty} / n_{NO}^{0,\infty} \sim 0.6$ do not correlate with the ratios $V_{(NO)2}^{free} / V_{NO}^{free}$ (steric effect), that range from0.86 to 0.99; see Table 5.12. The lower $n_{(NO)2}^{0,\infty} / n_{NO}^{0,\infty}$ values with respect to the $V_{(NO)2}^{free} / V_{NO}^{free}$ values indicate significant influence of non-spherical shape of the $(NO)_2$ molecule ($l/\sigma = 0.705$) on the adsorption behaviour. On the other hand, the lowering of the adsorption capacity observed in the models R with respect to the models S correlates well with the V_i^{free} ratios between the models S and models R. This lowering is due to the smaller pores exhibited by the models R.

Before presenting and discussing our results for the adsorption isotherms of the $2NO \leftrightarrow (NO)_2$ system for T = {110, 125, 140} K, and *P* up to *P**, for the cs400, cs1000 and cs1000a structures, we show in Fig. 5.27 an example of the performance of the macroscopic models to predict the reactive adsorption isotherms at T = 125K in the cs1000a structure. We see from Fig. 5.27 that all models are able to predict quantitatively (MSL and IAS models, and FH-VSM) or qualitatively (LF model) the adsorption behaviour of the $2NO \leftrightarrow (NO)_2$ system. Similar conclusions except for the FH-VSM and IAS model can be drawn for the other structures. Although the FH-VSM and IAS model work quite well for the cs1000a structure at all T's considered, their predictions are rather poor for the cs400 and cs1000 structures (not shown here). Therefore in the following, we present predictions of the LF and MSL models for all structures, and predictions of the FH-VSM and IAS model for the cs1000a structure only.

Figures 5.28-5.30 present the simulation adsorption isotherms for the system $2NO \leftrightarrow (NO)_2$, together with predictions by the macroscopic models mentioned above. The most striking feature of the reaction adsorption isotherms is the substantial enhancement of dimerization in all structures in comparison with the vapour phase, where the conversion is less than a few percent. The dimerization enhancement is also captured by the macroscopic adsorption models. Such findings are in qualitative agreement with experimental results of (Kaneko et al., 1989) for the activated carbons, or others, and with the previous simulations results for the carbon slit nanopores (Turner et.al., 2001; Lisal et.al., 2006).

As in the case of the pure fluid adsorption isotherms, Figures 5.27-5.29 further show that the models R exhibit lower adsorption capacity in comparison with the models S. Differences in

the reactive adsorption behaviour between the models S and models R reflect different local chemistry (the neighbour distribution, bond angle distributions, and ring statistics) possessed by these models. Effects of the local chemistry are so significant that even qualitative trends in the reactive adsorption behaviour are not always the same for the models S and models R; see, e.g., Fig. 5.28c where n_{NO} is higher than $n_{(NO)2}$ over the entire P range for the models R, but $n_{(NO)2}$ is higher than n_{NO} for the models S over almost all the P range. The differences in the reactive adsorption behaviour are less pronounced for the cs1000a structure since the cs1000a structure contains small amount of hydrogen. It indicates that explicit consideration of hydrogen atoms in the carbon models is important to properly model the NO dimerization reaction equilibrium in the disordered carbons.

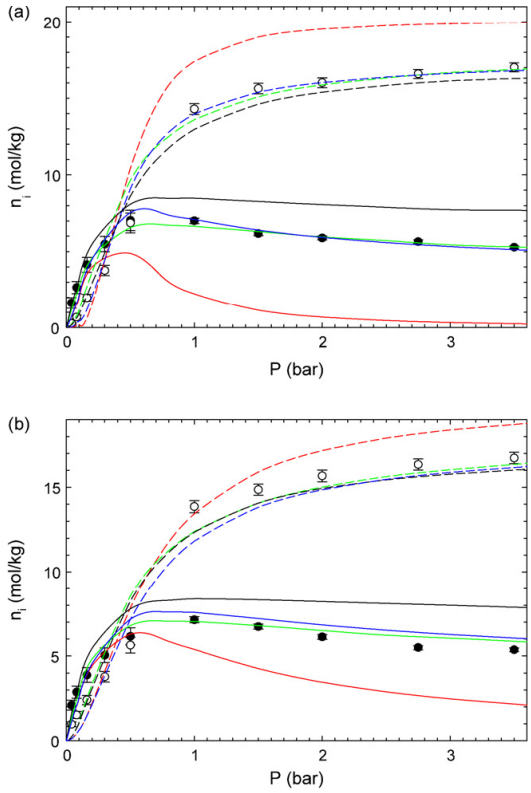

Figure 5.27: Simulated and predicted adsorption isotherms for the $2NO \leftrightarrow (NO)_2$ system at temperature 125K in the case of the cs1000a structure, (a) model S and (b) model R; n_i is the loading of species i and P is the bulk pressure. The filled and open symbols denote NO and $(NO)_2$, respectively. The red, green, black and blue lines represent prediction by the Langmuir–Freundlich and multisite Langmuir models, by the vacancy solution model and by the ideal adsorbed solution model, respectively. The solid and dashed lines correspond to NO and $(NO)_2$, respectively.

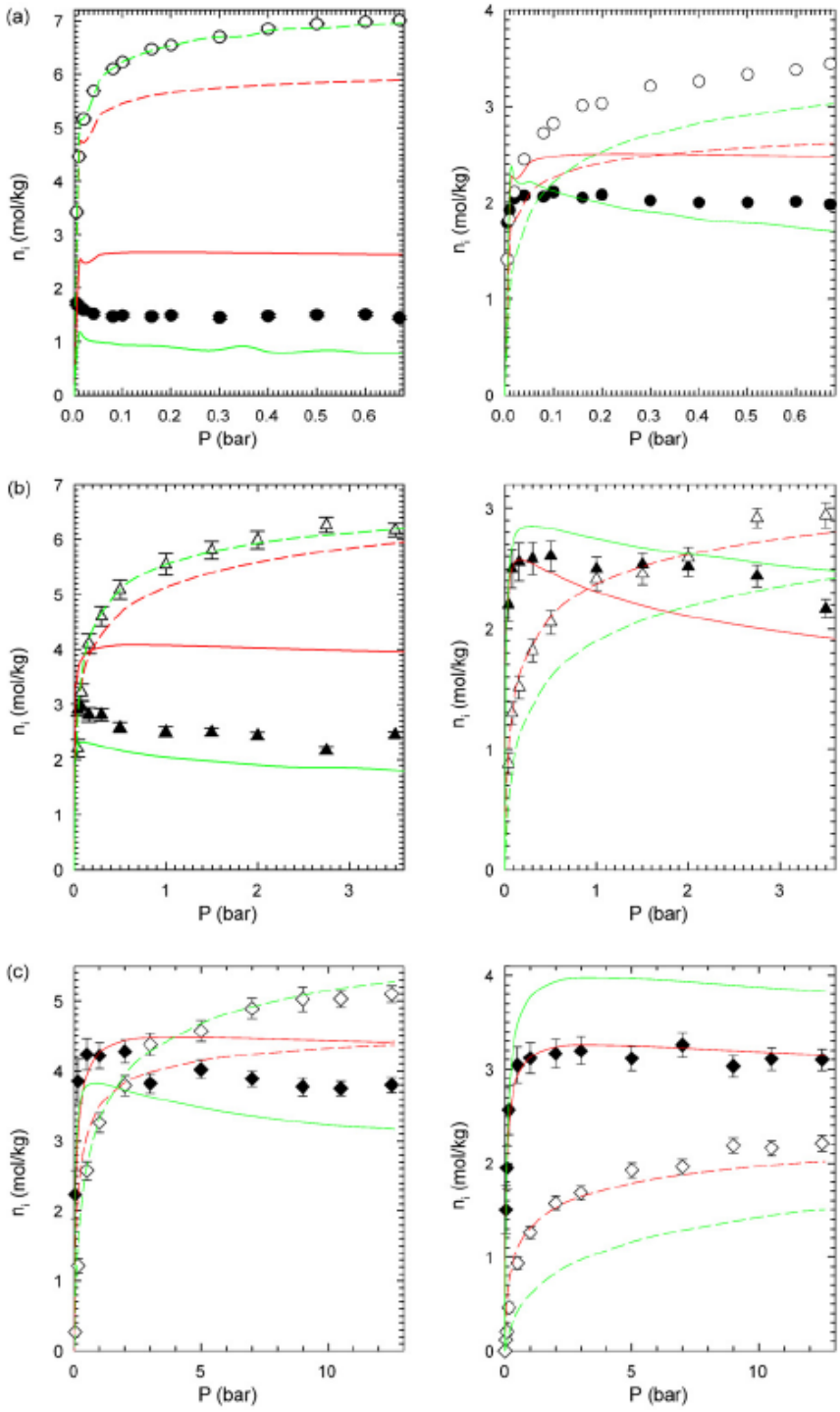

Figure 5.28: Simulated and predicted adsorption isotherms for the $2NO \leftrightarrow (NO)_2$ system at temperatures 110K (circles), 125K (triangles), 140K (diamonds) in the case of the cs400 structure, model S (left column) and model R (right column); n_i is the loading of species *i* and P is the bulk pressure. The filled and open symbols denote NO and $(NO)_2$, respectively. The red and green lines represent predictions by the Langmuir–Freundlich and multisite Langmuir models, respectively. The solid and dashed lines correspond to NO and $(NO)_2$, respectively.

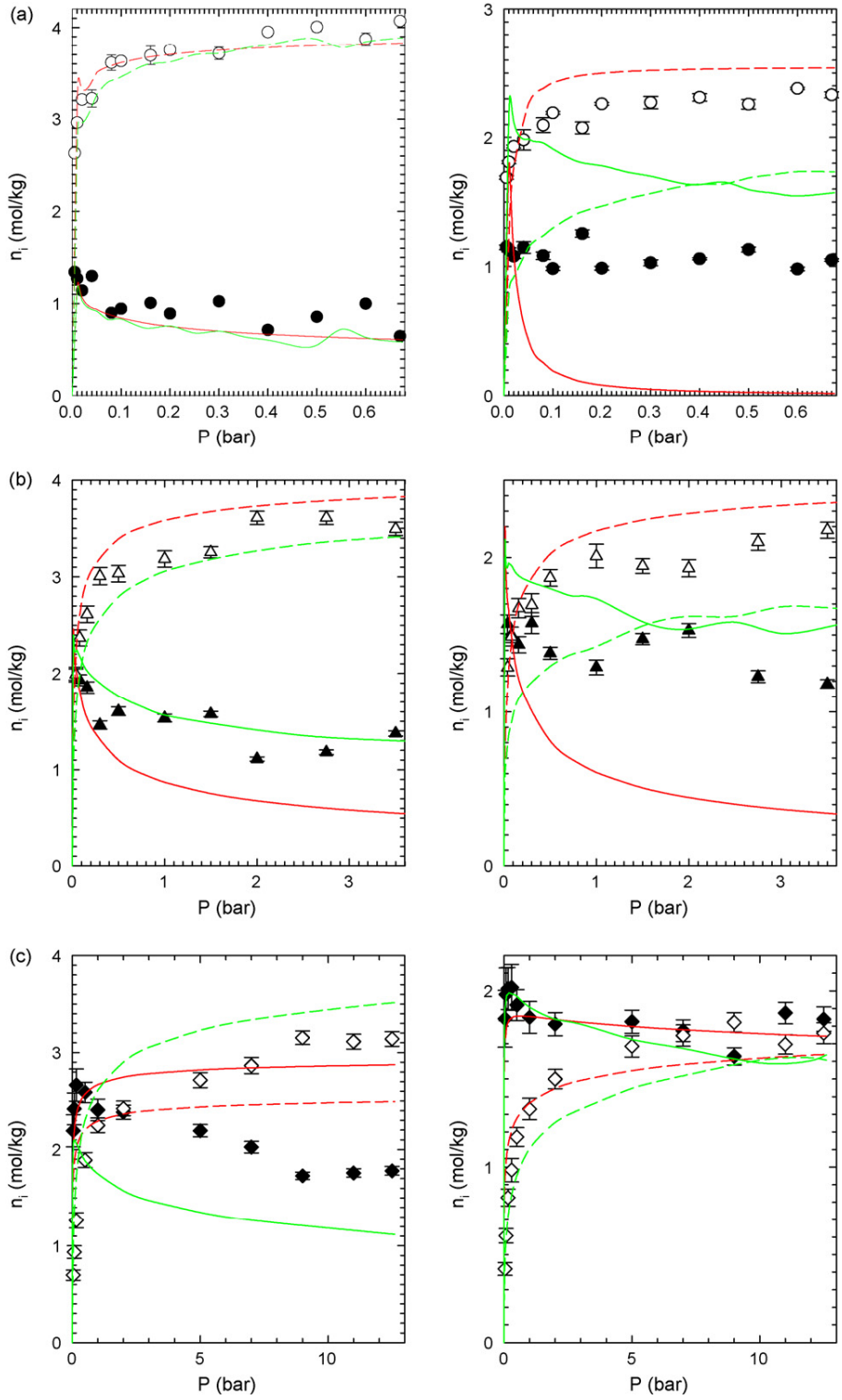

Figure 5.29: Simulated and predicted adsorption isotherms for the $2NO \leftrightarrow (NO)_2$ system at temperatures 110K (circles), 125K (triangles), 140K (diamonds) in the case of cs1000 structure, model S (left column) and model R (right column); n_i is the loading of species *i* and P is the bulk pressure. The filled and open symbols denote NO and $(NO)_2$, respectively. The red and green lines represent predictions by the Langmuir–Freundlich and multisite Langmuir models, respectively. The solid and dashed lines correspond to NO and $(NO)_2$, respectively.

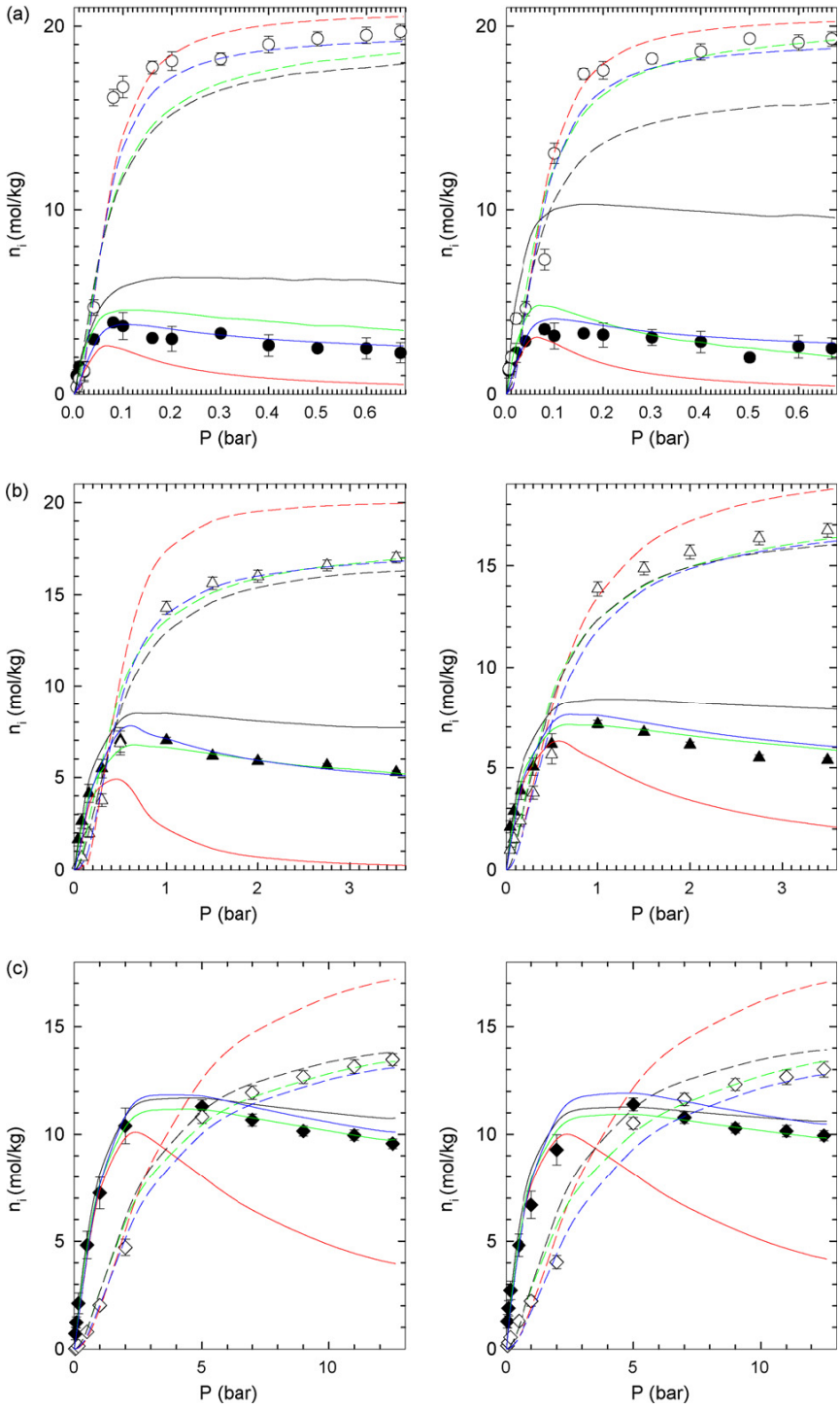

Figure 5.30: Simulated and predicted adsorption isotherms for the $2NO \leftrightarrow (NO)_2$ system at temperatures 110K (circles), 125K (triangles), 140K (diamonds) in the case of cs1000a structure, model S (left column) and model R (right column); n_i is the loading of species i and P is the bulk pressure. The filled and open symbols denote NO and $(NO)_2$, respectively. The red, green, black and blue lines represent prediction by the Langmuir–Freundlich and multisite Langmuir models, by the vacancy solution model and by the ideal adsorbed solution model, respectively. The solid and dashed lines correspond to NO and $(NO)_2$, respectively.

Furthermore, there is competition between monomers and dimers for adsorption sites when P increases. With increasing P, dimers push monomers away from adsorption sites and they simultaneously enhance adsorption in the structures. As a result, the n_{NO} values, after reaching a maximum at very low P, slightly decrease with increasing P; in contrast the $n_{(NO)2}$ values continuously increase with increasing P. In contrast to the pure fluid adsorption isotherms, T has a significant influence on the reaction adsorption behaviour due to the strong dependence of K on T; K decreases with increasing T as can be seen in Table 5.13. An increase in T results in a decrease of dimer conversion, i.e., the n_{NO} values increase with T, while the $n_{(NO)2}$ values decrease with T (as expected in reactions where the total number of moles decreases).

We can conclude that the MSL model is able to quantitatively predict reaction adsorption isotherms for the cs1000a structure and semi-quantitatively those for the cs400 and cs1000 structures. The LF model gives poorer results than the MSL model; nevertheless, the LF model always captures the qualitative trends in n_i versus P. As already mentioned, the FH-VSM works quite well for the cs1000a structures, but it gives very poor predictions for the cs400 and cs1000 structures. By close inspection of the ¸v coefficients of the FH-VSM, which characterize the non-ideality of the $2NO \leftrightarrow (NO)_2$ system in particular structures, we found that behaviour of the $2NO \leftrightarrow (NO)_2$ system in the cs400 and cs1000 structures is far more non-ideal than behaviour of this system in the cs1000a structure. This suggests that the Flory–Huggins activity model cannot capture highly non-ideal behaviour of the $2NO \leftrightarrow (NO)_2$ system in the cs400 and cs1000 structures. Similar conclusion can be drawn for the IAS model, which neglects non ideality in the adsorbed phase. It also explains why prediction of the reactive adsorption behaviour in the cs400 and cs1000 structures by the MSL and LF models worsens with respect to the same prediction in the cs1000a structures.

Previous simulation studies of the $2NO \leftrightarrow (NO)_2$ system were performed for ordered carbons represented by slit models(Turner et.al., 2001; Lisal et.al., 2006). It is therefore interesting to compare reaction conversion between the ordered and disordered carbons. Fig. 5.31 shows dimerization conversion and average fluid density in carbon slits of widths H= 0.8 and 1.0 nm (Lisal et.al., 2006), and in the disordered carbon structures investigated in this work. Fig. 5.31 suggests that based on Le Chatelier's principle the lowering of dimerization conversion in the disordered carbons (except for the cs1000a structure at T = 110 K) with respect to the ordered carbons is caused by lower values of in the disordered carbons with respect to the ordered carbons. The values of ρ (except for the cs1000a structure) do not change significantly with T and decrease of dimerization conversion with T is a result of the strong dependence of K on

T. In the case of the cs1000a structure, temperature dependence of dimerization conversion correlates with temperature dependence of ρ.

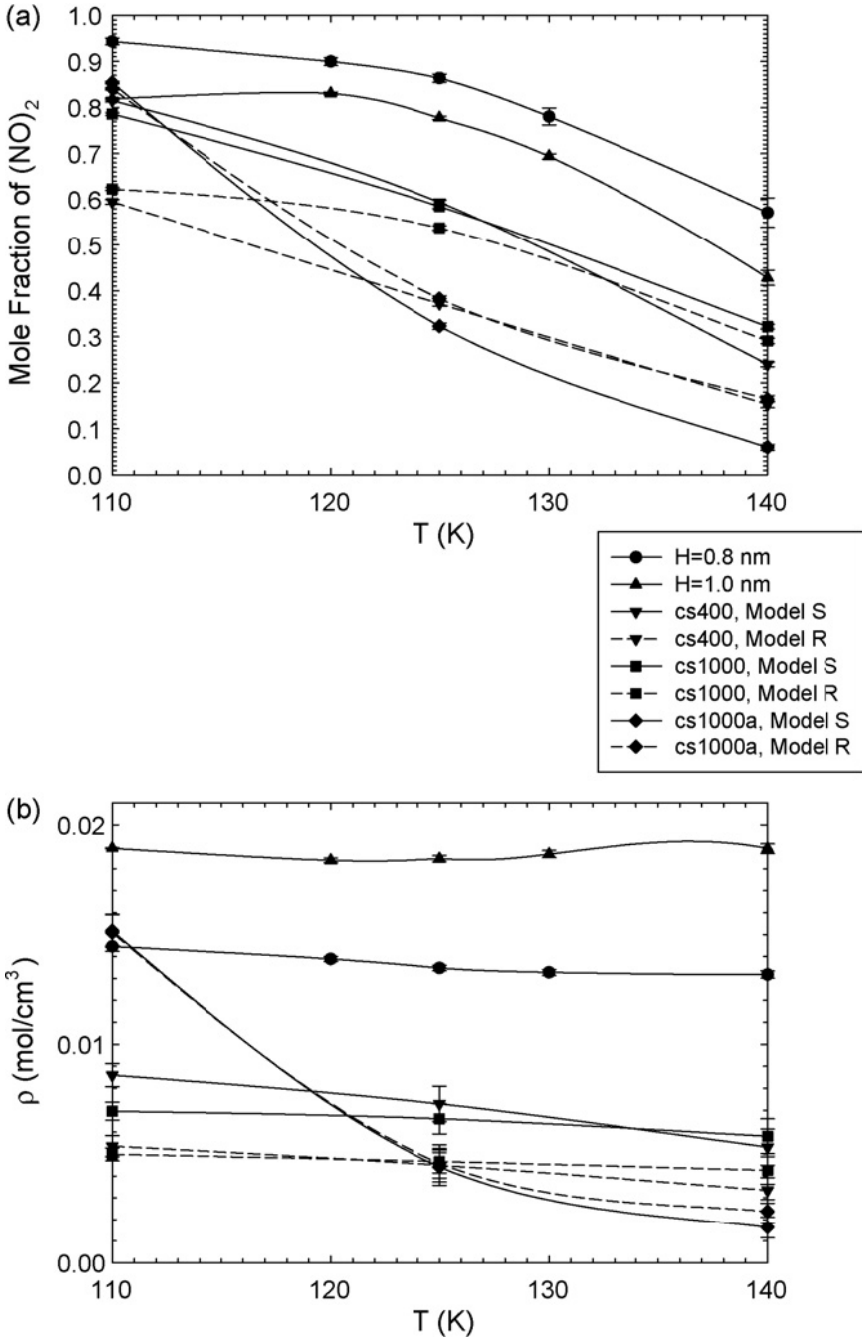

Figure 5.31: (a) Mole fraction of $(NO)_2$ dimers and (b) average fluid density as a function of temperature T in the carbon slit of widths H= 0.8 and 1.0 nm (Lisal et.al., 2006), and in the disordered carbon structures studied in this work at a bulk pressure of 0.16 bar.

Summarising the work done and the results achieved, we studied in details the influence of confinement on chemical reaction equilibrium and adsorption in disordered nanoporous materials by means of RxMC method. Atomistic models of the carbons were constructed

using the Hybrid Reverse Monte Carlo method in conjunction with experimental data. The effects of temperature, bulk pressure, and carbon structures on the reaction adsorption behaviour have been reported, discussed and compared with the corresponding simulations for the ordered porous carbons. This work also provides insights into NO dimerization reaction equilibrium in the vapour phase and adsorption behaviour for pure NO and $(NO)_2$ in the examined structures. A large increase in dimerization conversion in the adsorbed phase was found with respect to dimerization conversion in the vapour phase. However, the increase was lower than this exhibited by ordered carbons due to a lower fluid density in the disordered carbons with respect to the ordered porous carbons. The enhanced dimerization is due to the combined effects of the increased fluid density in the adsorbed phase with respect to the vapour phase and the preferential adsorption of the $(NO)_2$ dimer in the disordered carbon structures. Analogously to bulk phase behaviour, the extent of dimerization decreases with increasing temperature. The impact of the bulk pressure on the reaction conversion is quite dramatic and is accompanied by competition between monomers and dimers for adsorption sites. Finally, simple and robust macroscopic adsorption models such as the multisite Langmuir and Langmuir–Freundlich models were able to predict reasonably well the highly non-ideal reaction adsorption behaviour of the system

5.6 Case study generalization

The abovementioned case studies offer a wide variety of situations for pollution removal by adsorption. It is interesting and promising at the same time the fact that the architecture of the procedures described is quite the same for all the cases. Procedures are implementable and can be improved, as shown by the first, simplified case, to the very complex one, with simultaneous adsorption and reaction of a mixture in a disordered structure. The key, in this sector, is the choice of the proper force-field parameters; once the appropriate force-fields have been selected and validated, or properly modified, the procedure transfer to more complex cases is quite automatic.

The amount of possible applications for gas separation is huge (different conditions, membranes, mixtures), even larger if we imagine that this kind of techniques can be used for instance, with appropriate modifications, for water or wastewater treatment. Just to indicate one new field of interest, many progresses have been made about the mechanisms and potentialities of carbon nanotubes for gas separation, thanks to the use of molecular simulation techniques (Dabrowski, 2001).

Thus, these techniques demonstrated flexibility and adaptability to very different contexts. Moreover, they offer the chance of designing and customizing the process itself, but also the most appropriate membrane structure.

It is interesting that data obtained from this kind of simulations can be used as inputs for process simulations, like Aspen or others, to project the removal process at the real scale: a plan which really represents a full time and length scale integration and a full *in silico* design, from electrons up to the real process. Moreover, the possibility of calculating, for instance, reliable in-silico obtained adsorption isotherms would give the possibility to study macroscopic thermodynamic models and their applications in an easier (and faster) way, as obtaining experimental isotherms for mixtures in small fractions is a tedious and difficult operation. Finally, the introduction and amelioration of new techniques, not used in this thesis, such as Kinetic and Reverse Monte Carlo, will consistently help to study mechanisms of specific cases of diffusion and adsorption into ordered or disordered, *a priori* unknown structures.

All these aspects confirm the advantages and the potentialities of molecular simulation techniques listed in Chapter 2. Further ameliorations may regard the development at a commercial level of mesoscale techniques and software for solid, non-polymeric structures, to reduce the gap between atomistic and real scales further on, and study the dynamics of pollutant adsorption and diffusion for longer times and pathways.

Chapter 6

Pollution modelling and monitoring: soil contamination

Summary

In this chapter, adhesion and diffusion phenomena of pollutants by means of molecular modelling techniques are studied, with particular attention at pesticide behaviour in non-organic soils. This work has ben described in the following publication:
P. Cosoli, M. Fermeglia, M. Ferrone, "Molecular Simulation of Atrazine Adhesion and Diffusion in a Saturated Sand Model", Journal of Soil and Sediment Contamination, under review.

6.1 Soil pollution and molecular simulation techniques

The last part of this work is dedicated to the third major field of interest identified in the thesis: modelling techniques of pollution phenomena into environmental systems. In particular, we examined and afforded the study of interactions between contaminants and soils. Soils and sediments contamination is nowadays a known problem; it regards many kinds of different pollutants which cause soil alteration, limit the exploitation of soil resources (water, agricultural products) and a serious environmental problem of health risk.

If we refer to molecular modelling applications, as shown in Chapter 2, different studies involving interaction between inorganic or organic fractions of soils and various pollutants have been published. These studies mainly involve a heterogeneous series of contaminants and, as matrices, various clays (crystalline, inorganic fraction) or humic substances (organic fraction). Only in few cases different a different matrix, such as silica, is considered, as described in the following paragraph. Nevertheless, sand soils are the most important constituent of aquifers and, therefore, extensive studies are, potentially, of great interest. The case study exposed in the following paragraph will show an *in silico* application in this field. Even though this is the only case study being developed for this section of interest, both the approach and the procedure are highly reproducible, can be adapted or modified for different purposes. More interestingly, they can also be integrated in a multiscale calculation to obtain information at the real scale. This sector of research, definitely offer great opportunities of development, as it may be more clearly seen at the end of this Chapter.

6.2 Sand – water – atrazine modelling

In this paragraph we analyse the specific case study, which consists in the adhesion and diffusion analysis of atrazine in ideal, clean and saturated sand. The sand is also supposed to constitute a superficial layer of sediments.

Pesticides presence has become a serious problem in contaminated soils, especially in agricultural soils, due to their massive application in past decades (van Stralen and Rijn, 1998; van Straalen, 2002), to their toxicity and, in most cases, their persistency (Alikhanidi and Takahashi, 2004). One between the most diffused, extensively employed pesticides is atrazine (1-chloro-3-ethylamino-5-isopropylamino-2,4,6-triazine). This common pesticide was recently banned in some European countries, due to its proved persistency (Cox, 1961) and toxicity (EPA, 2006), but it is still one of the most employed pesticides in the world.

Although some atrazine-water-soil interactions are well known, such as solubility and binding with colloidal substances (Smalling and Aellion, 2004), up to now little information about diffusion and adhesion phenomena at microscopic level have been provided.

Molecular simulation techniques offer the unique opportunities to model and investigate systems at different conditions, such as temperature, pressure, composition, at a thermodynamic level. In last decades, molecular simulation started to tackle also some problems related to environmental issues, such adsorption or diffusion in porous or layered media (Auerbach, 2000). In recent years, some studies regarding deterministic Molecular Mechanics and Dynamics (MM/MD), Quantum Mechanics (QM), or Monte Carlo (MC) simulations and applications to pollutant adhesion and diffusion on minerals (Shulten, 1994; Teppen *et.al.*, 1997; Shevchenko and Bailey, 1998; Yu *et. al.*, 2003; Lock and Skipper, 2007; Farrell *et. al.*, 2002; J. Luo, J. Farrell, 2003; Greathouse and Cygan, 2006) have also revealed some of the potentialities of these techniques.

Although the huge number of MC, MM/MD publications in this area, only very few studies (Farrell *et. al.*, 2002; J. Luo and J. Farrell, 2003) regard sand (silica) matrices, being the others mainly focused on clay or organic matter. Even experimental studies about atrazine adsorption, binding, diffusion, and generally interaction with mineral soils are scarce or need deeper investigation. Although it is accepted that soil organic matter plays a major role about pesticide adhesion in general (Lin *et. al.*, 2006), numerous factors have been related to atrazine binding, diffusion and adsorption in aquifer sediments. Two important properties are soil mineralogy and particle size distribution (Rae *et. al.*, 1998); it is also well demonstrated how, in some cases and when the presence of organic carbon into soils is limited, mineral surfaces can have an important influence in pesticide adsorption and adhesion (Clausen *et.al.*, 2001). Although clay content seems to play a major role in such cases, this relatively unexplored field needs supplementary investigation, as quartz is one of the most important constituent of aquifers.

In this study, we considered a simplified system of silica α layers, water and atrazine to model a saturated, sand-type soil in presence of atrazine contamination. Simulations have then been performed, using a combination of MC, MM and MD (in different ensembles) to study atrazine behaviour in this simplified soil model. Pressure and temperature has been fixed; we considered as variables:

- different atrazine concentrations;

- different spacing between silica layers, to mimic different particle size distribution at atomistic level.

Then, as functions of spacing and concentration, we analysed self-diffusion coefficients, binding energies and spatial distribution (the last two are measures of atrazine preference to water or solid matrix). Validation of our procedure has been proved against available, experimental data of atrazine diffusion coefficient in water. Diffusion trends as function of interlayer distances, or pollutant concentration, have been compared to macroscopic models developed for similar systems.

Even in this case, calculations were performed on Intel quad-core bi-processors Xeon x5355 with a 6GB RAM. Sorption and Discover modules of Materials Studio® (v. 4.2, Accelrys, San Diego, CA, USA) have been employed in this work. Sorption is a Monte Carlo based modulus, particularly suitable for adsorption phenomena estimation over defined adsorbents; Discover is a MM/MD modulus for all deterministic simulations.

MM and MD basis theories have been described elsewhere (Allen and Tildesley, 1987; Frenkel and Smit, 1986; Leach, 2001), thus in what follows we will only provide a brief explications of the methods, giving more details about specific setting parameters for each kind of simulation.

Stochastic MC methods have been used in the Canonical (NVT, with a fixed loading) ensemble; in this case, temperature, cell volume and number of particles to be inserted is fixed, thus the simulation tries to generate configurations of a system by making random changes to the positions of the present species, together with their orientation and conformations, where appropriate (Leach, 2001).

Classic, MM/MD simulations have been performed by using the Compass FF (Sun, 1988).

Atrazine molecules were constructed and minimised with the same FF. Water molecules were modelled with the standard *TIP3P* model for water (Jorgensen *et. al.*, 1983). MC simulations in the Canonical Ensemble have been performed in order to place molecules in the framework with unique criteria. We used the Configurational Bias method (Siepman and Frenkel, 1992), as it is more suitable for flexible, relatively long molecule placement, such as atrazine. Non bonded terms have been computed with the Ewald and Group method (Karasawa and Goddard III, 1992) and the Atom Based direct method (Allen and Tildesley, 1987) for electrostatic and van der Waals interactions, respectively. Other simulation details are described in Table 6.1. At the end of each simulation, the lowest energy frame ahs been sampled for the subsequent deterministic simulations.

Loading steps	Equilibration steps	Production steps	Van der Waals interactions	Electrostatic interactions
$1 \cdot 10^5$	$1 \cdot 10^6$	$1 \cdot 10^7$	cut off: 10 Å; spline width: 1 Å	cut off 10 Å; accuracy $1 \cdot 10^{-5}$

Table 6.1: Setting parameters for MC Canonical simulations.

In the first part of the work, with the interlayer vacuum kept fixed at 40 Å for MC simulations, we varied the atrazine concentration, always keeping the pressure as constant, thus varying the atrazine / water ratio. Thus, sets of simulations with variable ratios of atrazine / water molecules in the basis cell, corresponding to concentrations of 22.7, 37.27, 51.42, and 71.87 g/kg of soil have been performed. We set these compositions in order to have a sufficient, significant number of atrazine molecules in the cell for our purposes. Although these concentrations seem to be too high to be commonly found in real soils, we were rather interested in the adhesion and diffusion trends. For all simulations, 3D periodic boundary conditions have been imposed.

For each simulation, the low energy frame from the MC simulations was then subjected to a MD, NPT ($P = 1 \cdot 10^6$ Pa, $T = 298$ K) simulation, in order to guarantee a more precise equilibration of the whole system at a constant pressure. During the simulation, all cell parameters were taken fixed, with the exception of the *c* cell parameter, corresponding to the length in the *z* direction (see Figure 6.1). More precisely, in Figure 6.1, atrazine molecular model (a), and a snapshot of an NVT simulation (b) are shown.

(a)

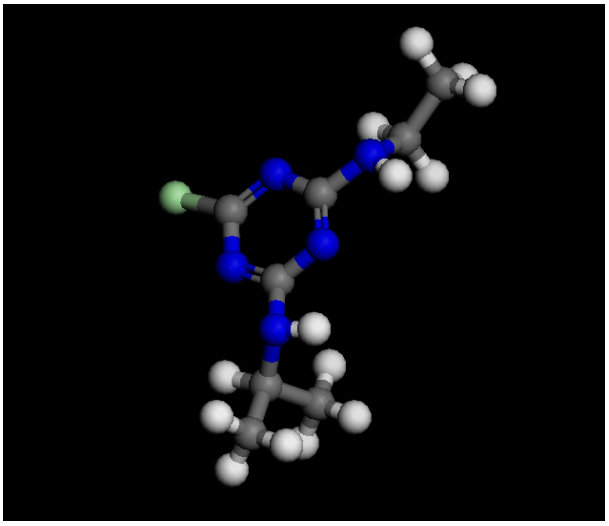

(b)

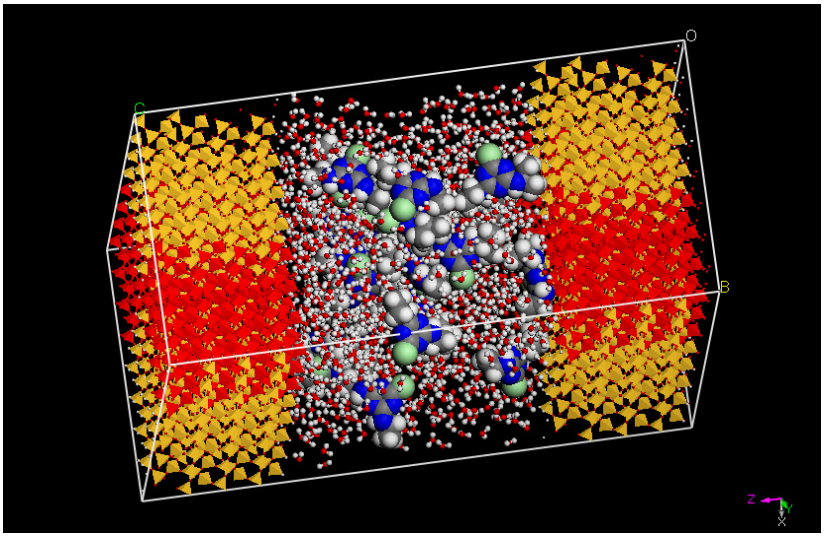

Figure 1: 3D visualisation of atrazine molecule model (a, top) and (b, bottom) snapshot of MD, NVT of silica-water-atrazine system.

As a first step, $1 \cdot 10^5$ ps of NPT dynamics have been performed for equilibration. For barostat and thermostat pressure and temperature control methods we used the Andresen method (Andersen, 1980), particularly suited for simulations involving liquids. Again, electrostatic and van der Waals non-bonded terms have been taken into account with the Ewald and Atom Based methods, respectively. Simulation details of NPT simulations are described in Table 6.2.

Energy deviation	Thermostat	Barostat	Van der Waals interactions	Electrostatic interactions
5000 kcal/mol	T difference: 10K; Q ratio: 1; collision ratio: 1; decay constant: 0.1 ps	Cell mass: 20amu; decay constant: 0.1 ps	cut off: 10 Å; spline width: 1 Å	accuracy $1 \cdot 10^{-5}$

Table 6.2: Simulation parameters for NPT simulations.

The last frame of NPT simulations was then enlarged two times in the *x* and *y* direction. This structure was used for the final MD, NVT simulation, where $5 \cdot 10^5$ ps have been performed, at the same conditions of the previous NPT simulations, but with a fixed volume. Frames of the NVT trajectory have been sampled for analysis; diffusion coefficient, by means of the mean-squared displacement evaluation, concentration profiles, and binding energies have been considered.

Diffusion *D* can be estimated via the mean-square displacement by the use of Einstein - Smoluchowski equation for species *i* (Einstein, 1905), via the use of Mean Square Displacement (MSD); in a 3D periodic system:

$$D_i = \frac{1}{6N_i} \lim_{\Delta t \to \infty} \frac{1}{\Delta t} \left\langle \sum_{l=1}^{N_i} \left(\vec{r}_{l,i}(\Delta t) - \vec{r}_{l,i}(t_0) \right)^2 \right\rangle \qquad [1.6]$$

Where *Ni* is the number of diffusive atoms in the system, $r_{l,i}$ is the position vector of atom *i,* Δt the time step. The expression is valid for long-time simulations.

Binding energy (E_{BIND}) evaluation has been used in molecular simulation to evaluate thermodynamic behaviour and stability of several complexes (Tanaka and Goettler, 2002), as shown in previous chapters; E_{BIND} has been employed in this study to evaluate affinity of each couple of component

Concentration profiles are calculated by averaging the centre of mass position of considered molecules over NVT trajectory frames and plotting their relative concentrations in layers parallel to the specific plans and distanced by 0.5 Å. In this case, we considered a plan parallel to the *z* axe.

In the second session, we kept atrazine concentration as fixed, varying the interlayer distances. Procedure and simulation parameters applied in this part are equivalent at the previous ones. We only changed the number of atrazine and water molecules to be inserted in the MC simulations, in order to maintain a constant density and a constant atrazine concentration, which was fixed at 27 g/kg of soil. Interlayer distances considered were 15, 20, 27 and 40 Å; diffusion coefficient obtained for water-atrazine system only was also taken into account, as if it would mimic a limit situation in which silica layers are at an infinite distance.

Analogously to the first set of simulations, we analysed diffusion coefficients, binding energies and concentration profiles.

Finally, for comparison with available experimental data, a water-atrazine only system was modelled. Analogously to the previous simulations, atrazine and water molecules have been inserted with a MC procedure into an empty cubic cell with an initial side of 40 Å. We performed three simulations with different atrazine / water molecules ratios (e.g. with different atrazine concentrations), to examine possible influences in MSD. Ratios were equals to 0.022, 0.037 and 0.044. After an NPT equilibration, MD (NVT) gave us information about diffusion, binding energy evaluation, and concentration profiles.

Comparison with available data found in literature for atrazine self-diffusion coefficient in water gave us encouraging results. Mean diffusion coefficient obtained by MSD analysis for the atrazine-water system $D_0 = 7.84 \cdot 10^{-6}$ cm^2/s ($R^2 = 0.99$) while literature data range between $6.5 \cdot 10^{-6}$ cm^2/s (J.-H. Park *et. al.*, 2003), and $6.6 \cdot 10^{-6}$ cm^2/s (M. F. Helmke *et. al.*, 2005). No considerable differences or trends have been noticed by examining D_0 values for the three different simulations, as we obtained a standard deviation of $1.14 \cdot 10^{-7}$ cm^2/s. Moreover, as we obtained D_0 in a highly ideal simulation system (no salts, metal traces or different components were added to water), the agreement is quite fair.

Finally, we calculated water – atrazine binding energy obtaining a value of $E_{BIND} = -410$ kcal/mol, thus the complex is thermodynamically favoured.

Once procedure was validated, we performed simulation with variable atrazine concentration. The first step was the MSD analysis. We obtained linear trends for all simulations ($R^2 \geq 0.988$), thus the Einstein's equation was applicable.

Our results show how, in the considered range of concentrations, diffusion coefficient was not constant, as assumed in different models (Künz and Lavallée, 2004) and also in Smoluchowski formulation of Equation 1.6, (Islam, 2004).

In Figure 6.2, D is plotted against atrazine concentration. The trend seems to testify how atrazine displacement during the NVT dynamics is relatively hindered by their increasing concentration. From a microscopic and thermodynamic point of view, this trend is probably due to the fact that atrazine relatively big shapes, and its rigid structure given by the triazine ring, have an influence to the random walk, by limiting their movement. In fact, although system pressure remains the same to guarantee equal density for all simulations, the number of water molecules (which are smaller) in the system decreases in favour of atrazine

molecules for higher atrazine concentrations. It is also interesting to examine binding energies trends, as shown in Figure 6.3.

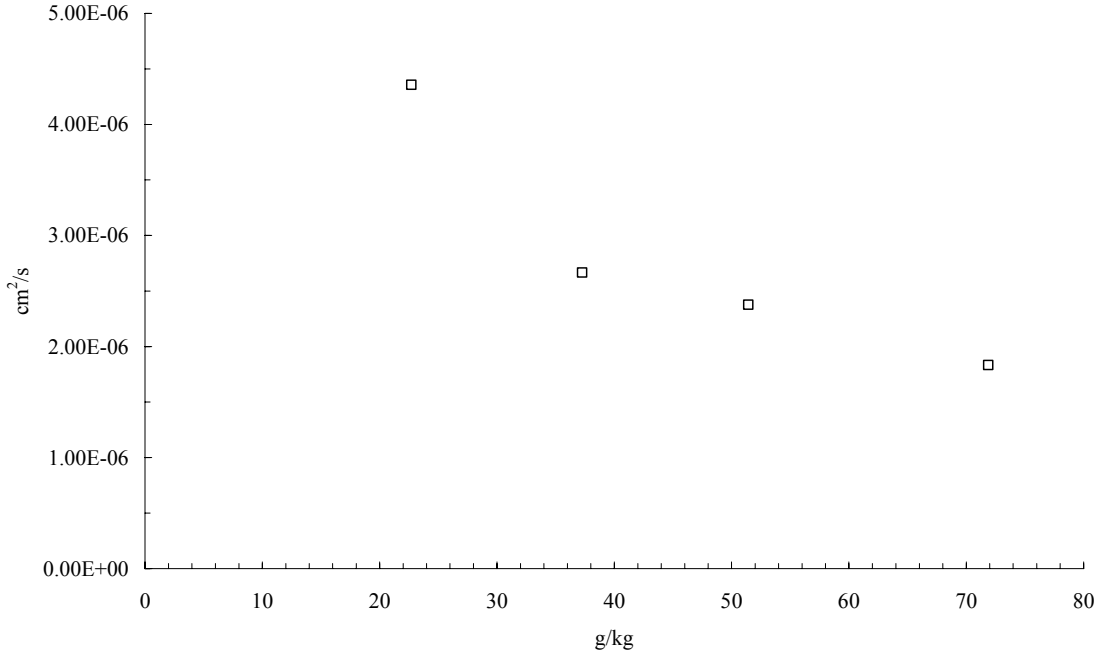

Figure 2: diffusion coefficient D as a function of atrazine concentration.

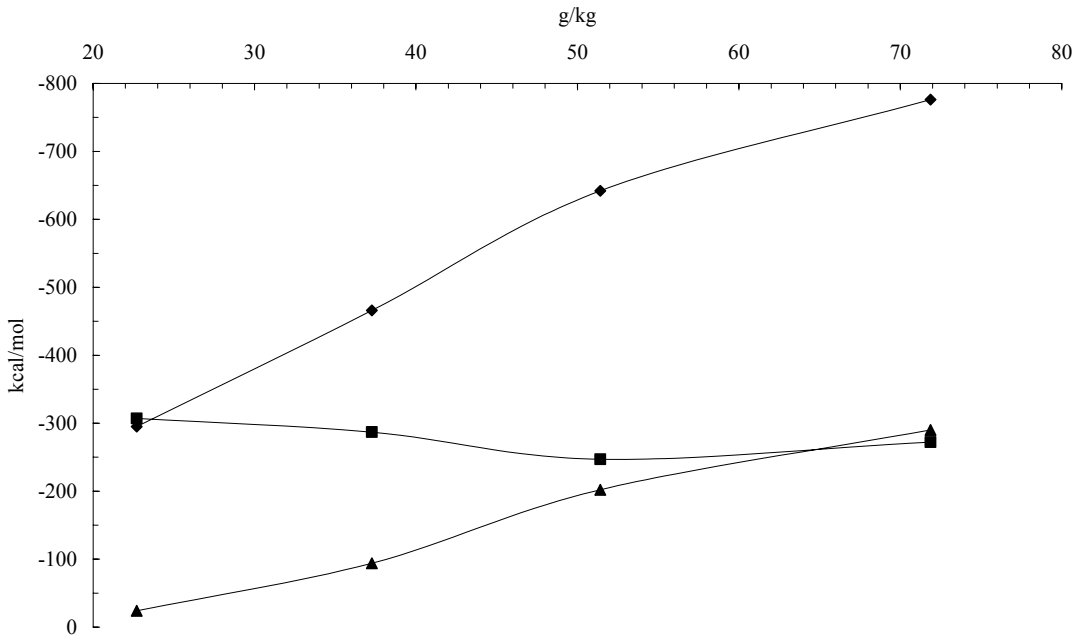

Figure 3: Binding energies as a function of atrazine concentration; ♦: atrazine – water binding energies; ■: water – silica binding energies; ▲: atrazine – silica binding energies. Lines are a guide for the eye.

Even though water and atrazine seem to have a greater affinity, all binding energies are negative, thus favourable. While E_{BIND} for water and silica remains almost constant, E_{BIND} between atrazine and water, and atrazine and silica increases with atrazine concentration.

Thus, higher atrazine – water binding energies confirm that atrazine is relatively soluble in water, even for higher atrazine concentrations, where binding energy is even higher in its absolute value. Moreover, the favourable (negative) and improving binding energies for atrazine and silica suggest also that atrazine tends to adhere to the silica framework, and that the adhesion is moderately enhanced by higher concentrations.

Then, we examined concentration profiles towards the z direction, where water and atrazine molecules can displace in the range 20-60 Å. In Figure 6.4 it can be noticed how, while water molecules are distributed quite uniformly, atrazine molecules have the tendency to aggregate together (as demonstrated by one or two peaks in the distribution) and, except for the case of Figure 6.4a (with an atrazine concentration of 22.7 g/kg), they also mainly lay next to the boundary of the polar silica framework.

(a)

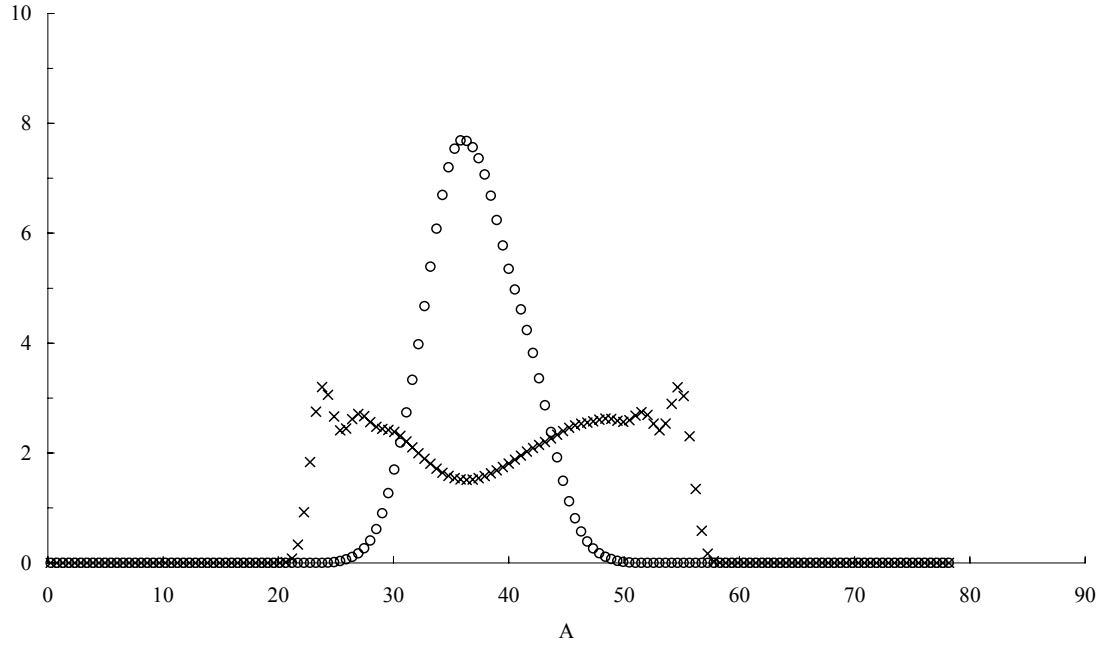
10
8
6
4
2
0
0
10
20
30
40
50
60
70
80
90
A

(b)

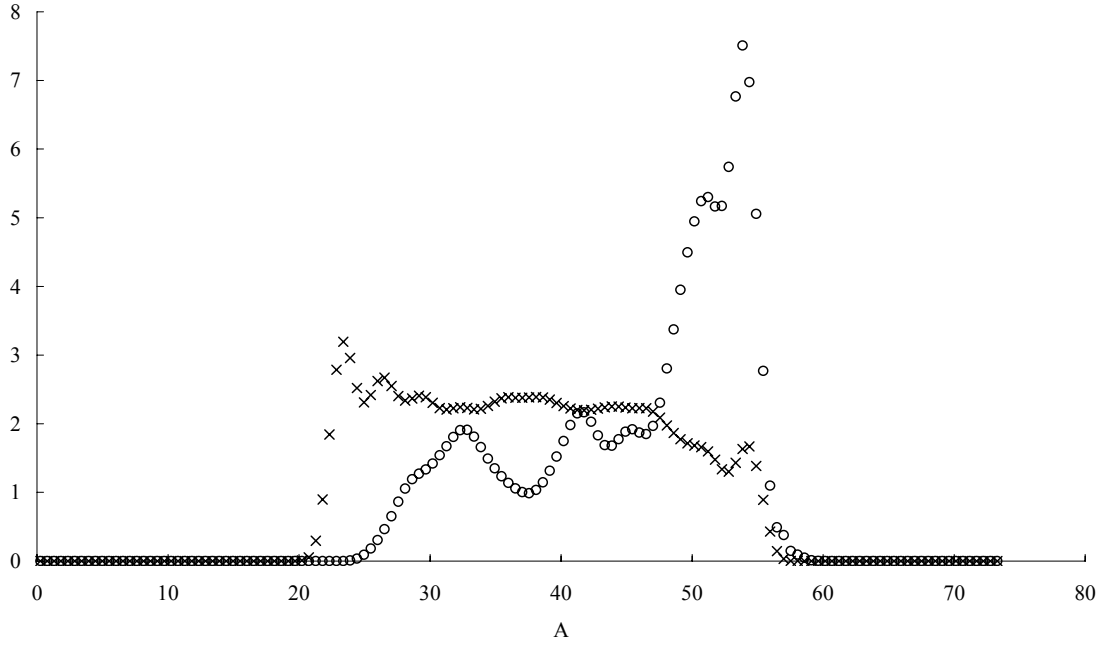
8
7
6
5
4
3
2
1
0
0
10
20
30
40
50
60
70
80
A

(c)

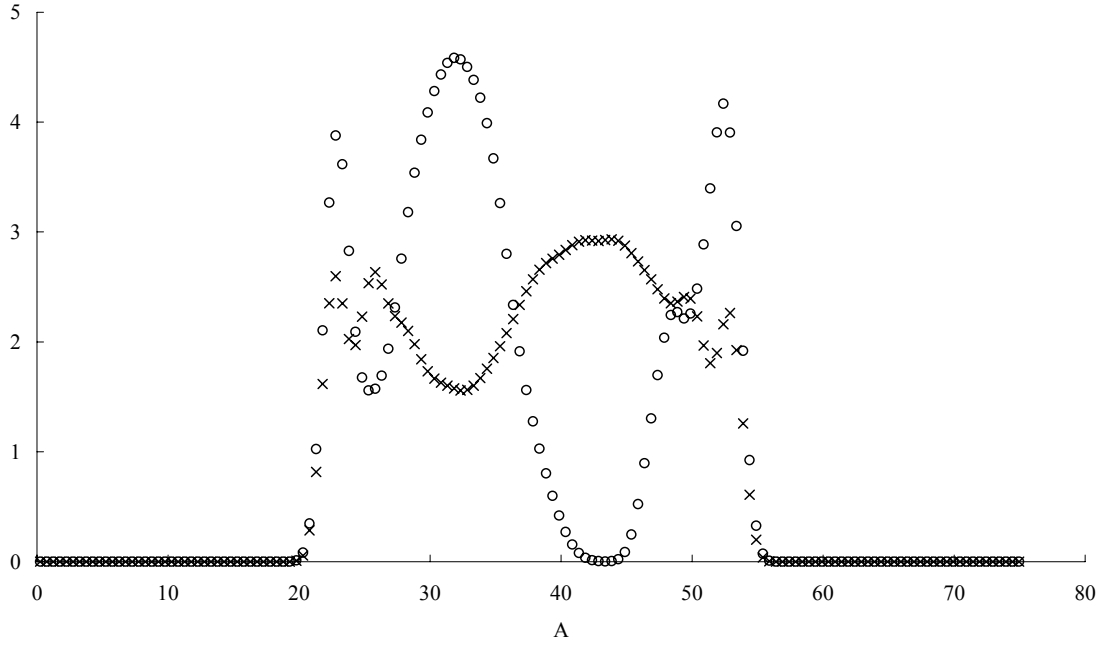

(d)

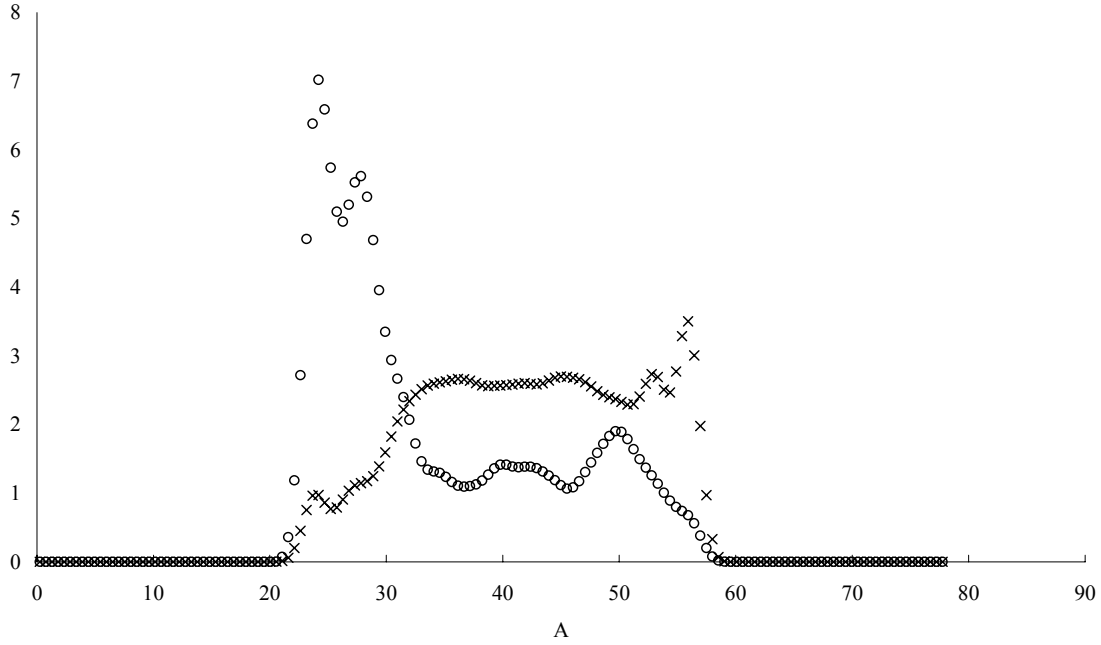

Figure 6.4: Concentration profiles of water (×) and atrazine (○) for atrazine concentration of 22.7 (a), 37.27 (b), 51.42 (c), and 71.87 (d) g/kg of soil.

These behaviours also confirm the moderate atrazine tendency to adhere to the mineral matrix and, on the other hand, to aggregate in group of molecules, preferably (with the exception of Figure 6.4a) next to the silica framework boundaries. Nevertheless, binding energies between water and atrazine remain higher. This decidedly confirms a better compatibility of the water – atrazine complex rather than adhesion to the silica framework, as expected from previous works about atrazine adsorption into quartz (Clausen *et. al.*, 2001).
In the second part of our work, we performed simulations with variable silica interlayer. Once again, we obtained linear trends for all simulations ($R^2 \geq 0.956$). As expected, diffusion coefficient is interlayer dependant, as shown in Figure 6.5.

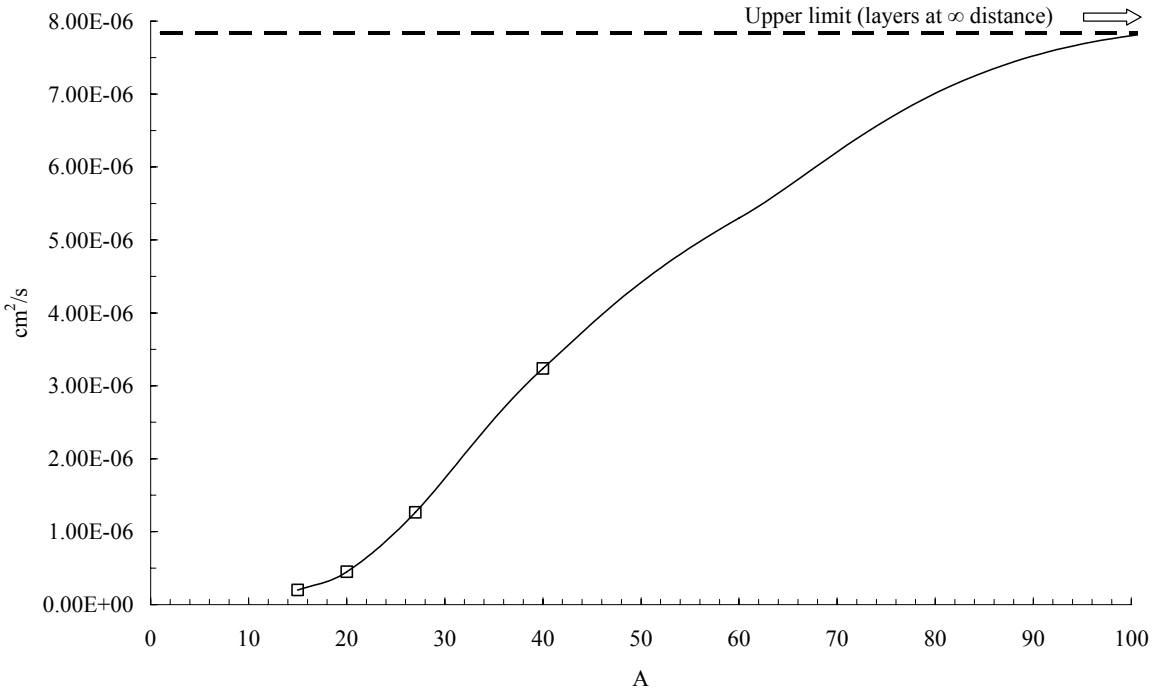

Figure 6.5: diffusion coefficient D as a function of interlayer distance. Lines are a guide for the eye.

Increasing interlayer distances allow rigid and big atrazine molecules to displace more easily throughout the consequently wider pores. The value of D_0 in pure water was taken as the upper diffusion coefficient limit, as if layers were at an infinite distance. Similar trends have been obtained by (Liu *et. al.*, 2004) for transport modelling of water in slit and nanopores, and by (Klochko et. al., 1996) for noble gases diffusion in graphite pores. In some analogous cases (Yu and Zhang, 2007) correlation models have also been proposed. Nevertheless, fitting

of obtained results with existing models for diffusion was out of the scope of the present work.

Binding energies for the complexes water – atrazine – silica framework are shown in Figure 6.6. Concentration profiles for this set of simulations are shown in Figure 6.7. Analogous considerations to the ones given for simulations at variable concentration can be made in this case, by considering both Figure 6.6 and 6.7.

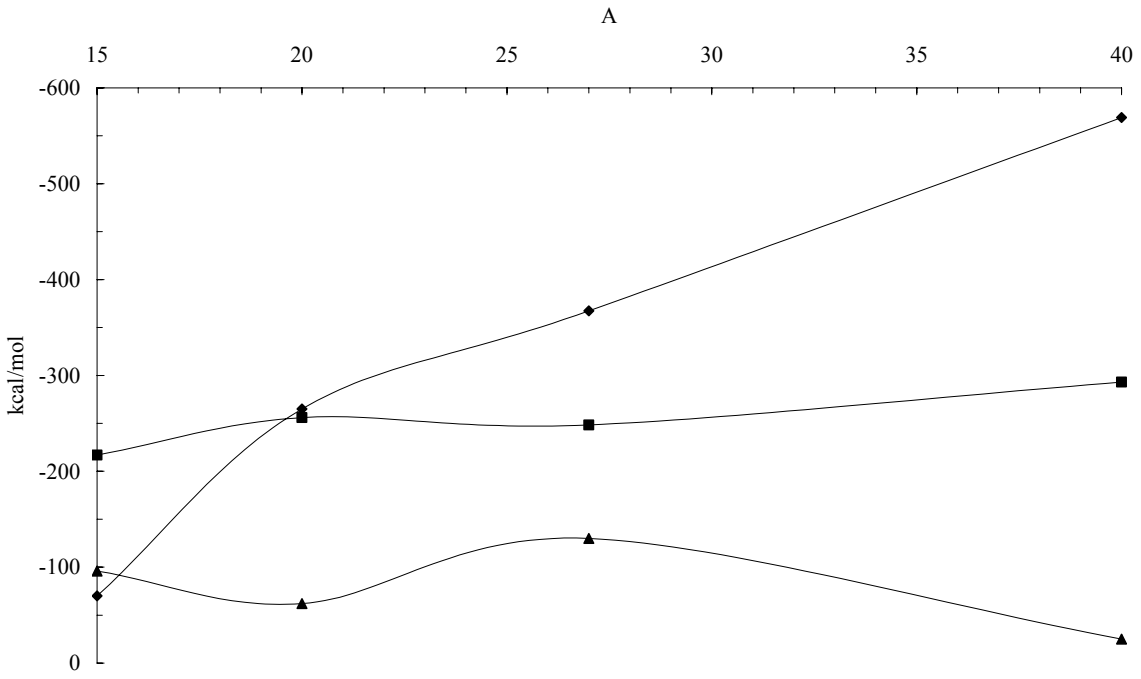

Figure 6.6: Binding energies as a function of interlayer distance; ♦: atrazine – water binding energies; ■: water – silica binding energies; ▲: atrazine – silica binding energies. Lines are a guide for the eye.

(a)

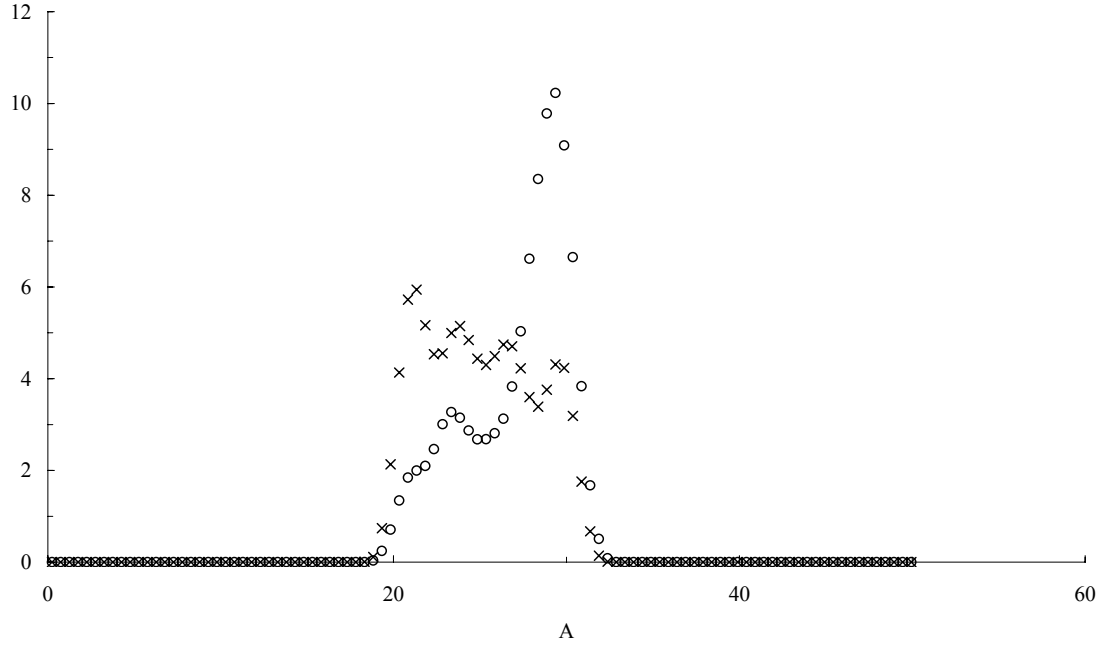

(b)

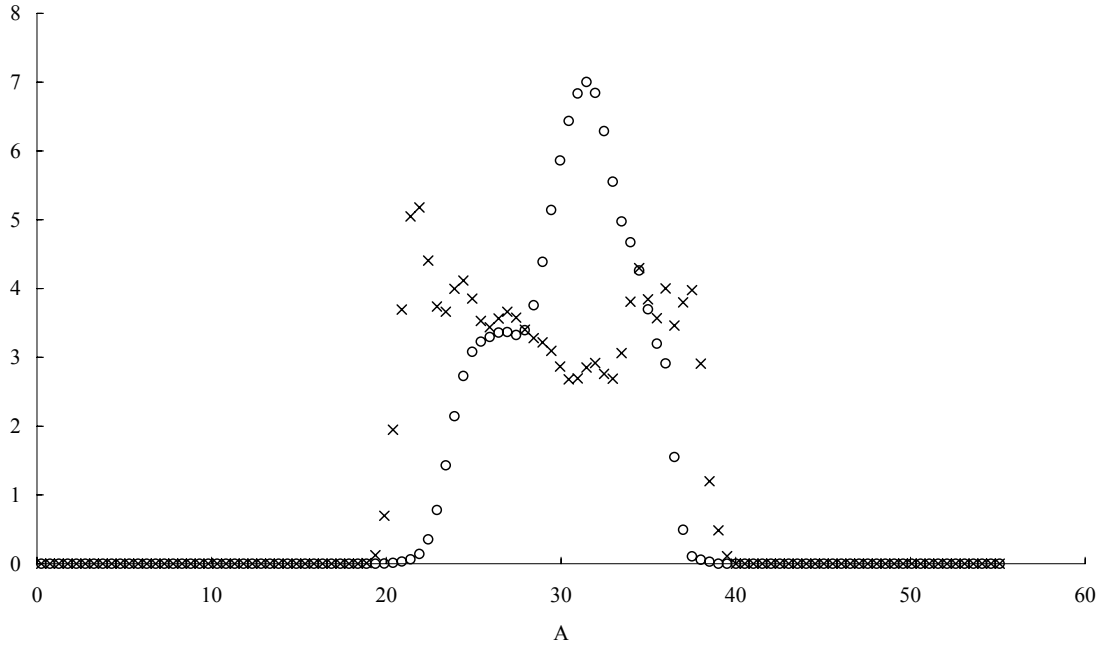

(c)

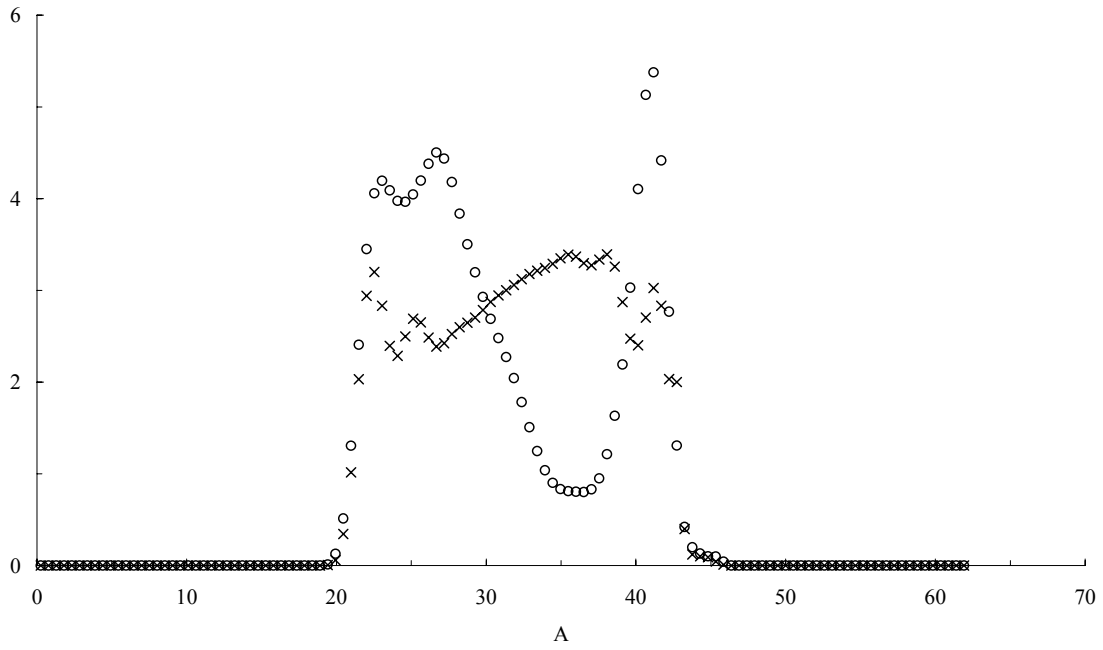

(d)

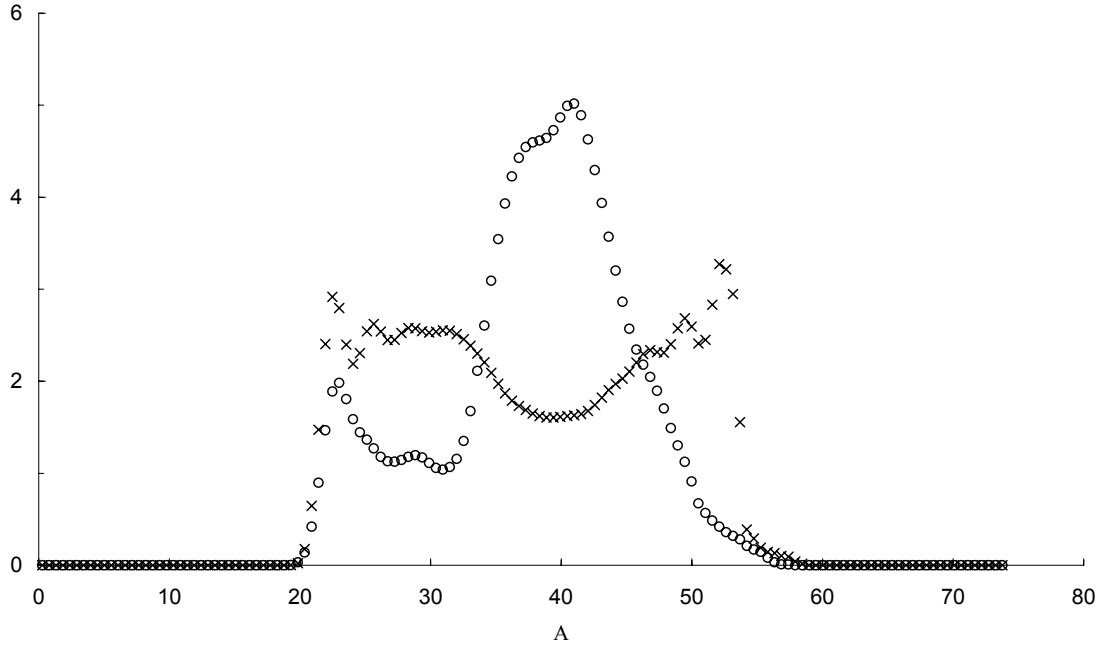

Figure 6.7: Concentration profiles of water (×) and atrazine (○) for interlayer distances of 15 Å (a), 20 Å (b), 27 Å (c), 40 Å (d).

For thin water layers, atrazine – water binding energy is lower in its absolute value, while atrazine – silica and water – silica values are more constant. Atrazine tend to form aggregates, mainly next to silica walls (even more evidently than the previous set of simulations), as testified by the presence of one, or no more than two peaks, while water distribution is rather constant.

Atrazine adhesion to silica layers is more pronounced, from a thermodynamic point of view, for smaller interlayer distances, while for bigger distances atrazine – water aggregation is more favoured. Even in this case, as expected, atrazine tend prevalently to remain in water.

To summarise the results of our MC and MM/MD simulations, we confirm that our procedures have been nicely validated against experimental data of atrazine diffusion coefficient in water. Diffusion and adhesion results for atrazine in silica matrices saturated with water pointed out what follows:

- Atrazine diffusion coefficients D are not constant, since for variable atrazine concentration D decreases for higher atrazine concentrations; in simulations where water interlayer is variable, D decreases for thin interlayer, confirming what demonstrated in previous simulations with analogous systems;
- Binding energy are negative (thus favourable) for each binary complex in both sets of simulations. In particular, their trends testify a moderate atrazine tendency to adhere to the silica matrix. This tendency is enhanced for higher atrazine concentrations, and for smaller water interlayers.
- Concentration profiles for water are quite constant for all simulations, thus water distributes more uniformly into the available interlayer volumes; on the contrary, atrazine show one or more peaks, creating aggregations, mainly close to silica layers.
- As a general trend, atrazine tendency to bind with water instead of silica is more pronounced. Thus, simulations confirm how atrazine adhesion onto the silica mineral matrix, although not insignificant, is relatively weak.

6.3 Case study generalisation

Methods and procedures here employed can be improved, considering for instance the presence of ions (and different pH values) in water. Further modifications can be made to consider different temperature and / or pressures, as if the considered soil was a constituent of layers at different depth; it is also possible to perform comparative simulations with crystalline different matrices and soil organic matters (humic substances or others) to take into

account more realistic, different soil compositions. These improvements could be made to obtain a more complex / consistent, thus reliable, model.

Results can also be used to develop multi-scale procedures, where diffusion coefficients or other relevant parameters can be used as input data for finite element calculations at higher scales, or, by extrapolating trends, to study –for instance– diffusion models at macroscopic level. This, once again, would result in considerable time and money savings. Moreover, even in this case study, methods and procedure used here are easy to generalise; therefore, they can be applied to different soil matrices (organic or crystalline) and to different pollutants, using the same procedure.

From a more specific standpoint, results gained from molecular simulation can constitute a useful database for programs like FEMWATER (Finite Element software for predicting pollution pathways and diffusion into aquifers), (EPA, 2008), or risk analysis software like RBCA (Risk Based Corrective Action), (Groundwater Software, 2008), or others, for contaminated soils assessment. In fact, all these predictive software usually rely upon specific assumptions about pollutant dispersion (diffusion, distribution in environment compartments such as soil, water, air) which are sometimes difficult to determine, together with the model of diffusion / dispersion in each kind of environment. These factors are usually already labelled as previously obtained for general cases. Since our days, for more specific and accurate investigations the only way to obtain input parameters is to conduct expensive experimental sessions. In this sense, molecular simulation approach could constitute an elegant and, above all, consistent and alternative way to determine general models and input coefficients.

Even for the study of pollutant phenomena into soils – but, generally speaking, for the study of environmental pollution in general – molecular simulation techniques offer unique potentialities of improvement, are largely implementable, and procedures can be easily transferred to analogous systems, confirming all the advantages stated in the previous chapters.

Chapter 7

Conclusions

Summary

In this chapter, general conclusions about this work and the results achieved are listed.

The general purpose of this thesis consisted in exploring techniques and potentialities of multi-scale simulations, to prove the feasibility and advantages of such applications in the chemical – environmental engineering sector. Both fields (molecular simulation and environmental engineering) are rightly gaining considerable interest in recent years. Thus, it seemed reasonable and attractive to study common potentialities and applications: can we assert that general advantages of multi-scale molecular simulation are valid also in this field, as already accepted for different disciplines?

This general scope has been achieved. We considered different, heterogeneous context in three main environmental fields, to determine the flexibility of the procedure, if applied to different case-studies. Such approach is also congruent with the multi – disciplinary (if not holistic) philosophy which is necessary in environmental studies, which represent a very heterogeneous field of application.

In the material recycling and requalification field, we considered polymer blend requalification as a starting point, studying the morphologies and the local and global physical or mechanical properties: the same technique concatenation (from QM to FEM) to obtain different properties and, finally, to study a nanocomposite, (the best preparation and its mechanical properties). In the pollution removal from gaseous stream field, we investigated simple gas removal by adsorption, up to study more complicated mixtures to be separated in homogeneous and heterogeneous materials, with simultaneous adsorption and reaction, and introducing macroscopic thermodynamic model for isotherm fitting. In the last field, pollution phenomena description, we imagined an ideal model of inorganic, saturated soil to study the interaction (adhesion and diffusion) between the pollutant (a pesticide) the water and soil matrix at different conditions.

Moreover, for material recycling and pollution removal, we started from simplified, easier contexts to complicate progressively the systems, considering case studies more and more realistic. In fact, one of our purposes was to move away from traditional molecular simulation studies, generally accurate but still theoretically driven, to examine processes which can be more close to “real”, relevant cases from engineering point of view: one of the most critical tasks. In this research, even the last case study (pollution phenomena description and prediction), although very simplified, or less developed than the others in this work, show promising potentialities for practical applications and implementations. Different techniques, at different time and length scales, proved to be reliable as all validated against experimental data. Furthermore, all the case studies presented in this thesis, as indicated in previous

chapters, have been published in different international journals, and / or presented at international congresses.

We can definitely consider the application of these techniques as useful for different research perspectives and for opening new frontiers in environmental applications in the following years. Implementations and generalizations are absolutely possible and attractive in most cases. Molecular simulation techniques are thus applicable for studying processes or phenomena in very different conditions, bringing all the advantages and promising development, which are already present in life and material sciences.

References

Accelrys Software Inc. (2008), available from: http://accelrys.com

A.W. Adamson, Physical Chemistry of Surfaces, Wiley, New York, 1990.

E.D. Akten, R. Siriwardane, D.S. Sholl, "Monte Carlo Simulation of Single and Binary Component Adsorption of CO_2, N_2, and H_2 in Zeolite Na-4A", Energy & Fuels, 17, N. 4, p. 977, (2003).

Y. Alexeev, T.L. Windus, C-Z. Zhan, D.A. Dixon, "Accurate Heats of Formation and Acidities for H_3PO_4, H_2SO_4, and H_2CO_3 From Ab Initio Electronic Structure Calculations", International Journal of Quantum Chemistry, 102, p. 775, (2005).

S. Alikhanidi, Y. Takahashi, "Pesticide persistence in the environment – collected data and structure – based analysis". Journal of Computer Chemistry, Japan, 3, p. 59, (2004).

M.P. Allen, D.J. Tildesley, "Computer simulation of liquids", Clarendon Press, Oxford, UK, (1987).

P. Altevogt, O.A. Evers, J.G.E.M. Fraaije, N.M. Maurits, B.A.C. van Vlimmeren, "The MesoDyn project: software for mesoscale chemical engineering", Journal of Molecular Structure (Theochem), p. 139, (1999).

R.A. Alvarez-Puebla, J.J. Garrido, C. Valenzuela-Calahorro, P.J.G. Goulet, "Retention and induced aggregation of Co(II) on a humic substance: sorption isotherms, infrared absorption, and molecular modeling", Surface Science, 575, p. 136, (2005).

H. C. Andersen, "Molecular dynamics simulations at constant pressure and/or temperature", Journal of Chemical Physics, 72, p. 2384, (1980).

S.M. Auerbach, N.J. Henson, A.K. Cheetham, H.I. Metiu, "Transport theory for cationic zeolites: Diffusion of benzene in Na-Y", Journal of Physical Chemistry, 99, p. 10600, (1995).

S. M. Auerbach, "Theory and simulation of jump dynamics, diffusion and phase equilibrium in nanopores", International Reviews in Physical Chemistry, 19, p. 155, (2000).

A. Bagchi, T.C. Ghosh, "Structural insight into the interactions of SoxV, SoxW and SoxS in the process of transport of reductants during sulfur oxidation by the novel global sulfur oxidation reaction cycle", Biophysical Chemistry, 119, p. 7, (2006).

A. Bagreev, J. Teresa, T.J. Bandosz, "Study of Hydrogen Sulfide Adsorption on Activated Carbons Using Inverse Gas Chromatography at Infinite Dilution", Journal of Physical Chemistry B, 104, p. 8841, (2000).

F. J. Baltá Calleja, L. Giri, H. G. Zachmann, "New aspects of the microstructure of PET/PEN blends as revealed by microhardness", Journal of Polymer Science, 32, p. 1117, (1997).

C. Beauvais, A. Boutin, A.H. Fuchs, " Adsorption of Water and Aromatics in Faujasite Zeolites: A Molecular Simulation Study", Adsorption, 11, p. 279, (2005).

J. Bicerano, "Prediction of Polymer Properties", Third Edition, Marcel Dekker Inc., New York, 2002.

S. W. Blocki, "Hydrophobic Zeolite Adsorbent: A Proven Advancement in Solvent Separation Technology", Environmental Progress, 12, p. 226, (1993).

H.L. Bohn, B. L. McNeil B.L, G. A. O'Connor, "Soil Chemistry", ed. by John Wiley & Sons, New York, NY, USA, 1985.

D.W. Brenner, "Empirical potential for hydrocarbons for use in simulating the chemical-vapor deposition of diamond films", Physical Review B, 42, p. 9458, (1990).

S. Brunauer, P.H. Emmett, E. Teller, "Adsorption of gases in multimolecular layers", Journal of American Chemical Society, 60, p. 309, (1938).

O. Byl, P. Kondratyuk, J.T. Yates Jr., "Adsorption and dimerization of NO inside single-walled carbon nanotubes – an infrared spectroscopy study", Journal of Physical Chemistry B, 107, p. 4277, (2003).

R. Car, N. Parrinello, "Unified Approach for Molecular Dynamics and Density-Functional Theory", Physical Reviews Letters, 55, p.2471, (1985).

M. V. Chandak, Y. S. Lin, W. Ji, R. J. Higgins, "Sorption and diffusion of VOCs in DAY zeolite and silicalite-filled PDMS membranes", Journal of Membrane Science, 133, p. 231, (1997).

S.G. Charati, S.A. Stern, "Diffusion of Gases in Silicone Polymers: Molecular Dynamics Simulations", Macromolecules, 31, p. 5529, (1998).

M. Chase, Jr., NIST-JANAF Thermochemical Tables, J. Phys. and Chem. Reference Data Monograph No. 9, Am. Chem. Society, Am. Inst. Physics, 1998.

A. Chatterjee, D. Vlachos, "An overview of spatial microscopic and accelerated kinetic Monte Carlo methods", Journal of Computer-Aided Materials Design, 14, N. 2, p. 253, (2007).

B. Chen, A.A. Bowden, H.C. Greenwell, P.Boulet, P.V. Coveney, A. Whiting, J.R.G. Evans, "Morphology and elastic modulus of novel poly[oligo(ethylene glycol) diacrylate]-montmorillonite nanocomposites" , Journal of Polymer Science: Part B: Polymer Physics 43, p. 1785, (2005).

L. Clausen, I. Fabricius, L. Madsen, "Adsorption of pesticides onto quartz, calcite, kaolinite, and a-alumina", Journal of Environmental Quality, 30, p. 846, (2001).

CNR, (2008), available from:
http://www.cnr.it/commesse/Scheda_Commessa_Descrizione.html?co=5429

T. W. Cochran, R. L. Kabel, R. P. Danner, "The Vacancy Solution Model of Adsorption – Improvement and Recommendations", AIChE Journal, 31, p. 2075, (1985).

M.L. Connolly, "Solvent-accessible surfaces of proteins and nucleic acids", Science, 221, p. 709, (1983).

J. R. Cox, "Triazine derivatives as non-selective herbicides", Journal of the Science of Food and Agricolture, 13, p. 99, (1962).

"CRC Handbook of Chemistry and Physics", ed. by D.R. Lide, 79th Edition, CRC press, Boca Raton, FL, USA (1999).

A. J. Cruz, J. Pires, A. P. Carvalho, M. Brotas de Carvalho, "Physical Adsorption of H_2S Related to the Conservation of Works of Art: The Role of the Pore Structure at Low Relative Pressure", Adsorption, 11, p. 569, (2005).

CULGI (Chemistry Unified Language Interface) software (2008), available from: http://www.culgi.com/

A. Dabrowski, "Adsorption - from theory to practice", Advances in Colloid and Interface Science, p. 93, 135 (2001).

P. G. de Gennes, "Scaling Concepts in Polymer Physics", Cornell University Press, Ithaca, NY, USA, 1979.

Dlgs 152/2006 (2006), available from: http://www.borsarifiuti.com/dlgs152/index.html

P. Demontis, G.B. Suffritti, "Sorbate-Loading Dependence of Diffusion Mechanism in a Cubic Symmetry Zeolite of Type ZK4. A Molecular Dynamics Study ", Journal of Physical Chemistry B, 101, p. 5789, (1997).

Directive 2000/53/EC of the European Parliament and of the Council of 18 September2000 on end-of life vehicles, Official Journal of the European Communities, L 269/34, 21.10.2000.

S.A. Edgerton, M.W. Holdren, D. I. Smith, "Inter urban comparison of ambient volatile organic compound concentration", Journal of Air Pollution Control Association, 39, p. 729, (1989).

A Einstein, "On the motion of small particles suspended in liquids at rest required by the molecular-kinetic theory of heat", Annalen der Physsik - Leipzig 17, p. 549, (1905).

J. S. Eow; "Recovery of Sulfur from Sour Acid Gas: A Review of the Technology", Environmental Progress, 21, p. 143, (2002).

EPA (1998), "Volatile Organic Compounds (VOC) Recovery Seminar", United States of America, September 16-17 (1998), Cincinnati, OH, USA, available at: http://www.epa.gov/nrmrl/pubs/625r99005/625r99005.pdf

EPA (1999), "Choosing an adsorption system for VOC: carbon, zeolite or polymers?", U.S.

Environmental protection Agency, Clean Air Technology Center, Technical Bulletin, Research Triangle Park, North Carolina, USA, 1999.

EPA (2006), available from: http://www.epa.gov/garbage/pubs/06data.pdf

EPA (2006), Decision documents for atrazine. Available from: http://www.epa.gov/oppsrrd1/reregistration/REDs/atrazine_combined_docs.pdf

EPA (2008), FEMWATER software, available at:

http://www.epa.gov/ceampubl/gwater/femwater/index.html

EU 2006/12/CE, European directive (2006), available from: http://eur-lex.europa.eu/LexUriServ/LexUriServ.do?uri=OJ:L:2006:114:0009:0021:EN:PDF.

D.H. Everett, "IUPAC Manual Appendix II, Part I", Pure and Applied Chemistry, 31, 1979; "Part II: Heterogeneous Catalysis," Pure and Applied Chemistry, 31, 1976.

J. Farrell, J. Luo, P. Blowers, J. Curry, "Experimental molecular mechanics, and ab initio investigations of activated adsorption and desorption of trichloroethylene in mineral micropores", Environmental Science and Technology 36, p. 1524, (2002).

M. Fermeglia, S. Pricl, "A novel approach to thermophysical properties prediction for chloro-fluoro-hydrocarbons", Fluid Phase Equilibria, 166, p.21, (1999).

M. Fermeglia, S. Pricl, "Prediction of phase equilibria for binary mixtures by molecular modeling", AIChE Journal, 47, p. 2371, (2001).

M. Fermeglia, S. Pricl, "Atomistic molecular dynamic simulations of gas diffusion and solubility in rubbery amorphous hydrocarbon polymers", Chemical Engineering Communications, 190, p. 1267, (2003).

M. Fermeglia, M. Ferrone, S. Pricl, "Computer simulation of nylon/organoclay nanocomposites: prediction of the binding energy", Fluid Phase Equilibria 212, p. 315, (2003).

M. Fermeglia, M. Ferrone, S. Pricl, "Estimation of the binding energy in random poly(butylene terephtalate-co-thiodiethylene terephtalate) copolyesthers / clay nanocomposites via molecular simulation", Molecular Simulation, 30, p. 289, (2004).

P. J. Flory, "Principles of Polymer Chemistry", Cornell University Press, Ithaca, USA (1953).

W. M. C. Foulkes; L. Mitáš, R. J. Needs, G. Rajagopal, "Quantum Monte Carlo simulations of solids", Reviews in Modern Physics, 73, p. 33, (2001).

D. Frenkel, B. Smit, "Understanding molecular simulation", Academic Press, San Diego, USA (1996).

H. Freundlich, "Colloid and Capillary Chemistry", translated from German by Hatfield, H.S., 3rd ed., E.P. Dutton and Company, New York, 1922.

C. L. Garcia, J. A. Lercher, "Adsorption of H_2S on ZSM5 zeolites", Journal of Physical Chemistry, 96, p. 2230, (1992).

A. R. George, C. M. Freeman, C. R. A. Catlow, "A computational investigation of zeolite-clorofluorocarbon interactions", Zeolites, 17, p. 466, (1996).

N.M. Ghoniem, E.P. Busso, N. Kioussis, H. Huang, "Multiscale modelling of nanomechanics and micromechanics: an overview", 2003, Philosophical Magazine, vol. 83, Nos 31-34, p. 3475 (2003).

W.A. Goddard III, B.V. Merinov, A.C.T. van Duin, T. Jacob, M. Blanco, V. Molinero, S.S. Jang, Y. H. Jang, "Multi-paradigm Multi-scale Simulations for Fuel Cell Catalysts and Membranes", Molecular Simulation, 32, Nos. 3-4, p- 251, (2006).

P. Gramatica, E. Papa, "Screening and ranking of POPs for Global Half-Life: a QSAR approach for prioritization", Environmental Science and Technoogy, 41, N. 8, p. 2833, (2007).

J.A. Greathouse, R.J. O'Brien, G. Bemis, R.T. Pabalan, "Molecular Dynamics Study of Aqueous Uranyl Interactions with Quartz (010)", Journal of Physical Chemistry B, 106, p. 1646, (2002).

J. Greathouse, R. T. Cygan, "Water structure and aqueous uranyl(VI) adsorption equilibria onto external surfaces of beidellite, montmorillonite, and pyrophyllite: results from molecular simulations", Environmental Science and Technology, 40, p. 3865, (2006).

R. D. Groot, P. B. Warren, "Dissipative Particle Dynamics: Bridging the gap between atomistic and mesoscopic simulation", Journal of Chemical Physics, 107, p. 4423, (1997).

Groundwater Software, 2008, available at:

http://www.groundwatersoftware.com/rbca_tool_kit.htm

K. E. Gubbins, N. Quirke, "Molecular Simulation and Industrial Application", Gordon and Breach Science Publishers, Amsterdam, The Netherlands, 1997.

E.A. Guggenheim, "Dimerization of gaseous nitric oxide", Molecular Physics 10, p.401, (1966).

M. Guillemot, J. Mijoin, S. Mignard, P. Magnoux, "Adsorption of Tetrachloroethylene on Cationic X and Y Zeolite: Influence of Cation Nature and of Water Vapor", Industrial Engineering Chemical Research, 46, N. 13, p. 4614, (2007).

C. J. Guo, O. Talu, D. T. Hayhurst, "Phase transition and structural heterogeneity; benzene adsorption on silicalite", AIChE Journal, 35, p.573, (1989).

V. M. Gun'ko, "Competitive Adsorption", Theoretical and Experimental Chemistry, 43, No. 3, p. 139, (2007).

M. Guo, H. G. Zachmann, "Intermolecular cross-polarization nuclear magnetic resonance studies of the miscibility of poly(ethylene naphthalene dicarboxylate)/poly(ethylene terephthalate) blends" Polymer, 34, p. 2503, (1993).

V. K. Gupta, N. Verma, "Removal of volatile organic compounds by cryogenic condensation followed by adsorption", Chemical Engineering Science, 57, p. 2679, (2002).

A. A. Gusev, "Representative volume element size for elastic composites: A numerical study", Journal of the Mechanics and Physics of Solids, 45, N. 9, p. 1449, (1997).

A. A. Gusev, "Numerical Identification of the Potential of Whisker- and Platelet-Filled Polymers", Macromolecules, 34, p.3081, (2001).

H. B. Habdul-Reheman, M. A. Hasanain, K. F. Loughlin, "Quaternary, ternary, binary and pure component sorption on zeolite. 1. Light alkanes on Linde S-115 silicate at moderate to high pressure", Industrial & Chemical Engineering Research, 29, p 1525, (1990).

J. M. Haile, "Molecular Dynamics Simulation, ed. by John Wiley & Sons, New York, NY, USA, 1992.

C. Hansenne, F. Jousse, L. Leherte, D. P. Vercauteren, "Dynamics of benzene in zeolite KL", Journal of Molecular Catalysis A: Chemical, 166, p. 147, (2001).

M. F. Helmke, W. W. Simpkins, R. Horton, "Fracture-controlled nitrate and atrazine transport in four Iowa till units", Journal of Environmental Quality, 34, p. 227, (2005).

S.C. Hendy, "Molecular dynamics simulation of oxide surfaces in water", Current Applied Physics, 4, Nos. 2-4, p. 144, (2004).

M. Heuchel, R. Q. Snurr, E. Buss, "Adsorption of CH_4-CF_4 Mixtures in Silicalite: Simulation, Experiment, and Theory", Langmuir, 13, p. 6795, (1997).

J-R. Hill, A. R. Minihan, E. Wimmer, C. J. Adams, "Framework dynamics including computer simulations of the water adsorption isotherm of zeolite Na-MAP", Physical Chemistry Chemical Physics, 2, p. 4255, (2000).

A. Hiltner, R. Y. F. Lin, Y. S. Hu, J. Boer, "Oxygen transport as a solid-state structure probe for polymeric materials: a review", Journal of Polymer Science, Part B, 43, p. 1047, (2005).

P.J. Hine, H.R. Lusti, A.A. Gusev, "Direct numerical predictions for the elastic and thermoelastic properties of short fiber composites", Computer Science Technology, 62, p. 1445, (2002).

P. J. Hoogerbrugge, J. M. V. A. Koelman, "Simulating microscopic hydrodynamic phenomena with dissipative particle dynamics", Europhysics Letters, 19(3), p.155, (1992).

P. Hohemberg, W. Kohn, "Inhomogeneous Electron Gas", Physical Review, 158, N. 2, p. 864, (1964).

W. Huang, W. J. Jr. Weber, "Thermodynamic Considerations in the Sorption of Organic Contaminants by Soils and Sediments. 1. The Isosteric Heat Approach and Its Application to Model Inorganic Sorbents", Environmental Science and Technology, 31, p. 3238, (1997).

J. R. Hufton, R. P. Danner, "Chromatographic study of alkane in silicalite: equilibrium properties", AIChE Journal, 39, p. 954, (1993).

Y. Ichikawa, K. Kawamura, N. Theramast, K. Kitayama, "Secondary and tertial consolidation of bentonite clay: consolidation test, molecular dynamics simulation and multiscale homogenization analysis", Mechanics of Materials, 36, p. 487, (2004).

D. W. Ihm, S. Y. Park, C. G. Chang, Y. S. Kim, H. K. Lee, "Miscibility of poly(ethylene terephthalate)/poly(ethylene 2,6 – naphthalate) blends by transesterification", Journal of Polymer Science, Part A, Polymer Chemistry, 34, p. 2841, (1996).

International Zeolite Association Website (IZA) (2005), available at: http://www.iza-structure.org/

M. A. Islam, "Einstein – Smoluchowski diffusion equation: a discussion", Physica Scripta, 70, p. 120, (2004).

S. K. Jain, J. P. Pikunic, R. J.-M. Pellenq, K.E. Gubbins, "Effects of Activation on the Structure and Adsorption Properties of a Nanoporous Carbon using Molecular Simulation", Adsorption, 11, p. 355, (2005).

S. K. Jain, K.E. Gubbins, R. J.-M. Pellenq, J. P. Pikunic, "Molecular modeling and adsorption properties of porous carbons", Carbon, 44, p.2445, (2006a).

S.K. Jain, R.J.-M. Pellenq, J.P. Pikunic, K.E. Gubbins, "Molecular modeling of porous carbons using the hybrid reverse Monte Carlo method", Langmuir, 22, p. 9942, (2006).

H. Jobic, A.I. Skoulidas, D.S. Scholl, "Determination of Concentration Dependent Transport Diffusivity of CH_4 in Silicalite by Neutron Scattering Experiments and Molecular Dynamics", Journal of Physical Chemistry B, 108, N. 30, p. 10613, (2004).

J. K. Johnson, A. Z. Panagiotopoulos, K. E. Gubbins, "Reactive Canonical Monte Carlo", Molecular Physics, 81, p. 717, (1994).

W. L. Jorgensen, J. Chandrasekhar, J. Madura, and R. W. Impey, M. L. Klein, "Comparison of simple potential functions for simulating liquid water", Journal of Chemical Physics, 79, p. 926, (1983).

R. L. June, A. T. Bell, D. N. Theodorou, "Molecular Dynamics Study of Methane and Xenon in Silicalite", Journal of Physical Chemistry, 94, p. 8232, (1990).

N. Kanari, J.-L. Pineau, and S. Shallari, "End-of-Life Vehicle Recycling in the European Union", JOM: The Member Journal of TMS, 2003, available at: http://www.tms.org/pubs/journals/JOM/0308/Kanari-0308.html

K. Kaneko, N. Fukuzaki, K. Kakei, T. Suzuki, S. Ozeki, "Enhancement of nitric oxide dimerization by micropore fields of activated carbon fibers", Langmuir, 5, p. 960, (1989).

N. Karasawa, W.A. Goddard, "Force Fields, Structures, and Properties of Poly(vinylidene fluoride) Crystals", Macromolecules, 25, p. 7268, (1992).

S. Kirkpatrick, C. D. Gelatt, M. P. Vecchi, "Optimization by Simulated Annealing", Science, 220, p.671, (1983).

A. V. Klochko, E. M. Piotrovskaya, E. N. Brodskaya, "Computer simulations of the structural and kinetic characteristics of binary argon-krypton solutions in graphite pores", Langmuir 12, p. 1578, (1996).

F. Kohler, M. Bohn, J. Fischer, R. Zimmermann, „The excess properties of nitric oxid mixtures", Monatshefte für Chemie / Chemical Montly, 118, p. 169, (1987).

W. Kohn, L. J. Sham, "Self-Consistent Equations Including Exchange and Correlation Effects", Physical Reviews, 140, p.1133, (1965).

R. Kotdavala, A.O. Yazaydin, N. Kazantzis, R. W. Thompson, "A Molecular Simulation Approach to the Study of Adsorption of Hydrogen Cyanide and Methyl Ethyl Ketone in Silicalite, Mordenite and Zeolite Beta Structures", Molecular Simulation, 33, p. 843, (2007).

P. Kowalczyk, R. Holyst, "Efficient Adsorption of Super Greenhouse Gas (Tetrafluoromethane) in Carbon Nanotubes", Environmental Science and Technology, 42, p. 3821, (2008).

J.D. Kubicki, S.E. Apitz, "Models of natural organic matter and interactions with organic contaminants", Organic Geochemistry, 30, p. 911, (1999).

M. Künz, P. Lavallée, "Anomalous diffusion is the rule in concentration – dependent diffusion properties", Journal of Physics D: Applied Physics, 37, p. 5, (2004).

T. S. C. Lawb, C. Chaoa, G. Y. W. Chanb, A. K. Y. Lawb, "Confined catalytic oxidation of volatile organic compounds by transition metal containing zeolites and ionizer", Atmospheric Environment, 37, p. 5433, (2003).

I. Langmuir, "The constitution and fundamental properties of solids and liquids, part I, solids", Journal of the American Chemical Society, 38, p.2221, (1916).

A.R. Leach, "Molecular Modelling: Principles and Application, 2nd ed.", Prentice-Hall, Englewood Cliffs, NJ, (2001).

M. Levy, "Universal variational functionals of electron densities, first-order density matrices, and natural spin-orbitals and solution of the v-representability problem", Proceedings of the National Academic Science, U. S. A., 76, p. 6062, (1979).

B. Li, F. Pan, Z. Fang, L. Liu, Z. Jiang, "Molecular Dynamics Simulation of Diffusion Behavior of Benzene/Water in PDMS-Calix[4]arene Hybrid Pervaporation Membranes", Industrial Engineering Chemical Research, ASAP, (2008).

W. Ling, J. Xu, Y. Gao, "Dissolved organic matter enhances the sorption of atrazine by soil", Biology and Fertility of Soils, 42, p. 418, (2006).

M. Lisal, J.K. Brennan, W.R. Smith, F.R. Siperstein, "Dual control cell reaction ensemble molecular dynamics: a method for simulations of reactions and adsorption in porous materials", Journal of Chemical Physics, 121, p. 159, (2004a).

M. Lísal, K. Aim, M. Mecke, J. Fischer, "Revised equation of state for two-center Lennard-Jones fluids", International Journal of Thermophysics, 25, p. 159, (2004).

M. Lísal, J.K. Brennan, W.R. Smith, "Effects of confinement on chemical reaction equilibrium in naoporous materials", Journal of Chemical Physics, 124, p. 743, (2006)

Y. Liu, Q. Wang, L. Lu, "Transport properties and distribution of water molecules confined in hydrophobic nanopores and nanoslits", Langmuir 20, p. 6921, (2004).

J-C. Liu, P.A. Monson, "Molecular Modeling of Adsorption in Activated Carbon: Comparison of Monte Carlo Simulations with Experiment", Adsorption, 11, p. 5, (2005).

P. A. Lock, N. T. Skipper, "Computer simulation of the structure and dynamics of phenol in sodium montmorillonite hydrates", European Journal of Soil Science, 58, p. 958, (2007).

W. Loewenstein, "The distribution of aluminium in the tetrahedra of silicates and aluminates", American Mineralogist, 39, p. 92, (1954).

J. Luo, J. Farrel, "Examination of Hydrophobic Contaminant Adsorption in Mineral Micropores with Grand Canonical Monte Carlo Simulations", Environmental Science and Technology, 37, p. 1775, (2003).

M.B.M. Lupe, "Molecular Atomistic Simulations of Clay Swelling in Water Dispersions", Molecular Engineering, 7, p. 367, (1997).

H. R. Lusti, I. A. Karmilov, A. A. Gusev, Effect of Particle Agglomeration on the Elastic Properties of Filled Polymers, Soft Materials, 1, p. 115-120, (2003).

U. Marchaim, "Biogas Technology as an Environmental solution to Pollution", Bull. FAO Agric. Services, Rome, Italy, 1992.

J. E. Mark, "Physical Properties of Polymers Handbook", American Institute of Physics, Woodbury, NY, 1997.

Matsim, 2003, available from: http://www.matsim.com

Mattice WL, Suter UW, "Conformational Theory of Large Molecules: the Rotational Isomeric State Model in Macromolecular Systems", John Wiley & Sons, New York, USA, 1994.

F. Maugé, A. Sahibed-Dine, M. Gaillard, M. Ziolek, "Modification of the Acidic Properties of NaY Zeolite by H_2S Adsorption - An Infrared Study", Journal of Catalysis, 207, p. 353, (2002).

E. A. McGonigle, J. J. Liggat, R. A. Pethrick, S. D. Jenkins, J. H. Daly, D. Hayward, "Permeability of N_2, Ar, He, O_2 and CO_2 through biaxially oriented polyester films: dependence on free volume", Polymer, 42, p. 2413, (2001).

S.C. McGrother, K.E. Gubbins, "Constant pressure Gibbs ensemble Monte Carlo simulations of adsorption into narrow pores", Molecular Physics, 97, p. 955, (1999).

R. M. Medina, D. Likhatchev, L. Alexandrova, A. Sánchez-Solís, O. Manero, "Mechanisms and kinetics of transesterification in poly(ethylene terephthalate) and poly(ethylene 2,6 – naphthalene dicarboxylate) polymer blends", Polymer, 45, p. 8517, (2004).

H. Meirovitch, "Computer simulation of self-avoiding walks: Testing the scanning methods", Journal of Chemical Physics, 79, p. 502, (1983).

N. Metropolis, A. W. Rosenbluth, M. N. Rosenbluth, A. H. Teller, E. Teller, "Equation of state calculations by fast computing machines", Journal of Chemical Physics, 21, p. 1087, (1953).

T. H. Milby, R. C. Baselt; "Hydrogen Sulfide Poisoning: Clarification of Some Controversial Issues", American Journal of Industrial Medicine, 35, p. 192, (1999).

R. Millini, "Application of modeling in zeolite science", Catalysis Today, 41, p.41, (1998).

V. Milman, M.C. Warren, "Elastic properties of TiB_2 and MgB", Journsl of Physics: Condensed Matter, 13, p. 5585, (2001).

B. Minofar, L. Vrbka, M. Mucha, P. Jungwirth, "Interior and Interfacial Aqueous Solvation of Benzene Dicarboxylate Dianions and Their Methylated Analogues: A Combined Molecular Dynamics and Photoelectron Spectroscopy Study", The Journal of Physical Chemistry A, 109, N. 23, p. 5042, (2005).

F. Müller-Plathe, "Scale-Hopping in Computer Simulations of Polymers", Philosophical Magazine, 1, N. 1, p. 1, (2003).

S. Murad, J. Lin, "Using Thin Zeolite Membranes and External Electric Fields To Separate Supercritical Aqueous Electrolyte Solutions", Industrial Engineering Chemical Research, 41, p. 1076, (2002).

S. Murad, K. Oder, J. Lin, "Molecular Simulation of Osmosis, Reverse Osmosis, and Electro-Osmosis in Aqueous and Methanolic Electrolyte Solutions", Molecular Physics, 95, p. 401, (1998).

A.L. Myers, J.M. Prausnitz, "Thermodynamics of Mixed-Gas Adsorption", AIChE Journal, 11, p.121, (1965).

M. Nakano, K. Kawamura, Y. Ichikawa, "Local structural information of Cs in smectite hydrates by means of an EXAFS study and molecular dynamics simulations", Applied Clay Science, 23, p.15, (2003).

R. Nagumo, H. Takaba, S. Suzuki, S. Nakao, "Estimation of inorganic gas permeability through an MFI-type silicalite membrane by a molecular simulation technique combined with permeation theory **",** Microporous and Mesoporous Materials 48, p. 247, (2001).

Nanoclay, available at: http://www.nanoclay.com

National Center for Computational Toxicology (NCCT) of EPA (2008), available from: http://www.epa.gov/comptox/comptoxfactsheet.html

I. Nezbeda, J. Kolafa, "The use of control quantities in computer simulation experiments: application to the exp-6potential fluid", Molecular Simulation, 14, p. 153, (1995).

K. Nieszporek, "Application of the vacancy solution theory to describe the enthalpic effects accompanying mixed-gas adsorption", Langmuir 22, p.963, (2006).

S. Nishimura, M. Yoda, "Removal of hydrogen sulphide from an anaerobic biogas using a bioscrubber", Water, Science & Technology, 36, p. 349, (1997).

T. Nitta, T. Shigetomi, M. Kuro-oka, T. Katayama, "An adsorption isotherm of multi-site occupancy model for homogeneous surface", Journal of Chemical Engineering of Japan, 17, p. 39, (1984).

OCTA (Integrated simulation system), (2007), available from: http://octa.jp/index.html

A. Okada, A. Usuki, "Twenty years of polymer-clay nanocomposites", Macromolecular Materials and Engineering, 291, p. 1449, (2006).

E. Papa, J. Dearden, P. Gramatica, "Linear QSAR regression models for the prediction of bioconcentration factors by physicochemical properties and structural theoretical molecular descriptors", Chemosphere, 67, p. 351, (2007).

J.-H. Park, Y. Feng, J. Pingsheng, T. C. Voice, S. A. Boyd, "Assessment of Bioavailability of Soil-Sorbed Atrazine", Applied and Environmental Microbiology, 69, p. 3288, (2003).

T. D. Patcheak, S. A. Jabarin, "Effects of molecular weight on phase structure of poly(ethylene terephthalate)/poly(ethylene 2,6 – naphthalate) blends", Polymer, 42, p. 8975, (2001).

J.B. Pedley, Thermodynamical Data and Structures of Organic Compounds, TRC Data Series, Thermodynamic Research Center, College Station, TX, 1994.

J. Pikunic, C. Clinard, N. Cohaut, K.E. Gubbins, J.-M. Guet, R.J.-M. Pellenq, I. Rannou, J.-N. Rouzaud, "Structural modeling of porous carbons: constrained reverse Monte Carlo method", Langmuir, 19, p. 8565, (2003).

J. Pires, A. Carvalho, M. B. Carvalho, M.B, "Adsorption of volatile organic compounds in Y zeolites and pillared clays", Microporous and Mesoporous Materials, 43, p.277, (2001).

J. E. Rae, C. S. Cooper, A. Parker, A. Peters, "Pesticide sorption onto aquifer sediments", Journal of Geochemical Exploration, 64, p. 263, (1998).

M. B. Rao, S. Sircair, "Thermodynamic Consistency for Binary Gas Adsorption Equilibria", Langmuir 1999, 15, 7258.

M.H.M. Reis, H.P.M. de Oliveira, T.D.Z. Atvars, L.F.S. Mascolo, M.R. Wolf-Maciel, "Density functional theory applied to thermochemical calculation for phenol reactions", Fluid Phase Equilibria, 228-229, p.459, (2005).

M.J. Sanborn, R.Q. Snurr, "Predicting membrane flux of CH_4 and CF_4 mixtures in Faujasite from molecular simulations", AIChE Journal 47, p. 2032, (2001).

S.I. Sandler, S-T. Lin, A.K. Sum, "The use of quantum chemistry to predict phase behavior for environmental and process engineering", Fluid Phase Equilibria, 194 – 197, p.61, (2002).

E. Santiso, K.E. Gubbins, "Multi-scale molecular modeling of chemical reactivity", Molecular Simulation, 30, p. 699, (2004).

G. Sastre, C.R.A. Catlow, A. Corma, "Influence of the intermolecular interactions on the mobility of heptane in the supercages of MCM 22 zeolite", Journal of Physical Chemistry B, 106, p. 956, (2002).

G. Sastre, A. Corma, "Ordinary diffusion and single file diffusion in zeolites with monodimensional channels. Benzene and n-butane in ITQ-4 and L zeolites", Topics in Catalysis 24, Nos. 1–4, p.7, (2003).

S.M. Shevchenko, G.W. Bailey, "Non-bonded organo-mineral interaction and sorption of organic compounds at soil surfaces: a model approach", Journal of molecular Structure (Theochem), 422, p. 259, (1998).

Y. Shi, S. A. Jabarin, Transesterification reaction kinetics of poly(ethylene terephthalate)/poly(ethylene 2,6 – naphthalate) blends, Journal of Applied Polymer Science, 80, p. 2422, (2001).

W. Shinoda, M. Mikami, T. Baba, M. Hato, "Dynamics of a highly branched lipid 416 bilayer: a molecular dynamics study", Chemical Physics Letters, 390, p. 35, (2004).

H.-R. Shulten, "The three-dimensional structure of soil organo-mineral complexes studied by analytical pyrolysis", Journal of Analytical and Applied Pyrolysis, 32, 111-126, (1995).

J.I. Siepmann, and D. Frenkel**,** "Configurational-bias Monte Carlo - A new sampling scheme for flexible chains", Molecular Physics, 75**,** p. 59, (1992).

R. Sips, "Structure of a Catalyst Surface", Journal of Chemical Physics, 16, p. 490, (1948).

S. Sircair, T.C. Golden, and M.B. Rao, "Activated carbon for gas separation and storage", Carbon, 34, No 1, p. 1, (1996).

S. Sircar, "Publications on Adsorption Science and Technology", Adsorption, 6, p. 359, (2000).

R. V. Siriwardane, M.-S. Shen, E. P. Fisher, J. A. Poston, "Adsorption of CO_2 on Molecular Sieves and Activated Carbon", Energy & Fuels, 15, p. 279, (2001).

A.I. Skoulidas, D.S. Sholl, "Direct Tests of the Darken Approximation for Molecular Diffusion in Zeolites Using Equilibrium Molecular Dynamics", Journal of Physical Chemistry B, 105, p.3151, (2001).

K. L. Smalling, C. M. Aellion, "Distribution of atrazine into three chemical fractions: impact of sediment depth and organic carbon content", Environmental Toxicology and Chemistry, 23, p. 1164, (2004).

W.R. Smith, R.W. Missen, "Chemical Reaction Equilibrium Analysis: Theory and Algorithms", ed. Wiley – Interscience, New York, 1982; reprinted with corrections, Krieger Publishing, Malabar, FLA, 1991.

M.K. Song, K.T. No, "Molecular simulation of hydrogen adsorption in organic zeolite", Catalysis Today, 120, Nos. 3-4, p.374, (2007).

L. Song, Z.-L. Sun, H.-Y. Ban, M. Dai, L.V.C. Rees, "Benzene Adsorption in Microporous Materials", Adsorption, 11, p. 325, (2005),.

R.E. Speece, "Anaerobic biotechnology for industrial wastewaters", ed. Archae Press, Nashville, Tennessee, U.S.A, 1996.

H.A. Stretz, D.R. Paul, P.E. Cassidy, "Poly(styrene-co-acrylonitrile)/montmorillonite organoclay mixtures: a model system for ABS nanocomposites", Polymer 46, p. 3818, (2005).

H. Sun, "COMPASS: an ab initio force-field optimized for condensed-phase applications - Overview with details on alkane and benzene compounds", Journal of Physical Chemistry B, 102, p. 7338, (1998).

R. Sutton, G. Sposito, "Molecular simulation of humic substance–Ca-montmorillonite complexes", Geochimica and Cosmochimica Acta, 70, p. 3566, (2006).

S. Suwanayuen, R. P. Danner, "A Gas Adsorption Isotherm Equation Based on Vacancy Solution Theory", AIChE Journal, 26, p.68, (1980a).

S. Suwanayuen, R. P. Danner, "Vacancy Solution Theory of Adsorption from Gas Mixture", AIChE Journal, 26, p.76, (1980b).

G. Tanaka, L. A. Goettler, "Predicting the binding energy for nylon 6,6/clay nanocomposites by molecular modeling", Polymer 43, p. 541, (2002).

C.M. Tenney, C.M. Lastoskie, "Molecular simulation of carbon dioxide adsorption in chemically and structurally heterogeneous porous carbons", Environmental Progress, 25, p. 243, (2006).

B. Teppen, C-H. Yu, D.M. Miller, L. Schäfer, "Molecular Dynamics Simulations of Sorption of Organic Compounds at the Clay Mineral / Aqueous Solution Interface", Journal of Computational Chemistry, 19, N. 2, p. 144, (1998).

SS. R. Tharmapuram, S. A. Jabarin, "Processing characteristics of PET/PEN blends, part I: Extrusion and transesterification reaction kinetics", Advances in Polymer Technology, 22, p. 137, (2003).

D. N. Theodorou, U. W. Suter, "Detailed molecular structure of a vinyl polymer glass", 18, N.7, p. 1467, (1985).

D. N. Theodorou, U. W. Suter, "Atomistic modelling of mechanical properties of polymeric glasses", Macromolecules, 18, p. 1467, (1985).

K.T. Thomson, K.E. Gubbins, "Modeling Structural Morphology of Microporous Carbons by Reverse Monte Carlo", Langmuir, 16, p. 5761, (2000).

C. Tong, M. Blanco, W.A.III Goddard, J.H. Seinfeld, "Thermodynamic Properties of Multifunctional Oxygenates in Atmospheric Aerosols from Quantum Mechanics and Molecular Dynamics: Dicarboxylic Acids", Environmental Science and Technology, 38, N.14, pag. 3941, (2004).

R. Toth, A. Coslanich, M. Ferrone, M. Fermeglia, S. Pricl, S. Miertus, E. Chiellini, "Computer simulation of polypropylene/organoclay nanocomposites: characterization of atomic scale structure and prediction of binding energy", Polymer 45, p. 8075, (2004).

R. Toth, M. Ferrone, S. Miertus, E. Chiellini, M. Fermeglia, S. Pricl, "Structure and energetics of biocompatible polymer nanocomposite systems: a molecular dynamics study", Biomacromolecules, 7, p. 1714, (2006).

C.H. Turner, J.K. Johnson, K.E. Gubbins, "Effect of confinement on chemical reaction equilibria: the reactions $2NO \leftrightarrow NO_2$ and $N_2 + 3\ H_2 \leftrightarrow 2NH_3$", Journal of Chemical Physics, 114, p. 1851, (2001).

C. H. Turner, J. K. Brennan, M. Lisal, W. R. Smith, J. K. Johnson, K. E. Gubbins, "Simulation of chemical reaction equilibria by the reaction ensemble Monte Carlo Method: a review", Molecular Simulation, 34 (2), p. 119, (2008).

L.A. Utracki, "Clay-Containing Polymer Nanocomposites", Rapra Technology Ltd, Shawbury**,** Shrewsbury, Shropshire, UK, 2004.

P.K. Valavala, G.M. Odegard, "Modeling techniques for determination of mechanical properties of polymer nanocomposites", Reviews of Advanced Materials Science, 9, p.34, (2005).

A.C.T. van Duin, S.R. Larter, "Molecular dynamics investigation into the adsorption of organic compounds on kaolinite surfaces", Organic Geochemistry, 32, p. 143, (2001).

D. W. Van Krevelen, "Properties of Polymers", 3rd Edition, Elsevier B.V., Amsterdam, The Netherlands, 1990.

N. M. van Straalen, "Assessment of soil contamination – a functional perspective", Biodegradation 13, p. 41, (2002).

L. Verlet, "Computer Experiments on Classical Fluids. I. Thermodynamic Properties od Lennard-Jones Molecules", Physical Reviews, 159, p. 98, (1967).

U. von Barth, l. Hedin, "A local exchange-correlation potential for the spin polarized case: I", Journal of Physics C: Solid State Physics, 5, p. 1629, (1972).

T. Vuong, P.A. Monson, "Monte Carlo Simulations of Adsorbed Solutions in Heterogeneous Porous Materials", Adsorption, 5, p. 295, (1999).

S. Wang, Y. Hu, F. You, L. Song, Z. Chen, W. Fan, "Self-assembly of polycarbonate/acrylonitrile-butadiene-styrene/montmorillonite nanocomposites**"** Journal of Applied Polymer Science, 90, p. 1445, (2003).

D. Wang, A. Sakoda, M. Suzuki, " Effects of Surface Oxygen of Activated Carbon on Alkaloid Adsorption: A Molecular Dynamics Simulation Study", Adsorption, 5, p. 97, (1999).

Waste on Line (2008), available from:
http://www.wasteonline.org.uk/resources/InformationSheets/Plastics.htm

K. Watanabe, N. Austin, and M. R. Stapleton, "Investigation of the air separation properties of zeolites types A, X, and Y by Monte Carlo simulations", Molecular Simulation, 15, p.197, (1995).

Wikipedia (2008a), available from: http://en.wikipedia.org/wiki/Moore's_law

G. Wu, J. A. Cuculo, "Structure and morphology of PET/PEN polymer blends", Polymer, 40, p. 1011, (1999).

Q. Wu, L. Zhou, J. Wu, and Y. Zhou, "Adsorption Equilibrium of the Mixture $CH_4 + N_2 + H_2$ on Activated Carbon", Journal of Chemical Engineering Data, 50, p. 635, (2005).

Wuppertal Institut, "End-of-life regulation in Germany and Europe – problems and perspectives", discussion paper of the project "Autoteille per Mausklick", (2001), available from:
http://www.wupperinst.org/Publikationen/WP/WP113.pdf#search=%22motor%20cars%20plastic%22

A.O. Yazaydin, R.W. Thompson, "Molecular Simulation of the Adsorption of MTBE in Silicalite, Mordenite, and Zeolite Beta", The Journal of Physical Chemistry B, 110, p. 14458, (2006).

Y.F. Yin, T. Mays, B. McEnaney, "Molecular Simulations of Hydrogen Storage in Carbon Nanotube Arrays", Langmuir, 16, N. 26, p. 10521, (2000).

K. H. Yoon, S. C. Lee, I. H. Park, H. M. Lee, O. O. Park, T. W. Son, "The change of the molecular weight of poly(ethylene 2,6 – naphthalate) and poly(ethylene terephthalate) blend with reaction time", Polymer, 38, p. 6079, (1997).

D. M. Young, A. D. Crowell, "Physical Adsorption of Gases", Butterworths ed., London, 1962.

H. Y. Young, K. Yang, W. H. Young, K. Seff, "Crystal structure of a hydrogen sulfide sorption complex of zeolite LTA", Zeolites, 17, p. 495, (1996).

C.H. Yu, S.Q. Newton, M.A. Norman, L. Schäfer, D.M. Miller, "Molecular Dynamics Simulations of Adsorption of Organic Compounds at the Clay Mineral/Aqueous Solution Interface", Structural Chemistry, 14, N. 2, p. 175, (2002).

C.H. Yu, M.A. Norman, S.Q. Newton, D.M. Miller, B.J. Teppen, L. Schäfer, "Molecular dynamics simulations of the adsorption of proteins on clay mineral surfaces", Journal of Molecular Structure, 556, p. 93, (2000).

Y. Yu, B.-J. Zhang, "Diffusion of methane in a mica slit pore: Molecular dynamics simulations and correlation models. Physics Letters A, 364, p. 313, (2007).

X. S. Zhao, Q. Ma, G. Q. Lu, "VOC Removal: Comparison of MCM-41 with Hydrophobic Zeolites and Activated Carbon", Energy & Fuels, 12, p. 1051, (1998).

W. Zhu, J. M. van de Graaf, L. J. P. van den Brooke, F. Kapteijn, J. A. Moulijn, "TEOM: a unique technique for measuring adsorption properties. Light alkanes in silicalite-1", Industrial & Chemical Engineering Research, 37, p. 1934, (1998).

Our publications

The following list represents the most important publications where the results of this thesis have been fully or partly presented by our group.

Chapter 4, Paragraph 2: Fermeglia M., Cosoli P., Ferrone M., Piccarolo S., Mensitieri G., Pricl S., PET/PEN Blends of Industrial Interest as Barrier Materials. Part I. Many-Scale Molecular Modeling of PET/PEN Blends, Polymer, 47:5979-5989, 2006.

Chapter 4, Paragraph 3: P.Cosoli, M. Fermeglia, M. Ferrone, P. Posocco, S. Pricl, G. Scocchi, "New materials from multiscale modelling procedures: properties prediction and customisation of polymeric nanocomposites", I-Cheap-8, The eight International conference on Chemical & Processing engineering, Ischia, 2007. P. Cosoli, M. Fermeglia, M. Ferrone, S. Pricl, L. Toma, "Molecular simulation techniques for sustainable technology and environmental applications - general overview and case studies", CISAP-3, 3° International conference on safety and environment in the process industry, Roma, 2008. P. Cosoli, G. Scocchi, S. Pricl, M. Fermeglia, "Many-scale molecular simulation for ABS-MMT nanocomposites: upgrading of industrial scraps", Microporous and Mesoporous Materials, 107, p.169, (2008).

Chapter 5, Paragraph 2: P. Cosoli, M. Ferrone, S. Pricl, M. Fermeglia, "Grand Canonical Monte Carlo simulations for VOCs adsorption in non-polar zeolites", International Journal of Environmental Technology and management, 7, p. 228, (2007).

Chapter 5, Paragraph 3: P. Cosoli, M. Ferrone, S. Pricl, M. Fermeglia, "Hydrogen sulphide removal from biogas by zeolite adsorption-part I: GCMC simulations", The Chemical Engineering Journal, 145, p.86, (2008). P. Cosoli, M. Ferrone, S. Pricl, M. Fermeglia, "Hydrogen sulphide removal from biogas by zeolite adsorption-part II: MD simulations", The Chemical Engineering Journal, 145, p. 93, (2008).

Chapter 5, Paragraph 4: P. Cosoli P., M. Fermeglia, M. Ferrone, "GCMC Simulations in Zeolite MFI and Activated Carbon for Benzene Removal from Exhaust Gaseous Streams", Molecular Simulation, 34, p. 1231, (2008).

Chapter 5, Paragraph 5: M. Lisal, P. Cosoli, W. R. Smith, S. K. Jain, and K. E. Gubbins, Molecular-level simulations of chemical reaction equilibrium for nitric oxide dimerization reaction in disordered nanoporous carbons, Fluid Phase Equilibria, 235, p. 18, 2008.

Chapter 6, Paragraph 2: P. Cosoli, M. Fermeglia, M. Ferrone, "Molecular Simulation of Atrazine Adhesion and Diffusion in a Saturated Sand Model", Journal of Soil and Sediment Contamination, under review.